

---

# Temporal dynamics of the longitudinal bunch profile in a laser wakefield accelerator

Matthias Heigoldt

---



München 2017



---

# **Temporal dynamics of the longitudinal bunch profile in a laser wakefield accelerator**

**Matthias Heigoldt**

---

Dissertation  
an der Fakultät für Physik  
der Ludwig–Maximilians–Universität  
München

vorgelegt von  
Matthias Heigoldt  
aus Schweinfurt

München, den 10.04.2017

Erstgutachter: Prof. Dr. Stefan Karsch

Zweitgutachter: Prof. Dr. Malte Kaluza

Tag der mündlichen Prüfung: 19.05.2017



---

## Deutsche Zusammenfassung

Diese Doktorarbeit beschäftigt sich mit der Messung des zeitlichen Profils von Elektronenpulsen aus lasergetriebenen Plasmabeschleunigern. Bei der sogenannten *laser wakefield acceleration* (LWFA) treibt ein hochintensiver Ultrakurzpulslaser eine Plasmawelle, die Beschleunigungsfelder von mehreren hundert GV/m aufrechterhalten kann, und somit die von derzeitigen Radiofrequenzbeschleunigern erreichbaren Felder um vier Größenordnungen übertrifft. Dies eröffnet die Möglichkeit die Größe und somit die Kosten derartiger Beschleuniger in Zukunft zu reduzieren.

Da der zu beschleunigende Elektronenpuls notwendigerweise auf die im Bereich von  $\mu\text{m}$  liegende Größe der Plasmawelle limitiert ist, liefern LWFAs darüber hinaus ultrakurze und brillante Elektronenpakete, die geeignet sind kompakte Kurzpuls-Röntgenquellen zu realisieren, sei es mittels Thomson-Rückstreuung, Betatronstrahlung oder durch Freie-Elektronen-Laser (FELs). Insbesondere für letztere Anwendung ist das Profil des Elektronenpakets ausschlaggebend, da es den zur Verfügung stehenden Spitzenstrom bestimmt, der eine wichtige Ausgangsgröße für ein Undulator-Design darstellt, welches den Selbstverstärkungsprozess optimal unterstützt.

Die in dieser Doktorarbeit beschriebenen Experimente dienten dazu, sowohl das zeitliche Profil des durch LWFA erzeugten Elektronenpakets zu vermessen, als auch dessen Entwicklung in Abhängigkeit von der Beschleunigungsstrecke und der Plasmadichte zu bestimmen. Durch Messung des Frequenzspektrums der von den beschleunigten Elektronenpaketen emittierten Übergangsstrahlung gelang es, das zeitliche Profil der Elektronenpulse mit einzigartiger Präzision zu rekonstruieren. Im Vergleich zu vorherigen Experimenten ist eine entscheidende Verbesserung durch die Einzelschuss-Messung eines breiten Frequenzbereichs von über vier Oktaven erreicht worden, wodurch eine Zeitauflösung des rekonstruierten Profils im Sub-Femtosekundenbereich ermöglicht wurde. Die durchgeführten Experimente regten weiterhin die Entwicklung eines neuartigen Algorithmus durch unsere Kollaboration mit der Universität von Oxford an. Im Gegensatz zu herkömmlichen Methoden benötigt dieser weder a priori Annahmen über eine bestimmte Profilform noch eine Extrapolation des gemessenen Spektrums.

Die vorgestellten Experimente benutzten den 50 TW Ti:Sa-Laser ATLAS sowie eine längenveränderliche Gaszelle. Unter optimierten Bedingungen wurden einzelne Elektronenpakete mit einer kürzesten Pulsdauer von  $4.8 \pm 0.2 \text{ fs}$  erzeugt, die eine maximale Energie von 650 MeV, eine Ladung von 30 pC und einen Spitzenstrom von  $5.7 \pm 1.2 \text{ kA}$  aufwiesen. Durch die Einzelschussmessung, sowie die Möglichkeit die Beschleunigungsstrecke zu variieren, war es erstmals möglich die zeitliche Entwicklung des Elektronenpakets in Abhängigkeit der Beschleunigungsstrecke zu bestimmen. Die Experimente geben Aufschluss über verschiedene Stadien der Beschleunigung, die letztlich durch sogenanntes Elektronen-Dephasing bzw. Defokussierung des Laserpulses charakterisiert sind, sowie die zugrundeliegende Plasmadynamik. Es konnte gezeigt werden, dass es nach Überschreiten der Dephasinglänge möglich wird ein zweites Elektronenpaket in die dem Laserpuls folgende oder eine spätere Periode der Plasmawelle zu injizieren. Die Dichte des ursprünglichen Elektronenpakets ist dabei ausreichend, um nach Defokussierung des Laserpulses eine rein Elektronenstrahl-getriebene Plasmawelle aufrechtzuerhalten. Der erzeugte Elektronen-Doppelpuls eignet sich somit hervorragend für weiterführende, ausschließlich Elektronenstrahl-getriebene Experimente und eröffnet die Möglichkeit eines Demonstrationsexperiments der sogenannten *afterburner acceleration*, bei der der zweite Elektronenpuls in der Plasmawelle des ersten Pulses nachbeschleunigt werden kann.



---

## Abstract

This thesis deals with the temporal characterisation of electron bunches produced by a laser plasma accelerator. In the so-called *laser wakefield acceleration* (LWFA) scheme, an ultra-short high-intensity laser pulse excites a plasma wave, which can sustain accelerating electric fields of several hundred GV/m, thus exceeding the fields attainable by current state-of-the-art radio frequency (RF) accelerators by four orders of magnitude, offering the prospect of downsizing both the size and cost of such machines.

Furthermore, by intrinsically confining the accelerated electron beam to the  $\mu\text{m}$ -scale size of the plasma wave, LWFAs provide ultra-short and highly brilliant beams, sparking great scientific interest for their application as a driver for compact sources of ultra-short X-ray pulses, e.g. Thomson-scattering, betatron sources or table-top free-electron lasers (FELs). The bunch profile is an important quantity for the application of these sources. With particular regard to the envisioned table-top FELs, it also determines the available peak current, an import input parameter for an appropriate undulator design that is optimized to support the self-amplified spontaneous emission (SASE) process.

The experiments presented in this thesis comprise the measurement of the temporal profile of electron bunches produced by LWFA and further investigation of the evolution of the temporal profile in dependence of the acceleration distance and the plasma density. By measuring the intensity spectrum of coherent transition radiation (CTR) emitted by LWFA-driven electron bunches in the frequency domain, the experiments allow a reconstruction of the longitudinal bunch profiles with unprecedented resolution. Compared to earlier work, a key improvement is the single-shot coverage of a broadband spectral range of more than four octaves, which yields a time resolution of the reconstructed bunch profile in the sub-femtosecond region. This work further inspired the development of a new iterative reconstruction algorithm by our collaborators from Oxford University. A major benefit of their algorithm is to avoid any a priori assumptions about the bunch shape or extrapolation of the spectrum outside the measured range, which are usually necessary in traditional methods.

In the presented experiments, the ATLAS 50TW Ti:Sa based laser system was used in conjunction with a hydrogen-filled gas cell. Under optimized conditions, the shortest bunch duration was determined to  $4.8 \pm 0.2$  fs for single electron bunches with a maximum energy of 650 MeV, a charge of 30 pC and a resulting peak current of  $5.7 \pm 1.2$  kA. In combination with the length-tunable gas target, the single-shot measurement technique allows for the first time to study the temporal evolution of the electron bunch profile as a function of the acceleration distance. This technique sheds new light onto the acceleration regimes characterized by electron dephasing and laser depletion as well as the involved plasma dynamics. The results show that after electron dephasing a second electron bunch can be injected in the first or subsequent plasma periods. After laser depletion, the first bunch is further found to be dense enough to drive its own beam-driven wakefield. The obtained double bunch structure is well suited for further beam-driven experiments and may enable a demonstration scheme for an energy boost by afterburner acceleration in the near future.



# Table of Contents

<b>1</b>	<b>Introduction</b>	<b>1</b>
<b>2</b>	<b>Plasma wakefield acceleration</b>	<b>5</b>
2.1	Basic laser-particle interaction . . . . .	5
2.1.1	Properties of electromagnetic radiation . . . . .	5
2.1.2	Single electron in a plane wave laser field . . . . .	7
2.1.3	Ponderomotive force . . . . .	10
2.2	Basic plasma properties . . . . .	11
2.3	Wakefield generation . . . . .	15
2.3.1	Fundamental equations . . . . .	15
2.3.2	Linear wakefields . . . . .	17
2.3.3	Nonlinear wakefields . . . . .	19
2.3.4	Wave breaking . . . . .	22
2.3.5	The bubble regime . . . . .	22
2.4	Trapping and acceleration . . . . .	24
2.5	Injection mechanisms & beam loading . . . . .	26
2.6	Laser pulse evolution in plasma . . . . .	30
2.7	Acceleration limits and scaling laws . . . . .	33
<b>3</b>	<b>Transition radiation</b>	<b>37</b>
3.1	Transition radiation emitted by a single electron . . . . .	37
3.1.1	The particle's self-field . . . . .	38
3.1.2	General framework . . . . .	39
3.1.3	Spectral and angular distribution . . . . .	41
3.1.4	Radiation from a finite-size target . . . . .	44
3.1.5	Radiation in the near-field . . . . .	45
3.2	Coherent transition radiation . . . . .	46
3.2.1	The form factor . . . . .	48
3.2.2	Effects of the bunch's spatial and momentum distribution . . . . .	49
3.2.3	The emittance . . . . .	53
3.2.4	Effects of beam propagation and phase space correlations . . . . .	54
3.3	The Bubblewrap reconstruction algorithm . . . . .	59
<b>4</b>	<b>Experimental Setup</b>	<b>65</b>
4.1	The ATLAS laser system . . . . .	65
4.2	Overview of the experimental setup . . . . .	68

4.3	Gas target . . . . .	69
4.4	Electron spectrometer . . . . .	69
4.5	CTR diagnostics . . . . .	71
4.6	The mid-infrared spectrometer . . . . .	73
4.6.1	Working principle . . . . .	74
4.6.2	Detection system . . . . .	78
4.7	Laser beam alignment . . . . .	79
4.8	Spectral response . . . . .	80
<b>5</b>	<b>Transmission of CTR through the detection optics</b>	<b>81</b>
5.1	Fourier optics beam propagation . . . . .	81
5.2	Model representation . . . . .	83
5.3	Numerical calculation . . . . .	85
5.4	Discussion . . . . .	86
<b>6</b>	<b>Momentum and transverse spatial distribution of LWFA electron bunches from a length-variable gas target</b>	<b>89</b>
6.1	Beam divergence . . . . .	89
6.2	Phase space separability . . . . .	91
6.3	Energy evolution . . . . .	93
6.4	Comparison to theory . . . . .	96
6.5	Summary . . . . .	99
<b>7</b>	<b>Characterisation of the longitudinal bunch profile by CTR</b>	<b>101</b>
7.1	Single-shot bunch profile reconstruction . . . . .	101
7.2	Temporal evolution of the longitudinal bunch profile . . . . .	106
7.2.1	Bunch evolution at $n_1 = 3.4 \times 10^{18} \text{ cm}^{-3}$ . . . . .	106
7.2.2	Bunch evolution at $n_2 = 7.7 \times 10^{18} \text{ cm}^{-3}$ . . . . .	110
7.2.3	Discussion . . . . .	113
7.3	Dependence of the bunch separation on plasma density . . . . .	115
7.4	Comparison with PIC simulations . . . . .	119
7.4.1	LWFA to PWFA transition . . . . .	119
7.4.2	Bunch separations exceeding $\lambda_p$ . . . . .	124
7.4.3	Conclusion . . . . .	126
7.5	Coherent enhancement at visible frequencies . . . . .	128
<b>8</b>	<b>Outlook</b>	<b>135</b>
<b>A</b>	<b>Spectral response of the mid-infrared spectrometer</b>	<b>139</b>
A.1	Measurement uncertainty in the frequency domain . . . . .	142
A.2	Measurement uncertainty in the time domain . . . . .	144
	<b>Bibliography</b>	<b>147</b>
	<b>List of abbreviations</b>	<b>161</b>

<b>List of publications</b>	<b>164</b>
<b>List of figures and data archiving</b>	<b>167</b>
<b>Acknowledgements</b>	<b>172</b>





---

# Chapter 1

## Introduction

Particle accelerators are one of the most versatile tools in physics research, having led to numerous scientific breakthroughs. Starting from the discovery of the electron, over nuclear and particle physics up to the recent discovery of the long-sought Higgs boson [1], these machines are an established driving force of fundamental research. Although the present energy frontier in particle physics requires ever increasing facilities such as the Large Hadron Collider (LHC) (with a circumference of 27 km), accelerators on any scale are nowadays also indispensable for industrial as well as medical applications [2].

On the other hand, the invention of lasers has triggered scientific discoveries and technological advances of no less importance. Founding an entirely new field of physics by enabling laser cooling and trapping of cold atoms (i.a. enabling the experimental demonstration of Bose-Einstein condensation [3]), these sources of coherent light have also become essential for applications in high speed communication, chemical and biological analysis, material processing and medicine, to name just a few.

Based on the reciprocal time-energy and space-momentum relations, just as higher output energies of particle accelerators are desired to resolve the fine structure of space and time, short-wavelength light sources experience great demand in order to investigate the structure of matter on the nm scale. Before the recent realization of free-electron lasers (FELs) [4, 5], advanced imaging applications mostly relied on synchrotron light sources in which radiation is generated by sending a GeV-scale electron beam through a bending magnet or an alternating magnetic field structure, causing the deflected electron beam to emit X-ray radiation. With the advent of FELs in 2002, coherent sources of X-ray radiation have become available, which hold promise for single-shot diffractive imaging of individual molecules, avoiding the need for a crystalline structure of the sample [6]. Furthermore, the high peak currents needed to start the self-amplified spontaneous emission (SASE) process in FELs are usually accompanied by electron bunch durations in the femtosecond range, which translate into bursts of X-rays with durations of the same order. Ultimately, such pulses may permit to observe the virtually unexplored area of extremely fast processes in biological and chemical reactions on a molecular level [7].

All these sources, be it high energy particle accelerators, synchrotron light sources or FELs, currently rely on radio frequency (RF) accelerators that typically provide acceleration gradients of several tens of MV per meter. In order to reach electron energies around 15 GeV that are needed to seed the LCLS (at present, the most advanced FEL light source located at SLAC National

## 1. Introduction

---

Accelerator Laboratory (SLAC)), an accelerator tunnel of approximately 1 km length is needed. Thus, relatively large and expensive facilities are required for FELs seeded by RF technology, which limits their proliferation to a few dedicated research facilities worldwide. As an extreme example of the scaling limits of current accelerator technology, the next projected design for a high energy collider (termed the International Linear Collider (ILC), which will provide collision energies between electron and positron beams of 1 TeV) will need a length of 32 km and require an estimated funding around 20 billion dollar [8]. This machine may likely mark the end of what can be practically realized by current accelerator technology.

For these reasons, alternative acceleration concepts have attracted increasing attention, as they may not only constitute viable alternatives to lower the cost and size of future high-energy accelerators, but also support the proliferation of accelerator-based light sources, including the aforementioned FELs.

Among these concepts, plasma based accelerators are considered as some of the most promising candidates. In contrast to RF accelerators, which are limited by material breakdown [9], plasma waves can sustain electric fields of several hundred GV/m at plasma densities around  $10^{18} \text{ cm}^{-3}$ . In the wakefield acceleration scheme, plasma electrons are either expelled by the electric field of a laser pulse (referred to as *laser wakefield acceleration (LWFA)*) or a dense bunch of charged particles (called *plasma wakefield acceleration (PWFA)*), leaving behind the ions, which can be regarded as a static homogeneous charge density due to their much higher inertia. The induced charge separation subsequently forces the expelled electrons to oscillate around the ion column, forming a wakefield behind the driver. This concept, first proposed by Tajima and Dawson [10] for LWFA and Chen et al. [11] for PWFA, has been demonstrated to achieve acceleration gradients of  $\sim 300 \text{ GV/m}$  [12] and  $\sim 40 \text{ GV/m}$  [13], respectively.

Since the first demonstration of quasi-monoenergetic LWFA beams in 2003 [14–16], significant progress has been achieved by optimizing the beam parameters, e.g. pushing the single stage gain to 4.2 GeV [17] and enhancing the stability and energy spread [18, 19] as well as characterizing important parameters such as the beam emittance and pulse duration [20–22]. Regarding PWFA, important milestones have been realized by the energy doubling of a fraction of 42 GeV electrons in a 85 cm long plasma wakefield accelerator [13] and the demonstration of monoenergetic acceleration of a discrete witness bunch [23].

Besides the high acceleration gradients, one of the unique benefits of wakefield accelerators is the small size of the acceleration structure that naturally confines the beam size to a fraction of the plasma wavelength (with a typical extent on the order of  $\mu\text{m}$ ). This results in a transverse beam emittance that rivals the one of state-of-the-art RF accelerators and in bunch durations in the fs range. The ultra-short bunch duration is a significant intrinsic advantage of wakefield accelerators compared to conventional technology. For the latter, substantial effort has to be invested in order to compress a previously intentionally chirped beam by magnetic chicanes to durations of several tens of fs, which are usually needed in order to reach the beam currents necessary for FEL operation or PWFA experiments.

Here, LWFA (which avoid the need for an external particle accelerator) hold promise to significantly simplify the acceleration process and shrink the required acceleration length by 3-4 orders of magnitude, lowering both the cost and footprint of these machines. In the future, plasma accelerators are therefore envisioned as a cost-effective driver for brilliant X-ray light sources, which may lead to their widespread availability for fundamental research at university-scale lab-

---

oratories as well as for medical and industrial imaging applications. The precise measurement of the temporal bunch shape is important for monitoring and optimizing LWFA electron bunches for the success of these applications. For example, besides the bunch's energy spread, the performance of an LWFA-driven FEL is largely determined by the available bunch profile [24].

On the other hand, experimental access to the detailed form of the longitudinal bunch profile and its evolution with acceleration distance is crucial for a deeper understanding of the physical mechanisms involved in wakefield accelerators. As will be shown in this work, under certain conditions a double bunch structure may be generated in a single LWFA stage. Such multi-bunch structures are of particular interest as a test bed for PWFA, enabling driver-witness type experiments, e.g. afterburner acceleration, in which a subsequent lower charge witness bunch is accelerated in the first bunch's wakefield [25]. In particular, PWFA has the benefit of avoiding the relative phase slippage between the laser driver and the accelerated bunch that is inherent to LWFA and ultimately limits the achievable energy gain per stage [12]. In such experiments, knowledge of the bunch profile is important for optimizing the experimental conditions and analysing its outcomes.

While originally predicted by particle-in-cell (PIC) simulations, the ultra-short bunch duration of LWFA electron beams has been confirmed experimentally in previous work by several authors [21, 22, 26]. However, neither a detailed shape of the electron bunch profile nor its dynamics could be assessed in these measurements. Similar to the experiments performed by Lundh et al. [21, 27], the bunch profile diagnostic developed in this work is based on a frequency-domain technique by measurement of the intensity spectrum of coherent transition radiation (CTR). In comparison, the presented measurements advance this earlier work in several key aspects:

- (i) the bandwidth of the recorded spectrum covers a broadband spectral range of more than 4 octaves, facilitating a time resolution of the reconstructed bunch profile in the sub-fs region.
- (ii) the CTR spectrum is recorded in a single shot, preventing shot-to-shot fluctuations in the electron bunch parameters distorting the measured spectrum and permitting to determine the shape of each generated bunch.
- (iii) the CTR spectrum is analysed with a new algorithm developed by our collaborators from Oxford University [28], which allows to reconstruct the electron bunch profile from the measured spectrum without the need to assume a specific form for the bunch profile or extrapolation of the spectrum outside the measured range.

These improvements enable us to obtain a detailed longitudinal bunch profile for each shot, quantify the shot-to-shot reproducibility and study its dependence on a wide range of experimental conditions, based on large shot statistics.

Besides using the well-controlled ATLAS laser system, the experiments described in this thesis employ a turbulence-free, steady-state flow and length-tunable gas cell, which delivered reproducible electron beams with low fluctuations in spectral shape, charge and cut-off energy. By varying the length of the gas cell, the experimental setup allows for the first time to study the temporal evolution of the bunch profile as a function of the acceleration distance and to probe the physics bunch evolution.

## 1. Introduction

---

The structure of this work is the following:

- Chapter II** introduces the physics behind wakefield excitation and electron acceleration.
- Chapter III** introduces the theoretical foundations of **CTR**, which is emitted when a charged particle beam crosses the boundary between two materials of different dielectric index. As derived in this chapter, the spectral shape of the emitted **CTR** contains information about the bunch's longitudinal charge profile. We also introduce the algorithm developed by our collaborators from Oxford University, which enables us to reconstruct the bunch profile from the measured **CTR** spectrum.
- Chapter IV** describes the experimental setup used for **LWFA** of electron bunches, including the layout of the employed **ATLAS** laser system and the spectrometer setup designed to measure the **CTR** spectrum. Particular focus is laid on the custom-built mid-infrared spectrometer, which is based on a design developed by our collaborators from **DESY**.
- Chapter V** gives details about the numerical calculation of the detectors' spectral response. Due to the peculiar emission characteristics of **CTR** as well as a possible contribution of a parasitic source of **CTR**, this procedure is necessary in order to obtain an accurate spectral measurement and a reliable reconstruction of the bunch profile.
- Chapter VI** describes the experimentally observed electron beam energy evolution in dependence of the target length. These measurements allow to determine important parameters of the acceleration process, including the laser depletion and electron dephasing lengths.
- Chapter VII** presents the main results of this thesis. The retrieved longitudinal bunch profiles are investigated in dependence of the acceleration parameters. The experimental results are discussed and further supported by numerical simulations.

---

## Chapter 2

# Plasma wakefield acceleration

In this chapter, the theoretical framework of laser and particle bunch driven wakefields will be presented. Starting from first principles, the generation of plasma waves is obtained alongside the involved physical phenomena of electron trapping and acceleration. Finally, the laser pulse evolution in plasma is discussed and scalings and limits on energy gain are established. This chapter gives an extensive overview of the involved physics that is needed to understand and interpret the experimental results presented in this thesis. An in-depth treatment of the underlying physics can be found in ref. [12, 29].

## 2.1 Basic laser-particle interaction

In this section we start out to study the basic single electron dynamics in laser fields which will lead to the concept of the ponderomotive force. First, some basic properties of light are introduced.

### 2.1.1 Properties of electromagnetic radiation

A laser beam can be described by a coherent electromagnetic wave. In classical electrodynamics, the propagation of light as an electromagnetic wave is governed by the Maxwell equations [30]

$$\begin{aligned}\nabla \cdot \mathbf{E} &= \frac{\rho}{\epsilon_0}, \\ \nabla \times \mathbf{E} &= -\frac{\partial \mathbf{B}}{\partial t}, \\ \nabla \cdot \mathbf{B} &= 0, \\ \nabla \times \mathbf{B} &= \frac{1}{c^2} \frac{\partial \mathbf{E}}{\partial t} + \mu_0 \mathbf{j}.\end{aligned}\tag{2.1}$$

Here,  $\mathbf{E}$  and  $\mathbf{B}$  denote the electric and magnetic fields,  $\epsilon_0$  is the vacuum permittivity,  $\mu_0$  the vacuum permeability and  $c = 1/\sqrt{\epsilon_0\mu_0}$  is the speed of light,  $\rho$  denotes the charge density and  $\mathbf{j}$  is the current density. The six (scalar) fields given by  $\mathbf{E}$  and  $\mathbf{B}$  may be reduced to four fields by

## 2. Plasma wakefield acceleration

introducing the vector and scalar potentials  $\mathbf{A}$  and  $\Phi$ , defined by

$$\begin{aligned}\mathbf{E} &= -\nabla\Phi - \frac{\partial\mathbf{A}}{\partial t}, \\ \mathbf{B} &= \nabla \times \mathbf{A}.\end{aligned}\tag{2.2}$$

Applying the Lorenz gauge ( $\nabla \cdot \mathbf{A} = -1/c^2 \partial\Phi/\partial t$ ), the Maxwell equations reduce to the simple wave equations [30]

$$\begin{aligned}\left(\Delta - \frac{1}{c^2} \frac{\partial^2}{\partial t^2}\right)\Phi &= -\frac{\rho}{\epsilon_0}, \\ \left(\Delta - \frac{1}{c^2} \frac{\partial^2}{\partial t^2}\right)\mathbf{A} &= -\mu_0 \mathbf{j}.\end{aligned}\tag{2.3}$$

When dealing with electromagnetic wave propagation in vacuum, the charge density  $\rho$  and current density  $\mathbf{j}$  vanish. A general solution to the homogeneous Maxwell equations is then given by a linear superposition of plane wave solutions with amplitude  $a_{\mathbf{k}}$ , i.e.

$$\mathbf{A}(\mathbf{r}, t) = \frac{1}{2} \left( \int a_{\mathbf{k}} \exp[i(\mathbf{k} \cdot \mathbf{r} - \omega t + \phi)] d\mathbf{k} + \text{c.c.} \right),\tag{2.4}$$

where the angular frequency  $\omega$  is related to the wave vector  $\mathbf{k}$  by the dispersion relation in vacuum  $\omega(\mathbf{k}) = c|\mathbf{k}|$  and  $\phi$  represents an absolute phase offset. Splitting this solution into a term that accounts for the center or *carrier frequency*  $\omega_L$  and an envelope function  $E_0(\mathbf{r}, t)$  that describes the pulse shape, the electric and magnetic fields of a laser pulse can be expressed by

$$\mathbf{E}(\mathbf{r}, t) = E_0(\mathbf{r}, t) \sin(\mathbf{k}_0 \cdot \mathbf{r} - \omega_L t + \phi),\tag{2.5}$$

$$\mathbf{B}(\mathbf{r}, t) = B_0(\mathbf{r}, t) \sin(\mathbf{k}_0 \cdot \mathbf{r} - \omega_L t + \phi).\tag{2.6}$$

Thus, in vacuum, the electric and magnetic fields oscillate in phase and from eq. (2.2) and eq. (2.4) follows that  $\mathbf{E} \perp \mathbf{k}, \mathbf{B} \perp \mathbf{k}, \mathbf{E} \perp \mathbf{B}$  and  $|\mathbf{B}| = |\mathbf{E}|/c$ . The energy flux density of the wave is given by the Poynting vector  $\mathbf{S} = (\mathbf{E} \times \mathbf{B})/\mu_0$  and the intensity  $I$  is obtained from the cycle averaged Poynting vector [30]

$$I = \langle |\mathbf{S}| \rangle_T = \frac{1}{\mu_0} \langle |\mathbf{E} \times \mathbf{B}| \rangle_T = \frac{\epsilon_0 c}{2} E_0^2.\tag{2.7}$$

In practical terms, the intensity may also be expressed as the laser pulse energy  $E$  that is transported through a surface perpendicular to the propagation direction within a certain time window. Assuming a Gaussian profile in space and time with a full width at half maximum (FWHM) pulse duration of  $t_{\text{FWHM}}$  and spot diameter of  $d_{\text{FWHM}}$ , the peak intensity is given by

$$I_0 = \frac{\left(2\sqrt{\frac{\ln 2}{\pi}}\right)^3 E}{t_{\text{FWHM}} d_{\text{FWHM}}^2} \approx \frac{0.83 E}{t_{\text{FWHM}} d_{\text{FWHM}}^2}.\tag{2.8}$$

This equation can be used for a simple estimate of the peak intensities that are commonly provided by high power laser systems. Typical parameters for the laser beam delivered by the [ATLAS](#) system during the experimental campaign presented in this thesis were a pulse energy of  $E = 1.5$  J, a time duration of  $t_{\text{FWHM}} = 28$  fs and a focused spot size of  $d_{\text{FWHM}} = 22 \mu\text{m}$ . With these values, a peak intensity of  $I_0 \approx 9 \times 10^{18} \text{ W/cm}^2$  is attainable, which corresponds to an extreme electric field strength of 8 TV/m.

### 2.1.2 Single electron in a plane wave laser field

Laser-plasma interactions generally represent a complex many-body problem that typically cannot be solved analytically. In weakly coupled systems such as underdense plasmas, the formation of collective dynamics is initiated by the interaction of individual charged particles with the laser pulse. In order to understand more complex phenomena, it is therefore instructive to approach the physics of LWFA by starting from the simple case of a single electron interacting with a plane wave linearly polarised laser field.

The equation of motion of a charge  $q$  moving with velocity  $\mathbf{v}$  in the electromagnetic field is governed by the Lorentz force

$$\frac{d\mathbf{p}}{dt} = q(\mathbf{E} + \mathbf{v} \times \mathbf{B}). \quad (2.9)$$

To obtain the conserved quantities of this system it proves beneficial to resort to the Lagrangian formalism. Expressing the electromagnetic field by its potentials  $\mathbf{A}$  and  $\Phi$ , the Lagrangian  $L$  of a relativistic particle with mass  $m$  is given by [30, 31]

$$L = -mc^2 \sqrt{1 - \frac{\mathbf{v}^2}{c^2}} + q\mathbf{v} \cdot \mathbf{A} - q\phi. \quad (2.10)$$

The Lorentz force equation can be recovered from the Lagrangian by the Euler-Lagrange equation  $\frac{\partial L}{\partial \mathbf{r}} = \frac{d}{dt} \frac{\partial L}{\partial \mathbf{v}}$ . The merit of the Lagrangian formalism is that the conserved quantities of the system can be easily obtained from its symmetries and invariants without explicitly solving the differential of eq. (2.9) [31]. We first compile the canonical momentum  $\mathbf{p}^{can}$ , which is conjugate to the spatial coordinate  $\mathbf{r}$

$$\mathbf{p}^{can} = \frac{\partial L}{\partial \mathbf{v}} = m\gamma\mathbf{v} + q\mathbf{A}, \quad (2.11)$$

where  $\gamma$  denotes the Lorentz factor defined by  $\gamma = (1 - \mathbf{v}^2/c^2)^{-1/2}$ . In the case of a linearly polarized plane wave travelling along the  $z$ -direction, the potentials can be expressed as a sole function of time  $t$  and longitudinal coordinate  $z$ , i.e.  $\phi = \phi(z, t)$  and  $\mathbf{A} = \mathbf{A}_\perp(z, t)$ . Applying Noether's theorem [32], one directly obtains the conservation laws. Since the system is invariant under translations in the transverse coordinate  $\mathbf{r}_\perp$ , the canonical momentum in transverse direction is conserved

$$\frac{d}{dt} \mathbf{p}_\perp^{can} = \frac{d}{dt} \frac{\partial L}{\partial \mathbf{v}_\perp} = \frac{\partial L}{\partial \mathbf{r}_\perp} = 0 \quad \rightarrow \quad \mathbf{p}_\perp + q\mathbf{A}_\perp = \mathbf{c}_1. \quad (2.12)$$

A second conserved quantity is found by considering the propagation of the waveform with time, i.e.  $\mathbf{A}_\perp(t, z) = \mathbf{A}_\perp(t - z/c)$ . We now use the Weyl gauge  $\phi = 0$  [33]. The energy of the particle is given by the Hamiltonian  $H(\mathbf{r}, \mathbf{p}, t) = E$ . Using the relation  $dH/dt = -\partial L/\partial t$ , one obtains

$$\frac{dH}{dt} = -\frac{\partial L}{\partial t} = c \frac{\partial L}{\partial z} = c \frac{d}{dt} \frac{\partial L}{\partial v_\parallel} = c \frac{d}{dt} p_\parallel^{can} = c \frac{d}{dt} p_\parallel, \quad (2.13)$$

where in the last step  $A_\parallel = 0$  has been used as we consider a purely transverse wave. Integration of eq. (2.13) yields the second conserved quantity

$$E - cp_\parallel = \mathbf{c}_2. \quad (2.14)$$



## 2. Plasma wakefield acceleration

---

For an electron initially at rest the integration constants are  $c_1 = 0$  and  $c_2 = m_e c^2$ . Using the relativistic energy-momentum relation  $E = \gamma m_e c^2 = \sqrt{(m_e c^2)^2 + (p_\perp c)^2 + (p_\parallel c)^2}$  together with both constants of motion (eq. (2.12) and eq. (2.14)), the kinetic energy can be expressed by

$$E_{kin} = (\gamma - 1)m_e c^2 = p_\parallel c = \frac{p_\perp^2}{2m_e} = \frac{e^2 \mathbf{A}_\perp^2}{2m_e} \quad (2.15)$$

and a relation between  $p_\perp$  and  $p_\parallel$  is established:

$$\tan(\theta) = \frac{p_\perp}{p_\parallel} = \sqrt{\frac{2}{\gamma - 1}}. \quad (2.16)$$

For a linearly polarised wave  $\mathbf{A} = (A_0, 0, 0)$  travelling along the z-direction, the trajectory of an electron is now obtained from the conserved quantities. Using normalized units, the equations of motion take the simple form

$$\mathbf{a} = \frac{e\mathbf{A}}{mc}, \quad (2.17)$$

$$\mathbf{p}'_\perp = \frac{\mathbf{p}_\perp}{mc} = \frac{\gamma}{c} \frac{d\mathbf{r}_\perp}{dt} = \mathbf{a} = (a_0, 0, 0), \quad (2.18)$$

$$p'_\parallel = \frac{p'_\perp}{2} = \frac{\gamma}{c} \frac{dr_\parallel}{dt} = \frac{a^2}{2}, \quad (2.19)$$

$$\gamma = 1 + \frac{a^2}{2}. \quad (2.20)$$

For a laser pulse with  $\mathbf{a} = (a_0, 0, 0) \sin(\omega\tau)$ , where  $\tau = t - z/c$ , the equations of motion can be directly integrated (using  $d\tau = dt/\gamma$ )

$$\begin{aligned} x(\tau) &= \frac{ca_0}{\omega} \cos(\omega\tau), \\ z(\tau) &= \frac{ca_0^2}{4} \left( \tau + \frac{1}{2\omega} \cos(2\omega\tau) \right). \end{aligned} \quad (2.21)$$

The trajectory of an electron is thus composed of two terms. A transverse motion with the laser frequency  $\omega$  that scales linearly with  $a_0$  and a longitudinal motion consisting of a drift term

$$z_d(t) = \frac{a_0^2}{a_0^2 + 4} ct \quad (2.22)$$

superimposed by an oscillation with frequency  $2\omega$ . Since the drift velocity scales with  $a_0^2$  for highly relativistic pulses with  $a_0 \gg 1$ , the trajectory is dominated by the longitudinal motion and strongly bent in the forward direction with an angle  $\theta$  to the laser propagation direction given by eq. (2.16). In the drift frame with coordinates  $(x', z')$  this results in a figure-8 motion described by:

$$x' = \frac{ac}{\omega} \cos(\omega t), \quad z' = \frac{a_0 c}{8\omega} \cos(2\omega\tau). \quad (2.23)$$



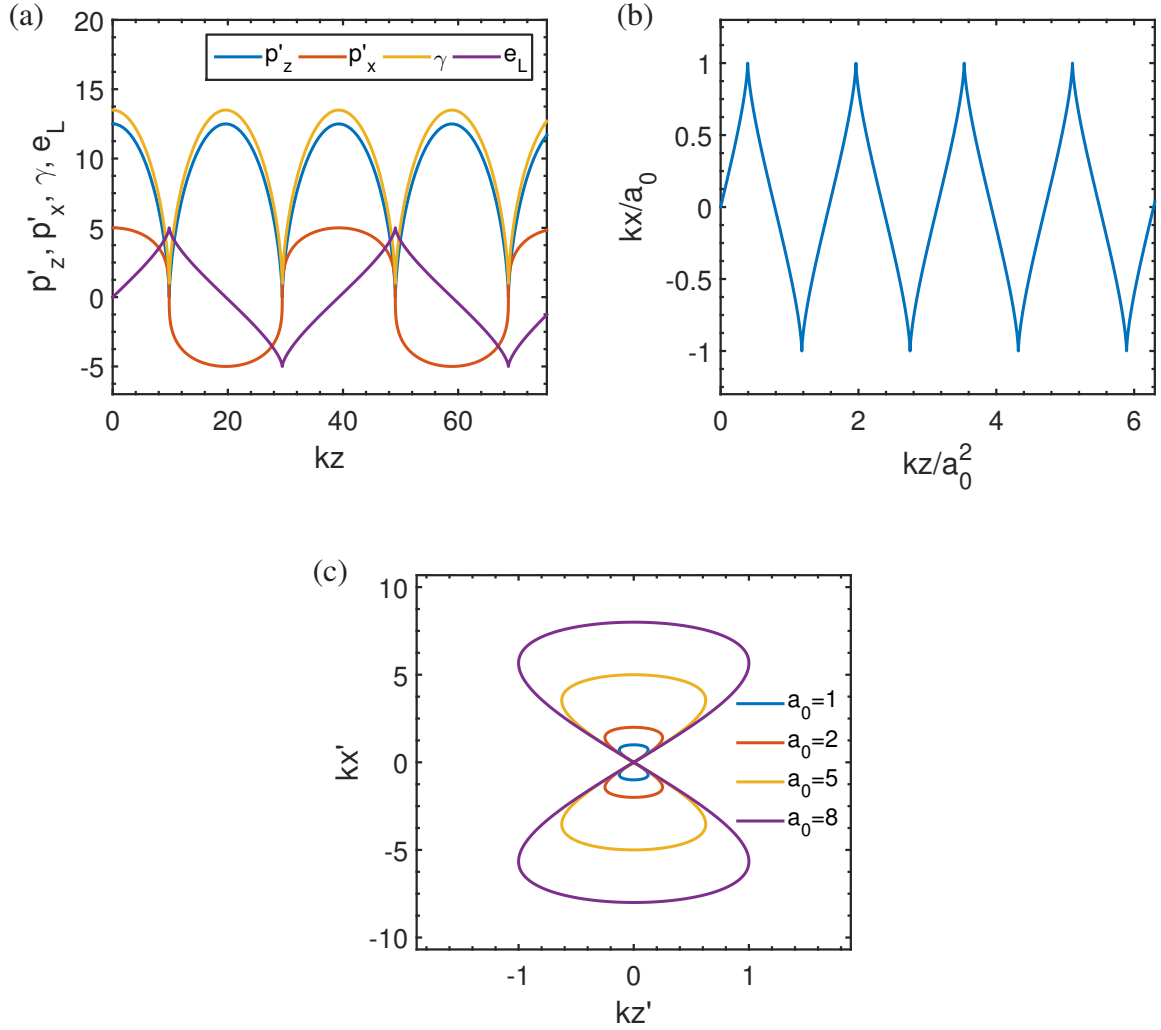


**Figure 2.1:** Electron dynamics in a plane wave laser field. (a) shows the particle's momentum and kinetic energy during its slippage through the laser field  $e_L$  ( $a_0 = 5$ ). The resulting motion in the laboratory frame is shown in (b). While oscillating in polarisation direction, the electron is pushed forward by the  $\mathbf{v} \times \mathbf{B}$  force and drifts in laser propagation direction. (c) shows the characteristic figure-8 motion in the drift frame.

The electron dynamics are depicted in Fig. 2.1. As shown in Fig. 2.1a, each half cycle of the driving field the electron is accelerated and decelerated again, both in longitudinal and transverse direction. However, its kinetic energy is only dependent on the transverse electric field strength (cf. eq. (2.20)). The forward acceleration is due to the  $\mathbf{v} \times \mathbf{B}$  term of the Lorentz force, which transforms the transverse velocity into a forward motion. Since this force always acts perpendicular to the trajectory, no energy is transferred. The resulting particle position in the laboratory frame is plotted in Fig. 2.1b and, after subtracting the drift term, results in the typical figure-8 motion in the drift frame as shown in Fig. 2.1c.

In the case of a plane wave of infinite transverse extent, no net energy transfer from the laser

## 2. Plasma wakefield acceleration

pulse to a charged particle takes place, even in the case of a finite pulse length, where the electron motion simply stops after the laser pulse has passed. However, a net energy gain can be achieved if the laser has an intensity gradient in space. An electron initially located in the center of the focal spot will then be displaced by the transverse electric field of the laser to a region of lower intensity. As the electric field changes sign the restoring force is smaller, such that the electron can not return to its initial position. This results in a drift motion of the electron's oscillation center towards regions of lower intensity, while at the same time its mean kinetic energy is increased. This so-called *ponderomotive force* arising from the cycle averaged Lorentz force will now be derived.

### 2.1.3 Ponderomotive force

For non-relativistic velocities, the ponderomotive force is easily derived from the Lorentz force. In this case, the  $\mathbf{v} \times \mathbf{B}$  term can be neglected, as  $|\mathbf{B}| = |\mathbf{E}|/c \ll |\mathbf{E}|$ . Considering a position dependent laser field  $\mathbf{E}(\mathbf{x}, t) = \mathbf{E}(\mathbf{x}) \cdot \sin(\omega t)$  the equation of motion reads

$$\frac{d\mathbf{v}}{dt} = \frac{\partial \mathbf{v}}{\partial t} + (\mathbf{v} \cdot \nabla) \mathbf{v} = -\frac{e}{m_e} \mathbf{E}(\mathbf{x}) \sin(\omega t). \quad (2.24)$$

We now decompose the spatial dependence of the electric field by Taylor expansion, i.e.  $\mathbf{E}(\mathbf{x}) = \mathbf{E}_0 + (\Delta \mathbf{x} \cdot \nabla) \mathbf{E}(\mathbf{x}_0)$ . To the lowest order of  $\mathbf{E}(\mathbf{x})$  its solution is

$$\mathbf{v} = \frac{e\mathbf{E}(\mathbf{x})}{m_e\omega} \cos(\omega t), \quad (2.25)$$

which describes the transverse oscillation of the electron. By averaging over the fast oscillation cycle of the carrier frequency and requiring the electric field envelope to not change significantly during this time scale, one obtains

$$m_e \frac{\partial \langle \mathbf{v} \rangle_T}{\partial t} = -e \langle \mathbf{E}(\mathbf{x}, t) \rangle_T - m_e \langle \mathbf{v} \cdot \nabla \mathbf{v} \rangle_T = -\frac{1}{4} \frac{e^2}{m_e \omega^2} \nabla E^2(\mathbf{x}). \quad (2.26)$$

Thus, as the quiver motion is averaged out, the electron's oscillation center experiences a force proportional to the gradient of the laser intensity, the ponderomotive force

$$\mathbf{F}_p = -\frac{1}{4} \frac{e^2}{m_e \omega^2} \nabla E^2(\mathbf{x}) = -\frac{q^2}{8\pi^2 \epsilon_0 m_e c^3} \nabla (I \lambda^2), \quad (2.27)$$

$$= -m_e c^2 \nabla \left\langle \frac{a^2}{2} \right\rangle = -m_e c^2 \nabla \frac{a^2}{4}. \quad (2.28)$$

In the relativistic case also the longitudinal momentum has to be taken into account. Employing the Lagrange formalism, a relativistic expression for the ponderomotive force is given by Bauer et al. [34]

$$\mathbf{F}_{p,rel} = -m_e c^2 \nabla \bar{\gamma}, \quad (2.29)$$

where  $\bar{\gamma}$  is the particle's Lorentz factor averaged over one oscillation cycle. Comparing eq. (2.28) and eq. (2.29), we also find that  $\bar{\gamma} = a^2/4$  (cf. eq. (2.20)).

Another quantity of interest is the electric field strength required for the electron quiver motion to become relativistic. From eq. (2.25), the maximum velocity is given by

$$v_{max} = \frac{eE}{m_e \omega} = \frac{eA_0}{m_e}. \quad (2.30)$$

Thus, in the non-relativistic treatment, the electron's quiver velocity reaches  $c$  for  $a_0 = 1$ . Although this classical derivation is not stringent for relativistic speeds, the definition of  $a_0$  provides a convenient quantity to distinguish between the non-relativistic ( $a_0, v/c \ll 1$ ) and relativistic ( $a_0 \gg 1$ ) regimes. As an engineering formula, the laser intensity (eq. (2.7)) is conveniently expressed in terms of  $a_0$  by

$$I_0 = \frac{2\pi^2 \epsilon_0 m_e^2 c^5}{e^2 \lambda^2} a_0^2 \approx \frac{1.37 a_0^2}{\lambda^2 [\mu\text{m}]} \times 10^{18} \text{ W/cm}^2. \quad (2.31)$$

## 2.2 Basic plasma properties

So far the basic interaction of a single charged particle with laser light has been discussed. In this section collective phenomena arising from the interaction of laser light with plasma are considered. Plasma is a state of matter containing unbound positively and negatively charged particles. It is distinguished from an only locally ionized medium by its definition of being a quasi-neutral gas of charged (and neutral) particles that also exhibits collective effects [35].

### Debye length

An essential characteristic of plasma is that the unbound charges can interact with a number of nearby neighbours, which enables the emergence of collective effects. The range over which interactions can occur before the electrostatic field of a particle is screened by the surrounding plasma is given by the Debye length  $\lambda_D$  and the electrostatic potential of a test charge in plasma decays as  $\phi(r) \propto \exp(-r/\lambda_p)$ .

Beyond this length the plasma is effectively neutral. The Debye length is given by

$$\frac{1}{\lambda_D^2} = \frac{1}{\lambda_{D,e}^2} + \frac{1}{\lambda_{D,ion}^2}, \quad (2.32)$$

where  $\lambda_{D,e}^2$  and  $\lambda_{D,ion}^2$  denote the respective shielding length of the electron and ion species. In the case of laser-matter interactions, the ion species are commonly treated as an immobile positively charged background due to their high inertia. This assumption is justified by the ion's much lower vector potential of  $a = eA/m_{ion}c \ll 1$  (achievable with present laser technology) and the short timescale of the interaction. Thus, when treating laser produced plasmas, only the electrons have to be considered. For the latter the Debye length is given by

$$\lambda_D = \sqrt{\frac{\epsilon_0 k_B T_e}{n_e e^2}}, \quad (2.33)$$

where  $T_e$  denotes the electron temperature,  $k_B$  is the Boltzmann constant and  $n_e$  is the electron density.

## 2. Plasma wakefield acceleration

The average number of particles within a sphere with a radius equal to the Debye length is given by the Debye number

$$N_D = \frac{4\pi}{3} n_e \lambda_D^3. \quad (2.34)$$

For the common definition of a plasma the Debye number has to satisfy  $N_d \gg 1$ . The more particles can interact electrostatically within the Debye sphere, the less pronounced is the effect of collisions. While the latter influence the particle motion locally, the range of the electric and magnetic fields of moving charges affects the motion of other charged particles far away. Thus,  $N_D$  can be used of as measure of the dominance of collective interactions over collisions [36]. In laser plasma interactions this is guaranteed by the energy transfer from the wake driver to the electrons, which leads to a high particle temperature. Additionally, in plasma wakefield experiments,  $n_e$  is typically on the order of  $(10^{18} - 10^{19}) \text{ cm}^{-3}$ . Thus,  $\lambda_D$  is large, the Debye sphere is densely populated and the coupling between particles is weak.

The notion of charge neutrality implies that the dimensions  $d$  of the plasma are much larger than  $\lambda_D$  such that local charge concentrations or fields are shielded in a relatively short distance. Then the plasma appears neutral to an external observer and the bulk of the plasma remains field-free over a length scale  $\gg \lambda_D$ . Thus, a second criterion for an ionized gas to be a plasma is that  $\lambda_D \ll d$  [35].

### Ionization

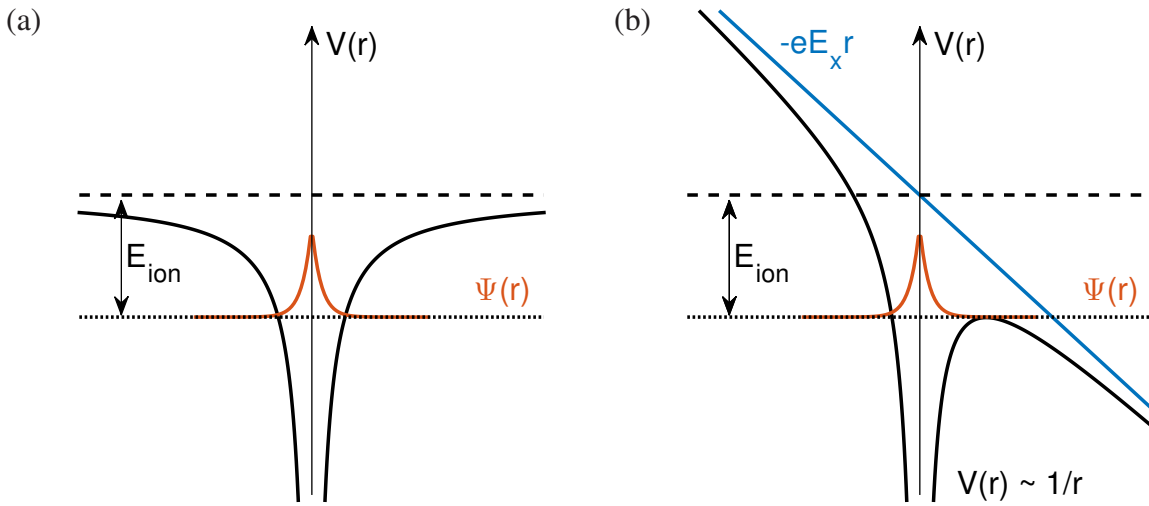


**Figure 2.2:** Ionization mechanisms. Schematic drawing of (a) an electron bound in an unperturbed Coulomb potential and (b) in a Coulomb potential disturbed by an external laser field. The unperturbed wave function  $\Psi(r)$  of an s-electron is depicted for reference. If the potential barrier is suppressed below its ground state energy (represented by the dotted line) barrier suppression ionization occurs, for lower laser fields the tunnel probability is increased.

For plasma generation, ionization can be accomplished by high temperatures or strong electromagnetic fields. In the case of **LWFA** it is usually produced by a high voltage or, most easily, by the strong electromagnetic field of the laser pulse itself. In order to ionize a specific element, the bound electron has to overcome the potential barrier of the nucleus. For hydrogen the ionization energy amounts to  $E_{ion} = 13.6 \text{ eV}$ . The photon energy of the employed **Ti:Sa** laser ( $\lambda_L \approx 800 \text{ nm}$ ) of  $E_{ph} = \hbar\omega_L \approx 1.6 \text{ eV}$  is insufficient to ionize a hydrogen gas target directly by the photoelectric effect. However, in the presence of a strong laser field, ionization can take place via alternative mechanisms called *multi-photon*, *tunnel* or *barrier-suppression ionization*. The occurrence of the different processes depends on laser intensity and can be classified by the Keldysh parameter [37, 38]

$$\gamma_K = \omega_L \sqrt{\frac{2E_{ion}}{I_L}}, \quad (2.35)$$

where  $I_L$  is the laser intensity. The Keldysh parameter is a measure for the ratio between the tunnelling time and one half of the laser period [39]. When  $\gamma_K > 1$ , the binding potential of the nucleus remains practically undisturbed and the only process leading to ionization is absorption of multiple photons. For  $\gamma_K < 1$ , the laser field becomes comparable to the core's Coulomb field and the potential barrier is lowered, which increases the electron's tunnelling probability. For even higher laser intensities ( $\gamma_K \ll 1$ ), the potential is strongly disturbed and suppressed even below the electron's ground state potential such that the electron is released from the binding potential. This mechanism, called barrier suppression ionization, occurs for laser intensities exceeding [38]

$$I_{BSI} = \frac{\pi^2 c \epsilon_0^3 E_{ion}^4}{2Z^2 e^6}, \quad (2.36)$$

where  $Z$  is the effective nuclear charge of the element. For hydrogen  $I_{BSI} = 1.4 \times 10^{14} \text{ W/cm}^2$ . The typical laser intensity provided by the **ATLAS** laser is on the order of  $I_L \sim 10^{18} \text{ W/cm}^2$ . Hence, even the pedestal of the main laser pulse is intense enough to ionize the employed hydrogen gas target before arrival of the main pulse. One can therefore safely assume a fully ionized plasma during the main interaction.

## Plasma waves

In a neutral plasma, electrons displaced from their equilibrium position feel a restoring force caused by the unshielded positive ion background and start to oscillate about their equilibrium position. Assuming a small density perturbation, the harmonic oscillation contains only one frequency component, i.e.  $\mathbf{E}(\mathbf{r}, t) = \text{Re} [\mathbf{E}_k e^{i(\mathbf{k}\mathbf{r} - \omega t)}]$ . Resorting to the Maxwell equations and combining the Faraday equation with Ampere's law yields

$$\nabla \times \nabla \times \mathbf{E} = -\mu_0 \partial_t \mathbf{j} - \mu_0 \epsilon_0 \frac{\partial^2 \mathbf{E}}{\partial t^2}. \quad (2.37)$$

The partial derivative of the current density  $\partial_t \mathbf{j} = -en_e \partial_t \mathbf{v}$  is obtained from the Lorentz force by  $\partial_t \mathbf{v} = -e\mathbf{E}/m_e$ . Hence, dropping the oscillatory terms, the solution of eq. (2.37) in Fourier space is given by

$$\mathbf{k} \times \mathbf{k} \times \mathbf{E}_k = \mu_0 \left( \frac{n_e e^2}{m_e} - \epsilon_0 \omega^2 \right) \mathbf{E}_k. \quad (2.38)$$

## 2. Plasma wakefield acceleration

---

### Langmuir waves

For  $\mathbf{k} \parallel \mathbf{E}_k$ , the left hand side of eq. (2.38) equals zero. The right hand side describes an oscillation of the electron density with the plasma frequency  $\omega_p$ , where

$$\omega_p = \sqrt{\frac{e^2 n_e}{m_e \epsilon_0}}. \quad (2.39)$$

This longitudinal electrostatic plasma wave is called a Langmuir wave. Our simple derivation implicitly assumes a collision-less plasma where the thermal motion of the electrons has been neglected, which is also termed the *cold plasma approximation*. When including thermal effects, a general dispersion relation valid for a finite temperature plasma was derived by Bohm and Gross [40]:

$$\omega^2 = \omega_p^2 + 3v_{t,e}^2 k^2, \quad (2.40)$$

where  $v_{t,e} = k_B T / \gamma m_e$  is the thermal speed of the electrons.

### Electromagnetic waves

For  $\mathbf{k} \perp \mathbf{E}_k$ , eq. (2.38) yields the dispersion relation of electromagnetic waves propagating in plasma

$$\omega_L^2 = \omega_p^2 + c^2 k^2. \quad (2.41)$$

Depending on the ratio of  $\omega_L / \omega_p$ , eq. (2.41) identifies two distinct cases. If  $\omega_L > \omega_p$ , the frequency of the electromagnetic field is higher than the plasma frequency and the plasma response is too slow to follow these oscillations. In this case the wavenumber  $k$  is real, the plasma is transparent to light and called underdense. If  $\omega_p > \omega_L$ , the plasma is called overdense. Here,  $k$  becomes imaginary and describes an evanescent wave inside the plasma as the electron response time  $\tau \sim \omega_p^{-1}$  is fast enough to follow  $\omega_L$  and shield the electromagnetic field. The plasma density at which  $\omega_p = \omega_L$  is called the *critical density* and is given by

$$n_c = \frac{\epsilon_0 m_e}{e^2} \omega_L^2 = \frac{1.12}{\lambda_L^2 [\mu\text{m}]} \times 10^{21} \text{ cm}^{-3}. \quad (2.42)$$

The dispersion relation (eq. (2.41)) determines the non-relativistic group and phase velocities of a laser pulse propagating through underdense plasma:

$$v_{gr} = \frac{d\omega_L}{dk} = \eta c, \quad (2.43)$$

$$v_{ph} = \frac{\omega_L}{k} = \frac{c}{\eta}, \quad (2.44)$$

$$\text{and } \eta = \sqrt{1 - \frac{\omega_p^2}{\omega_L^2}}, \quad (2.45)$$

where  $\eta$  is the refractive index. Thus, for underdense plasmas,  $0 < \eta \leq 1$  is real and light propagates with group velocity  $v_{gr} = c\eta$  and phase velocity  $v_{ph} = c/\eta$ , while for overdense

plasmas ( $\omega_p > \omega_L$ )  $\eta$  becomes imaginary and the incident light is fully reflected. We further define the rapidity and Lorentz factor associated with  $v_{gr}$  by

$$\beta_{gr} = \frac{v_{gr}}{c} = \sqrt{1 - \frac{n_e}{n_c}}, \quad (2.46)$$

$$\gamma_{gr} = \left( \sqrt{1 - \beta_{gr}^2} \right)^{-1} = \sqrt{\frac{n_c}{n_e}} = \frac{\omega_L}{\omega_p}. \quad (2.47)$$

## 2.3 Wakefield generation

A high intensity laser pulse or a dense bunch of charged particles can excite plasma waves by its respective ponderomotive force or Coulomb potential. In contrast to the purely longitudinal Langmuir waves derived above, in these cases plasma electrons are also expelled in transverse direction and the resultant plasma wave exhibits a more complex three-dimensional structure. In the following we will derive the fundamental equations needed to describe wakefield excitation. These allow to analytically solve the resulting wakefield in the 3D linear and in the 1D nonlinear regime.

### 2.3.1 Fundamental equations

We revert to the inhomogeneous Maxwell equations given in eq. (2.1). The positive charge density of the immobile ion background is denoted by  $n_0$ ,  $n_e$  describes the electron density and  $n = n_e/n_0$ . Using  $\rho = e(n_0 - n_e)$  and  $\mathbf{j} = -en_e\mathbf{v}$ , where  $\mathbf{v}$  is the electron fluid velocity, the Maxwell equations read

$$\nabla \cdot \mathbf{E} = \frac{e(n_0 - n_e)}{\epsilon_0}, \quad (2.48)$$

$$\nabla \times \mathbf{E} = -\frac{\partial \mathbf{B}}{\partial t}, \quad (2.49)$$

$$\nabla \cdot \mathbf{B} = 0, \quad (2.50)$$

$$\nabla \times \mathbf{B} = \mu_0 \epsilon_0 \frac{\partial \mathbf{E}}{\partial t} - \mu_0 en_e \mathbf{v}. \quad (2.51)$$

We also recall the electromagnetic potentials introduced in eq. (2.2)

$$\begin{aligned} \mathbf{E} &= -\nabla \Phi - \frac{\partial \mathbf{A}}{\partial t}, \\ \mathbf{B} &= \nabla \times \mathbf{A}, \end{aligned} \quad (2.52)$$

and use the Coulomb gauge  $\nabla \cdot \mathbf{A} = 0$ .

#### Poisson equation

With the definition of the normalized potential  $\phi = e\phi/m_e c^2$ , the Poisson equation becomes

$$\boxed{\nabla^2 \phi = \frac{\omega_p^2}{c^2} (n - 1)}. \quad (2.53)$$

## 2. Plasma wakefield acceleration

---

### Continuity equation

Neglecting recombination and assuming a fully ionized plasma, the total charge in each fluid element is conserved. Taking the divergence of eq. (2.51) and using eq. (2.48) yields the continuity equation

$$\boxed{\frac{\partial n}{\partial t} + c \nabla(n\boldsymbol{\beta}) = 0}. \quad (2.54)$$

### Electro-magnetic wave equation

We now express eq. (2.51) in terms of the potentials and use the vector identity  $\nabla \times (\nabla \times \mathbf{A}) = \nabla \cdot (\nabla \cdot \mathbf{A}) - \nabla^2 \mathbf{A}$ :

$$\nabla \times \nabla \times \mathbf{A} = -\mu_0 en_e \mathbf{v} - \frac{1}{c^2} \frac{\partial}{\partial t} \left( \nabla \Phi + \frac{\partial \mathbf{A}}{\partial t} \right), \quad (2.55)$$

$$\left( c^2 \nabla^2 - \frac{\partial^2}{\partial t^2} \right) \mathbf{A} = \frac{en_e}{\epsilon_0} \mathbf{v} + \frac{\partial}{\partial t} \nabla \Phi, \quad (2.56)$$

$$\boxed{\left( c^2 \nabla^2 - \frac{\partial^2}{\partial t^2} \right) \mathbf{a} = \omega_p^2 n \boldsymbol{\beta} + c \frac{\partial}{\partial t} \nabla \phi}, \quad (2.57)$$

where  $\omega_p$  denotes the undisturbed plasma frequency. We have now obtained the normalized wave equation which describes the propagation of electromagnetic modes through plasma.

### Equation of motion

Expressing the equation of motion (eq. (2.9)) in terms of the electromagnetic potentials and using  $\mathbf{p} = \gamma m \mathbf{v}$  yields

$$\frac{d\mathbf{p}}{dt} = \left( \frac{\partial}{\partial t} + \mathbf{v} \cdot \nabla \right) \mathbf{p} = -e(\mathbf{E} + \mathbf{v} \times \mathbf{B}) = e \left( \nabla \Phi + \frac{\partial \mathbf{A}}{\partial t} - \mathbf{v} \times \nabla \times \mathbf{A} \right). \quad (2.58)$$

Together with the vector identity  $\nabla p^2 = 2[(\mathbf{p} \cdot \nabla) \mathbf{p} + \mathbf{p} \times (\nabla \times \mathbf{p})]$  and

$$(\mathbf{v} \cdot \nabla) \mathbf{p} = \frac{1}{2m\gamma} \nabla p^2 - \mathbf{v} \times (\nabla \times \mathbf{p}) = mc^2 \nabla \gamma - \mathbf{v} \times (\nabla \times \mathbf{p}), \quad (2.59)$$

the partial derivative of  $\mathbf{p}$  with respect to time is

$$\frac{\partial}{\partial t} \mathbf{p} = e \nabla \Phi + e \frac{\partial \mathbf{A}}{\partial t} - mc^2 \nabla \gamma + \mathbf{v} \times (\nabla \times (\mathbf{p} - e\mathbf{A})). \quad (2.60)$$

Taking the curl of this equation,

$$\frac{\partial}{\partial t} (\nabla \times (\mathbf{p} - e\mathbf{A})) = \nabla \times (\mathbf{v} \times (\nabla \times (\mathbf{p} - e\mathbf{A}))), \quad (2.61)$$

shows that  $\nabla \times (\mathbf{p} - e\mathbf{A}) = 0$  for all times for the initial condition of an unperturbed plasma before arrival of the laser pulse [41]. The equation of motion thus becomes

$$\boxed{\frac{\partial}{\partial t} \mathbf{p} = e \nabla \Phi + e \frac{\partial \mathbf{A}}{\partial t} - mc^2 \nabla \gamma}. \quad (2.62)$$



### 2.3.2 Linear wakefields

In the non-relativistic regime the induced wakefields can be solved analytically. In the following, we derive the wakefield produced by a weak laser (with an envelope given by  $a$ ) or particle bunch driver (with a charge profile given by  $n_b$ ). Both induce a plasma density perturbation described by  $\delta n$ . For small density perturbations ( $n_e = n_0 + \delta n$ ,  $\delta n \ll n_0$ ), linear perturbation theory can be applied to the cold-fluid Maxwell equations. In this case, the linearised continuity equation, the equation of motion and Gauss's law read [42]

$$\frac{\partial}{\partial t} \delta n + n_0 \nabla \cdot \mathbf{v} = 0, \quad (2.63)$$

$$\frac{\partial \mathbf{v}}{\partial t} = -\frac{e\mathbf{E}}{m_e} - c^2 \nabla \frac{a^2}{4}, \quad (2.64)$$

$$\nabla \cdot \mathbf{E} = \frac{-e(n_b + \delta n)}{\epsilon_0}. \quad (2.65)$$

By taking the time derivative of eq. (2.63), the divergence of eq. (2.64) and plugging both into eq. (2.65), we obtain a wave equation for the plasma density perturbation

$$\left( \frac{\partial^2}{\partial t^2} + \omega_p^2 \right) \frac{\delta n}{n_0} = c^2 \nabla^2 \frac{a^2}{4} - \omega_p^2 \frac{n_b}{n_0}. \quad (2.66)$$

The density perturbation that forms the plasma wave follows the wake driver and thus has a phase velocity determined by the velocity of the wake driver. Therefore, it proves convenient to perform a variable transform from the laboratory frame to a co-moving frame ( $\xi, \tau$ ) with  $\xi = z - ct$  and  $\tau = t$ . The co-moving frame follows the driver with a velocity of  $v \approx c$  and  $\xi$  specifies the distance from the center of the wake driver at a specific time  $\tau$ .

In the co-moving frame eq. (2.66) can be simplified considerably by introducing the so-called *quasi-static approximation* [43, 44] which assumes that the envelope of the driver does not change significantly during the time it takes to transit a plasma electron, which is given by the driver's pulse duration. In this case  $\partial/\partial\tau \approx 0$  and the partial derivatives are given by  $\partial/\partial z = \partial/\partial\xi$  and  $\partial/\partial t = \partial/\partial\tau - c\partial/\partial\xi \approx -c\partial/\partial\xi$ . Thus, in the co-moving frame eq. (2.66) reads

$$\left( \frac{\partial^2}{\partial \xi^2} + k_p^2 \right) \frac{\delta n}{n_0} = \left( \nabla_\perp^2 + \frac{\partial^2}{\partial \xi^2} \right) \frac{a^2}{4} - k_p^2 \frac{n_b}{n_0}, \quad (2.67)$$

which is recognized as an inhomogeneous Helmholtz equation.

The electric field  $E_z$  can then be obtained with the help of eq. (2.53):

$$(\nabla_\perp^2 - k_p^2) \frac{E_z}{E_0} = k_p \frac{\partial}{\partial \xi} \left( \frac{a^2}{4} - \frac{\delta n}{n_0} - \frac{n_b}{n_0} \right), \quad (2.68)$$

where  $E_0 = m_e c \omega_p / e$  is the maximum attainable field amplitude, also called the *cold non-relativistic wave breaking limit* (to be discussed in detail in subsection 2.3.4).

For the case of an electron beam driver ( $a^2 = 0$ ) and assuming a cylindrically symmetric drive beam the solution of eq. (2.67) is [45]

$$\frac{\delta n}{n_0} = k_p \int_0^\xi d\xi' \sin[k_p(\xi - \xi')] \frac{n_b(\xi')}{n_0} \quad (2.69)$$

## 2. Plasma wakefield acceleration

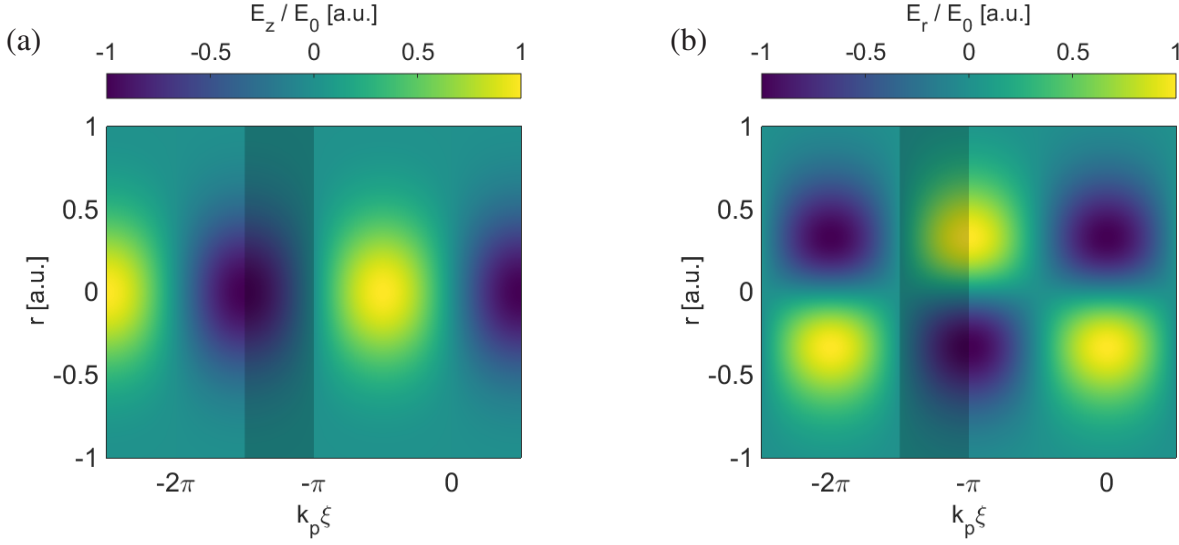


**Figure 2.3:** Longitudinal (a) and radial (b) electric field of a linear laser-driven wakefield. The colormap depicts the electric field strength behind the driver in a plane along its propagation axis. The interval  $-3\pi/2 \leq k_p \xi < -\pi$  of the wakefield phase in which an electron is exposed to both a longitudinally accelerating and a transversely focusing field is indicated by the transparent region.

and for the case of a sole laser driver in the absence of an electron bunch ( $n_b = 0$ )

$$\frac{\delta n}{n_0} = k_p \int_0^\xi d\xi' \sin[k_p(\xi - \xi')] \left( \nabla_\perp^2 + \frac{\partial}{\partial \xi'^2} \right) \frac{a^2(\xi')}{4}. \quad (2.70)$$

Equation (2.69) and eq. (2.70) can be solved analytically. For a beam driver of bi-Gaussian charge distribution  $n_b(\xi, r_\perp) = n_{b,0} \exp(-\xi^2/2\sigma_\parallel^2) \exp(-r_\perp^2/2\sigma_\perp^2)$ , the wake amplitude on the propagation axis ( $r = 0$ ) behind the beam ( $\xi \ll 0$ ) is given by [46]

$$\frac{E_z(\xi, 0)}{E_0} = -\sqrt{2\pi} \frac{n_{b,0}}{n_0} k_p \sigma_z e^{-k_p^2 \sigma_z^2/2} R(0) \cos(k_p \xi), \quad (2.71)$$

where

$$R(0) = \frac{k_p^2 \sigma_r^2}{2} e^{k_p^2 \sigma_r^2/2} \Gamma(0, k_p^2 \sigma_r^2/2) \quad (2.72)$$

and  $\Gamma(\alpha, \beta) = \int_\beta^\infty t^{\alpha-1} e^{-t} dt$ .

For laser drivers of Gaussian shape the longitudinal field is [47, 48]

$$\frac{E_z(\xi, r)}{E_0} = \sqrt{\frac{\pi}{2}} \frac{\omega_p \tau_L}{2} a_0^2 e^{-w_p^2 \tau_L^2/2} e^{-2r^2/w_0^2} \cos(k_p \xi) \quad (2.73)$$

and in the radial direction

$$\frac{E_r(\xi, r)}{E_0} = -\sqrt{2\pi} c \tau_L \frac{r}{w_0^2} a_0^2 e^{-w_p^2 \tau_L^2/2} e^{-2r^2/w_0^2} \sin(k_p \xi), \quad (2.74)$$

where  $\tau_L$  denotes the root mean square (rms) pulse duration and  $w_0$  is the beam waist.

For both, laser and beam drivers in the linear regime, the plasma wave is thus given by a sinusoidal density perturbation behind the wake driver. The longitudinal and radial electric fields are phase shifted by  $\pi/2$ <sup>1</sup>. The electric fields of a linear laser-driven wakefield are shown in Fig. 2.3. The wake structure not only provides regions for longitudinal acceleration but also regions with transverse focusing and defocusing fields. Regarding wakefield acceleration of electron beams, the useful phase of the plasma wave that provides both accelerating and focusing fields is found between  $-3\pi/2 \leq k_p \xi < -\pi$ . For both types of drivers, the wake amplitude scales linearly with  $a_0^2$  and  $n_b/n_0$ , respectively. By taking the derivative of eq. (2.71) and eq. (2.73) with respect to  $\sigma_{||}$ , it can further be shown that the amplitude is maximized for  $k_p \sigma_{||} = \sqrt{2}$ .

### 2.3.3 Nonlinear wakefields

For wakefields in the relativistic regime ( $a_0^2 > 1$  or  $n_b/n_0 > 1$ ), the perturbation analysis presented above is no longer valid. Here, an analytic theory only exists in a one-dimensional description, while more general cases must be modelled numerically. However, nonlinear effects such as wave steepening and period lengthening can already be derived from the 1D model. Furthermore, the model may be used to obtain scaling laws as well as a general understanding of the involved physics. In the following section the fully relativistic one-dimensional description of a laser or bunch driven wakefield is derived, which also encompasses arbitrary velocities  $v_{gr}$  of the driver laser.

**Transverse momentum conservation.** For the one dimensional derivation we resort to a laser pulse propagating along the  $z$ -direction which is linearly polarised along  $\mathbf{e}_x$  with  $\mathbf{a} = \mathbf{e}_x a_0(z - v_{gr}t)$ . Recalling eq. (2.12), we make use of the transverse momentum conservation  $p_x = eA_x$  that is valid in a 1D scenario. After normalizing by  $m_e c$ , this yields

$$\gamma \beta_x = a_0. \quad (2.75)$$

With the conservation of transverse momentum, the relativistic  $\gamma$ -factor can be expressed by<sup>2</sup>

$$\gamma = \frac{1}{\sqrt{1 - \beta_{\perp}^2 - \beta_z^2}} = \frac{\sqrt{1 + a_0^2}}{\sqrt{1 - \beta_z^2}} = \gamma_{\perp} \gamma_{||}. \quad (2.76)$$

- 
1. In the purely beam driven case the same behaviour is found. The longitudinal field (eq. (2.71)) shows a  $\cos(k_p \xi)$  dependence and the radial component, which can be obtained from the Panofsky-Wenzel theorem [49], also exhibits a  $\sin(k_p \xi)$  dependency [50].
  2. Since the transverse momentum of the electron is only determined by the laser vector potential, this dependence is frequently expressed by splitting the Lorentz factor into a transverse and a longitudinal component by

$$\gamma = \gamma_{\perp} \gamma_{||} \quad (2.77)$$

with

$$\gamma_{\perp} = (1 + a_0^2)^{1/2} \quad \text{and} \quad \gamma_{||} = (1 - \beta_z^2)^{-1/2}. \quad (2.78)$$

## 2. Plasma wakefield acceleration

**Longitudinal electron fluid momentum.** In the longitudinal  $z$ -direction the electron fluid momentum equation (eq. (2.62)) in 1D becomes

$$\frac{\partial(\gamma\beta_z)}{\partial t} = c \frac{\partial(\varphi - \gamma)}{\partial z}. \quad (2.79)$$

**Co-moving frame.** Analogous to the linear case we now apply a coordinate transform to a reference frame co-propagating with the laser pulse. However, this time the frame is co-moving with the group velocity  $v_{gr}$ , such that  $\xi = z - v_{gr}t$ . The partial derivatives are then given by  $\partial/\partial z = \partial/\partial \xi$ ,  $\partial/\partial t = \partial/\partial \tau - v_{gr}\partial/\partial \xi$  and the total derivative with respect to time is  $\frac{d}{dt} = \frac{\partial}{\partial \tau} - v_{gr}\frac{\partial}{\partial \xi} + c\beta_z\frac{\partial}{\partial \xi}$ . Thus, the longitudinal fluid momentum equation (2.79) in the co-moving frame becomes

$$\frac{1}{c} \frac{\partial(\gamma\beta_z)}{\partial \tau} = \beta_{gr} \frac{\partial(\gamma\beta_z)}{\partial \xi} - \beta_z \frac{\partial(\gamma\beta_z)}{\partial \xi} + \frac{\partial(\varphi - \gamma)}{\partial \xi} = \frac{\partial}{\partial \xi} [\varphi - \gamma(1 - \beta_{gr}\beta_z)]. \quad (2.80)$$

Analogously, the one-dimensional continuity and Poisson equations read

$$\frac{1}{c} \frac{\partial n}{\partial \tau} = \frac{\partial[n(\beta_{gr} - \beta_z)]}{\partial \xi}, \quad (2.81)$$

$$\frac{\partial^2 \varphi}{\partial \xi^2} = \frac{\omega_p^2}{c^2} \left( n - 1 + \frac{n_b}{n_0} \right). \quad (2.82)$$

Making use of the quasi-static approximation, the time derivatives can be neglected and eq. (2.80) and eq. (2.81) are easily integrated, yielding

$$\gamma(1 - \beta_{gr}\beta_z) - \varphi = 1, \quad (2.83)$$

$$n(\beta_{gr} - \beta_z) = \beta_{gr}, \quad (2.84)$$

where the integration constants have been determined from the requirement that for  $\xi \rightarrow \infty$  an undisturbed cold plasma ( $n = 1$  and  $\beta_z = \varphi = 0$ ) is recovered.

The electrostatic potential of eq. (2.82) can now be expressed by

$$\frac{\partial^2 \varphi}{\partial \xi^2} = \frac{\omega_p^2}{c^2} \left[ \frac{\beta_z}{\beta_{gr} - \beta_z} + \frac{n_b}{n_0} \right]. \quad (2.85)$$

Using the expression for  $\beta_{gr}$  given by eq. (2.83) and eq. (2.76) one obtains

$$\frac{\partial^2 \varphi}{\partial \xi^2} = \frac{\omega_p^2}{c^2} \gamma_{gr}^2 \left[ \beta_{gr} \left( 1 - \frac{\gamma_{\perp}^2}{\gamma_{gr}^2 (1 + \varphi)^2} \right)^{-1/2} - 1 \right] + \frac{\omega_p^2}{c^2} \frac{n_b}{n_0}, \quad (2.86)$$

where  $\gamma_{\perp}^2 = 1 + a_0^2$  is the relativistic Lorentz factor stemming from the electrons' quiver motion in the transverse laser field and  $\gamma_{gr} = (1 - \beta_{ph})^{1/2}$  is the Lorentz factor associated with the wake phase velocity. In the limit  $v_{gr} \rightarrow c$ , the expression for the electrostatic potential  $\varphi$  of the wake simplifies to

$$\frac{\partial^2 \varphi}{\partial \xi^2} = \frac{\omega_p^2}{2c^2} \left[ \frac{1 + a_0^2}{(1 + \varphi)^2} - 1 \right] + \frac{\omega_p^2}{c^2} \frac{n_b}{n_0}. \quad (2.87)$$

Equation (2.86) and eq. (2.87) can only be solved numerically. Once the solution for  $\varphi$  is known,  $n$  and  $\beta_z$  can be calculated from eq. (2.82) and eq. (2.84) and the normalized longitudinal electric field  $e_z$  is given by  $e_z = -c\omega_p^{-1}\partial\varphi/\partial\xi$ .

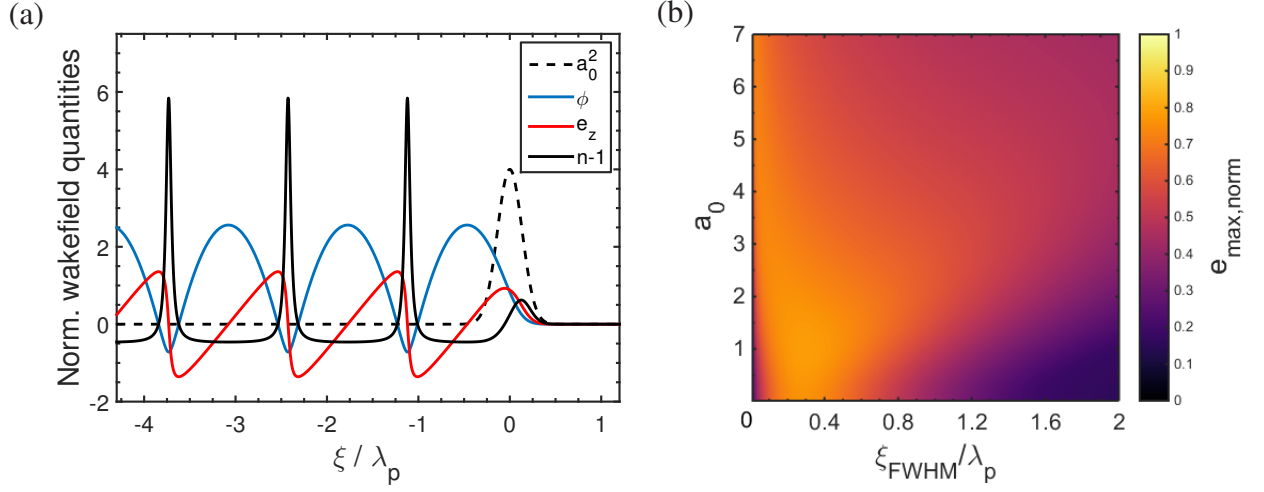


**Figure 2.4:** One-dimensional nonlinear laser driven wakefield. (a) shows the normalized wakefield properties for a driver laser with  $a_0 = 2$  and a Gaussian longitudinal profile with  $\xi_{\text{FWHM}}/\lambda_p = 0.2$ . (b) depicts the efficiency of wake excitation in dependence of the peak normalized vector potential  $a_0$  and the laser pulse width. The colormap shows the peak electric field normalized by  $a_0^2/(a_0^2 + 1)^{1/2}$ , where the latter is the maximum field amplitude attainable by a square pulse of optimal duration.

In Fig. 2.4a these quantities are plotted for a Gaussian laser pulse with  $a_0 = 2$  and a Gaussian temporal profile with a pulse duration of  $\tau_{\text{FWHM}} = 0.2\lambda_p/c$ . The main characteristics of nonlinear wakefields are reproduced by the one-dimensional theory. These include the elongation of the wave period due to the relativistic mass increase of the electrons forming the wake and the sharp spikes in the electron density at the minima of the electrostatic potential. In contrast to the linear regime, the longitudinal electric field exhibits a sawtooth like profile with an almost constant field gradient between the wave crests.

In the special case of a circularly polarised laser pulse with a square temporal profile the wakefield can be solved analytically. For an optimized pulse duration the maximum attainable field strength and wake potential scale as [51]

$$\phi_{\text{max}} \propto a_0^2 \quad \text{and} \quad \epsilon_{\text{max}} \propto \frac{a_0^2}{\sqrt{a_0^2 + 1}}. \quad (2.88)$$

For different pulse durations the maximum efficiency for wake excitation is dependent on  $a_0$  and the ratio between laser pulse length and plasma wavelength. The excitation efficiency for Gaussian laser pulses is depicted in Fig. 2.4b, where the maximum field strength normalized by the scaling of eq. (2.88) is shown in dependence of the laser amplitude and pulse length. For  $a_0 \ll 1$  the linear result  $k_p \sigma_{\parallel} = \sqrt{2}$  is recovered. For relativistic intensities optimal wake excitation is obtained for shorter pulse durations, while at the same time the dependence on laser pulse duration is relaxed due to a broader resonance of the excitation.

## 2. Plasma wakefield acceleration

### 2.3.4 Wave breaking

A major advantage of plasma accelerators compared to conventional microwave cavities is that plasma waves can sustain electric fields in the order of several hundred GV/m. These fields<sup>1</sup> are limited by wave breaking, which occurs when the velocity of the electrons constituting the wake exceeds the phase velocity of the wake itself. A first estimate about the attainable field strength can be obtained from linear theory for which the maximum density perturbation is given by  $\delta n/n_0 = 1$ . For a phase velocity of  $v_{ph} = c$  all electrons are oscillating with  $k_p = \omega_p/c$ . The Poisson equation (eq. (2.53)) then reads  $\partial E_z/\partial z = E_0 \omega_p/c = \omega_p^2 m_e/e$  or

$$E_0 = \frac{m_e c \omega_p}{e} \approx 96 \sqrt{n_0 [\text{cm}^{-3}]} \frac{\text{V}}{\text{m}}, \quad (2.89)$$

which is known as the cold non-relativistic wave breaking limit [52].

Taking into account nonlinear effects, plasma waves can sustain even higher fields. The same procedure can be applied to the 1D nonlinear theory, for which it can be shown that as the electron velocities  $v_e$  approach  $v_{ph}$ , the electron density diverges and  $\partial^2 \phi / \partial \xi^2 \rightarrow \infty$ . This leads to the following expression for the cold relativistic wave breaking limit [53]

$$E_{WB} = E_0 \sqrt{2(\gamma_{ph} - 1)}, \quad (2.90)$$

where  $\gamma_{ph} = (1 - v_{ph}^2/c^2)^{-1/2}$  is the relativistic factor associated with the wake phase velocity.

The theory may be extended to include temperature effects. For warm plasmas, the wave breaking limit is lower, as the thermal motion leads to a velocity distribution with an effective velocity spread  $v_{th}$ . Thus, a fraction of the background electrons with  $v_e + v_{th} \geq v_{ph}$  can get trapped in the wake [54]. A derivation for warm plasmas, including relativistic fluid momenta, is given in ref. [55, 56]. Apart from the simple 1D model, a more accurate description of wave breaking also has to account for the transverse motion of plasma electrons, which can influence the wave breaking threshold.

### 2.3.5 The bubble regime

So far wake generation has been discussed in the 3D linear and 1D nonlinear regime, assuming a non-evolving static laser or particle bunch driver. These models have the advantage of being tractable within analytic theory and capture the basic features of the involved physics. Nevertheless, a realistic description necessarily needs a three-dimensional treatment as the wake driver not only expels plasma electrons longitudinally but also in transverse direction. Since a strict analytic solution in the nonlinear regime does not exist, a full description ultimately requires the use of numerical simulations. This is usually done by PIC simulations that evaluate the dynamics of the electromagnetic fields and the charged particles on a computational grid in a self-consistent manner.

For short relativistic wake drivers ( $a_0$  or  $n_b/n_0 \gg 1$  and  $\sigma_{\parallel} < \lambda_p$ ), the transverse component of the electric field or the ponderomotive force dominates the wake formation process by expelling

1. For plasma densities in the range of  $10^{18} - 10^{19} \text{ cm}^{-3}$  that are commonly used in LWFA experiments, the maximum attainable electric field is in the range of 100 – 300 GV/m.



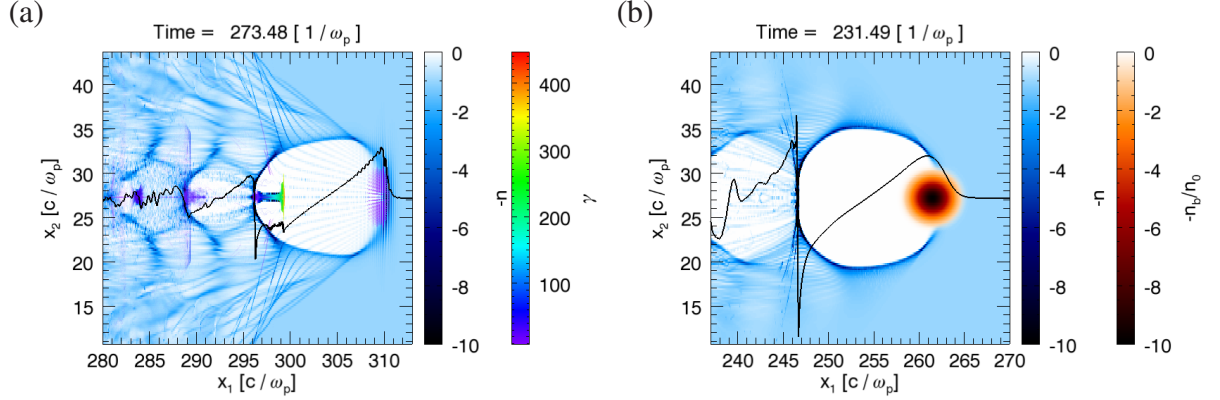


**Figure 2.5:** PIC simulations showing the shape of the wakefield in the blow-out regime. (a) depicts the electron density (blue colorbar) and longitudinal electric field (black lineout, [a.u.]) of the central slice through a 3D PIC simulation box for a matched laser driver with  $a_0 = 10$ . The  $\gamma$  factor of the injected electrons is shown by the right colorbar. In (b), the wake is excited by an electron bunch (red colorbar) with  $n_b/n_0 = 10$  and  $k_p \sigma_{\perp} = k_p \sigma_{\parallel} = \sqrt{2}$ .

the plasma electrons radially, leaving behind a pure ion column of uniform charge density  $+en_0$ . The plasma electrons are then pulled back by the channel and perform a harmonic motion after which their trajectories cross each other on the propagation axis and create a large density spike at a distance of around  $\lambda_p$ . The nonlinearities induced by the large amplitude wake cause initial position dependent frequency shifts. Further downstream, this phase mixing of the returning electrons leads to trajectory crossing and therefore a non-laminar motion, which destroys the wake structure [52, 57]. Due to the solitary shape of the plasma cavity it is called a bubble. Using numerical simulations, the so-called *bubble* or *blowout* regime was first identified for PWFA by Rosenzweig et al. [58] and later by Pukhov and Meyer-ter Vehn [59] for LWFA.

A major benefit of the bubble regime is the radially independent linear acceleration field and a transverse focusing field that is constant along  $\xi$  and therefore preserves the transverse emittance of an accelerated electron bunch (cf. subsection 3.2.3). The structure of the bubble is an approximately spherical ion cavity surrounded by a thin dense layer of expelled electrons, radially followed by a weakly disturbed plasma with an extent of one skin depth. In the ultrarelativistic limit and for short wake drivers the shape of the bubble is given by [60]

$$r_b \frac{d^2 r_b}{d\xi^2} + 2 \left( \frac{dr_b}{d\xi} \right)^2 + 1 = 0, \quad (2.91)$$

where  $r_b$  denotes the bubble radius. This equation resembles a sphere, except for the extra term  $(dr_b/d\xi)^2$ , which causes the trajectories to steepen at the rear side of the bubble. While for PWFA this shape is accurate for ultrarelativistic and narrow beam drivers for which the potential extends far beyond the bunch dimensions, the ponderomotive potential of a laser driver is limited by the outer edges of the pulse. Furthermore, the laser cannot be guided by self-focusing if its spot size is too small. Thus, for LWFA, the shape slightly deviates from a sphere, as shown in Fig. 2.5. Using PIC simulation, Lu et al. [61] found that a refined condition for LWFA leading to a well defined sheet accompanied by laser self-guiding without significant oscillations in spot

## 2. Plasma wakefield acceleration

size is obtained for a laser waist  $w_0$  satisfying

$$k_p r_b \simeq k_p w_0 = 2\sqrt{a_0}. \quad (2.92)$$

The axial electric field and the effective radial focusing field within the bubble are given by [12, 62]

$$E_z \simeq \frac{k_p \xi}{2} E_0 \quad \text{and} \quad E_r \simeq \frac{k_p r}{2} E_0, \quad (2.93)$$

where  $E_z$  is maximal when  $\xi = r_b$  and, using eq. (2.92), the maximum acceleration field scales as  $E_{\max} \simeq \sqrt{a_0} E_0$ . Note that the effective focusing field  $E_r$  is independent of  $\xi$ .

PIC simulations further show that in the LWFA case a characteristic spherical bubble is reached for  $a \gtrsim 2$  [61]. In order to reach the blowout regime with particle beam drivers,  $k_p \sigma_\perp < 1$ ,  $k_p \sigma_\parallel < 2$  and  $n_b/n_0 > 1$  is required [58].

## 2.4 Trapping and acceleration

Once the plasma wave breaks or an electron is injected by other means into the potential of the wakefield it can co-propagate if a sufficient initial momentum is exceeded. The electron is then trapped within the potential of the wakefield, where the latter is moving with the wake's phase velocity, and permanently exposed to its electric field.

Having determined the wake's potential (e.g. from eq. (2.86)), it is instructive to examine the trajectory of a test electron in phase space. The longitudinal dynamics of an electron in the presence of the laser pulse vector potential  $A_\perp$  and the wakefield potential  $\Phi$  are described by the Hamiltonian given by [63]

$$\mathcal{H} = \sqrt{m^2 c^4 + c^2 P_\parallel^2 + (c P_\perp + e A_\perp(z, t))^2} - e \Phi(z, t). \quad (2.94)$$

Transformation to the co-moving frame, averaging over the fast laser oscillation cycle and using normalized units yields [64]

$$h(\xi, p_\parallel) = \sqrt{\gamma_\perp^2 + p_\parallel^2} - \varphi(\xi) - \beta_{ph} p_\parallel = h_0(\xi_0, p_0), \quad (2.95)$$

where  $\gamma_\perp = (1 + a_0^2/2)^{1/2}$  for a linear polarised laser pulse (cf. eq. (2.76)). As  $h$  does not explicitly depend on time, the energy of the system is conserved and the electron orbit is only dependent on its initial coordinates before arrival of the wakefield, i.e. the trajectory is solely determined by its initial energy  $h(\xi_0, p_0) = h_0$ .

### The separatrix

Solving eq. (2.95) for the normalized longitudinal momentum yields [64]

$$p_\parallel = \beta_{ph} \gamma_{ph}^2 (h_0 + \varphi) \pm \gamma_{ph} \sqrt{\gamma_{ph}^2 (h_0 + \varphi)^2 - \gamma_\perp^2}. \quad (2.96)$$



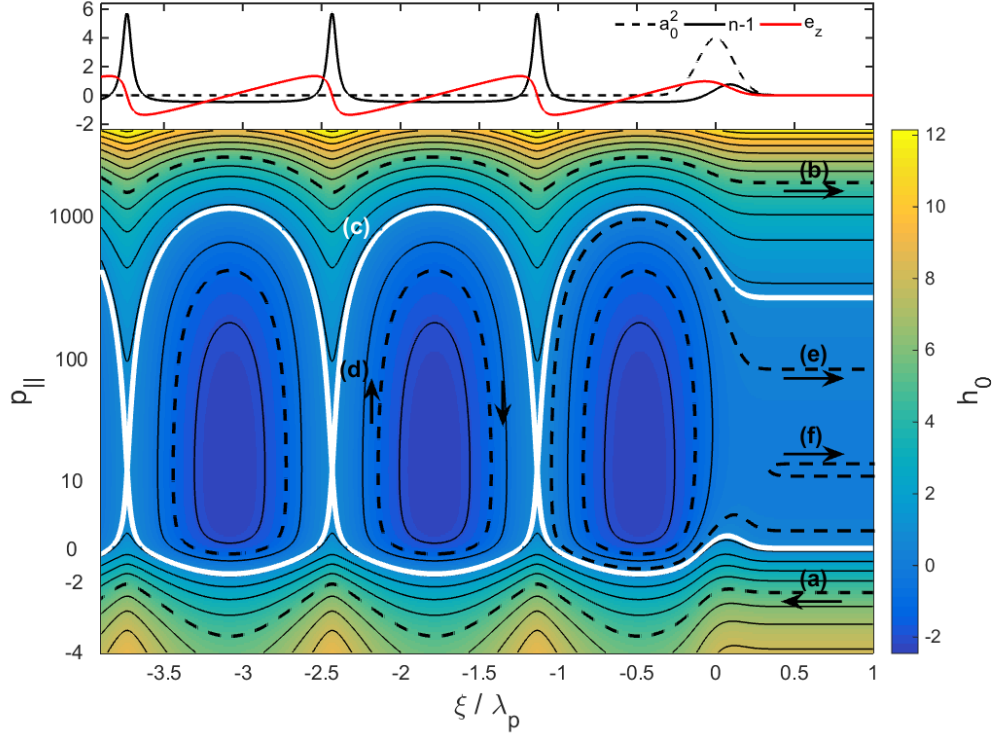


**Figure 2.6:** Longitudinal phase space of the wake. The upper part shows the properties of a 1D nonlinear laser driven wakefield in the co-moving frame ( $a_0 = 2$ ,  $\xi_{FWHM} = 0.14\lambda_p$ ,  $\gamma_{ph} = 13$ ). The lower part shows the resulting longitudinal phase space of a test electron in the wakefield. Different classes of electron trajectories are labeled by characters and described in the main text. The total energy of the test electron is given by the colormap.

This equation describes individual electron orbits which are distinguished by their initial energy  $h_0$ . In Fig. 2.6, the Hamiltonian defined in eq. (2.95) is plotted for the longitudinal phase space  $(p_{\parallel}, \xi)$ , where the colour code corresponds to the initial energy  $h_0$ . Individual electron trajectories are highlighted by lines. Each line represents the motion of an electron with a certain initial energy  $h_0$ , which moves in phase space along trajectories of constant energy. On top of the phase space plot the laser pulse envelope, electron density and longitudinal electric field are shown for comparison. From Fig. 2.6 it is evident that, depending on their initial energy, some electrons are moving on closed orbits (d) and are trapped in the wake potential. As time proceeds, electrons follow their trajectories in the direction indicated by arrows. Trapped electrons are therefore periodically accelerated and decelerated. To distinguish these orbits from untrapped orbits, an import criterion in phase space is the separatrix (c), which refers to the limiting orbits that separate both types of trajectories.

The separatrix is the solution to eq. (2.95) for the minimum energy  $h_s$  for which closed orbits are achieved. These orbits join at singular points at which the 2<sup>nd</sup> term on the right hand side of eq. (2.96) vanishes. Therefore  $h_s$  has to satisfy  $\gamma_{ph}^2(\phi(\xi) + h_s)^2 - \gamma_{\perp}^2 = 0$  [63, 64]. The initial momentum for an electron to get trapped in the wake structure is obtained by using  $h = h_s$  and

## 2. Plasma wakefield acceleration

---

solving for  $p_{\parallel}$ , which yields [64]

$$p_{\parallel,min} = \gamma_{ph} \left( \beta_{ph}(\gamma_{\perp} - \gamma_{ph}\Phi_{min}) - \sqrt{(\gamma_{\perp} - \gamma_{ph}\Phi_{min})^2 - 1} \right), \quad (2.97)$$

where  $\gamma_{ph}$  is set by the laser's group velocity  $\gamma_{gr}$ . An orbit with  $p_{\parallel,min}$  corresponds to an electron moving with  $\gamma_{min}$  in laser propagation direction before arrival of the wake driver. At  $\xi/\lambda_p = -1$  its velocity exactly equals the phase velocity of the wake. The separatrix orbit also determines the maximum attainable acceleration. After the turning point at  $\xi/\lambda_p = -1$ , the electron circulates along the separatrix and is accelerated to velocities exceeding  $\gamma_{ph}$ . When it has travelled half the plasma wavelength ( $\xi/\lambda_p = -0.5$ ), the maximum energy is obtained. Ideally, acceleration should be stopped at this so-called *dephasing* point, otherwise the electron continues to follow the separatrix and is decelerated again.

If a test electron's initial momentum is too low to get trapped, it simply follows the wave motion but moves backward with respect to the wake frame (a). These low-momentum electrons form the wake itself and their momentum oscillates around the initial value. On the other hand, if an electron's initial velocity is too high it overtakes the wake without being trapped (b).

In the first bucket behind the laser driver the trapping potential is modified by the laser potential and only electrons with lower energies  $< h_s$  are truly trapped. Between these and the separatrix a further class of orbits called runaway orbits exists (c). These electrons get reflected by the wake potential, asymptotically overtake the driver and can gain substantial energy comparable to the trapped orbits. A further class of orbits is also directly reflected from the driver potential (f).

### Plasma wave phase velocity

As seen from eq. (2.90) and eq. (2.97), the plasma wave phase velocity determines the wave breaking limit, the minimum kinetic electron energy needed for injection and also the dephasing length, i.e. the acceleration length after which the electron enters the decelerating phase of the wake. For non-evolving wake drivers the phase velocity is determined by the driver's velocity. Thus, in the case of LWFA  $v_{ph} = v_{gr}$ , while for PWFA it equals the velocity of the driver beam, which, for relativistic drive beams, is  $v_{ph} \approx c$ . As seen from eq. (2.97), the injection threshold is lowered for decreased phase velocities and greater wake amplitudes. For amplitudes approaching the wave breaking field  $E_{WB}$  (eq. (2.90)) this threshold simplifies to  $\gamma_{min} = \gamma_{ph}$  [65].

Due to the high phase velocity  $\sim c$  of wakes driven by relativistic beam drivers, wave breaking can normally not be achieved for PWFA in homogeneous plasma and has not been reported up to date. Thus, either more complex gas targets have been proposed or an external electron bunch must be injected in the wakefield.

The following section will deal with electron injection either by nonlinear wave breaking or by altering the wake phase velocity which will lower the trapping threshold.

## 2.5 Injection mechanisms & beam loading

If the wake driver is highly relativistic, nonlinear plasma waves exceeding the wave breaking threshold given by eq. (2.90) can be driven. At this point the electrons forming the density

spike would move faster than the phase velocity of the wake. As a result, the wakefield loses its coherent nature, the fluid description breaks down and the electron motion becomes non-laminar. The wave is said to break and a portion of plasma electrons with  $\gamma \geq \gamma_{min}$  from the density spike of the background electrons can get injected into the preceding wave bucket. Usually, this process is further assisted by the laser pulse evolution in plasma (discussed in section 2.6), which increases the laser vector potential and leads to even higher wake amplitudes. Wave breaking is routinely observed in PIC simulations if the plasma wave becomes nonlinear. By approximating the electron sheet in the bubble regime with elliptical orbits, Thomas [66] analytically derived a condition for trapping to occur:

$$\frac{\sqrt{\ln(2\gamma_{ph}) - 1}}{k_p r_b} \lesssim \frac{1}{2}. \quad (2.98)$$

Using the phenomenological scaling of the bubble radius  $k_p r_b \simeq 2\sqrt{a_0}$  (eq. (2.92)) and  $\gamma_{ph} \approx (\omega_L^2/3\omega_p)^{1/2}$  [67], a condition for the necessary vector potential can be obtained

$$a_0 \gtrsim \ln \left( \frac{\omega_L^2}{3\omega_p^2} \right) - 1. \quad (2.99)$$

This trapping threshold is routinely reached experimentally even for mildly relativistic laser pulses after sufficient propagation and laser evolution in plasma [67].

Although self-injection requires the least complex target design, it inherently depends on various nonlinear effects related to the dynamics of laser pulse and wakefield evolution. The accelerator is therefore prone to variations of the beam parameters caused by even small fluctuations of the laser and target parameters. Furthermore, the injection position and amount of trapped charge cannot be controlled precisely, where the former leads to variations in acceleration length and thus cut-off energy, while the latter can cause beam loading effects that increase the energy spread.

## Controlled injection

The acceleration process can be optimized by choosing other means of injecting an electron bunch into the wakefield. Since in this case the wave breaking threshold must not be exceeded, either the laser intensity or the plasma density can be decreased. This concept not only allows to optimize the energy gain for a given  $a_0$  (by lowering the plasma density, cf. section 2.7), but also enables control over the amount of injected charge and can avoid beam loading effects. Since the wakefield is driven weaker, this scheme also decreases nonlinear effects.

Even though an external accelerator may be used to provide electron bunches with sufficient energy to get trapped in the wakefield, this approach is demanding since the injected bunch has to be synchronized with the wake driver at the correct phase to a precision determined by a fraction of the acceleration structure's size, i.e. the plasma wavelength, which is in the order of  $10\mu\text{m}$  at typical plasma densities used in LWFA. As this is a demanding task even for state-of-the-art accelerators (mainly due to the temporal synchronization between the laser pulse and the electron bunch), experiments up to date rely on the control of the injection process by the gas target design or additional laser pulses.

To this point various schemes to exert control over this process have been developed, including

## 2. Plasma wakefield acceleration

---

the use of a second laser pulse propagating in perpendicular direction (ponderomotive injection [68]), counter-propagating geometry (colliding pulse injection [69]) or exploiting intensity dependent tunnel ionization of core electrons (ionization injection [70]).

### Lowering the trapping threshold

Another possibility to exert control over the injection process is to modify the plasma wavelength and thereby simultaneously alter the wake phase velocity and the trapping threshold.

Assuming a relativistic velocity  $\sim c$  of the driver, the wake phase velocity behind the driver ( $\xi < 0$ ) is given by  $\Psi = k_p(z)(z - ct)$ , where  $k_p(z)$  takes into account possible changes of the plasma wavelength with propagation distance  $z$ . Since  $v_{ph}/c = (-\partial\Psi/\partial ct)/(\partial\Psi/\partial z)$ , the local phase velocity behind the driver reads [71]

$$\beta_{ph} = \left(1 + \frac{\xi}{k_p} \frac{dk_p}{dz}\right)^{-1}. \quad (2.100)$$

Hence, an elongation of the plasma wavelength with increasing propagation distance  $z$  yields  $dk_p/dz < 0$ , which effectively reduces the wake phase velocity  $\gamma_{ph} = \beta_{ph}c$  with increasing distance from the driver. As outlined in section 2.4, a lower  $\gamma_{ph}$  will reduce the required  $\gamma_{min}$  needed for injection. Additionally, the reduction in phase velocity leads to a build-up of electron density at the crest of the wake. This can lead to wave breaking even if the initial wake amplitude is below the wave breaking threshold [72].

For example, a negative slope of the plasma density ( $dn/dz < 0$ ) will increase  $\lambda_p$  and yields  $dk_p/dz < 0$ . This concept of density down ramp assisted injection has been demonstrated experimentally for LWFA [19, 73, 74], while PIC simulations show that it can also lead to injection even in a purely beam-driven case [75].

An increase of the plasma wavelength with propagation distance can also be obtained by enhancing the nonlinearity of the wake during propagation. As outlined in the following section, such an increase of the wakefield strength can also happen at a late stage of the acceleration process if the wakefield driven by the trapped electron bunch adds up constructively with that of the laser driver.

### Beam loading

Electrons being trapped and accelerated in the wake will themselves drive a wakefield and thus modify the acceleration dynamics by lowering the attainable acceleration fields. Reverting to eq. (2.87), the wake's potential is given by

$$\frac{\partial^2 \phi}{\partial \xi^2} = \frac{\omega_p^2}{2c^2} \left[ \frac{1 + a_0^2}{(1 + \phi)^2} - 1 \right] + \frac{\omega_p^2}{c^2} \frac{n_b}{n_0}, \quad (2.101)$$

where the wakefield produced by a (trapped) electron bunch is described by the second term. If the wakefield amplitude generated by the electron bunch approaches the magnitude of the accelerating wakefield, the latter will be significantly altered, leading to a degradation of the bunch properties, an effect called *beam loading*.

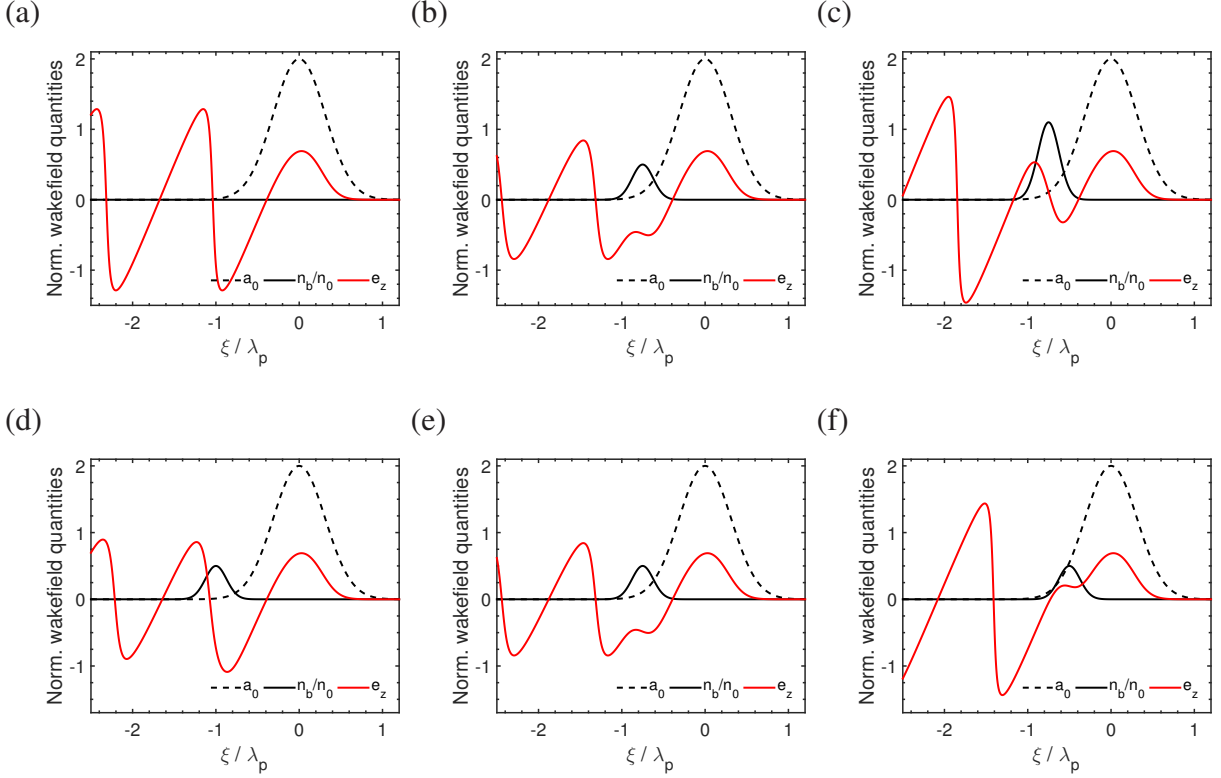


**Figure 2.7:** Effects of beam loading. (a) shows the wakefield of a laser pulse with  $a_0 = 2$  and  $\tau_{FWHM} = 0.2\lambda_p/c$ . (b,c): When an electron bunch is trapped and accelerated, the wake induced by the bunch itself modifies the accelerating electric field shown in red. The bunch is located at  $\xi/\lambda_p = -0.75$  with a peak charge density of (b)  $n_b/n_0 = 0.5$  and (c)  $n_b/n_0 = 1.1$ . (d-f) show the evolution of the longitudinal field as a bunch with  $n_b/n_0 = 0.5$  advances towards the wake driver. Its position is (d):  $-1\xi/\lambda_p$ , (e):  $-0.75\xi/\lambda_p$  and (f):  $-0.5\xi/\lambda_p$ .

The impact of beam loading is illustrated in Fig. 2.7 for varying charge density and distance of the electron bunch from the wake driver. Figure 2.7a shows the wakefield of a laser pulse of optimal duration and  $a_0 = 2$ . In the case of PWFA, a beam driver would analogously be situated in the first half of its own wakefield and therefore experience a decelerating electric field throughout most of its profile. We now consider a laser pulse as the wake driver and a trapped electron bunch. As seen from Fig. 2.7b, if the trapped bunch and the driver are out-of-phase (the bunch is located in the accelerating phase of the driver's wake) the wake amplitude is reduced. This effect will also terminate the initial self-injection once the wake is sufficiently loaded and limit the process to a short time. However, if the wake driver is strong enough, the injection process can continue and even increase the plasma wavelength and wake amplitude as shown in Fig. 2.7c. This process is typically observed in PIC simulations in the highly relativistic regime. Nevertheless, in both cases the overall electric field at the position of the bunch is reduced and the achievable energy gain is thus lower. Furthermore, dependent on the trapped charge (cf. Fig. 2.7b and Fig. 2.7c), electrons at different longitudinal position experience a varying field, which will increase the bunch's energy spread. Although a specifically tailored beam load can theoretically lead to a uniform electric field across the bunch and create favourable acceleration

## 2. Plasma wakefield acceleration

conditions as each part of the bunch is exposed to the same electric field strength, uncontrolled beam loading will normally significantly alter the wakefield and degrade the quality and energy distribution of the electron bunch.

Finally, as the bunch progresses towards the laser driver (Fig. 2.7d-f), both wakefields will be more and more in phase and the field strength is enhanced over the initial wakefield of the driver alone. As seen in Fig. 2.7f, the increased nonlinearity of the wake is accompanied by an enlarged plasma wavelength and therefore also a reduced wake phase velocity during this process. This in turn can lead to further injection.

A simple method to estimate the threshold for beam loading to become significant is to compare the peak amplitude of the wakefield driven by the electron bunch to that of the main wake driver. In the case of LWFA, using non-relativistic linear theory and assuming an electron bunch with a step-like temporal profile and a laser pulse with a Gaussian radial and half-sine temporal profile, this ratio is approximately given by [45]

$$\alpha \approx \frac{k_p \sigma_z}{a_0^2} \frac{n_b}{n_0} R(0), \quad (2.102)$$

with the radial profile function  $R(0)$  as defined in eq. (2.72). Beam loading can only be neglected if  $\alpha \ll 1$ . It further imposes a constraint on the number of electrons that can be accelerated in a plasma wave without deterioration of the beam properties.

In the bubble regime, Tzoufras et al. [76] give the following relation between the trapped charge  $Q$  and the accelerating field  $E_z$

$$\frac{QE_z}{mc^2/r_e} = \frac{1}{4^3} (k_p r_b)^4, \quad (2.103)$$

where  $r_b$  denotes the blowout radius and  $r_e$  is the classical electron radius.

## 2.6 Laser pulse evolution in plasma

For LWFA, the wakefield properties and thus the performance of the accelerator is strongly determined by the laser pulse evolution in plasma. Its most important effects will now be discussed.

We start out with the refractive index of an underdense plasma given in eq. (2.45),

$$\eta = \sqrt{1 - \frac{\omega_p^2}{\gamma_\perp \omega_L^2}} \approx 1 - \frac{\omega_p^2}{2\gamma_\perp \omega_L^2}, \quad (2.104)$$

where  $\gamma_\perp = (1 + a_0^2)^{1/2}$  accounts for the relativistic mass increase of plasma electrons exposed to an intense laser pulse and  $\omega_p = (e^2 n_0 / \epsilon_0 m_e)^{1/2}$ . The refractive index is thus affected by changes to either the plasma density, the laser amplitude or its frequency. In the weakly relativistic regime, the refractive index can be expanded to first order by [77]

$$\eta \simeq 1 - \frac{\omega_p^2}{2\omega_L^2} \left( 1 + \frac{\delta n}{n_0} - \frac{\langle a^2 \rangle}{2} - \frac{2\delta\omega_L}{\omega_L} \right). \quad (2.105)$$



We now compile the expressions for the laser phase and group velocity in plasma

$$v_{ph} = \frac{c}{\eta} = c \left[ 1 + \frac{1}{2} \frac{\omega_p^2}{\omega_L^2} \left( 1 + \frac{\delta n}{n_0} - \frac{\langle a^2 \rangle}{2} - \frac{2\delta\omega_L}{\omega_L} \right) \right], \quad (2.106)$$

$$v_{gr} = c\eta = c \left[ 1 - \frac{1}{2} \frac{\omega_p^2}{\omega_L^2} \left( 1 + \frac{\delta n}{n_0} - \frac{\langle a^2 \rangle}{2} - \frac{2\delta\omega_L}{\omega_L} \right) \right]. \quad (2.107)$$

### Defocusing effects

The term  $\delta n/n_0$  of eq. (2.105) describes the variation of the refractive index due to variations in plasma electron density. Such variations exist at the front of a pulse focused into a neutral gas, as the higher intensity on axis will first ionize the medium. The resulting transverse gradient in refractive index leads to so-called *ionization defocusing*. However, in the context of high intensity lasers with intensities many orders of magnitude above the ionization threshold of hydrogen, this effect is of minor importance as it only affects the leading edge of the main pulse's pedestal. A more relevant effect emerges for higher laser intensities during wake excitation, as the ponderomotive force also expels plasma electrons in the forward direction, which creates a swell in electron density directly in front of the main pulse. The resulting defocusing counteracts the relativistic self-focusing effect described below. However, PIC simulations show that pulse etching due to energy transfer to the plasma is fast enough to deplete the front of the pulse before it diffracts [78], such that this effect is of minor importance in practical applications as well.

### Relativistic self-focusing

The term  $-\langle a^2 \rangle/2$  of eq. (2.105) accounts for the relativistic effect due to the mass increase of plasma electrons during the interaction. The intensity gradient of  $\langle a_0(r_\perp)^2 \rangle$  in the transverse dimensions leads to a curved profile of the refractive index. The retardation of the phase fronts on axis causes the so-called *relativistic self-focusing* effect. Calculating the phase difference between the center and the edge of the beam waist shows that the focusing effect can counteract diffraction if the following condition is met [77]

$$\frac{a_0^2 w_0^2 \omega_p^2}{32c^2} > 1, \quad (2.108)$$

where  $w_0$  denotes the focal spot size in vacuum. This leads to a power threshold condition  $P/P_c > 1$  for self-guiding, with the critical power  $P_c$  given by [79]

$$P_c = 8\pi\epsilon_0 c \left( \frac{m_e c^2}{e} \right)^2 \frac{\omega_L^2}{\omega_p^2} \simeq 17.4 \frac{\omega_L^2}{\omega_p^2} [\text{GW}]. \quad (2.109)$$

If  $P > P_c$ , guiding over several Rayleigh lengths can be achieved. It has to be noted that these dynamics describe the pulse evolution down to the scale set by  $\lambda_p$ . Ultimately, the final self-focused spot size is limited by higher order nonlinearities that are not included in the first order expansion of the refractive index [79]. For example, it is obvious that for high enough laser powers self-focusing will reduce the beam diameter and therefore  $a_0$  until complete electron

## 2. Plasma wakefield acceleration

---

blow-out of plasma electrons occurs, leaving only a positively charged ion channel. In this case, further self-focusing cannot occur inside the channel due to the lack of plasma electrons. This plays an important role for self-guiding of ultra-short laser pulses. Although the response of the plasma and therefore the changes in the refractive index happen on a time scale of  $\tau = \omega_p^{-1}$ , electron blowout enables the back side of the pulse to be guided inside the ion channel, even for pulse lengths  $t < \lambda_p/c$  [80, 81]. In this regime, phenomenological investigations conducted by Lu et al. [61] show with the help of PIC simulations that a stable self-guided spot size is reached if the condition

$$w_0 k_p = 2\sqrt{a_0} \quad (2.110)$$

is fulfilled. This condition can be reformulated to yield

$$a_0 = 2 \left( \frac{P}{P_c} \right)^{1/3}. \quad (2.111)$$

In order to achieve maximum electron energies, self-focusing must be maintained over the dephasing length  $L_d$  (cf. section 2.7). Lu et al. [61] further show that this imposes a condition on  $a_0$

$$a_0 \sim \left( \frac{\omega_L}{\omega_p} \right)^{2/5}. \quad (2.112)$$

By combining eq. (2.111) and eq. (2.112), we finally obtain an equation for the laser power that is needed in order to maintain self-guiding over  $L_d$  at a specific plasma density [82]:

$$\frac{P_{L_d}}{P_c} = \frac{1}{8} \left( \frac{\omega_L}{\omega_p} \right)^{6/5}. \quad (2.113)$$

Finally, the evolution of the laser spot size in plasma will lead to an increase of  $a_0$ . Starting the self-focusing effect from the vacuum focus of a Gaussian beam, the evolution of the beam waist is described by [12]

$$\frac{w(z)^2}{w_0^2} = 1 + \left( 1 - \frac{P}{P_c} \right) \frac{z^2}{z_R^2}, \quad (2.114)$$

where  $z_R = kw_0^2/2$  is the Rayleigh length and  $z$  is the longitudinal distance from the vacuum focus. Compared to diffraction in vacuum, the evolution of a Gaussian pulse in plasma differs by an additional term  $-P/P_c (z^2/z_R^2)$ .

The laser power of  $\sim 50$  TW used in the experiments presented in this thesis is significantly higher than  $P_c$  which was in the range of 3 – 10 TW at the employed plasma densities. Thus, laser self-focusing plays an important role in the acceleration dynamics.

### Pulse compression and photon deceleration

So far we have mainly considered transverse variations of the refractive index. Nevertheless, analogous effects on the longitudinal variation of  $\eta$  play an important role in the laser evolution. We first consider its dependence on  $\delta n$ . As mentioned above, at the front of the pulse, electrons are pushed forward, resulting in an aggregation of plasma electrons and a decrease in  $\eta$ . However,



the back part of the pulse, exposed to the density perturbation of the wake, propagates in a region with a lower electron density. Therefore  $\eta$  increases towards the front of the pulse and its tail travels at a higher group velocity than the front part, resulting in a temporal pulse compression and steepening of the back of the pulse. Simultaneously, due to the reduced phase velocity at the rear side, these photons become red-shifted, an effect known as photon deceleration [83].

The situation becomes more complex when also including the relativistic term

$$\delta\eta \approx \frac{\omega_p^2 (a^2/4 - \delta n)}{2\omega_L^2}, \quad (2.115)$$

which tends to cancel the variations of  $\eta$  imposed by  $\delta n$  at the front of the pulse [84, 85]. However, beyond this first maximum of  $n_e$ , the decreasing density and increasing intensity still cause an increasing  $\eta$  and thus a higher  $v_{gr}$  and reciprocal decrease in  $v_{ph}$  [85]. Thus, self-compression and photon deceleration remain the dominant effects [83]. This was also confirmed experimentally, where Ti:Sa laser pulses of  $\tau_{FWHM} = 38$  fs and  $\tau_{FWHM} = 45$  fs were compressed down to 12 fs and 18 fs, respectively [85, 86]. Naturally, the pulse compression entails an intensity increase of  $a_0$ , which results in an increased wakefield amplitude.

## 2.7 Acceleration limits and scaling laws

### Laser energy depletion

By excitation of a plasma wave laser energy is continuously transferred to the plasma. The length after which only a fraction  $1/e$  of the initial energy remains is called the laser *pump depletion length*  $L_{pd}$ . In one-dimensional theory, a simple estimate can be derived from energy conservation arguments by comparing the initial pulse energy to the energy contained in a wakefield of length  $L_{pd}$ . For a flattop pulse of optimal length and for resonant excitation,  $L_{pd}$  is given by [12, 87]

$$L_{pd} = \left(\frac{\omega_L}{\omega_p}\right)^2 \lambda_p \begin{cases} 2/a_0^2 & \text{if } a_0 \ll 1, \\ (\sqrt{2}/\pi) a_0 & \text{if } a_0 \gg 1. \end{cases} \quad (2.116)$$

For a driver pulse of Gaussian shape, a slightly different numeric factor was found empirically with the help of PIC simulations by Shadwick et al. [88]:

$$L_{pd} \simeq 8.7 \left(\frac{\omega_L}{\omega_p}\right)^2 \lambda_p \begin{cases} 1/\pi a_0^2 & \text{if } a_0 \ll 1, \\ 1/2\pi & \text{if } a_0 \gg 1. \end{cases} \quad (2.117)$$

For the bubble regime, a further estimate valid for laser pulses with  $a_0 \geq 2$  has been derived by Lu et al. [61]. Here, only the front of the laser pulse is interacting with the plasma, while the remainder is guided in the plasma cavity such that only the front is etched away with a velocity of  $v_{etch} \simeq c\omega_p^2/\omega_L^2$ . For a pulse duration of  $\tau$  this leads to a depletion length of

$$L_{pd,3D} = \frac{\omega_L^2}{\omega_p^2} c\tau_{FWHM}. \quad (2.118)$$

## 2. Plasma wakefield acceleration

### Electron dephasing

A severe constraint to the achievable energy gain in an LWFA is electron dephasing. As discussed in section 2.4, acceleration of electrons only takes place in the rear half of each bucket that carries a positive gradient of the wake potential. In the case of LWFA, upon being accelerated to relativistic energies, electrons will catch up with the laser driver which propagates with  $v_{gr} < c$ . The propagation length up to the dephasing point is called the *dephasing length*  $L_d$  and is given by  $L_d(1 - v_{gr}/c) = \lambda_p/2$ . For relativistic wakefields,  $\lambda_p$  is elongated and approximately given by  $\lambda_{p,nonlin.} \simeq \lambda_p(2\sqrt{2}/\pi)a_0$  [51, 89]. Thus, in one-dimensional theory  $L_d$  is given by

$$L_d = \left(\frac{\omega_L}{\omega_p}\right)^2 \lambda_p \begin{cases} 1 & \text{if } a_0 \ll 1, \\ (\sqrt{2}/\pi)a_0 & \text{if } a_0 \gg 1. \end{cases} \quad (2.119)$$

Note that this limitation does not exist in the PWFA case, as the beam driver also propagates with relativistic velocity  $\sim c$ . In the LWFA case,  $L_d$  can be elongated by an appropriate tapering of the plasma density profile. When increasing the plasma density with propagation distance,  $\lambda_p$  decreases such that the wake phase velocity at the position of the accelerated bunch becomes closer to  $c$ , i.e. the accelerated bunch is continuously re-phased to remain in the same phase of the accelerating field, resulting in a larger single stage gain [84, 91]. Although to completely counteract dephasing, ultimately infinite plasma densities would be required, this scheme can delay dephasing issues until acceleration is eventually limited by other factors such as pump depletion.

### LWFA energy gain and scaling laws

The energy gain in a wakefield accelerator is determined by the attainable electric field strength and the acceleration distance, i.e.  $\Delta E = -e \int_0^{L_{acc}} E_z(z) dz$ . A limit to the former is set by wave breaking. For PWFAs, a limit to the energy gain is imposed by the transformer ratio which will be discussed shortly. For LWFAs, the acceleration length is largely determined by the evolution of the laser pulse and is ultimately limited by either laser energy depletion and diffraction or electron dephasing.

Analytical expression for the characteristic lengths have already been obtained from linear and 1D nonlinear theory. For the three-dimensional relativistic case simulations are required. A complete scaling theory in the bubble regime, which relies on a mixture of analytical approaches and PIC simulations, is given by Lu et al. [61] for laser intensities of  $a_0 \gtrsim 2$ . A summary of the most important scalings found by the different approaches is given in table 2.1.

The laser power available during the experimental campaign exceeded the critical power for self-focusing at the employed plasma densities. Therefore, the vacuum Rayleigh length, which would otherwise constitute a severe constrain to the energy gain, is ineffectual. Comparing the dephasing and pump depletion lengths of mildly relativistic laser pulses with  $a_0 \gtrsim 1$ , the different theories predict that both are approximately of the same order ( $L_d \sim L_{pd}$ ). The dominating effect is eventually dependent on the laser propagation dynamics in plasma, which are inherently nonlinear and therefore difficult to predict exactly. Nevertheless, if the acceleration length is limited by dephasing, the gas target length should ideally match  $L_d$  in order to achieve the maximum energy gain. If it is limited by  $L_{pd}$ , the target length should be adjusted to achieve the maximum

	$a_0$	$w_0$	$L_d$	$L_{pd}$	$\gamma_{ph}$	$E_{max}/m_e c^2$
Linear	$< 1$	$\lambda_p$	$\frac{\omega_L^2}{\omega_p^2} \lambda_p$	$\frac{\omega_L^2}{\omega_p^2} \frac{8.7 \lambda_p}{\pi a_0^2}$	$\frac{\omega_L}{\omega_p}$	$a_0^2 \frac{\omega_L^2}{\omega_p^2}$
1D Nonlinear	$> 1$	-	$\frac{\omega_L^2}{\omega_p^2} \frac{\sqrt{2} a_0 \lambda_p}{\pi}$	$\frac{\omega_L^2}{\omega_p^2} \frac{8.7 \lambda_p}{2\pi}$	$\sqrt{a_0} \frac{\omega_L}{\omega_p}$	$4 a_0^2 \frac{\omega_L^2}{\omega_p^2}$
3D Bubble	$> 2$	$\frac{\sqrt{a_0}}{\pi} \lambda_p$	$\frac{4}{3} \frac{\omega_L^2}{\omega_p^2} \frac{\sqrt{a_0}}{k_p}$	$\frac{\omega_L^2}{\omega_p^2} c \tau_0$	$\frac{1}{\sqrt{3}} \frac{\omega_L}{\omega_p}$	$\frac{2}{3} a_0 \frac{\omega_L^2}{\omega_p^2}$

**Table 2.1:** Overview of the scaling laws obtained from analytical linear and 1D nonlinear theory and the phenomenological scaling laws derived from *PIC* simulations by Lu et al. [61].

energy gain without possible deterioration of the beam properties caused by beam head erosion due to propagation through the gas medium.

From the 3D phenomenological theory, some fundamental scalings can be considered to predict the best parameters for **LWFA**. In general, neglecting energy depletion, a lower plasma density allows for higher energy gains as  $L_d$  is increased. In the bubble regime, the energy gain is approximately given by [61]

$$\Delta[\text{GeV}] = 3.8 \left( \frac{P}{P_c} \right)^{-3/2} \frac{P[\text{TW}]}{100} \propto n_0^{-2/3}. \quad (2.120)$$

Thus,  $n_0$  should be chosen as low as possible. On the other hand, the available laser power has to exceed  $P_{L_d}$  (eq. (2.113)) in order to maintain self-guiding over the dephasing length.

From an experimental point of view, the available laser pulse energy and the pulse duration are usually fixed. The energy gain can thus be maximized by choosing an appropriate plasma density and focal spot size. Since, by eq. (2.112), self-guiding over the dephasing length requires  $a_0 \sim (\omega_L/\omega_p)^{2/5}$ , this condition set a lower bound to the plasma density and an upper bound to the focal spot size. Within this constraint, both can then be optimized by satisfying  $w_0 k_p = 2\sqrt{a_0}$  (eq. (2.110)).

The optimized parameters can be deduced from Fig. 2.8. Assumed is a laser energy on target of 1.5 J and a pulse duration of  $t_{FWHM} = 28$  fs, which were also used in the experiments described in this thesis. The blue surface shows the minimum  $a_0$  that is needed to maintain self-guiding over the acceleration length, where lower plasma densities require a larger  $a_0$ . On the other hand, the beam waist may not exceed the limit depicted by the red plane, as otherwise the required  $a_0$  can not be obtained with the provided laser energy and pulse duration. The condition for the matched spot size, i.e.  $a_0 = w_0^2 k_p^2 / 4$  is shown by the green triangular face and the black line shows the matched conditions that are accessible with the provided laser parameters.

In order to maximize the electron energy gain, the lowest plasma density has to be chosen. At the point where the three planes meet  $n_e = 3.3 \times 10^{18} \text{ cm}^{-3}$ ,  $w_0 = 11 \mu\text{m}$  and  $a_0 = 3.5$ . This plasma density is remarkably close to the optimal value found in the experiment of  $3.4 \times 10^{18} \text{ cm}^{-3}$ . Although the laser vacuum focus was  $w_0 = 19 \mu\text{m}$  (corresponding to  $a_0 = 1.7$ ), the latter will be significantly altered after pulse propagation in plasma due to self-focusing and temporal pulse compression.

## 2. Plasma wakefield acceleration

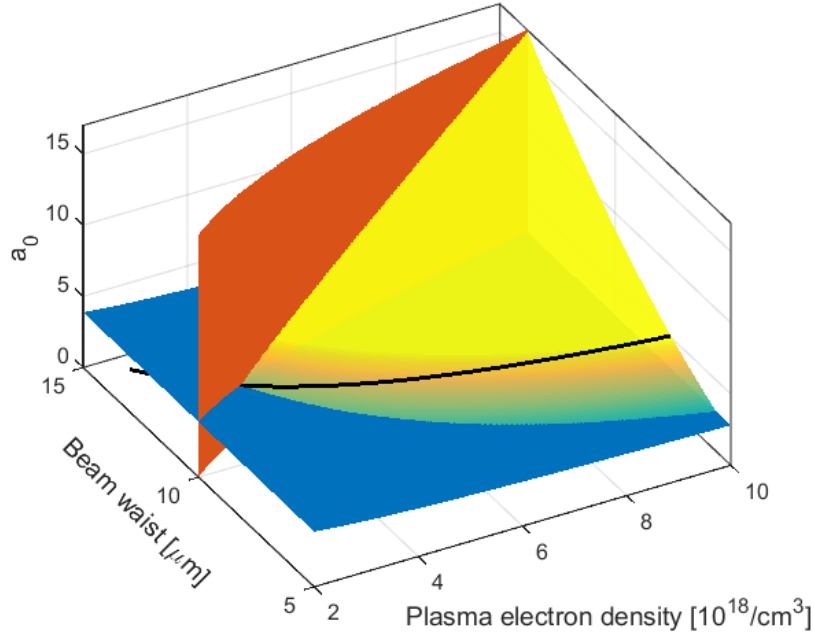


**Figure 2.8:** Optimal laser parameters in the bubble regime for a laser energy of 1.5 J and a pulse duration of  $t_{FWHM} = 28$  fs. The blue plane shows  $a_{0,min} \sim (\omega_L/\omega_p)^{2/5}$  that needs to be exceeded to maintain self-guiding over the dephasing length at the respective plasma density. The red plane shows the corresponding maximum laser waist size  $w_0$  compatible with the given laser parameters. The coloured triangular plane shows the matched beam condition  $w_0 k_p = 2\sqrt{a_0}$ . With the presumed laser energy and pulsed duration, these conditions can be simultaneously satisfied along the black line. In order to obtain maximum electron energies, the lowest density should be chosen, determined by the intersection of the 3 planes for which  $n_0 = 3.3 \times 10^{18} \text{ cm}^{-3}$ .

### The PWFA transformer ratio

In PWFA, electron dephasing does not take place because both, the relativistic driver and the accelerated witness bunch, propagate with the same speed of  $v \approx c$ . Analogous to laser energy depletion, the maximum energy a witness can extract from the driver bunch in a PWFA is limited by the so-called *transformer ratio*  $R$  defined by

$$R = \frac{\Delta\gamma}{\gamma_b} = \frac{E_+}{E_-}, \quad (2.121)$$

where  $\Delta\gamma$  is the maximum energy gain of the accelerated bunch,  $\gamma_b$  is the energy of the driving bunch and  $E_+, E_-$  are the mean accelerating and decelerating electric fields experienced by the witness and driver, respectively. In the linear regime ( $n_b < n_0$ ) the transformer ratio is  $R = 1$  for short Gaussian bunches with an upper limit of  $R \leq 2$  for any longitudinally symmetric bunch profile [92, 93]. It has been shown by simulations that this limit can be overcome by asymmetrically shaped triangular bunches with a linear ramp ( $R \sim 6$ ) or by operating in the nonlinear regime ( $R \sim 7$ ) [94, 95].

---

## Chapter 3

# Transition radiation

Transition radiation (TR) is emitted when a charged particle moves uniformly across the interface of two media with different dielectric constants. Although from classical electrodynamics it is easily seen that an accelerated charge acts as a source of electromagnetic radiation, it was long believed that a charge moving uniformly along a straight line does not emit radiation. This conception was first disproved with the discovery of Cherenkov radiation, which is emitted when the velocity of a charged particle passing through a dielectric exceeds the phase velocity of light in that medium. Later it was realized that although the motion of a charged particle is uniform, the presence of an inhomogeneous or time-varying dielectric medium also results in the emission of electromagnetic radiation. In this context, TR, diffraction radiation and Smith-Purcell radiation may be mentioned [96–98]. In all these cases radiation is emitted in the presence of an inhomogeneous material, either constituted by the interface between two media (TR), an aperture (diffraction radiation) or the surface of a grating (Smith-Purcell radiation). Transition radiation was first predicted in 1954 by Frank and Ginzburg [96]. The heuristic cause of TR is the abrupt change of the charged particle’s self-field at the discontinuity of the dielectric index, due to a different screening of the Coulomb fields inside both materials. To ensure the continuity condition for the tangential electric fields, transient surface currents are induced at the boundary, which act as the source of TR. In this chapter, first the radiation pattern formed by a single electron will be derived. Subsequently, an expression for the emission of a bunch of electrons will be compiled and shown that the emitted spectrum allows to draw conclusions about the bunch’s temporal shape.

### 3.1 Transition radiation emitted by a single electron

Mathematically, the emission process of TR can be approached by several methods [99]. The original derivation, employed by Frank and Ginzburg [96], relies on explicitly solving the Maxwell equations at a metal-vacuum boundary of infinite extent. This yields an expression for the far field energy radiated per unit frequency [96, 100, 101].

An alternative description of the TR formation process is given by the method of virtual quanta. In this model the electron’s self-field is described by the spatial Fourier components of an unperturbed moving charge, namely the pseudo- or virtual photons (Weizsäcker-Williams approximation [102]). Upon passing a metallic interface, these are converted into real photons due to

### 3. Transition radiation

---

the boundary condition. From this source field, the radiation field at an arbitrary distance can be calculated by solving the free space propagation. This method has the advantage that it is valid for an arbitrary distance from the source and thus allows to calculate the emission characteristic also in the near field. A comprehensive treatment of this method can be found in ref. [103, 104], which will be outlined in the following section.

#### 3.1.1 The particle's self-field

We start by considering an ultra-relativistic electron moving with constant velocity  $\mathbf{v}$  such that the current density  $\mathbf{j}$  and the charge density  $\rho$  are expressed by

$$\begin{aligned}\mathbf{j} &= -e\mathbf{v}\delta(\mathbf{r} - \mathbf{v}t), \\ \rho &= -e\delta(\mathbf{r} - \mathbf{v}t).\end{aligned}\tag{3.1}$$

Using the Maxwell equations in the Lorentz gauge, the inhomogeneous macroscopic wave equations (eq. (2.3)) for the electric and the magnetic potential read

$$\begin{aligned}\left(\Delta - \frac{1}{c^2} \frac{\partial^2}{\partial t^2}\right)\Phi &= -\frac{\rho}{\epsilon_0}, \\ \left(\Delta - \frac{1}{c^2} \frac{\partial^2}{\partial t^2}\right)\mathbf{A} &= -\mu_0\mathbf{j}.\end{aligned}\tag{3.2}$$

The solution to these equations can be found by expanding the potentials in the Fourier domain [100, 105], e.g.

$$\mathbf{A}(\mathbf{r}, t) = \int d\omega \int d\mathbf{k} \mathbf{A}(\mathbf{k}, \omega) e^{i(\mathbf{k}\cdot\mathbf{r} - \omega t)},\tag{3.3}$$

where

$$\mathbf{A}(\mathbf{k}, \omega) = \frac{1}{(2\pi)^4} \int dt \int d\mathbf{r} \mathbf{A}(\mathbf{r}, t) e^{-i(\mathbf{k}\cdot\mathbf{r} - \omega t)}.\tag{3.4}$$

The wave equation for the vector potential in the Fourier domain now reads

$$\left(\mathbf{k}^2 - \frac{\omega^2}{c^2}\right)\mathbf{A}(\mathbf{k}, \omega) = \mu_0\mathbf{j}(\mathbf{k}, \omega) = \mu_0 \frac{-e\mathbf{v}}{(2\pi)^4} \int dt \int d\mathbf{r} \delta(\mathbf{r} - \mathbf{v}t) e^{-i(\mathbf{k}\cdot\mathbf{r} - \omega t)}.\tag{3.5}$$

Analogous equations also hold for the electrostatic potential  $\phi$ . The integration over the  $\delta$  function in the space domain is trivial. Using  $\mathbf{r} = \mathbf{v}t$ , we now perform the integration with respect to time

$$\int dt e^{i(\omega - \mathbf{k}\cdot\mathbf{v})t} = 2\pi\delta(\omega - \mathbf{k}\cdot\mathbf{v}).\tag{3.6}$$

This leads to an expression for the frequency components of the potentials:

$$\begin{aligned}\mathbf{A}(\mathbf{k}, \omega) &= \frac{-\mu_0 e\mathbf{v}}{(2\pi)^3} \frac{\delta(\omega - \mathbf{k}\cdot\mathbf{v})}{k^2 - \omega^2/c^2}, \\ \phi(\mathbf{k}, \omega) &= \frac{-e}{(2\pi)^3\epsilon_0} \frac{\delta(\omega - \mathbf{k}\cdot\mathbf{v})}{k^2 - \omega^2/c^2}.\end{aligned}\tag{3.7}$$



To find the electric field we apply the definition of the potentials in the Fourier domain, i.e.  $\mathbf{E}(\mathbf{k}, \omega) = -ik\phi(\mathbf{k}, \omega) + i\omega\mathbf{A}(\mathbf{k}, \omega)$ . The electric field's Fourier components are thus given by

$$\mathbf{E}(\mathbf{k}, \omega) = \frac{-ie}{(2\pi)^3\epsilon_0} \frac{\omega\mathbf{v} - \mathbf{k}c^2}{k^2c^2 - \omega^2} \delta(\omega - \mathbf{k} \cdot \mathbf{v}). \quad (3.8)$$

We now have arrived at the inhomogeneous solution, which describes the electron's self-field in the wavenumber-frequency domain. The complete solution to eq. (3.2) is obtained by adding the solution of the homogeneous wave equation, given by

$$\mathbf{E}^{ph}(\mathbf{k}, \omega) = \mathbf{E}'(\mathbf{k}, \omega) \delta(k^2 - \omega^2/c^2), \quad (3.9)$$

which describes the divergence-free radiation field.

Equation (3.8) - the Fourier representation of the electron's Coulomb field - forms the basis of several approaches that deal with the description of the TR emission process. Depending on the specific problem to be solved, this topic has been addressed by several authors [99, 104–107].

### 3.1.2 General framework

Due to its appealing simplicity, the formula most often stated in the literature is the angular distribution of the spectral energy derived from the classic theory given by Frank and Ginzburg [96]

$$\frac{d^2W}{d\omega d\Omega} = \frac{e^2}{4\pi^3\epsilon_0 c} \frac{\beta^2 \sin^2 \theta}{(1 - \beta^2 \cos^2 \theta)^2}. \quad (3.10)$$

In this derivation, the authors make use of the electric field's continuity conditions at the interface to explicitly solve the Maxwell equations in the Fourier domain. Thus, the radiation field is found in the wavenumber-frequency domain, which allows a straightforward calculation of the angular dependence of the radiated energy. However, this approach is only valid in the far-field limit and for transversely infinite target dimensions, conditions which are not always justified in the experiment. To avoid these restrictions, it is necessary to also take into account the macroscopic size of the source field. This leads to a different field distribution in the so-called *pre-wave* zone, i.e. for observation distances from which the TR source can not be considered as a point, and also causes the finite size target effect [108].

As will be shown in the following, the pre-wave zone can easily extent up to several meters if considering long wavelength TR emitted by high-energy electrons and can exceed the size of the laboratory. Therefore, an accurate measurement of the TR spectrum needs to include these effects. We now derive a model valid in the pre-wave (near-field) zone as well as for arbitrarily shaped targets, analogous to that presented in [104]. Further, we will show that for sufficiently large observation distances and target dimensions the classic Ginzburg-Frank formula is recovered.

For this purpose, the electron's Coulomb field in terms of wavenumber is of minor interest but we are interested in its spatial extent. Reverting to eq. (3.8) and taking its Fourier transform, the field's frequency components in the spatial domain are obtained. In cylindrical coordinates

### 3. Transition radiation

$(\rho, \varphi, z)$  the result is [104, 105]

$$\mathbf{E}(\mathbf{r}, \omega) = \frac{-e\alpha}{(2\pi)^{3/2}\epsilon_0\beta c} \left( \mathbf{e}_\rho K_1(\alpha\rho) - \mathbf{e}_z \frac{i}{\gamma} K_0(\alpha\rho) \right) e^{i\frac{\omega}{\beta c}z} \quad (3.11)$$

$$\stackrel{(\gamma \gg 1)}{=} \frac{-e\alpha}{(2\pi)^{3/2}\epsilon_0\beta c} \mathbf{e}_\rho K_1(\alpha\rho) e^{i\frac{\omega}{\beta c}z}, \quad (3.12)$$

$$\text{with } \alpha = \frac{\omega}{\gamma\beta c},$$

and where  $K_0$  and  $K_1$  denote the 0<sup>th</sup> and 1<sup>st</sup> order modified Bessel functions.

Equation (3.11) is the exact representation of the electron's Coulomb field. From now on we restrict our treatment to the fields produced by highly relativistic electrons, as the experiments described in this thesis are performed in this regime. In this case the contribution of the 2<sup>nd</sup> term can be neglected as it vanishes with  $\gamma^{-1}$  and the particle's self-field is approximated as being purely transverse<sup>1</sup>. Since its Fourier components resemble the fields of plane electromagnetic waves, it is referred to as a disk of virtual photons, also called the *Weizsäcker-Williams approximation* [30, 109].

We now consider the case of forward TR produced by a relativistic electron traversing a metallic foil at normal incidence. The foil is assumed to be a perfect conductor positioned at  $z = 0$  and may possess an arbitrary shape. After passing the radiator foil, the total electric field  $\mathbf{E}^+(\mathbf{r}, \omega)$  in the half-space  $z > 0$  may be written as [103]

$$\mathbf{E}^+(\mathbf{r}, \omega) = \mathbf{E}_{rad}^+(\mathbf{r}, \omega) + \mathbf{E}_e(\mathbf{r}, \omega), \quad (3.13)$$

where  $\mathbf{E}_{rad}^+(\mathbf{r}, \omega)$  represents the radiation field and  $\mathbf{E}_e(\mathbf{r}, \omega)$  denotes the electron's self-field given by eq. (3.12). An analogous expression may be established for the backward radiation field. Since the total field inside the conductor vanishes and the particle fields are considered to be purely transverse, the continuity condition for the tangential component of the total field at the boundary yields

$$\mathbf{E}_{rad}^+(\mathbf{r}, \omega) = -\mathbf{E}_e(\mathbf{r}, \omega). \quad (3.14)$$

The radiation field at  $z = 0$  is thus simply given by a change in sign of the particle field and, as the latter, is radially polarised<sup>2</sup>. Now that the radiation field is known, the field distribution at an observation point located at  $\mathbf{r}' = (\rho', \varphi', z')$  can be calculated by the Huygens-Fresnel principle [110]. For targets of arbitrary shape  $S$ , the integral must be performed twice for orthogonal polarisations

$$E_{x/y}(\mathbf{r}', \omega) = -\frac{ik}{2\pi} \int_S \int E_{e,x/y}(\mathbf{r}, \omega) \frac{\exp(ik|\mathbf{r}' - \mathbf{r}|)}{|\mathbf{r}' - \mathbf{r}|} \rho d\rho d\varphi, \quad (3.15)$$

1. As shown by Shkvarunets and Fiorito [107], negligence of the 2<sup>nd</sup> term of eq. (3.11) only has a minor effect even for a mildly relativistic electron energy of  $\gamma = 5$ . Furthermore, considering the geometry used in the experiments (observation length, collection angle and radiator size), ref. [107] shows that an excellent agreement is reached for arbitrary particle energy.

2. This derivation is valid as long as the radiator can be considered an ideal conductor, i.e.  $\epsilon(\omega) = 1 - \omega_p/\omega \ll 0$ . For most metals the plasma frequency is on the order of  $10^{16}$  Hz. The experiments described in this thesis were performed in the range from infrared to optical frequencies in which  $\epsilon(\omega)$  approximates an ideal conductor. The radiator's plasma frequency constitutes a high-frequency cut-off of the radiation spectrum in the X-ray regime.



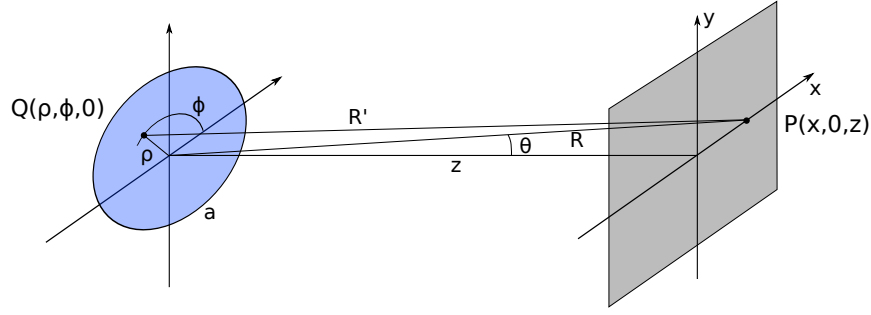


**Figure 3.1:** Sketch of the coordinate system used to calculate the diffraction integral of the *TR* source term for a circular radiator of finite radius.

where  $x, y$  denote the polarisation,  $k = \omega/c$  and  $|\mathbf{r}' - \mathbf{r}| \gg \lambda$ . For complex target shapes numerical calculation is required since usually analytic solutions do not exist.

We have now arrived at a description of the electric field distribution. However, from an experimental point of view, the quantity of interest is usually the spectral energy distribution that is more easily accessible by the use of spectrometers.

The total energy  $W$  radiated through an observation plane can be calculated by integrating the energy flux density given by the Poynting vector with respect to space and time. Applying Parseval's theorem yields

$$W = \frac{1}{\mu_0 c} \int_A \int_{-\infty}^{\infty} |\mathbf{E}(t)|^2 dt dA = 2\epsilon_0 c \int_A \int_0^{\infty} |\mathbf{E}(\omega)|^2 d\omega dA. \quad (3.16)$$

The spectral energy density is thus given by

$$\frac{d^2 W}{d\omega dA} = 2\epsilon_0 c |\mathbf{E}(\omega)|^2. \quad (3.17)$$

In contrast to the classical Ginzburg-Frank formula, we now have the tools at hand to describe the radiation field and spectral energy distribution quantitatively in a general model. In particular, finite target shapes as well as observation distances within the near-field region can be accounted for.

### 3.1.3 Spectral and angular distribution

We now study the example of the radiation pattern produced by a circular radiator of radius  $a$ . As this simple case possesses an analytical solution, it will be useful to derive the angular and spectral characteristics of *TR*. The geometry is sketched in Fig. 3.1. Note that on the observation screen a Cartesian coordinate system is chosen. Due to the radial symmetry of the target as well as the source field, it is sufficient to calculate the field along a radial lineout. Using eq. (3.15), the field amplitude along the  $x$ -axis at point  $P(x, 0, z)$  is

$$E_x(P, \omega) = \frac{-ik}{2\pi} \int_0^{2\pi} \int_0^a E_e(\mathbf{r}, \omega) \cos \phi \frac{\exp(ikR')}{R'} \rho d\rho d\phi, \quad (3.18)$$

### 3. Transition radiation

where  $R'$  is the distance between Q and P given by

$$R' = \sqrt{z^2 + (x - \rho \cos \phi)^2 + (\rho \sin \phi)^2} \approx R - \frac{x\rho \cos \phi}{R} + \frac{\rho^2}{2R} \quad (3.19)$$

with  $R^2 = z^2 + x^2$ .

We will first study the far-field case. For this purpose only the first two terms of the Taylor expansion of  $R'$  are considered, which results in the far-field approximation of a spherical wavefront. Using  $\sin \theta = x/R$  and the relativistic source term of eq. (3.12) we obtain

$$E_x(P, \omega) = \frac{iek^2}{(2\pi)^{(5/2)}\epsilon_0\beta^2\gamma c} \frac{\exp(ikR)}{R} \times \int_0^{2\pi} \int_0^a K_1\left(\frac{k\rho}{\beta\gamma}\right) \cos \phi \exp(-ik\rho \sin \theta \cos \phi) \rho \, d\rho \, d\phi. \quad (3.20)$$

Both integrals can be solved analytically, resulting in [104]

$$E_x(\theta, \omega) = \frac{e}{(2\pi)^{3/2}\epsilon_0 c} \frac{\exp(ikR)}{R} \frac{\beta \sin \theta}{1 - \beta^2 \cos^2 \theta} [1 - T(\theta, \omega)], \quad (3.21)$$

where

$$T(\theta, \omega) = \frac{ka}{\beta\gamma} J_0(ka \sin \theta) K_1\left(\frac{ka}{\beta\gamma}\right) + \frac{ka}{\beta^2\gamma^2 \sin \theta} J_1(ka \sin \theta) K_0\left(\frac{ka}{\beta\gamma}\right)$$

and  $J_1$  denotes the Bessel function of the first kind.

As a first case, we consider the radiation from a target of infinite size. In the limit  $a \rightarrow \infty$ , both Bessel functions tend to zero and  $\lim_{a \rightarrow \infty} T(\theta, \omega) = 0$  [104]. Using eq. (3.17) and relating the surface element to the solid angle by  $dA = R^2 d\Omega$ , we obtain the classical result

$$\frac{d^2 W}{d\omega d\Omega} = \frac{e^2}{4\pi^3 \epsilon_0 c} \frac{\beta^2 \sin^2 \theta}{(1 - \beta^2 \cos^2 \theta)^2}. \quad (3.22)$$

This rather simple formula is instructive to explore some of the basic properties of TR. A peculiar feature of eq. (3.22) is that the spectral energy distribution is frequency-independent, which accounts for the generation of broadband radiation (note that this property is exactly true only in the far-field approximation and for an infinite target size, as will be outlined below). The second term of eq. (3.22) describes a hollow cone, a slice of which is plotted in Fig. 3.2a. Differentiating with respect to  $\theta$ , we find that the angular distribution has its maximum at an opening angle of

$$\theta_{max} = \arcsin\left(\frac{1}{\beta\gamma}\right) \stackrel{(\gamma \gg 1)}{\simeq} \frac{1}{\gamma}. \quad (3.23)$$

Thus, for relativistic particle energies, the emission is strongly directed in forward direction. In this case, using the small angle approximation, the second term of eq. (3.22) can be simplified by [104]

$$\frac{\beta^2 \sin^2 \theta}{(1 - \beta^2 \cos^2 \theta)^2} \simeq \frac{\beta^2 \theta^2}{(1 - \beta^2(1 - \theta^2))^2} \simeq \gamma^2 \frac{(\theta\gamma)^2}{(1 + (\theta\gamma)^2)^2}. \quad (3.24)$$

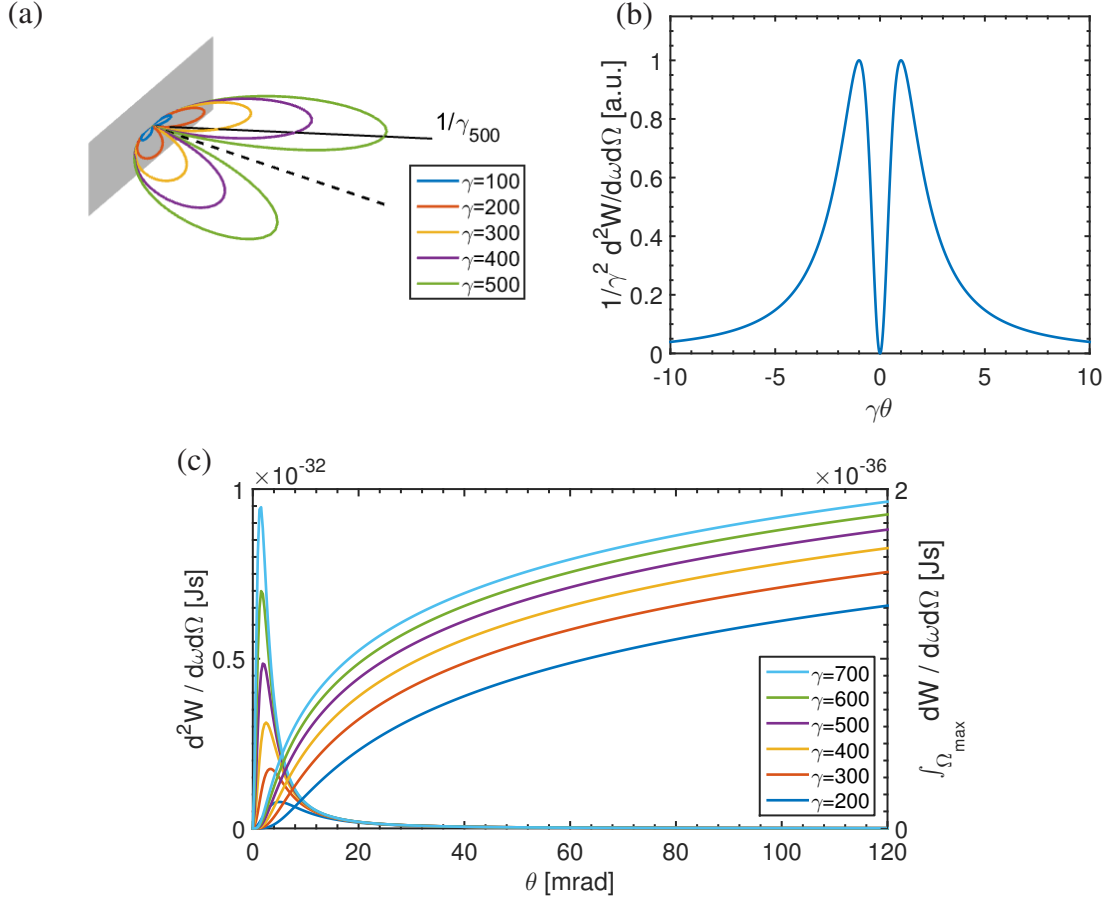


**Figure 3.2:** Angular distribution of *TR* in the far-field. (a) shows the angular emission characteristics in the horizontal plane for different values of  $\gamma$ . The opening angle is given by  $1/\gamma$  as shown by the black line for the lobe corresponding to the highest value of  $\gamma$ . The three-dimensional emission pattern (eq. (3.24)) is given by rotation of the lobes around the axis defined by the electron trajectory (shown by the dashed line). A lineout through its center is shown in (b), plotted over the scaled angle  $\gamma\theta$ . For  $\gamma \gg 1$ , the shape of the *TR* emission is only a function of this scaled angle, while the peak intensity scales with  $\gamma^2$ . In (c), the vertical axis on the right shows the integral of the spectral energy emitted in a forward cone with an opening angle of  $\theta$ , illustrating the logarithmic  $\gamma$  dependence determined in eq. (3.25). For comparison, the angular distributions, scaling with  $\gamma^2$ , are shown on the left.

For large  $\gamma$ , the shape of the distribution is a simple function of the quantity  $\theta\gamma$  as depicted in Fig. 3.2b and its magnitude scales with  $\gamma^2$ . Due to the radial symmetry and polarisation of the source term, the intensity in forward direction cancels exactly.

We finally compute the spectral energy emitted in the forward hemisphere. Using eq. (3.22) and integrating over all angles in the limit  $\gamma \gg 1$  yields [111]

$$\frac{dW}{d\omega} = \frac{e^2}{2\pi^2\epsilon_0 c} \ln \gamma. \quad (3.25)$$

### 3. Transition radiation

The last two equations show that although the peak of the angular distribution scales with  $\gamma^2$ , the total emission exhibits a rather weak, logarithmic  $\gamma$  dependence. The reason is the strong directionality of TR, which confines the peak emission to small angles around  $\gamma^{-1}$  and is of less consequence when considering larger collection angles. The radiated spectral energy in dependence of the collection angle is illustrated in Fig. 3.2c.

#### 3.1.4 Radiation from a finite-size target

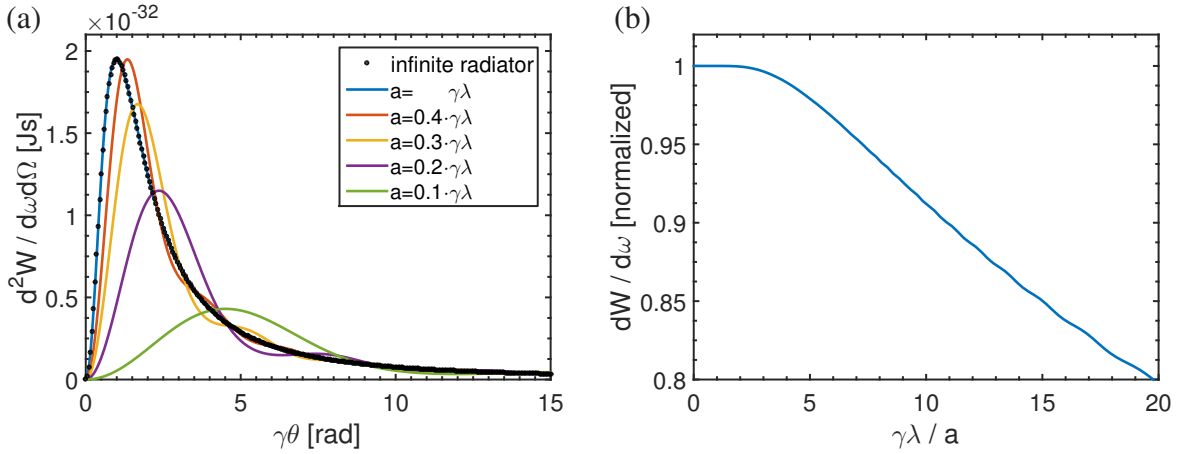


**Figure 3.3:** Far-field distribution of TR produced by a charged particle with  $\gamma = 1000$  traversing a finite, circular radiator of radius  $a$ . In (a), its effect on the angular distribution is shown for different values of  $a/(\gamma\lambda)$ . For small fractions of  $a/(\gamma\lambda)$ , the angular distribution is broadened such that the spectral content becomes a function of the emission angle. For radii exceeding the effective source size, the distribution is in perfect agreement with the infinite radiator described by eq. (3.22). (b) shows the spectral energy emitted into the forward cone with an opening half-angle of 133 mrad (corresponding to the collection angle as used in the experiments presented in this thesis) and  $\gamma = 1000$ . As the source size increases and exceeds the radiator dimensions, the outer parts of the particle's self-field do not contribute to the radiation process, which leads to a reduction of the spectral energy.

We now revert to eq. (3.21) in order to analyse the effect of a radiator with a finite radius  $a$  such that  $T(\theta, \omega) \neq 0$ . In this case, the spectral content of the radiation is no longer constant but becomes a function of the emission angle  $\theta$  [106]. This effect can be understood by considering the radial extent of the particle's self-field, which can be defined by taking its weighted mean, yielding a characteristic radius of [105, 108]

$$r_{\text{eff}} = \frac{\int_0^\infty \rho E(\rho, \omega) 2\pi\rho d\rho}{\int_0^\infty E(\rho, \omega) 2\pi\rho d\rho} = \frac{2\beta}{\pi^2} \gamma\lambda \sim \gamma\lambda. \quad (3.26)$$

The quantity of interest is the ratio between the extent of the source field and the radiator. If the source field exceeds the extent of the radiator, the outer parts do not contribute to the radiation process and the target surface effectively acts as an aperture. Consequently, diffraction effects arise, leading to an increased emission angle as well as diffraction rings. The smaller this ratio, the stronger will be its effect, as shown in Fig. 3.3a. When the target dimensions exceed the

extent of the self-field,  $T(\theta, \omega) \ll 1$  and the effect vanishes [104, 106]. Thus, the target may only be considered infinite if

$$a \geq \gamma\lambda. \quad (3.27)$$

For a quantitative analysis this is an important condition, because the effective aperture caused by a smaller radiator not only alters the angular distribution but also reduces the amount of radiation as shown in Fig. 3.3b. Utilizing Babinet's principle, this reduction can be interpreted as the sum of diffraction radiation (which would be produced by a circular hole of radius  $a$ ) and the conventional TR produced by an infinite target [106].

### 3.1.5 Radiation in the near-field

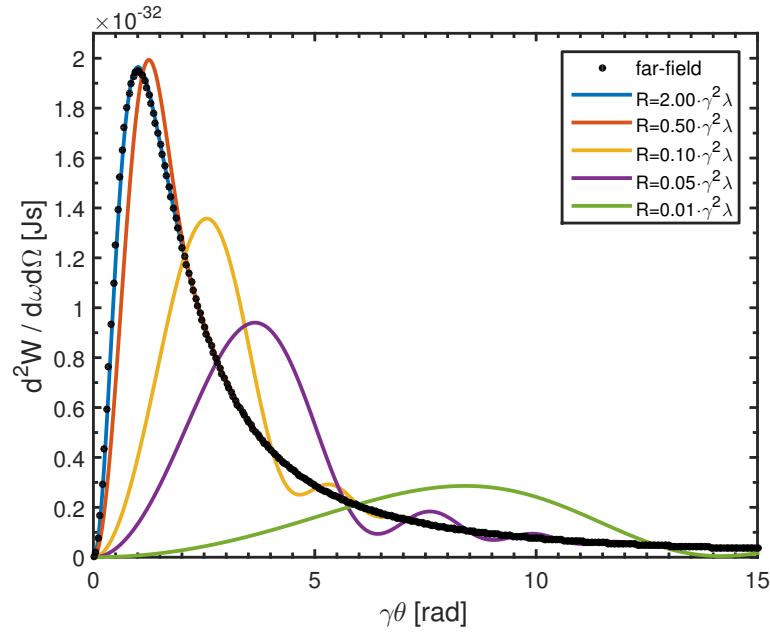


**Figure 3.4:** Near-field angular distribution of TR for a charged particle with  $\gamma = 1000$ . In this case the source condition  $a \geq \lambda\gamma$  is satisfied. The evolution is shown for different distances  $R$  from the source, given in units of the formation length  $L_f = \gamma^2\lambda$ . For  $R \gtrsim L_f$  the far field distribution is obtained. In the near-field, the distribution becomes wider and the macroscopic source size leads to strong, distance dependent interference effects.

To determine the effect of a finite observation distance we resort to eq. (3.19) and now include the 2<sup>nd</sup> term in the Taylor expansion of the distance from the source to the observation screen. This leads to an additional phase factor of the form  $\exp(ik\rho^2/2R)$  and eq. (3.20) becomes

$$E_x(P, \omega) \propto \int_0^{2\pi} \int_0^a K_1\left(\frac{k\rho}{\beta\gamma}\right) \cos\phi \exp(-ik\rho \sin\theta \cos\phi) \exp\left(ik\frac{\rho^2}{2R}\right) \rho \, d\rho \, d\phi. \quad (3.28)$$

Due to inclusion of the parabolic phase term, eq. (3.28) will be valid in the region of Fresnel diffraction, also called the near-field or pre-wave region [110, 112].

### 3. Transition radiation

---

Performing the integral with respect to the azimuthal angle and applying eq. (3.17) we obtain [104]

$$\frac{d^2W}{d\omega d\Omega} = 2\varepsilon_0 c \left| \frac{ek^2}{(2\pi)^{3/2}\varepsilon_0\beta^2\gamma c} \int_0^a K_1\left(\frac{k\rho}{\beta\gamma}\right) J_1(k\rho \sin\theta) \exp\left(ik\frac{\rho^2}{2R}\right) \rho d\rho \right|^2. \quad (3.29)$$

Since an analytical solution does not exist, the integration with respect to  $\rho$  has to be solved numerically. Note that eq. (3.29) differs from the far-field description only by the parabolic phase factor. By requiring the exponential to not contribute substantially to the integration, we can compile an expression for the validity range of the far-field description:

$$\frac{k\rho^2}{2R} < \pi. \quad (3.30)$$

The integrand will only contribute over the finite extent of the source size. Using eq. (3.26) we obtain

$$R > \frac{2\pi\gamma^2\lambda^2}{2\pi\lambda} = \gamma^2\lambda = L_f, \quad (3.31)$$

where  $L_f$  is commonly referred to as the *formation length*. The evolution of the angular distribution is shown in Fig. 3.4 for different distances to the source. Within the near-field ( $R/L_f < 1$ ), the distribution differs significantly from the far-field description and shows a complex behaviour that strongly depends on  $R/L_f$ . As  $R/L_f$  decreases, the beam becomes wider and exhibits a diffraction ring structure. Simultaneously, the emission into the range of angles  $\theta \sim \gamma^{-1}$  is suppressed. These effects can be attributed to interference between the elementary radiators from the macroscopic source [103, 112].

In the experiments described in this thesis, TR was produced by electron bunches with energies up to 700 MeV ( $\gamma \sim 1400$ ) and its spectral energy was measured in the range of  $\lambda = 0.4 - 7.1 \mu\text{m}$ . Due to the  $\gamma^2$  dependence of the formation length, for high-energy electrons  $L_f \approx 14\text{m}$ , which exceeds the dimensions of the vacuum chamber. Since the collection optics are necessarily placed within the near-field region, a thorough analysis needs to include the precise emission characteristics. Therefore, the spectral energy distribution in the near-field was determined by eq. (3.28) and subsequently propagated through the optical setup with the help of Fourier optics. The complete procedure will be presented in chapter 5.

## 3.2 Coherent transition radiation

With the characteristic distribution of the single particle TR at hand, we now focus on the emission produced by a bunch of electrons. In particular, we will address the question which kind of information can be retrieved by a measurement of the TR frequency spectrum.

The total electric field of an electron bunch consisting of  $N$  electrons is found by summing up the contribution produced by each individual particle. Again it is assumed that the energies are relativistic, such that  $\beta \approx 1$  for all particles and consequently their relative position within the bunch does not change significantly during the emission process. The coordinate system is shown in Fig. 3.5, where  $\mathbf{n}_R$  and  $\mathbf{n}_i$  denote unity vector directed towards the observation point  $P$ . At  $P$ , the

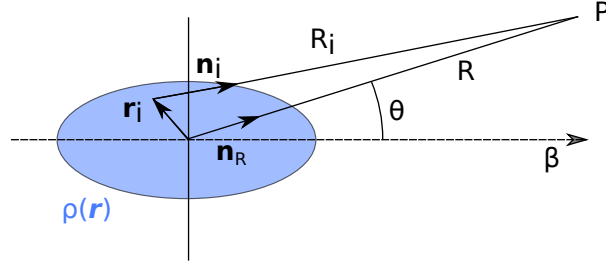


**Figure 3.5:** Schematic drawing of the coordinate system used to describe the electron bunch density distribution  $\rho(\mathbf{r})$ .

radiation field is given by the sum of the individual fields  $\mathbf{E}_i$ , taking into account their relative phase

$$\mathbf{E}_{tot}(\omega) = \sum_{i=1}^N \mathbf{E}_i(\omega) e^{i\phi_i}. \quad (3.32)$$

The relative phase delay between TR produced by a reference electron located in the middle of the bunch and an electron located at  $\mathbf{r}_i$  is given by  $\phi_i = \omega \Delta t = k(R - R_i)$ . Using  $\mathbf{r}_i + R_i \mathbf{n}_i = R \mathbf{n}_R$ , one obtains

$$R_i = R \mathbf{n}_R \cdot \mathbf{n}_i - \mathbf{n}_i \cdot \mathbf{r}_i \approx R \cos(\theta) - \mathbf{n}_i \cdot \mathbf{r}_i \approx R - \mathbf{n}_R \cdot \mathbf{r}_i. \quad (3.33)$$

This approximation is valid if the observer is located far from the radiator compared to the transverse extent of the electron bunch ( $|\mathbf{r}_i| \ll R$ ), which is usually true<sup>1</sup>. The relative phase delay is then given by

$$\phi_i = k \mathbf{n}_R \cdot \mathbf{r}_i = \mathbf{k} \cdot \mathbf{r}_i. \quad (3.34)$$

In the experimental measurement, the quantity of interest is the radiated spectral energy. Using eq. (3.32) and eq. (3.34) yields

$$\begin{aligned} \frac{d^2 W_{tot}}{d\omega d\Omega} &\propto |\mathbf{E}_{tot}(\omega)|^2 \\ &= \left| \sum_{i=1}^N \mathbf{E}_i(\omega) e^{i\mathbf{k} \cdot \mathbf{r}_i} \right|^2 \\ &= \sum_{i=1}^N \sum_{j=1}^N \mathbf{E}_i(\omega) \mathbf{E}_j^*(\omega) e^{i\mathbf{k} \cdot (\mathbf{r}_i - \mathbf{r}_j)} \\ &= \sum_{i=1}^N |\mathbf{E}_i(\omega)|^2 + \sum_{i,j=1, (i \neq j)}^N \mathbf{E}_i(\omega) \mathbf{E}_j^*(\omega) e^{i\mathbf{k} \cdot (\mathbf{r}_i - \mathbf{r}_j)}. \end{aligned} \quad (3.35)$$

The spectral energy at the observation point  $P$  is thus composed of a term linear in  $N$ , which describes the incoherent sum of the individual particle fields, and a 2<sup>nd</sup> term that scales with  $N^2$ . The latter describes coherent transition radiation (CTR) as it takes into account the phase relationship between the fields.

1. Considering the geometry of the experimental setup presented in chapter 4, the phase error introduced by this assumption amounts to less than 1 %.



### 3. Transition radiation

Since the number of particles per bunch is typically in the order of  $10^8$  (for charges in the pC range), the contribution of the incoherent term can be neglected.

To further simplify eq. (3.35) it proves convenient to represent the electron beam by its ensemble average. We therefore describe its charge distribution by a normalized continuous function  $h(\mathbf{r}, \mathbf{p})$ , where  $\mathbf{r}$  and  $\mathbf{p}$  denote the position and momentum of the distribution in six-dimensional phase space,  $\int \int h \, d\mathbf{r} \, d\mathbf{p} = 1$  and the momentum distribution is given by  $g(\mathbf{p}) = \int h \, d\mathbf{r}$ . In the limit of large  $N$ , the discrete summation of eq. (3.32) can now be replaced by an integral expression [111, 113]

$$\sum_{i=1}^N \mathbf{E}_i(\omega) e^{i\mathbf{k}\mathbf{r}_i} \rightarrow N \int \mathbf{E}(\omega, \mathbf{p}) \int h(\mathbf{r}, \mathbf{p}) e^{i\mathbf{k}\mathbf{r}} \, d\mathbf{r} \, d\mathbf{p} \quad (3.36)$$

and the coherent term of eq. (3.35) becomes

$$\begin{aligned} |\mathbf{E}(\omega)|^2 &= N^2 \left| \int \mathbf{E}(\omega, \mathbf{p}) \int h(\mathbf{r}, \mathbf{p}) e^{-i\mathbf{k}\mathbf{r}} \, d\mathbf{r} \, d\mathbf{p} \right|^2 \\ &= N^2 \left| \int \mathbf{E}(\omega, \mathbf{p}) g(\mathbf{p}) F \, d\mathbf{p} \right|^2, \end{aligned} \quad (3.37)$$

where  $F$  is the *form factor* defined by

$$F = \frac{1}{g(\mathbf{p})} \int h(\mathbf{r}, \mathbf{p}) e^{-i\mathbf{k}\mathbf{r}} \, d\mathbf{r}. \quad (3.38)$$

The degree of coherence is thus determined by the form factor, which is a function of the radiation frequency  $\omega = |\mathbf{k}|c$ , the observation direction  $\mathbf{k}/k$  and the phase space distribution  $h$ .

#### 3.2.1 The form factor

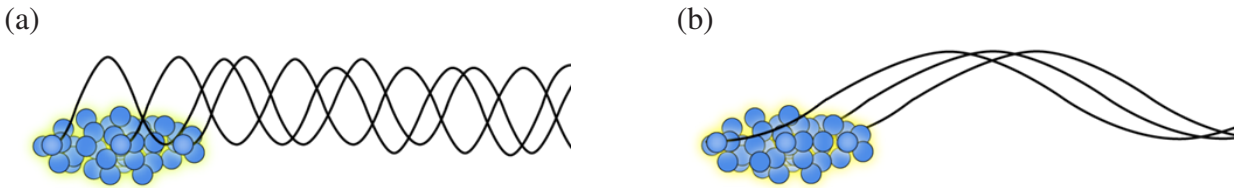


**Figure 3.6:** Illustration of the incoherent (a) and coherent (b) superposition of TR from individual electrons forming a bunch. Wavelengths longer than the bunch length add up coherently.

When the momentum distribution is known, the single particle fields can be calculated as described in the last section. As seen from eq. (3.37), the spectral energy distribution at an observation plane is then completely determined by the form factor and thus by the electron bunch's phase space distribution  $h$ .

To isolate information about the bunch shape we simplify our model by assuming that the momentum and spatial distributions are not correlated (the effect of possible correlations will be discussed in subsection 3.2.4). Then  $h$  is separable into a momentum distribution and a spatial



distribution by  $h(\mathbf{r}, \mathbf{p}) = g(\mathbf{p}) \rho(\mathbf{r})$  and the form factor becomes a simple Fourier transform of the latter

$$F(\mathbf{k}) = \int e^{-i\mathbf{k}\mathbf{r}} \rho(\mathbf{r}) d\mathbf{r}, \quad (3.39)$$

with the inverse transform given by

$$\rho(\mathbf{r}) = \frac{1}{2\pi} \int F(\mathbf{k}) e^{i\mathbf{k}\mathbf{r}} d\mathbf{k}. \quad (3.40)$$

The form factor is now completely determined by the bunch shape  $\rho(\mathbf{r})$  and describes the amplitude and phase of the spatial distribution in Fourier space. The transition from incoherent radiation to constructive interference can be visualized in a simple picture. The two limiting cases are depicted in Fig. 3.6.

For wavelengths short compared to the bunch length, the partial waves emitted by individual electrons add up incoherently ( $|F| = 0$ ). When the wavelength becomes comparable or larger than the bunch length, electrons within the bunch radiate roughly in phase, leading to a coherent enhancement. In the limiting case of an infinitely short bunch and fully constructive interference the form factor becomes  $|F| = 1$ .

The simple picture given above is true for observation in the forward direction. When the observer is placed under an angle, also the transverse coherence determined by the transverse bunch dimensions has to be considered. For the time being we assume a cylindrically symmetric charge distribution and also neglect correlations between the longitudinal and transverse distributions (which is found to be justified by the measurements presented in chapter 4) by using the separation ansatz

$$\rho(\mathbf{r}) = \rho_{\perp}(r_{\perp}) \rho_{\parallel}(z). \quad (3.41)$$

The form factor can then be written as  $F = F_{\perp} F_{\parallel}$  with the longitudinal and transverse components given by

$$F_{\perp}(k_{\perp}) = \int e^{-ik_{\perp}r_{\perp}} \rho_{\perp}(r_{\perp}) dr_{\perp}, \quad (3.42)$$

$$F_{\parallel}(k_{\parallel}) = \int e^{-ik_{\parallel}z} \rho_{\parallel}(z) dz. \quad (3.43)$$

Equation (3.37) can now be expressed by

$$\frac{d^2W}{d\omega d\Omega} \propto |\mathbf{E}(\omega)|^2 = N^2 \left| \int \mathbf{E}(\omega, \mathbf{p}) g(\mathbf{p}) d\mathbf{p} \right|^2 |F_{\perp}|^2 |F_{\parallel}|^2. \quad (3.44)$$

### 3.2.2 Effects of the bunch's spatial and momentum distribution

We now have a closer look at the individual terms, starting with the influence of the spatial bunch dimensions. To illustrate their effect on the spectral energy distribution, we discuss the analytical model of a bi-Gaussian shape given by

$$\rho(r_{\perp}, z) = \frac{1}{\sqrt{2\pi}^3 \sigma_{\perp}^2 \sigma_{\parallel}} \exp\left(-\frac{r_{\perp}^2}{2\sigma_{\perp}^2}\right) \exp\left(-\frac{z^2}{2\sigma_{\parallel}^2}\right), \quad (3.45)$$

### 3. Transition radiation

for which the resulting form factor is

$$F(\mathbf{k}) = F_{\perp} F_{\parallel} = \exp\left(-2\pi^2 \frac{\sigma_{\perp}^2}{\lambda^2} \sin^2 \theta\right) \exp\left(-2\pi^2 \frac{\sigma_{\parallel}^2}{\lambda^2} \cos^2 \theta\right). \quad (3.46)$$

#### Transverse form factor

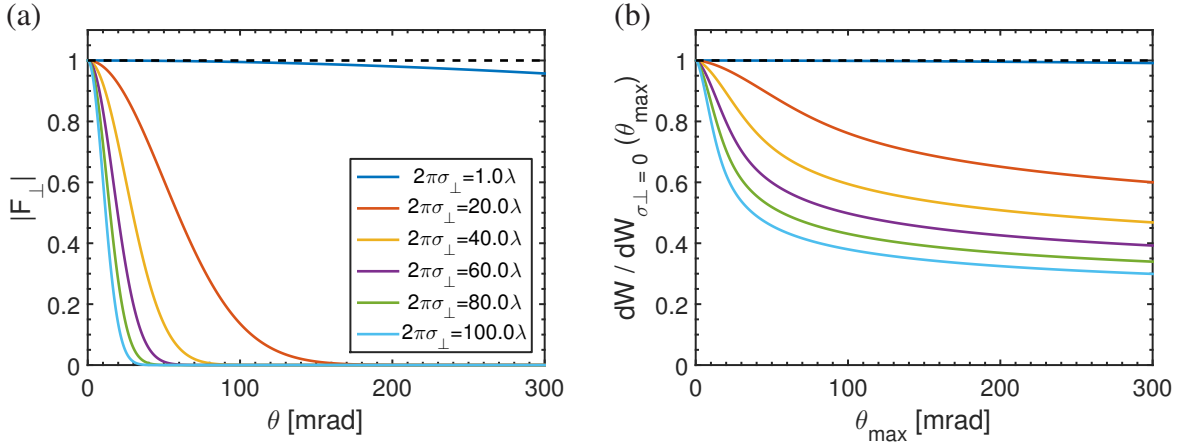


**Figure 3.7:** Transverse form factor. (a) Angular dependence of  $|F_{\perp}|$  for bunches of Gaussian transverse shape and different ratios of  $\sigma_{\perp}/\lambda$ . (b) Relative spectral energy radiated into a forward cone with an opening half angle  $\theta_{\max}$ , normalized to the energy radiated by a bunch with  $\sigma_{\perp} = 0$ , where  $F_{\parallel} = 1$  and  $\gamma = 1000$  is assumed. The light blue line ( $2\pi\sigma_{\perp} = 100\lambda$ ) corresponds to  $\lambda = 2\mu\text{m}$  for a transverse extent at the radiator of  $\sigma_{\perp} \sim 30\mu\text{m}$  (which is approximately the case in the experiments presented in chapter 7).

The impact of the transverse bunch extent is to reduce the coherence with increasing observation angle  $\theta$  and decreasing wavelength  $\lambda$ , due to an increase in path difference between CTR emitted along the transverse bunch extent. As can be seen from eq. (3.46), the effect may only be neglected if the exponent is much smaller than 1, i.e.

$$\sigma_{\perp} \ll \frac{1}{\sqrt{2\pi}} \frac{\lambda}{\sin \theta}. \quad (3.47)$$

Figure 3.7a displays the angular dependence of  $|F_{\perp}|$  with respect to the ratio of  $\sigma_{\perp}/\lambda$ . As shown in Fig. 3.7b, the relative reduction in spectral energy due to decreased coherence is less pronounced when restricting the acceptance angle  $\theta_{\max}$ , because otherwise eq. (3.47) is more heavily violated. However, in this case the detectable absolute energy would be severely diminished (cf. Fig. 3.2c). Regarding the experiments described in this thesis, the necessary acceptance angle is mainly determined by the detector sensitivity at long wavelengths, which are also less affected by the bunch's transverse dimensions. Due to the finite collection angle, the transverse form factor must be taken into account in a broadband measurement spanning many octaves towards shorter wavelengths.

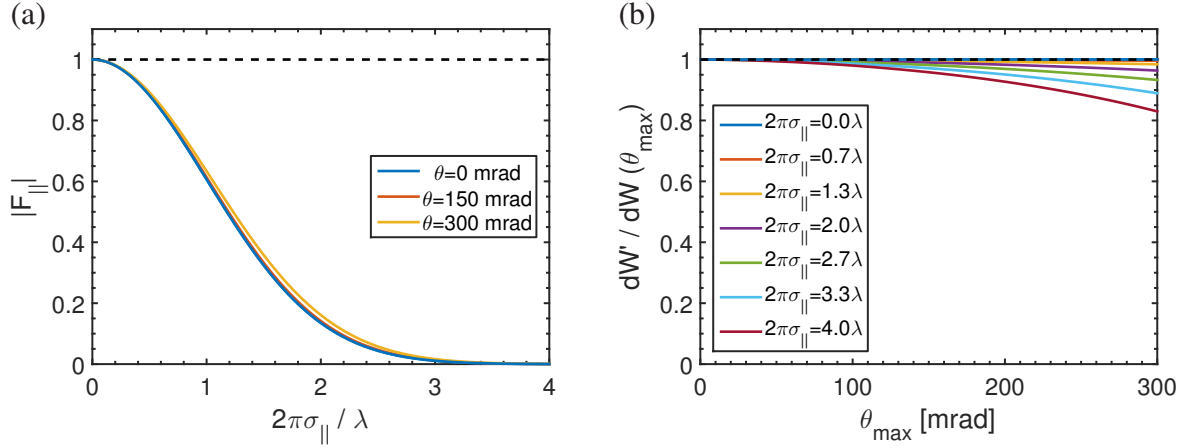


**Figure 3.8:** Longitudinal form factor. In (a),  $|F_{||}|$  is plotted in dependence of  $\sigma_{||}/\lambda$  for different observation angles  $\theta$ . The form factor approaches 1 for  $\lambda \lesssim 2\pi\sigma_{||}$ . (b) Relative error of the spectral energy contained in a forward cone with opening half-angle  $\theta_{\max}$  introduced by the approximation  $\cos\theta \approx 1$  (with  $\gamma = 1000$ ,  $|F_{\perp}| = 1$ ).  $W'$  denotes the radiated energy using this small angle approximation. The dark red line ( $2\pi\sigma_{||} = 4\lambda$ ) corresponds to a typical bunch duration of 5 fs FWHM ( $\sigma_{||} = 0.6 \mu\text{m}$  rms) observed at  $\lambda = 1 \mu\text{m}$ . Within an acceptance angle of  $\theta_{\max} = 133$  mrad the error is less than 4%.

## Longitudinal form factor

The quantity of interest to be determined by the measurement of the CTR spectrum is  $|F_{||}(k_{||})|$ , as it is related to the longitudinal charge distribution  $\rho_{||}$  by eq. (3.43). Figure 3.8a shows its magnitude in dependence of  $\sigma_{||}/\lambda$  for a Gaussian charge distribution. With decreasing  $\sigma_{||}$ , shorter wavelengths are coherently enhanced and the form factor and accordingly the radiated spectral energy are increased.

As seen from Fig. 3.8a and eq. (3.46), for increasing  $\theta$  the longitudinal coherence is now enhanced, due to a decrease in path difference between CTR emitted along the bunch's longitudinal extent. However, for small observation angles  $\theta$ , the longitudinal form factor is only weakly influenced by the observation direction due to its dependence on  $\cos\theta$ . Since the acceptance angle used in the experiment is  $\theta_{\max} = 133$  mrad, we make use of the small angle approximation  $\cos\theta \approx 1$ ,  $k_z \approx |\mathbf{k}| = \omega/c$ , and the longitudinal form factor becomes a sole function of  $\omega$ :

$$F_{||}(k_z) \approx \int dz e^{-i\omega z/c} \rho_{||}(z) dz = F_{||}(\omega). \quad (3.48)$$

Figure 3.8b quantifies the error introduced by this approximation. Due to negligence of the term  $\cos(\theta)$ , the radiated CTR is underestimated and, for a given bunch duration, the error increases with decreasing wavelength. As shown by the dark red line in Fig. 3.8b, for a typical bunch duration of 5 fs FWHM ( $0.6 \mu\text{m}$  rms), the error is less than 4% at a CTR wavelength of  $\lambda = 1 \mu\text{m}$  and  $\theta_{\max} = 133$  mrad. When further taking into account the finite transverse bunch size and resulting suppression of large angle emission by  $|F_{\perp}|$ , the relative error amounts to less than 0.5%. Within the small angle approximation, the longitudinal form factor can now be separated from the integral over the acceptance angle and the spectral energy radiated into a cone with

### 3. Transition radiation

opening angle  $\theta_{max}$  is given by

$$\frac{dW}{d\omega} \propto N^2 |F_{\parallel}(\omega)|^2 \int_{\Omega_{max}} \left| \int \mathbf{E}(\omega, \mathbf{p}) g(\mathbf{p}) d\mathbf{p} \right|^2 |F_{\perp}|^2 d\Omega. \quad (3.49)$$

Thus, when both the electron beam momentum distribution  $g(\mathbf{p})$  and the transverse spatial distribution  $\rho_{\perp}$  are known,  $|F_{\parallel}(\omega)|$  can be determined by a measurement of the CTR spectrum.

#### Influence of the momentum distribution

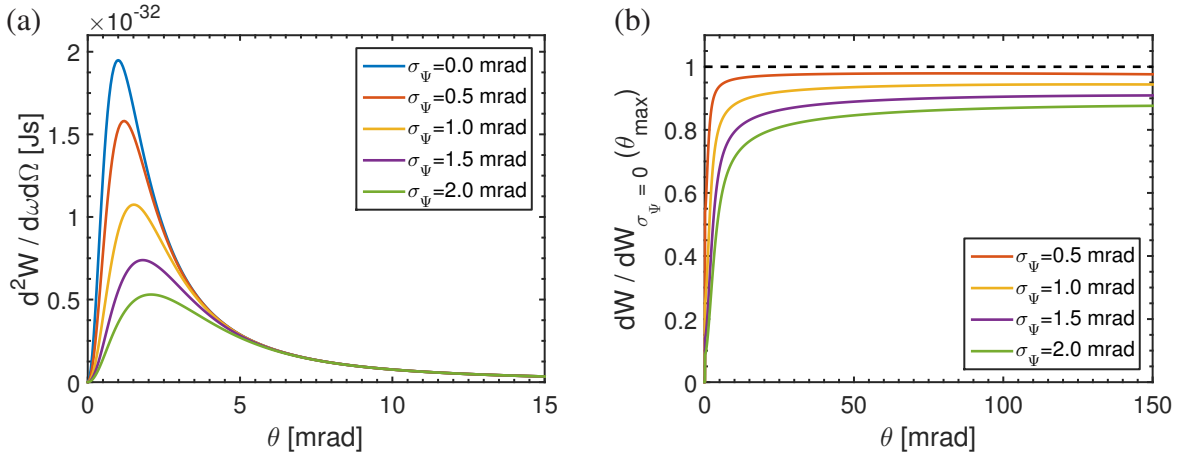


**Figure 3.9:** *Impact of divergence. (a) Dependence of the angular distribution on beam divergence for  $\gamma = 1000$ , normalized by the bunch charge. (b) Relative spectral energy radiated into a forward cone with an opening half-angle of  $\theta_{max}$ , normalized to the emission of a collimated beam.*

We are now left with the influence of the momentum distribution. To analyse its effect, we use eq. (3.49), set  $|F| = 1$  and separate the momentum distribution in absolute value and direction by  $g(\mathbf{p}) = g_p(p) g_{\Omega}(\psi, \phi)$ . As discussed in section 3.1, for a collimated beam the emitted energy scales roughly with  $\ln \gamma$  (cf. eq. (3.25)).

Figure 3.9 shows the impact of divergence for a cylindrically symmetric normally distributed beam divergence modeled by  $g(\mathbf{p}) = \delta(p) g_{\Omega}(\psi, \phi)$  with

$$g_{\Omega}(\psi, \phi) = \frac{1}{\sqrt{2\pi}\sigma_{\Psi}} e^{-\frac{\psi^2}{2\sigma_{\Psi}^2}}. \quad (3.50)$$

The angular spectral distribution of CTR was calculated numerically according to eq. (3.29). The effect of a finite beam divergence is to reduce the intensity in forward direction (Fig. 3.9a), as the radiation cones of the individual particles overlap less and partially cancel due to the radial polarisation. Naturally, this effect is more pronounced as the beam divergence is increased. Since the losses mainly occur within the cone of  $1/\gamma$ , the effect scales roughly as  $\sigma_{\Psi}\gamma$ . Low energy electrons can therefore tolerate a higher bunch divergence.

Nevertheless, the bunch divergence has a relatively weak influence on the collected spectral

energy when considering collection angles  $\theta_{max} \gg 1/\gamma$ . This can be seen from Fig. 3.9b, which shows the total spectral energy radiated into a forward cone with opening angle  $\theta_{max}$ , normalized by the emission of a collimated beam.

### Summary

The discussion so far set the theoretical foundations that relate the CTR spectrum to the longitudinal form factor and ultimately to the temporal bunch profile. The other main contributions to the CTR spectrum are the transverse form factor, the electron energy spectrum and the bunch divergence. As will be described in chapter 6, the transverse density distribution at the position of the radiator is known and almost entirely determined by the beam divergence. The latter was measured in a separate run and found to be stable with regard to shot-to-shot fluctuations, while the electron energy and CTR spectrum were recorded in single-shot measurements. The setup thus allows to determine  $|F_{||}(\omega)|$  for each shot.

In the following, we will first define the beam emittance and then proceed to analyse the effect of possible phase space correlations. The fundamental assumption of phase space separability will be discussed in chapter 6.

### 3.2.3 The emittance

A useful property to characterize an electron beam in terms of size, divergence and energy chirp is the emittance, a measure of the beam's volume in the six-dimensional phase space spanned by  $\mathbf{r}$  and  $\mathbf{p}$ . As before, the bunch is conveniently described by the normalized distribution function  $h(\mathbf{r}, \mathbf{p}, t)$  with its normalized charge density given by

$$\rho(\mathbf{r}, t) = \int h(\mathbf{r}, \mathbf{p}, t) d\mathbf{p}. \quad (3.51)$$

As by Liouville's theorem the emittance  $\epsilon$  is a conserved quantity in the absence of dissipative or time-varying forces, it is a useful beam property often used in accelerator physics. If the particle motion in the transverse and the longitudinal plane is not coupled and the transverse forces are cylindrically symmetric, the six-dimensional phase space can be decomposed and the emittance becomes separable into a transverse and a longitudinal component, both of which are conserved individually:

$$\epsilon = \epsilon_{||} \epsilon_{\perp}. \quad (3.52)$$

These conditions also apply for nonlinear wakefields, as the transverse focusing field inside the wave bucket is cylindrically symmetric and independent of the longitudinal position (cf. eq. (2.93)). Expressing the phase space coordinates relative to the beam centroid,  $\mathbf{r} = \langle \mathbf{r} \rangle + \delta \mathbf{r}$ ,  $\mathbf{p} = \langle \mathbf{p} \rangle + \delta \mathbf{p}$ , the transverse and longitudinal normalized rms emittances are given by [114, 115]

$$\epsilon_{n,||} = \frac{1}{m_e c} \sqrt{\langle \delta r_{||}^2 \rangle \langle \delta p_{||}^2 \rangle - \langle \delta r_{||} \delta p_{||} \rangle^2}, \quad (3.53)$$

$$\epsilon_{n,\perp} = \frac{1}{m_e c} \sqrt{\langle \delta r_{\perp}^2 \rangle \langle \delta p_{\perp}^2 \rangle - \langle \delta r_{\perp} \delta p_{\perp} \rangle^2}, \quad (3.54)$$

where  $\langle \rangle$  denotes the average over the beam distribution function  $h$  at a specific time  $t$ . If  $\langle \delta r_{\perp} \delta p_{\perp} \rangle = 0$ , the distribution function is said to be uncorrelated, otherwise it is correlated.

### 3. Transition radiation

The emittance in a transverse plane (e.g. spanned by  $(x, p_x)$ ) is more conveniently expressed using  $x$  and  $x' = p_x/p_{\parallel}$  as one is usually more interested in knowing about the size and the divergence of the beam. The space spanned by  $(x, x')$  is called *trace space* in which the geometric beam emittance is defined by [116]

$$\epsilon_{tr,x} = \sqrt{\langle x^2 \rangle \langle x'^2 \rangle - \langle xx' \rangle^2}. \quad (3.55)$$

In accelerators, as the particles' longitudinal momenta increase,  $\epsilon_{tr,x}$  decreases as  $1/p_{\parallel}$ , a process called adiabatic damping. The reason is that the transverse momenta of the particles are unaffected and thus the divergence angle  $\theta_x$  (given by  $\theta_x = \arctan(p_x/p_{\parallel})$ ) is reduced during acceleration. On this account another frequently used quantity is defined by the normalized trace-space emittance [114, 117]

$$\epsilon_{tr,n} = \frac{|\mathbf{p}|}{m_e c} \epsilon_{tr}, \quad (3.56)$$

which is conserved during acceleration.

On the other hand, if the beam possesses an energy spread, a free space drift will increase  $\epsilon_{tr,n}$  due to a correlation of transverse particle position with momentum, while the geometric emittance is conserved. This is the case because the geometric emittance only takes into account the position and propagation angle of each particle but is independent of energy [114, 116].

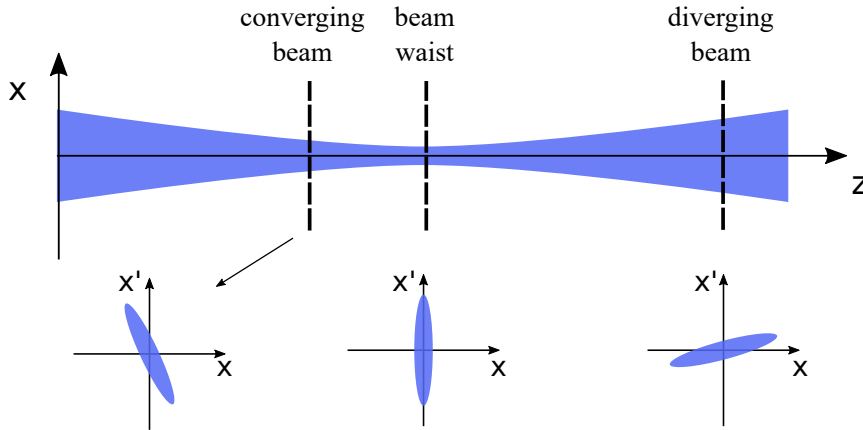


**Figure 3.10:** Example of emittance conservation during a free space drift.  $\epsilon_{tr,x}$  is the area in the  $(x, x')$  plane divided by  $\pi$ . While propagating along the longitudinal coordinate  $z$ , the orientation and aspect ratio of the phase space ellipse in the  $(x, x')$  plane varies but the area  $\epsilon_{tr,x}$  is conserved.

#### 3.2.4 Effects of beam propagation and phase space correlations

So far the effects of the transverse, longitudinal and momentum distributions have been discussed separately.

Due to the injection and acceleration mechanisms of LWFA, the accelerated bunch exhibits some degree of longitudinal position-momentum correlation because electrons constituting the head of the bunch are injected first (and therefore exposed longest to the accelerating field) and are also less affected by beam loading which can lower the acceleration field for electrons in the bunch's

tail. Such chirped LWFA beams have been confirmed recently [118].

From physical considerations it is further expected that the transverse phase space inside the wakefield can be approximated as being uncorrelated. This is due to the accelerated electrons performing betatron oscillations with different amplitude and phase determined by their different initial conditions after injection. This process, called betatron phase mixing, leads to a decoherence of transverse beam structure which may be initially present [119]. Nevertheless, during the free space propagation from the exit of the plasma wake to the CTR radiator foil, the transverse phase space will develop a position-angle correlation.

In the following, the effects of a possible correlation in transverse or longitudinal phase space will be quantified.

### Transverse phase space effects due to free-space propagation

The influence of the bunch divergence in the limit of  $|F| = 1$  has already been discussed in subsection 3.2.2. During the free space propagation of the electron beam from its release out of the confining potential of the wakefield to the CTR radiator, the geometric trace space emittance is conserved but the phase space is rotated as depicted in Fig. 3.10, which leads to an increase in spot size. This causes a reduction of  $F_{\perp}(\theta, \omega)$  with larger opening angles and blue-shifted CTR spectrum. As will be described in chapter 5, the measured CTR spectrum is corrected for this effect before retrieval of the longitudinal bunch profile.

Due to ballistic propagation from the exit of the plasma to the CTR radiator, the spatial bunch profile acquires the shape of a spherical shell since electrons propagating under an angle cover a longer path than on-axis electrons. These arrive slightly later at the CTR radiator, which leads to a coupling between the transverse and longitudinal phase space distributions and an elongation of the projected bunch profile. The relative lengthening after a drift length  $L_{drift}$  is given by  $\Delta l \approx (1 - \cos(\sigma_{\Psi}))L_{drift}$ . For the experimentally observed divergence of  $\sigma_{\Psi,FWHM} \sim 1.4$  mrad,  $L_{drift} \sim 50$  mm and a bunch duration of  $\sim 5$  fs, the relative lengthening is  $\Delta l < 1\%$  and thus negligible.

Finally, the rotation of the phase space during the ballistic propagation not only leads to an increased spot size but also introduces a transverse position-angle correlation. To quantify its influence on the measurement, the expected CTR spectra produced by an uncorrelated and a correlated transverse distribution were simulated. The respective trace space distributions in the  $(x, x')$  plane are shown in Fig. 3.11a and b. The correlated bunch distribution corresponds to the ballistic propagation of an initially uncorrelated distribution with a spatial transverse Gaussian distribution with  $\sigma_{\perp} = 1 \mu\text{m rms}$  (as expected at the exit of the gas cell) over a distance of 50 mm with a divergence of 1.4 mrad FWHM. Both distributions contain  $1 \times 10^5$  particles and the same transverse beam profile at the position of the CTR radiator. The longitudinal form factor is neglected, i.e.  $F_{\parallel} = 1$ . The computed CTR spectra are shown in Fig. 3.11c for different values of  $\gamma$ . The near perfect coincidence of the CTR spectra emitted by both distributions demonstrates that a transverse phase space correlation is insignificant to the measurement, moreover as the longitudinal form factor will essentially determine the spectrum at optical frequencies. The minor influence of the position-angle correlation is due to the large size of the CTR beam at the entrance plane of the collection optics compared to its small transverse size at the radiator foil.



### 3. Transition radiation

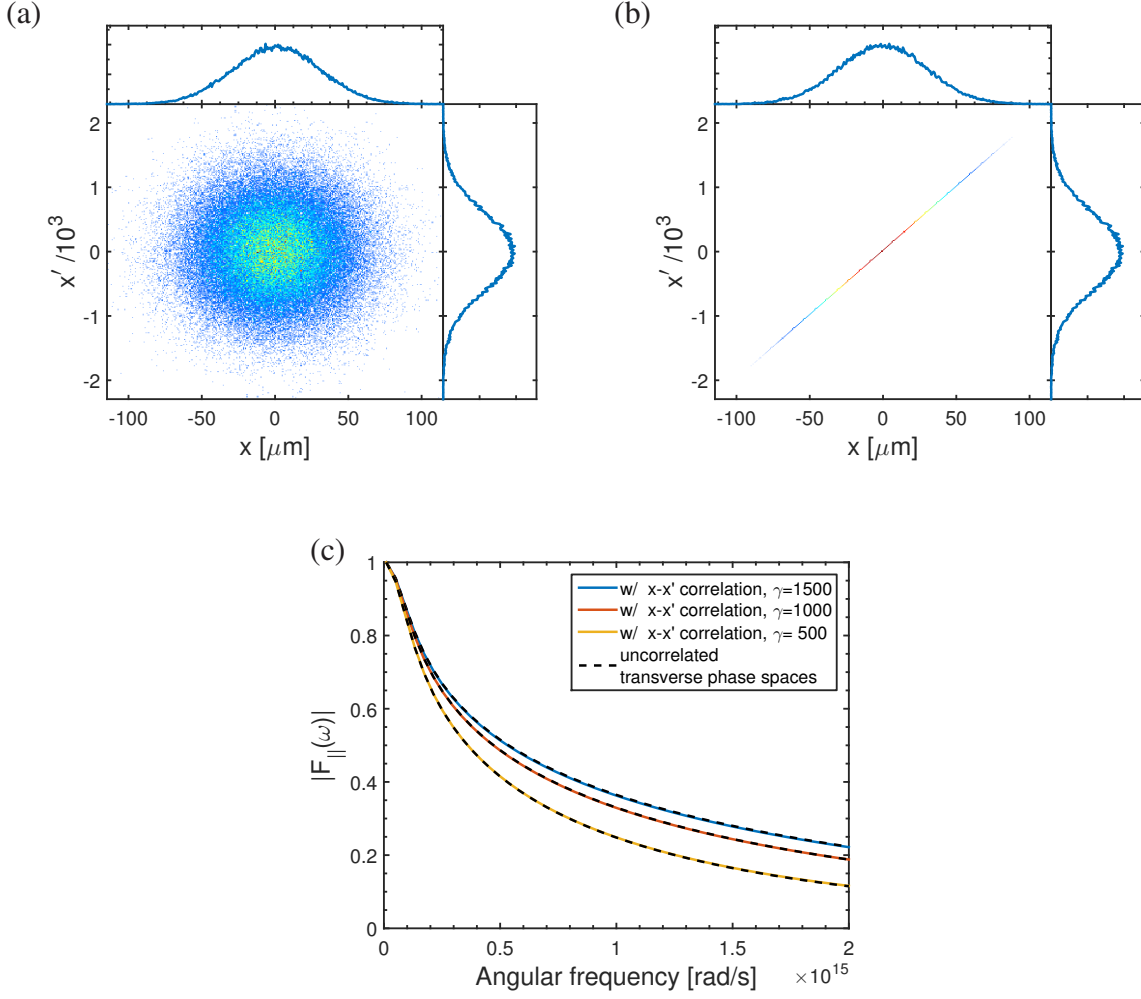


**Figure 3.11:** Influence of a transverse phase space correlation. (a) shows the trace space distribution in the  $(x, x')$  plane for an uncorrelated bunch and (b) for an electron bunch with  $\sigma_{\psi, FWHM} = 1.4 \text{ mrad}$  and  $\sigma_{\perp} = 1 \mu\text{m}$  after 50 mm of propagation. Both bunches contain  $10^5$  particles and exhibit the same radially symmetric Gaussian transverse charge profile. Coloured lines depicted in (c) show the computed CTR spectra corresponding to the correlated distribution (b) for an electron bunch with  $F_{\parallel} = 1$  and different values of  $\gamma$ . The dashed black lines show the respective CTR spectra produced by the uncorrelated distribution shown in (a). The near perfect coincidence of the spectra demonstrates that a correlated transverse phase space distribution does not influence the CTR spectrum significantly under the experimental conditions.

#### Effect of a position-momentum correlation

We now examine the effect of a correlation of electron energy with longitudinal position as even an initially unchirped bunch will acquire this correlation due to the free-space propagation to the radiator if it has a finite energy spread. Such an energy chirp in the longitudinal bunch profile will have two effects. First, since electrons with different energy have different velocity, the bunch is longitudinally compressed or elongated during propagation to the CTR radiator. Second, it can



influence the radiated CTR spectrum due to more intense CTR emitted by high-energy electrons.

To assess the influence of a longitudinal phase space correlation at the position of the radiator, the expected CTR spectra were again calculated for uncorrelated and correlated (chirped) longitudinal phase space distributions. The simulated phase space distributions are shown in Fig. 3.12 and were chosen such that the temporal bunch profile is Gaussian, while possessing a broadband energy spectrum (Fig. 3.12a), a flat-top energy spectrum (Fig. 3.12b) or an exponentially decaying energy spectrum (Fig. 3.12c).

The respective projections of the uncorrelated and correlated phase space distributions (1<sup>st</sup> and 2<sup>nd</sup> column of Fig. 3.12) on the energy axis result in an identical energy spectrum. The computed CTR spectra for chirped bunches of 5 fs FWHM duration and unchirped bunches of various FWHM durations are shown in the 3<sup>rd</sup> column of Fig. 3.12. For the same FWHM duration, the chirped bunches exhibit a broader CTR spectrum than the respective uncorrelated bunches. This is due to more intense CTR emitted by the high-energy electrons that are concentrated in a shorter temporal feature if a chirp is present. Since the total CTR emission scales as  $\ln \gamma$  (eq. (3.25)), the effect is relatively stronger if the electron spectrum contains mostly low-energy electrons (cf. Fig. 3.12c). The CTR spectra produced by the chirped bunches of 5 fs duration are generally bracketed by the spectra of unchirped bunches with shorter durations. Since the bunch profile retrieval process described in the next chapter cannot account for an energy chirp, the method would underestimate the real bunch duration by approximately 0.2 fs (4%), 0.5 fs (10%) or 0.9 fs (18%) if the respective chirp were present.

The maximal bunch lengthening (or compression) due to the free-space drift is given by  $\Delta l = (1 - \beta_{min}/\beta_{max})L_{drift}$ . For an electron bunch with energies in the range of 250 – 800 MeV and a duration of 5 fs, the maximal elongation or compression amounts to  $\sim 6\%$ . Thus, if the electron bunch carries a positive chirp (i.e. higher energy electrons reside in the head of the bunch), which appears highly likely in a LWFA before dephasing, the two effects partially cancel. In this case, the intrinsic energy chirp of the electron beam at the exit of the plasma contributes the most to the measurement error. Provided that the energy spectrum is sufficiently broadband (Fig. 3.12a and Fig. 3.12b), a measurement error of  $\lesssim 15\%$  due to the effect of a longitudinal phase space correlation appears justified.

### 3. Transition radiation

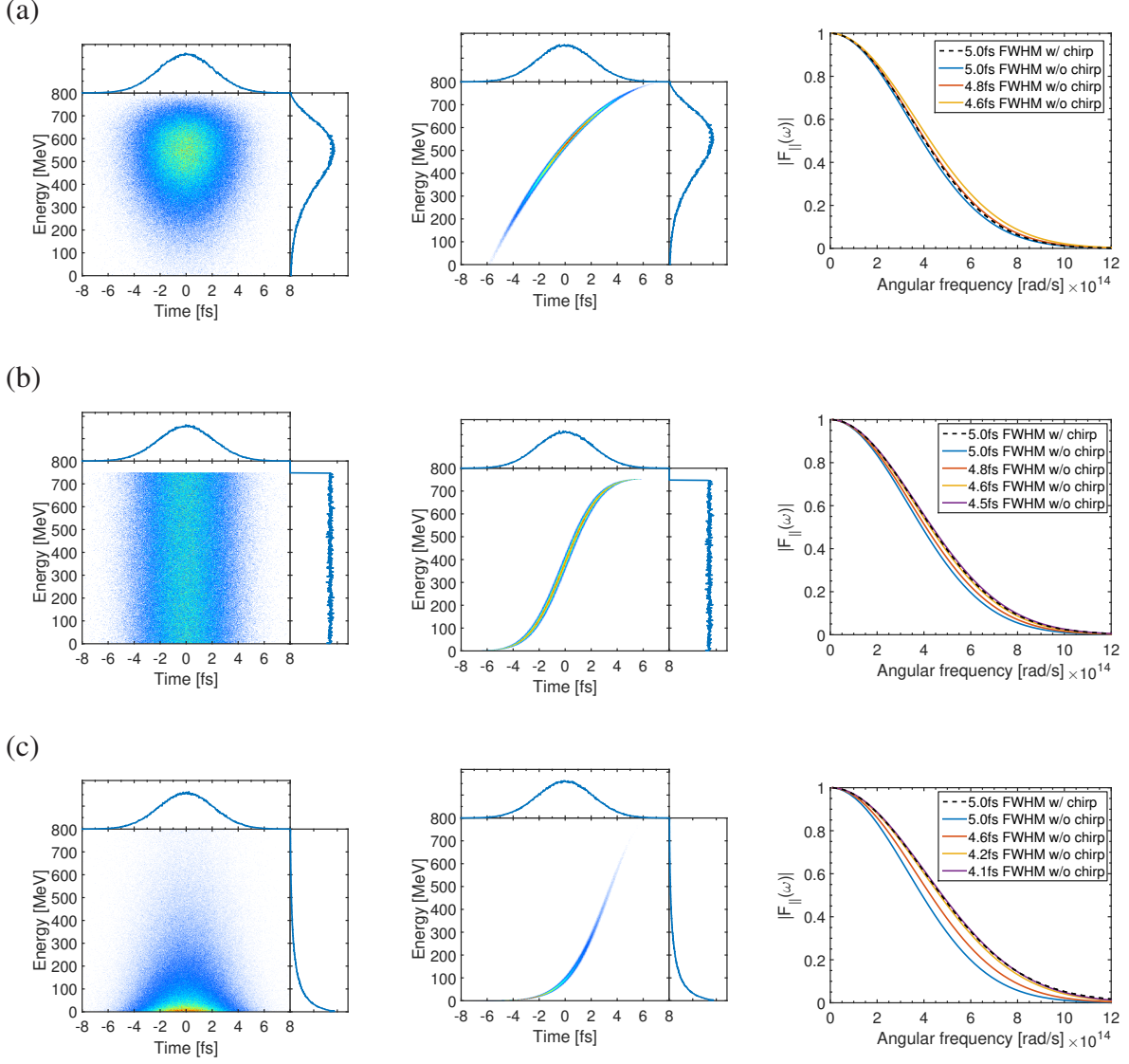


**Figure 3.12:** Influence of a longitudinal phase space correlation. Longitudinal phase space distribution of a bunch with (a) a broadband energy spectrum centered around 550 MeV, (b) a flat-top energy spectrum and (c) and exponentially decaying energy spectrum. The 1<sup>st</sup> column shows the respective uncorrelated and the 2<sup>nd</sup> column the respective correlated phase space distributions (with an uncorrelated energy spread of 5 %). All distributions contain  $5 \times 10^5$  electrons and exhibit a Gaussian temporal shape and an energy spectrum identical to that of the same row. The last column shows simulated CTR spectra corresponding to the distributions shown in the 1<sup>st</sup> and the 2<sup>nd</sup> column of the same row for different FWHM bunch durations.

### 3.3 The Bubblewrap reconstruction algorithm

Going back to eq. (3.48), the longitudinal bunch profile is related to the longitudinal form factor by an inverse Fourier transform

$$\rho_{\parallel}(z) = \frac{1}{2\pi} \int F_{\parallel}(\omega) e^{i\omega z/c} d\omega. \quad (3.57)$$

In general, the form factor is a complex quantity. According to eq. (3.49), a measurement of the CTR spectrum yields the absolute value of the longitudinal form factor. However, since phase information is not recorded, direct determination of the bunch profile by inverse Fourier transformation is not possible.

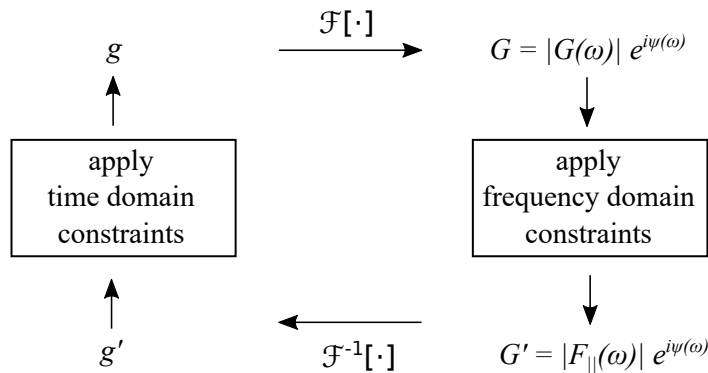
In CTR experiments, a commonly used method relies on the Kramers-Kronig relations, which relate the real and imaginary parts of the spectrum to each other, based on a causality condition. This procedure allows to approximate the missing phase information [120]. However, the amplitude of the spectrum has to be known for all frequencies. Since in practice this is impossible, assumptions about its shape at low and high frequencies have to be made, which can influence the deduced temporal profile [106, 121, 122]. As a further complication, only the so-called *minimal phase* is obtained<sup>1</sup>. Therefore, even if the complete spectrum is known, the incomplete phase information can lead to a further discrepancy between the real bunch profile and its reconstruction [122, 124].

In order to reconstruct the longitudinal bunch profile from the measured CTR spectrum, a new iterative algorithm was developed by our collaborators from Oxford University, capable of reconstructing the missing phase information. Such type of algorithms have been successfully deployed to a variety of problems including X-ray imaging and crystallography, in which the original signal is to be reconstructed from the magnitude of its Fourier transform [122, 125–127]. Recently, such algorithms have also been used to reconstruct the transverse profile of electron bunches from the spectrum of coherent optical transition radiation (COTR) [128, 129]. For the application of reconstructing the longitudinal bunch profile, the so-called *Bubblewrap* algorithm has been developed in the framework of a PhD thesis by Sevtoslav Bajlekov [130]. A detailed description has also been published in [28]. The main goal of the retrieval algorithm was to minimize the required assumptions. Particularly, it avoids any extrapolation of the spectral shape in frequency ranges that were not measured. In this section, an overview of its working principle will be presented.

1. The Kramers-Kronig relations connect the amplitude and phase of a complex function that is analytic in the upper half plane. Based on a causality condition, Lai and Sievers [120] show that the form factor satisfies this constraint and its phase is determined by

$$\psi_{min} + \psi_{Blaschke} = -\frac{2\omega}{\pi} P \int_0^{\infty} \frac{\ln |F_{\parallel}(x)|}{x^2 - \omega^2} dx + \sum_j \arg \left( \frac{\omega - \hat{\omega}_j}{\omega - \hat{\omega}_j^*} \right),$$

where  $P$  denotes the Cauchy principal value and  $\hat{\omega}_j$  identify the complex zeros of  $F_{\parallel}(\omega)$  in the upper half plane. Only the first phase term  $\psi_{min}$  (the so-called *minimal phase*) can be retrieved from the measurement [123].



1. A Fourier transform is applied to the current estimate of the bunch profile  $g_n(t)$ . This step yields the magnitude and phase of the corresponding Fourier transform  $G_n(\omega)$ .
2. The frequency domain constraints are enforced: the magnitude of  $G_n(\omega)$  is replaced by the measured form factor  $|F_{||}(\omega)|$ , while the phase information is retained. At frequencies that were not measured the candidate function remains unchanged. The resulting function satisfying the frequency domain constraints is now called  $G'_n$ .
3. An inverse Fourier transform of  $G'_n$  yields the updated bunch charge distribution function  $g'_n(t)$ .
4. The time domain constraints are applied based on a priori information about the bunch profile. This step yields the next estimate  $g_{n+1}(t)$  of the candidate function  $p_{||}(t)$ .

$$g_{n+1}(t) = \begin{cases} g'_n(t), & t \notin I, \\ 0, & t \in I. \end{cases} \quad (3.58)$$

In the  $n^{\text{th}}$  iteration the error in the time domain is given by

$$E_n = \sqrt{\sum_t |g_{n+1}(t) - g'_n(t)|^2}. \quad (3.59)$$

It can be shown that in each iteration cycle the error is either reduced or stays constant, for which reason the Gerchberg-Saxton algorithm is also called the error-reduction algorithm. However, although the error usually decreases rapidly during the first iterations, the algorithm is prone to stagnation or may converge towards a local minimum [131]. The convergence can be sped up by applying modifications to the Gerchberg-Saxton algorithm. A commonly used practice is to combine the latter with a faster converging algorithm, which is less prone to stagnation. In return, these algorithms typically exhibit less stability, i.e. the error is not necessarily reduced in each iteration. For the present application, best reconstruction results could be obtained by a combination with the so-called hybrid input-output algorithm.

### Ingredient 2: The hybrid input-output algorithm

The hybrid input-output algorithm differs from the Gerchberg-Saxton algorithm only in the last step. The first three operations are kept the same, and can be regarded as a nonlinear system with input  $g_n(t)$  and output  $g'_n(t)$ . In the last step, the real space constraints are abandoned. Therefore, the input function can be altered with more flexibility, which can lead to a faster convergence [131]. If a change  $\Delta g(t)$  in the output function is desired, a logical choice of the change in the input is  $-\beta_{hio} \Delta g(t)$ , where  $\beta_{hio}$  is a constant depending on the nonlinearity of the system. This leads to a new class of algorithms, the so-called input-output algorithms. One of its representations that simultaneously ensures a fast convergence while at the same time avoiding the problem of stagnation is given by the so-called hybrid input-output algorithm, for which the new input function  $g_{n+1}(t)$  is defined by

$$g_{n+1}(t) = \begin{cases} g'_n(t), & t \notin I, \\ g_n(t) - \beta_{hio} g'_n(t), & t \in I, \end{cases} \quad (3.60)$$

where  $\beta_{hio}$  denotes the amount of feedback. At points of  $I$  which violate the real-space constraints, the input is now driven in the opposite direction of the deviation. Depending on the value of  $\beta_{hio}$ , this type of feedback allows the algorithm to emerge from local minima and thus explore a wider set of target functions than the Gerchberg-Saxton algorithm [125].

### Ingredient 3: Adaptive support selection

In addition to the real space constraint of seeking a real non-negative function, one may further involve a support condition, i.e. the reconstructed function is limited to a certain time window. Such a condition can drastically improve the convergence of the algorithm. While for too restrictive support sizes a solution may not exist, a size of the support that is too large may lead to ambiguous solutions with poor convergence [122, 132]. It was found that a Gaussian of length  $1 \mu\text{m rms}$  was almost always correctly reconstructed on a support of size  $10 \mu\text{m}$  but the reconstruction failed for a support of  $15 \mu\text{m}$  length [28], which underlines the need for finding the correct support size for a viable reconstruction of the bunch profile. In many cases the support

### 3. Transition radiation

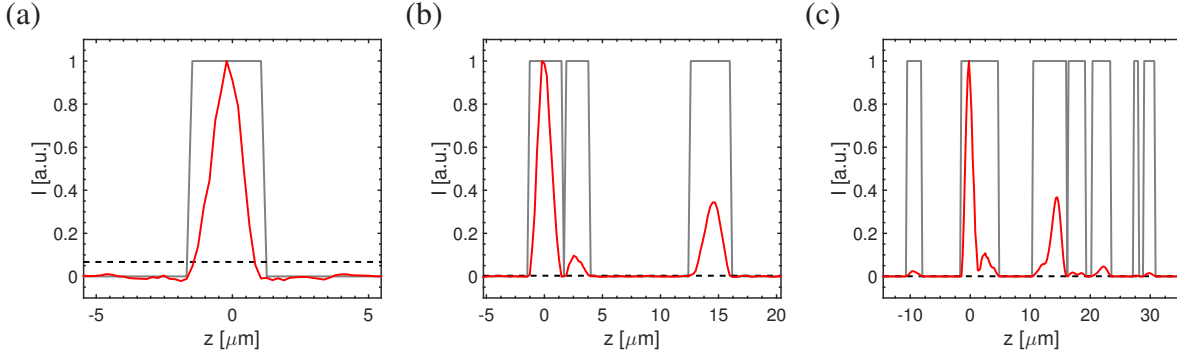


**Figure 3.14:** Adaptive support selection. From (a) to (c) the threshold for support recalculation (shown by the dashed line) is continuously decreased, allowing the appearance of low current features in the retrieved bunch profile. If the threshold is set too low, noise in the input *CTR* spectrum can lead to a number of artificial subsidiary bunches.

size can be estimated from an intensity autocorrelation [132]. However, in the present case, such information is not available. Therefore, it was opted to adaptively recalculate the support during the reconstruction, a method first introduced by the Shrinkwrap algorithm [125]. Compared to an a priori specification of the support, the authors showed improved reconstruction results even in the presence of noise. In this approach, the support is recalculated after each iteration cycle based on a threshold applied to the candidate function. For reconstruction of the bunch profile from the *CTR* spectrum, it was shown that accurate results could be obtained [28]. The threshold for support calculation is initially set to 20 % of the peak value. In order to permit also low current features in the bunch profile, this threshold is then continually reduced until reaching a final value on the sub-percent level.

The adaptive support selection is illustrated in Fig. 3.14, which shows the candidate function  $g'_n$  after different iteration numbers  $n$  before applying the real space constraints. The threshold for the support recalculation is shown by the dashed black line. To obtain the new current estimate function  $g$ , only values of  $g'_n$  that exceed this threshold are retained, while points with lower values are set to zero (only regions under the grey square boxes are retained). As the threshold is gradually lowered (from Fig. 3.14a to Fig. 3.14c), more subtle features in the retrieved bunch profiles appear. If the threshold is lowered too far, noise in the *CTR* measurement can lead to a number of subsidiary bunches (cf. Fig. 3.14c). The minimum threshold for support recalculation was therefore set to 0.5 % of the main peak, which yielded best results throughout a wide range of input spectra.

### Choice of the parameters

In order to establish the remaining parameters for best performance of the *Bubblewrap* algorithm, it was applied to the *CTR* spectra calculated from various synthetic bunch profiles. The simulated spectra were truncated to the limited spectral range that was also accessible experimentally and used as an input for the algorithm. The following procedure was found to yield the best results of the algorithm:



- The initial support size is set to  $20\,\mu\text{m}$  and is allowed to grow or shrink by the adaptive support selection.
- In each iteration cycle, the HIO algorithm is run for 45 iterations, followed by 5 iterations of the Gerchberg-Saxton algorithm.
- Before calculating the support, the function is smoothed by a Gaussian function of rms length  $\sigma$ . Its initial value is set to 3 data points and is reduced in each iteration cycle by 0.5 % until reaching a final value of 1.1 data points.
- The threshold for support recalculation is initially set to 20 % of the peak of the reconstructed profile and decreased by 2.5 % in each iteration cycle until reaching a final value of 0.5 %.
- The parameter  $\beta_{hio}$  of the hybrid input-output algorithm is initially set to 1 and decreased in each cycle until a final value of 0.05 is reached.

### Post-selection procedure

Although for two-dimensional phase retrieval problems a unique solution can exist, this is not generally the case for one-dimensional problems. Furthermore, considering the bunch profile  $\rho_{\parallel}(z)$ , an ambiguity in translation ( $\rho_{\parallel}(z + z_0)$ ) and time reversal ( $\rho_{\parallel}(-z)$ ) exists, as both distributions will lead to the same measured form factor [122].

However, for the same measured CTR spectrum, distinct retrieval processes started from random seeds normally lead to very similar results. To select a reliable reconstruction and ensure that the retrieved profile is the correct inversion of the CTR spectrum, the retrieval process is run five times. The peak of the resulting bunch profiles is used to align the profiles and the skewness of the distribution is used to remove the ambiguity in time direction between individual profiles. The aligned profiles are then compared to each other by calculating the square difference error. Subsequently, the profile that is most different from the others is removed from the set until three profiles remain. From these, the profile for which the sum of its square errors with the two remaining profiles is minimized is chosen as the reference for a given measurement. In ref. [28], the accuracy of the Bubblewrap algorithm is demonstrated for various synthetic test profiles. The algorithm and the selection procedure show a reliable reconstruction among a large variety of test cases.

### Recent developments

Recently, the Bubblewrap algorithm has attracted further attention and received suggestions for improvement. Pelliccia and Sen [122] proposed to alter the post-selection procedure. Instead of choosing the best solution by comparing the least squares difference of the retrieved profiles to each other and successively eliminating outliers, they pick the reconstruction with the smallest error to the measured spectrum and average all solutions whose cross correlation with this profile exceeds a certain threshold.

Bakkali Taheri et al. [133] alter the initialization of the algorithm and initially perform a reconstruction of the bunch profile by the Kramser-Kronig method. The obtained amplitude and

### 3. Transition radiation

---

minimal phase is then fed to an algorithm similar to [Bubblewrap](#), with the constraint that the retrieved phase must not fall below the minimal phase. In this way they eliminate the need to start the algorithm several times from random seeds as the deterministic input profile always leads to the same output. However, it remains unclear if the constraint to the calculated minimal phase may not lead to additional errors in the retrieved profile due to noise or uncertainties in the measured [CTR](#) spectrum.

These welcome improvements manifest the interest for the use of iterative algorithms in phase retrieval problems. Since the measurements presented in this thesis inspired the development of the [Bubblewrap](#) algorithm, it was opted to utilize its original version for retrieving the longitudinal bunch profiles. Retrieval examples of single-shot measurements will be presented in section [7.1](#).



---

# Chapter 4

## Experimental Setup

This chapter describes the setup used in the experiments. Generally, an [LWFA](#) experiment requires three major components: A laser system providing high-intensity ultra-short pulses, a gas target in which plasma wakefield acceleration takes place and a detection system to characterize the accelerated electron bunches.

The experimental results presented in this thesis were obtained by using the [ATLAS](#) laser system, which is described in the next section. A general overview of the rest of the experimental setup is given in section 4.2. The laser pulses were focused to the entrance of a gas cell (described in section 4.3) in which ionization of hydrogen, plasma wave excitation and electron acceleration took place. The electron energy diagnostic is presented in section 4.4. In order to simultaneously characterize the longitudinal bunch profile, [CTR](#) was produced by a metallic tape inserted into the electron beam path and the radiated spectrum was measured by three individual spectrometers. This [CTR](#) diagnostic is presented in detail in section 4.5 and section 4.6.

### 4.1 The ATLAS laser system

As outlined in chapter 2, in order to excite nonlinear plasma waves that reach the self-injection threshold, laser intensities of  $a_0 > 1$  with pulse durations  $\tau < \lambda_p/c$  are necessary. These requirements can be met by the combination of pulse energies on the Joule level with femtosecond pulse durations, corresponding to laser powers in the range of Terra- to Petawatt. Such powers are nowadays readily achieved even by commercial systems.

The experiments utilized the [ATLAS](#) high-field laser, which, at the time the experimental campaign took place, was located at the Max Planck Institut für Quantenoptik ([MPQ](#)) in Garching. Although the laser was originally supplied as a commercial system, several upgrades have turned this machine into a highly customized system. During the course of this thesis, one of these upgrades was carried out before the experimental campaign. Afterwards, the system was relocated to the newly established Laboratory for Extreme Photonics ([LEX](#)), completely rebuilt and a further upgrade raised its output power to the 300 TW level. In the following, the state of the system is described as it existed at the time the experiments were carried out.

[ATLAS](#) is a table-top laser system based on the principle of chirped pulse amplification ([CPA](#)) [134], using titanium-sapphire ([Ti:Sa](#)) as an amplification medium. By stretching the pulses in

## 4. Experimental Setup

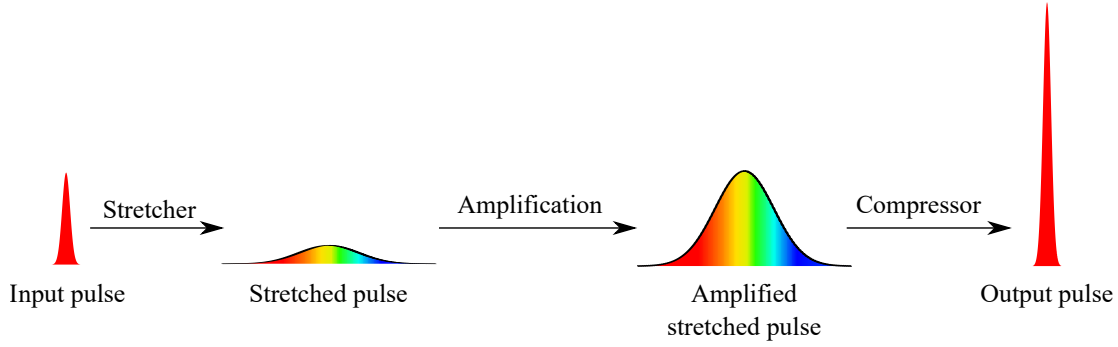


**Figure 4.1:** Sketch of the chirped pulse amplification (CPA) principle.

time, the CPA technique allows to lower the pulse intensity during amplification, avoiding problems associated with the damage threshold of optical components and nonlinear effects such as self-focusing or self-phase modulation. For these reasons state-of-the-art ultra-high intensity lasers usually employ this technique. By introducing a frequency dependent path difference, the low-intensity ultra-short pulses coming from a mode-locked oscillator are coherently stretched in time, resulting in a low intensity beam as sketched in Fig. 4.1. After amplification has taken place, an opposite path difference is introduced by the compressor. The ATLAS system employs a low-aberration, grating based Öffner stretcher [135] along with a grating compressor. Up to 3<sup>rd</sup> order, the matched compressor allows to compensate not only for the dispersion introduced by the stretcher, but also the material dispersion of the transmission optics employed in the laser chain.

## Laser Layout

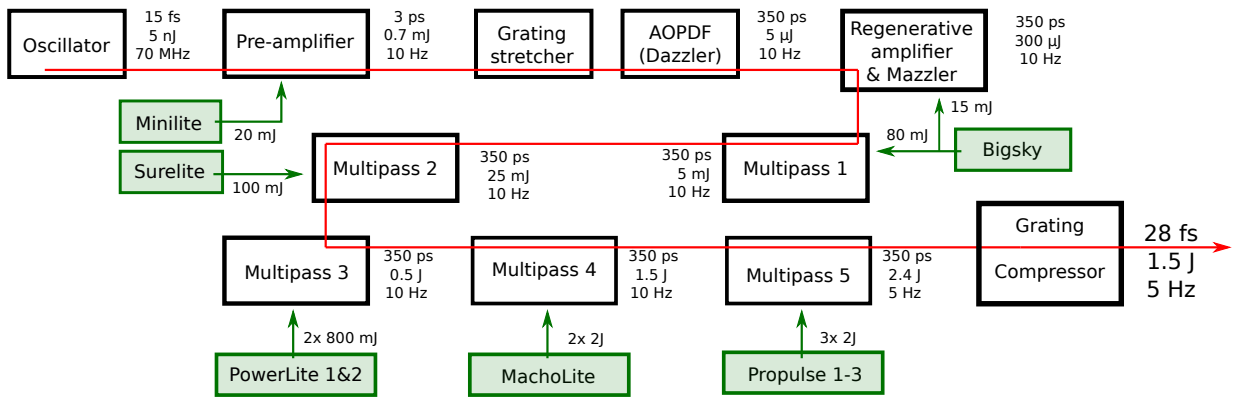


**Figure 4.2:** Schematic layout of the ATLAS laser system.

A schematic of the ATLAS system is shown in Fig. 4.2. The Ti:Sa crystals are pumped at  $\lambda = 532\text{ nm}$  by frequency-doubled flashlamp-based Nd:YAG lasers. The amplifier chain is seeded

by a broadband commercial Kerr-lense mode-locked Femtolasers Rainbow oscillator, providing a pulse train with 70 MHz repetition rate. Its output pulses with  $E \sim 5$  nJ,  $\tau_{FWHM} \sim 15$  fs are reduced to a 10 Hz repetition rate by using a Pockels cell in conjunction with polarisers. The pre-amplified pulses are then stretched with a positive chirp to a pulse duration of  $\sim 350$  ps. Subsequently, an acousto-optic programmable dispersive filter (AOPDF, *Dazzler* by Fastlite), allows to compensate residual spectral phase distortions up to higher order and is also used to optimize the pulse duration and chirp in the LWFA experiment. The stretched pulses are then amplified in a regenerative amplifier where a 2<sup>nd</sup> AOPDF is located within the cavity. Here, the so-called *Mazzler* (by Fastlite) allows enhancing the amplified spectral bandwidth by damping central frequency components of the spectrum and limiting the effects of gain-narrowing. The pulses are then further amplified by four successive multi-pass amplifiers to  $\sim 2.4$  J with 5 Hz repetition rate (intentionally limited by the repetition rate of the last three pump lasers) and sent into the compressor. The amplified bandwidth after the regenerative amplifier is  $\gtrsim 80$  nm and  $\sim 50$  nm before compression. The temporal pulse shape is diagnosed by a commercial GRENOUILLE

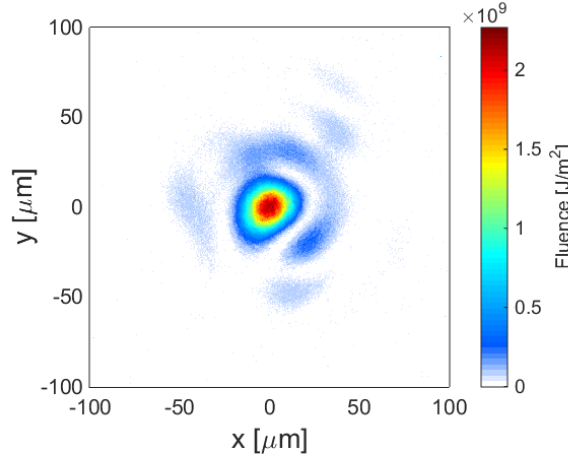


**Figure 4.3:** Intensity distribution of the *ATLAS* laser in the focal plane. Approximately 32 % of the laser energy is contained within the *FWHM* beam diameter.

device (by Swamp optics) based on the technique of frequency-resolved optical gating (*FROG*). The typically retrieved pulse duration of the *ATLAS* system is  $t_{FWHM} \approx 28$  fs. The system is further equipped with a deformable mirror and a Shack-Hartmann wavefront sensor in order to collimate the beam and compensate for residual wavefront distortions before entering the compressor. Inside the experimental chamber, the focal spot of the final f/22 focusing paraboloid can be imaged by a 20x microscope objective on a *CCD* camera. A typical focal spot image of the attenuated laser beam is shown in Fig. 4.3. After accounting for transmission losses in the compressor and the beamline of  $\sim 35$  % that result in an on-target energy of 1.5 J, the peak intensity amounts to  $5.8 \times 10^{18}$  W/cm<sup>2</sup> or  $a_0 = 1.66$ .

## 4. Experimental Setup

### 4.2 Overview of the experimental setup

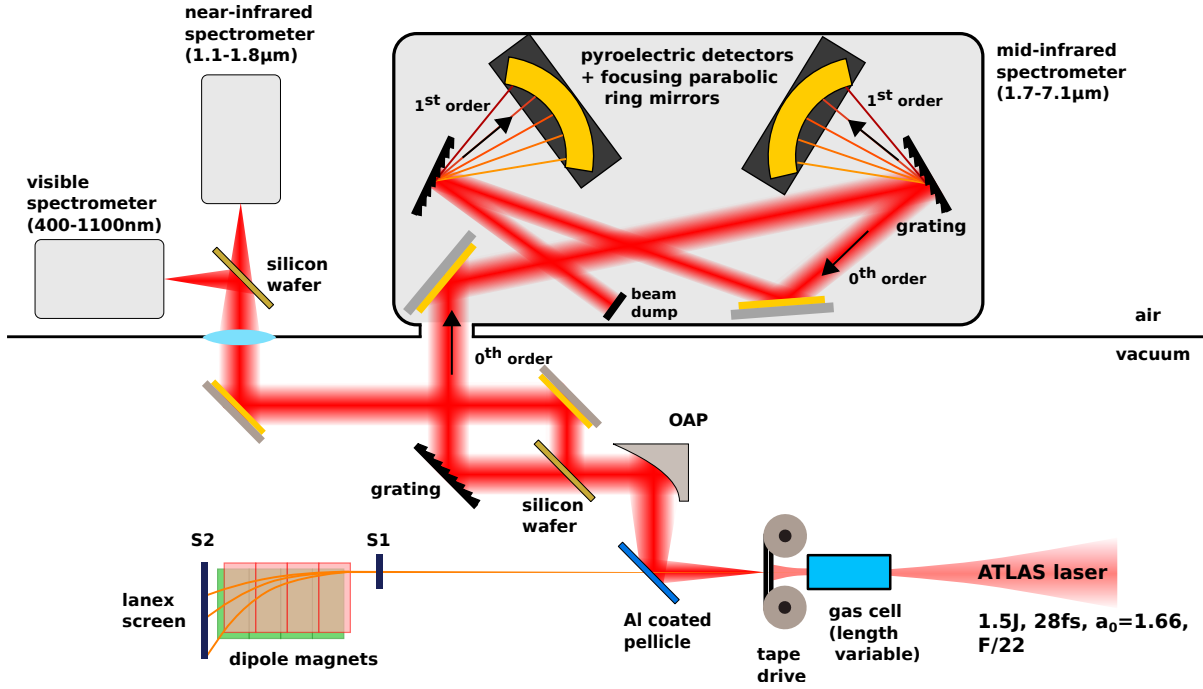


**Figure 4.4:** Overview of the experimental setup. The whole setup resides in interconnected vacuum chambers. Only the near-infrared and visible spectrometer are placed in air.

Figure 4.4 shows an overview of the experimental setup used for LWFA. The experiments were performed using the previously described ATLAS laser system which delivered  $1.5 \pm 0.1$  J on target with a pulse duration of  $\tau = 28 \pm 2$  fs FWHM. After being reflected to the experimental chamber, the beam was focused by a 1.5 m focal length off-axis paraboloid to the entrance hole of a steady-state-flow gas cell filled with hydrogen, length-tunable in the range of 1.5 – 14 mm. The FWHM focal spot size was  $d = 22 \pm 1.4$   $\mu\text{m}$ , which resulted in a normalized vector potential of  $a_0 = 1.66 \pm 0.13$ . Electron bunches were accelerated following self-injection in the weakly relativistic regime at plasma electron densities in the range of  $n_0 = 3 - 9 \times 10^{18} \text{ cm}^{-3}$ . After exiting the gas cell, the electron beam energy and charge was analysed by a dipole magnet and the scintillator screen S2. Optionally, a second scintillator screen S1 located in front of the magnets could be inserted to determine the beam divergence, pointing and transverse projection of the beam profile after 1.5 m of propagation.

The electron energy spectrometer and pointing screen are two of the basic tools to characterize the electron bunch in terms of its energy spectrum, charge and divergence and form the basic set of single-shot diagnostics commonly used in LWFA experiments. In order to also determine the longitudinal bunch profile, the setup was extended by a tape drive and three optical spectrometers that were used to measure the spectrum of CTR emerging from the tape. The following sections give a detailed description of the essential components of the setup.

### 4.3 Gas target

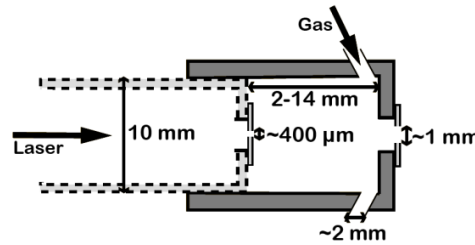


**Figure 4.5:** Sketch of the length-variable gas cell used in the experiment. Eight radially arranged holes in the outer cylinder serve as gas inlets. Image credit: Popp [136].

Commonly used gas targets for wakefield acceleration include sub- or supersonic gas jets, capillaries or cells containing larger volumes of gas, referred to as gas cells. The latter type was chosen for the experiment. It has the advantage that an appropriately designed cell allows to easily adjust the length of the gas reservoir during the experiment and avoids turbulences. A schematic drawing of the cell is shown in Fig. 4.5. Its piston-like design enables a length adjustment in the range of 1.5 – 14 mm. Its inner diameter amounts to 10 mm. The cell is mounted such that the entrance hole is static and the outer cylinder moves, which ensures that the entrance plane is fixed with respect to the longitudinal laser focus position. A sapphire plate (0.3 mm thickness) is glued on the entrance hole to reduce the gas flow to vacuum and, after a few laser shots, possesses a laser-drilled hole with a diameter of approximately 0.4 mm. Eight radially arranged holes in the rear cylinder serve as gas inlets, each 2 mm in diameter. The backing pressure is controlled by an electronic closed-loop PID controller with a maximum deviation of  $\pm 4$  mbar around the target value. The reference value at 100 mbar was taken from a calibrated pressure gauge. The gas cell is connected to a reservoir by a gas pipe of approximately 2 m length. Simulations with the computational fluid dynamics modelling software OpenFoam [137] show that by applying a constant backing pressure directly at the gas cell inlets, the density within the cell reaches a homogeneous steady-state after 1.5 ms [138]. In the experiment, the opening valve (located at a distance of 20 cm from the gas cell) is triggered 50 ms before the arrival of the laser pulse to ensure enough time to also fill the gas supply pipe. Due to the large cross section of the supply pipe (4 mm diameter) as well as the 8 inlet holes as compared to the cross section of the exit holes, a steady state should develop well within these 50 ms. The steady-state flow condition is beneficial, as it avoids turbulences and thus facilitates reproducible electron beams with low shot-to-shot fluctuations.

### 4.4 Electron spectrometer

The electron bunch energy spectrum is measured for each single shot by means of a dipole magnet and a scintillating screen inserted into the electron beam path. The screen is mounted on the outside of the last vacuum chamber's door and imaged by a CCD camera. The dipole has a total length of 40 cm and consists of 6 permanent magnets of type VACODYM 764 TP that are attached to a steel yoke with a gap between the magnets of 40 mm [136]. The resulting magnetic field strength is on the order of 1 T. In order to increase the spectral resolution of high-energy

## 4. Experimental Setup

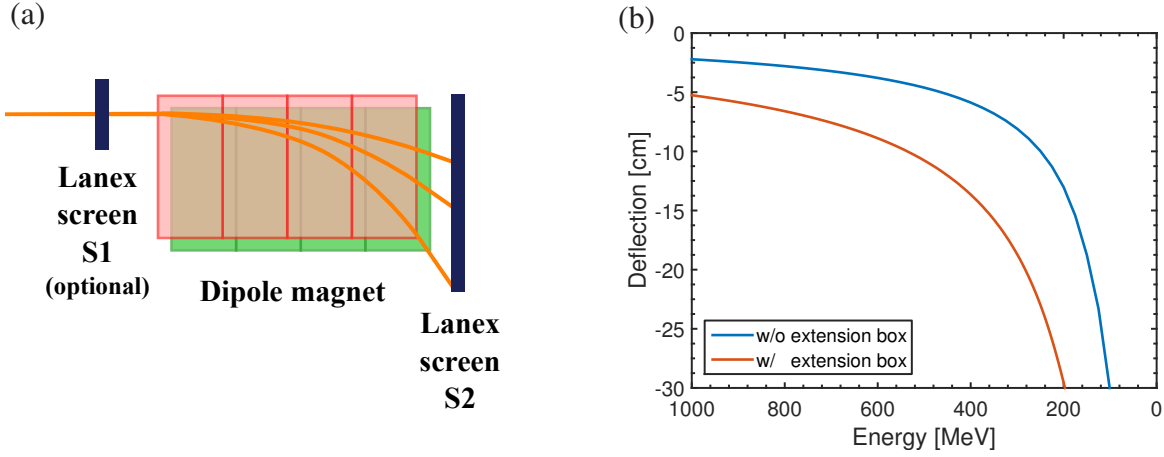


**Figure 4.6:** *Electron spectrometer. (a) shows a sketch of the electron spectrometer setup. An optional extension chamber can be inserted between the magnet and the screen S2 to increase the drift space and thus the spectrometer resolution. (b) shows the energy dependent deviation of an electron from its propagation axis. Tracking data by courtesy of J. Wenz and R. Weingartner.*

electron bunches, an extension chamber can be mounted between the magnet and the scintillating screen S2, which increases the drift space. The scintillating screen is thus placed at either 52 mm or 302 mm behind the exit plane of the magnet. The exact magnetic field map in the central plane was measured with a calibrated Hall sensor and the deflection from the propagation axis was traced for electrons of different kinetic energy using the software package General Particle Tracker [139], including the magnet's fringe fields. The dependence between this vertical deflection and the electron energy is shown in Fig. 4.6b. Due to the finite size of the milled-out portion of the vacuum chamber's last door, only deviations up to  $\approx 30$  cm can be observed. When the drift extension is used, this corresponds to a low energy cut-off of the spectrometer for electron energies  $\lesssim 190$  MeV, without the additional drift space the cut-off is  $\lesssim 110$  MeV.

The scintillating screen of type CAWO OG 16 [140] allows for an absolute measurement of the impinging beam charge using a layer of rare earth phosphors with a decay time of the metastable excited state on the order of 1 ms, which mainly decays by emission of photons with  $\lambda = 545$  nm. These screens exhibit a constant energy deposition for electron energies above 10 MeV and a linear response to the charge density, such that for relativistic energies the detected luminescent signal directly corresponds to the bunch charge<sup>1</sup>. Previous work by Buck et al. [141] established an absolute calibration of the screen, referenced to a constant light source. The latter is composed of tritium capsules covered with a fluorescent dye, which is excited by the tritium's beta decay. From the recorded CCD images, the relative brightness of the constant light source allows to obtain an absolutely calibrated electron energy spectrum for each shot, independent of the imaging optics.

1. The response is linear for charge densities below  $32.9 \text{ pC/mm}^2$  [141]. Above this threshold, the screen saturates and may suffer from irreversible damage, which is currently investigated. However, the experimentally obtained charge densities are usually far below this saturation limit at the position of the screen S2.

### Pointing and divergence

An additional scintillator screen S1 could be inserted in front of the dipole magnet to monitor the electron beam pointing and the transverse projection of the beam profile. The screen was imaged by a second CCD camera equipped with a 550 nm central wavelength bandpass filter, which transmits the fluorescent signal but is opaque for the laser wavelength. The screen allows to obtain the (energy integrated) divergence of the electron beam, taking into account its distance to the exit of the gas cell, which amounts to 1.46 m. The screen is only inserted if needed, as it leads to scattering of the electron beam and thus causes an increased beam divergence that reduces the spectrometer's energy resolution.

## 4.5 CTR diagnostics

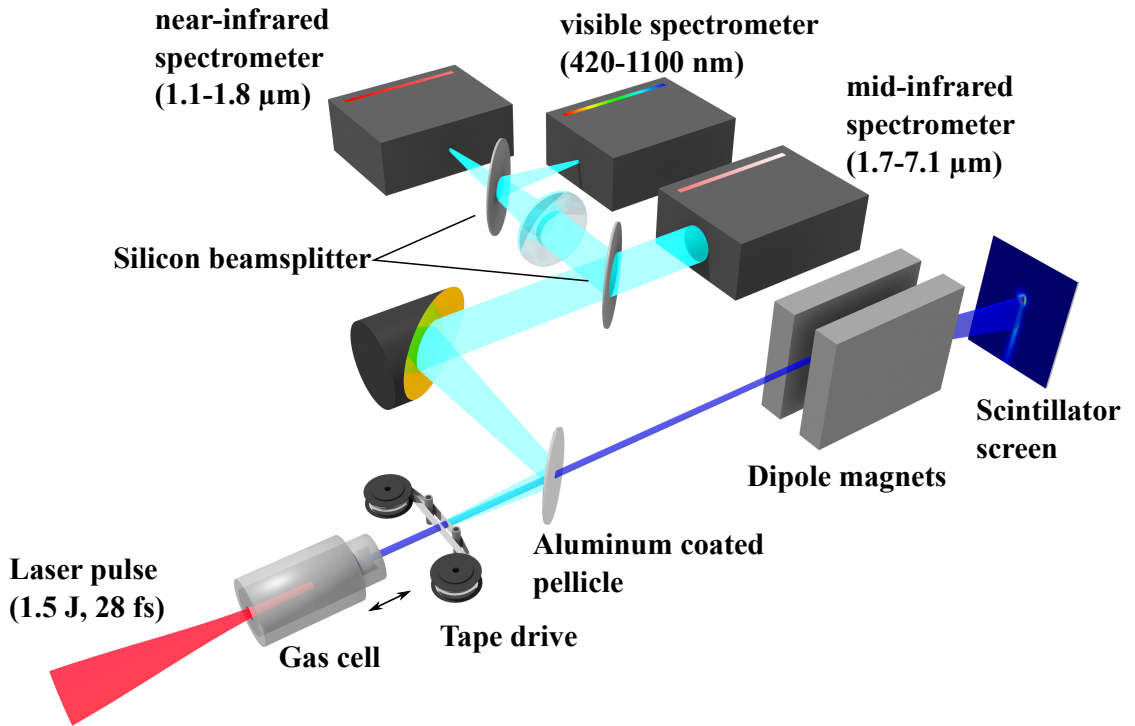


**Figure 4.7:** Rendering of the CTR diagnostics. Accelerated electrons (dark blue) leaving the gas cell generate coherent transition radiation (light blue) when they traverse the steel tapes. Forward CTR from the 2<sup>nd</sup> tape is separated from the co-propagating electron bunch, collimated by an off-axis paraboloid, split by silicon wafers and directed into 3 optical spectrometers covering a spectral range from 0.4 – 7.1 μm.

A schematic drawing of the CTR diagnostics is given in Fig. 4.7. The CTR radiator was realized by introducing a pair of steel tapes (20 μm thick, 12.5 mm wide) into the electron beam path, positioned 56 mm behind the gas cell entrance. Both tapes were attached to a motorized tape drive. Before each shot the tapes were advanced to provide a clean, undamaged surface. The 1<sup>st</sup> tape served the purpose of blocking the residual laser light as well as any thermal signal or plasma recombination glow and ensured that no such signal could reach the back of the



## 4. Experimental Setup

2<sup>nd</sup> tape, which served as the actual CTR radiator. The tapes with a thickness of 20  $\mu\text{m}$  each were chosen thick enough to avoid puncture by laser ablation but as thin as possible in order to avoid excessive degradation of the electron bunch divergence, which would deteriorate the resolution of the electron energy spectrum. Forward CTR generated at the downstream side of the 2<sup>nd</sup> tape was separated from the co-propagating electron beam by a reflective aluminium-coated pellicle positioned 10 cm behind the tape and collimated by a  $f/3.75$  off-axis paraboloid with an effective focal length of  $f_{\text{eff}} = 19.05$  cm. The beam was then split by silicon wafers and reflected to three individual spectrometers. The duration of LWFA electron bunches was expected to reside in the few femtosecond range (which was confirmed during the course of this work by ref. [21, 22]), which corresponds to wavelengths of peak CTR emission in the mid-infrared region. Since in this range commercial spectrometers are not widely available, the main CTR diagnostic was constructed as a custom-built spectrometer sensitive to mid-infrared wavelengths in the range of 1.7 – 7.1  $\mu\text{m}$ . Its design is based on a similar instrument that had been developed at DESY [142] and its detailed description will be given in section 4.6. This spectrometer was supplemented by two additional commercial imaging spectrometers that extended the wavelength coverage towards higher frequencies. The near-infrared part of the spectrum was covered by an Acton SP2150i imaging spectrometer equipped with a Princeton Instruments OMA-V 1024-element linear InGaAs photodiode array. The liquid nitrogen cooled diodes facilitated measurements in the wavelength range of 1.1 – 1.8  $\mu\text{m}$ . The range of 420 – 1096 nm was covered by a Oriel MS260 imaging spectrometer coupled to an Andor CV 420-OE silicon CCD camera with  $1024 \times 256$  pixels. Accordingly, these will be referred to as the mid-infrared, near-infrared and visible spectrometer.

### Silicon beam splitters

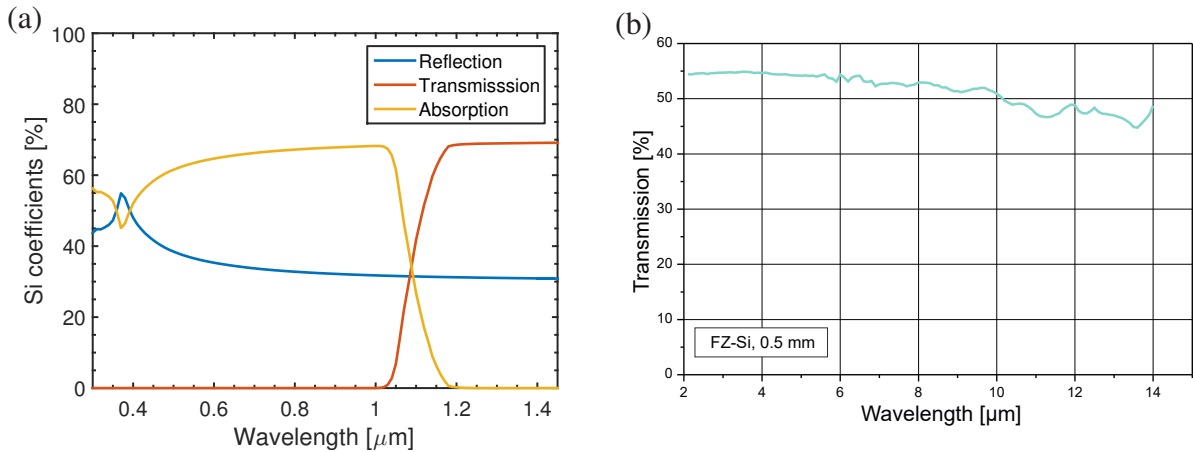


**Figure 4.8:** Optical properties of a silicon wafer of 1 mm thickness. (a) Reflectivity, transmittivity and absorption in the optical range. Reflective index data taken from ref. [143, 144]. (b) Transmission in the mid-infrared range (image taken from [www.tydex.ru](http://www.tydex.ru) [145]). Deviations from a flat transmission in the range of 6.5 – 25  $\mu\text{m}$  are due to the silicon lattice absorption band.

All spectrometers employ diffraction gratings, whose first diffraction order is used for wavelength separation. To avoid ambiguities in the measured spectra, the contribution of higher



diffraction orders has to be avoided, effectively limiting the bandwidth of a single grating to one octave. In order to distribute the **CTR** beam to the different spectrometers, silicon wafers were chosen as beam splitters as they possess the favourable feature of low-pass filtering the transmitted beam. The optical properties of silicon regarding transmission, reflection and absorption are shown in Fig. 4.8. For visible to mid-infrared wavelengths a reflectivity  $\gtrsim 30\%$  is obtained, while the transmission is limited to photon energies below the silicon band gap, i.e.  $\lambda \gtrsim 1.1\ \mu\text{m}$ .

Exploiting these properties, a first silicon wafer of 1 mm thickness was used to reflect a part of the **CTR** through a glass window out of the vacuum chamber. The transmitted beam was directed to the mid-infrared spectrometer, which was directly connected to the main vacuum chamber. To obtain a flat transmission of approx. 55% in the relevant spectral range from  $1.7 - 7.1\ \mu\text{m}$ , high purity silicon wafers produced by float-zone crystal growth were chosen. The transmission curve provided by the manufacturer is shown in Fig. 4.8b.

The collimated beam reflected outside the experimental chamber was refocused by a lens ( $f = 60\text{cm}$ ,  $f/5.9$ ) and split by a 2<sup>nd</sup> silicon wafer of similar type. The reflected part was focused on the entrance slit of the visible spectrometer and the transmitted radiation was focused on the slit of the near-infrared spectrometer. In the latter, the contribution of high order diffraction of the visible part of the **CTR** spectrum as well as of stray laser light was avoided, due to the low-pass characteristic of the wafer. High order diffraction of any UV light in the visible spectrometer did not contribute to the signal because of the sharp drop in quantum efficiency of the silicon **CCD** detector for wavelengths below 400 nm.

## 4.6 The mid-infrared spectrometer

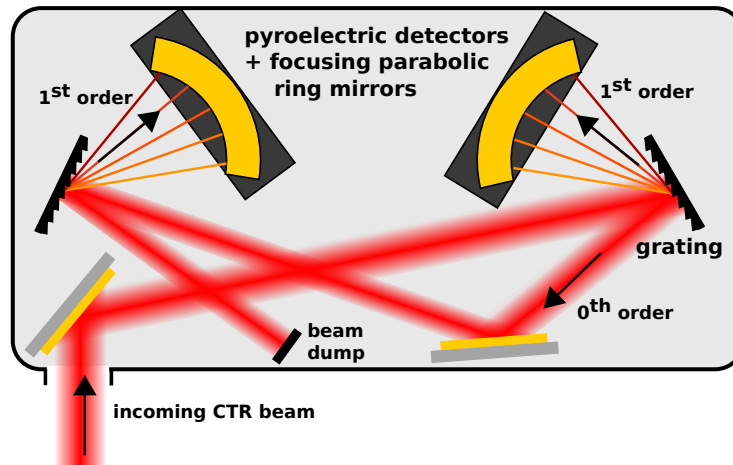


**Figure 4.9:** Layout of the mid-infrared spectrometer.

Since the peak of the **CTR** spectral intensity ( $dW/d\lambda$ ) was expected in the near- to mid-infrared region, a suitable spectrometer was needed for a meaningful measurement of the bunch's form factor. To this end, a custom spectrometer was built up, which relies on pyroelectric crystals for **CTR** detection. In contrast to semiconductor detectors like **CCD** cameras (for which the low

## 4. Experimental Setup

frequency detection limit is given by the material's bandgap), these offer good sensitivities over a wide spectral range in which the response is proportional to the energy of the absorbed radiation. As their response is mainly determined by the temperature change induced by the incoming radiation, these are in principle sensitive to radiation of arbitrary wavelength.

The mid-infrared spectrometer is based on a similar instrument developed at [DESY](#) in the group of B. Schmidt. Its detailed description can be found in ref. [113, 142, 146]. For the spectrometer set up in the course of this work, the building blocks consisting of pyroelectric crystal arrays, electronic pre-amplifiers, shaper boards and ring-shaped focusing mirrors were supplied by [DESY](#).

### 4.6.1 Working principle

The spectrometer is based on plane blazed reflection gratings and specifically designed ring mirrors that focus the dispersed radiation onto pyroelectric line arrays. Such an assembly constitutes one stage of the spectrometer. By tailoring the gratings' groove density, blaze angle and radiation incidence angle, a high efficiency for 1<sup>st</sup> order diffraction can be obtained while the grating can act simultaneously as a low pass filter for the specularly reflected beam. This allows a broadband spectral coverage by a sequential arrangement of multiple grating stages.

The staged setup requires a careful design of the gratings' diffraction efficiency. In particular, the wavelength range dispersed in each stage should be maximized. Simultaneously, an overlap with higher diffraction orders has to be avoided and long wavelength radiation should be specularly reflected with high efficiency in order to be analysed in a subsequent stage.

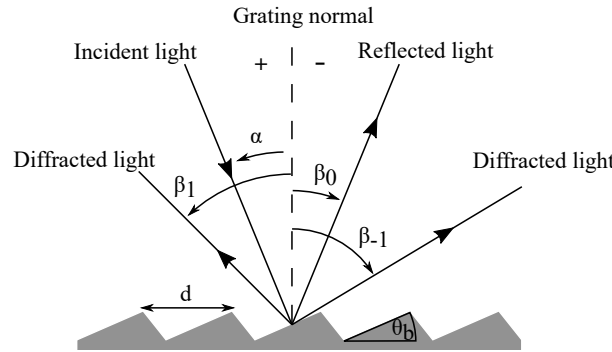


**Figure 4.10:** Diffraction by a blazed reflection grating. The angle of incidence  $\alpha$  and diffraction angle  $\beta$  are defined with respect to the grating normal and the sign convention is indicated by the + and - symbols. Also shown is the blaze angle  $\theta_b$ , which strongly determines the grating's diffraction efficiency.

For this purpose we start with the well-known grating equation that describes the wavelength dependence of the diffraction angle

$$\sin \alpha + \sin \beta_m = \frac{m\lambda}{d}. \quad (4.1)$$

Here,  $\alpha$  denotes the angle of incidence,  $\beta_m$  is the propagation direction of the  $m^{\text{th}}$  diffraction order (both angles are measured relative to the grating normal) and  $d$  is the grating's groove period, as depicted in Fig. 4.10. For  $m = 0$ , the solution is independent of  $\lambda$  and describes the

0<sup>th</sup> order specular reflection. For  $m \neq 0$ , the spectral components of the incident radiation are dispersed in different directions. Based on eq. (4.1), the dispersive power can be defined by

$$\frac{d\beta_m}{d\lambda} = \frac{m}{d \cos \beta_m} \quad (4.2)$$

and specifies the grating's ability to separate different wavelengths. We will first mention a couple of aspects that are easily seen from these equations. First, the larger the angle of diffraction, the higher is the dispersive power, meaning that the spectral bandwidth diffracted into a certain solid angle is diminished. Second, diffraction into higher order yields better resolution but, on the other hand, the dispersed wavelengths range is maximized for  $m = 1$ . Third, these effects scale with  $\lambda/d$ , thus it is sufficient to model one stage and adequately scale the groove period of subsequent stages.

One problem imposed by eq. (4.1) is the identical diffraction angle of different orders  $m$  if the product  $m\lambda$  is the same. To obtain a unique correspondence between  $\lambda$  and  $\beta_m$ , higher order wavelengths have to be filtered out beforehand. We will see shortly that the problem of higher order diffraction can be resolved with a special design in which multiple grating stages with appropriately engineered diffraction efficiencies are used.

### Diffraction efficiency

The diffraction efficiency  $\eta$  of a grating is defined as the optical power  $P$  of monochromatic light diffracted in a certain order relative to the incident power  $P_0$ :

$$\eta = \frac{P}{P_0}. \quad (4.3)$$

In general,  $\eta$  is dependent on the surface geometry (determined by the blaze angle  $\theta_b$ ), the incidence angle, the polarisation and the surface coating. A great amount of control is attainable by modifying  $\theta_b$ . The calculation of  $\eta$  is cumbersome and usually performed numerically solving the Maxwell equations at the surface of the grating. For the calculations presented in this work the code *Multilayer Rigorous Coupled Wave Analysis* was used [147].

For the case of the present single-shot spectrometer, the incidence angle needs to be fixed and a maximum usable spectral range is desired. The efficiencies have to be optimized to simultaneously fulfil the following requirements:

- the spectral range dispersed into the 1<sup>st</sup> order is maximized and the angles of emergence do not overlap with the incidence angle
- in this wavelength range diffraction into the 1<sup>st</sup> order is efficient
- the arrangement acts as a low-pass filter for wavelengths longer than the dispersive window which are specularly reflected and analysed in a next stage.

In ref. [113, 146] an optimized solution was found for p-polarised light at an incidence angle of approx. 20° and a blaze angle of 27°.

## 4. Experimental Setup

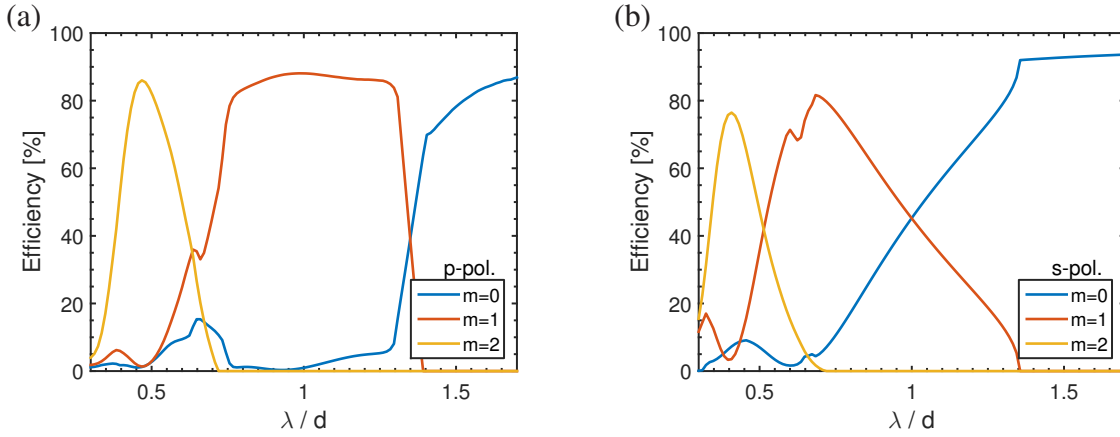


**Figure 4.11:** Diffraction efficiency for different orders of a blazed reflection grating for (a) p-polarisation and (b) s-polarisation.

In Fig. 4.11, the calculated grating efficiencies for these parameters are plotted over  $\lambda/d$  for p- and s-polarisation. For p-polarisation (for which the electric field is perpendicular to the grating grooves), a high efficiency  $\eta > 80\%$  is obtained for  $m = 1$  in the dispersive window from  $\lambda/d = [0.74 - 1.32]$  and consequently the leakage into the 0<sup>th</sup> order is  $\eta < 20\%$ . For s-polarisation, a high efficiency is obtained at the beginning of the dispersive window, which then continually drops at the expense of an increased reflection. In both cases, long wavelengths  $\lambda > d(1 + \sin \alpha)$ , for which the only solution to eq. (4.1) is given by  $m = 0$ , are specularly reflected. Although the efficiency curves of p-polarised light are more favourable for the cascading principle, in this work the use of polarisers was avoided for two reasons. First, highly transmissive polarisers were not available in the required broadband spectral range and the detectable energy would have not only been reduced by disregarding the s-polarised component but also by the transmission losses. Second, since in this wavelength regime calibrated light sources and detectors are not easily accessible, the usually non-flat, frequency dependent transmission curve of a polariser would lead to an additional measurement uncertainty. It was therefore opted for taking both polarisations into account.

The mid-infrared spectrometer employs a two-stage setup. For the second stage, the requirements defined above are more relaxed because the reflected 0<sup>th</sup> order does not need to be transported to a subsequent stage. Here, an incidence angle of  $\alpha = 5.8^\circ$  and a blaze angle of  $\theta_b = 13^\circ$  were chosen, which yields a broader usable wavelength range of  $\lambda/d = [0.34 - 1.09]$  (cf. Fig. 4.13b). The optimal grating parameters are summarized in table 4.1.

	$G [1/\text{mm}]$	$\theta_b [^\circ]$	$\alpha [^\circ]$	$\beta [^\circ]$	$\lambda [\mu\text{m}]$	$\lambda/d$
filter grating	830	27	20.7			
1 <sup>st</sup> stage	497	27	20.7	23 – 75	1.5 – 2.7	0.74 – 1.32
2 <sup>nd</sup> stage	150	13	5.8	14 – 82	2.3 – 7.3	0.34 – 1.09

**Table 4.1:** Grating parameters used for the two stage mid-infrared spectrometer.  $G = 1/d$  denotes the groove density,  $\lambda$  and  $\lambda/d$  is the usable wavelength range for 1<sup>st</sup> order diffraction and  $\beta$  denotes the corresponding range of diffraction angles.

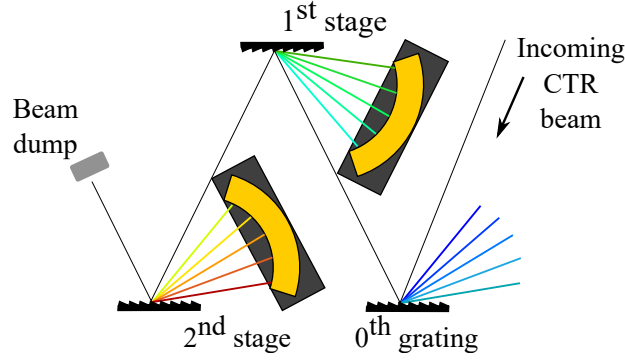


**Figure 4.12:** Cascaded spectrometer setup. Each grating disperses a particular wavelength range and acts as a low-pass filter for the subsequent stage. In principle the concept allows for the sequence of an arbitrary amount of stages and a single-shot spectral coverage much broader than one octave.

As seen from Fig. 4.11, short wavelengths ( $\lambda/d = [0.74 - 1.32]/2$ ) diffracted with high efficiency into the 2<sup>nd</sup> order can interfere with 1<sup>st</sup> order diffraction. Therefore, it is necessary to filter this wavelength range by using a preceding grating as a low pass filter. A sketch of the final cascaded setup is shown in Fig. 4.12. At each grating stage, the respective wavelengths of the polychromatic CTR beam are dispersed into the 1<sup>st</sup> order and longer wavelengths are reflected into the 0<sup>th</sup> order. In the next stage the subsequent wavelength range is analysed. The groove period  $d$  is chosen such that the longest diffracted wavelength equals the minimal wavelength of the subsequent stage. The 0<sup>th</sup> grating is used as a low pass filter to avoid second order diffraction in the 1<sup>st</sup> stage. In addition, wavelengths below  $1.1 \mu\text{m}$  were blocked by the silicon wafer.

The combined final diffraction efficiency of all three gratings at the 1<sup>st</sup> and 2<sup>nd</sup> stage, including transmission losses from the preceding gratings, is shown in Fig. 4.13. In both stages the erroneous signal due to higher order diffraction is limited to less than 20%. Furthermore, it may be inferred from the spectrum measured by the near-infrared spectrometer and subtracted from the measured signal to correct for the imperfect low-pass characteristics of the preceding gratings.

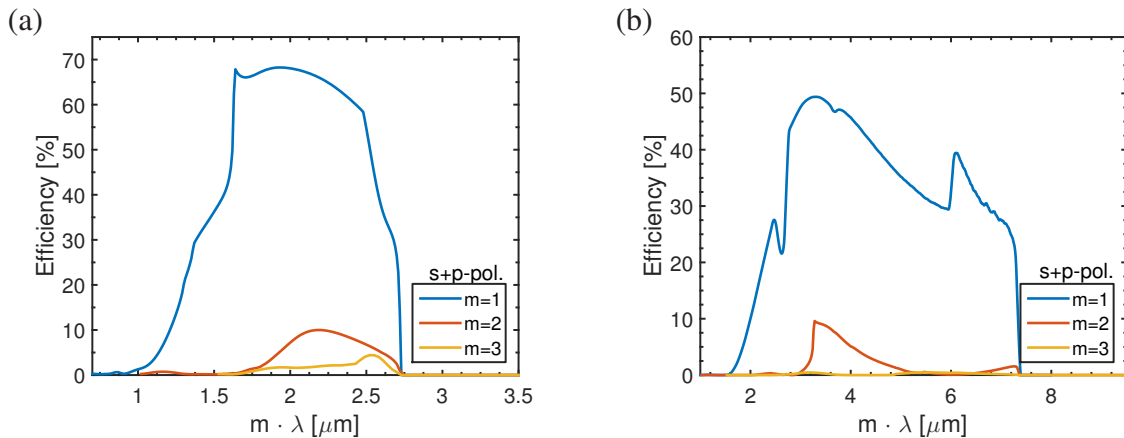


**Figure 4.13:** Total diffraction efficiency of the three grating setup at (a) the first and (b) the second grating stage. The contribution of higher orders (for short wavelength radiation) is due to the imperfect low-pass characteristic of the preceding grating(s).

## 4. Experimental Setup

### 4.6.2 Detection system

The angularly dispersed radiation is collected by specifically designed ring mirrors and detected by pyroelectric line arrays. These components together with the customized read-out electronics have been developed and supplied by [DESY](#) and shall only be briefly described here. More details can be found in the original work described in ref. [113, 146].

#### Parabolic ring mirrors

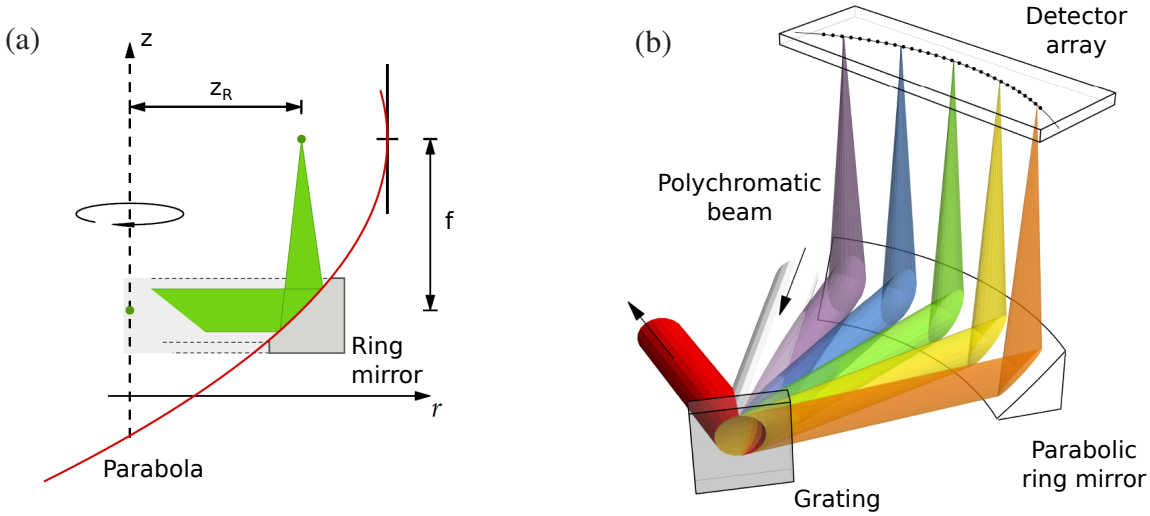


**Figure 4.14:** Sketch of the parabolic ring mirror used in the mid-infrared spectrometer to focus the incident [CTR](#) onto the pyroelectric detectors which are arranged in an arc. Image credit: Wesch [113].

In the experiment, the spectrally dispersed radiation has to be focused onto the individual pyroelectric crystals, where each angle of emergence corresponds to a monochromatic, collimated beam diffracted by the grating, and the focusing optic needs to cover the usable wavelength range dispersed by each grating. For this purpose specific ring mirrors were designed by [DESY](#) which are sketched in Fig. 4.14. In vertical direction these exhibit a  $90^\circ$  off-axis parabolic shape needed for optimal focusing. In the horizontal direction (the dispersion plane), this two-dimensional shape is rotated around the center of the grating by  $60^\circ$ , resembling the segment of a circle. The radius  $z_R$  of the circle (and therefore its focal length) as well as the focal length  $f$  of the off-axis parabolic shape are 150 mm. In this way focusing is achieved in both planes, approximating an ideal focal spot [113].

#### Pyroelectric line arrays & readout electronics

In the detection plane, the spectrally resolved beam is focused on the individual pyroelectric crystals. Figure 4.15 shows a schematic drawing of the line array that has been manufactured by InfraTec [148]. Each pyroelectric element of type X003 has a surface area of  $2 \times 2 \text{ mm}^2$  and consists of a specially coated  $\text{LiTaO}_3$  crystal. One array contains 30 such elements arranged in a circular arc of radius  $R = 150 \text{ mm}$  with a spacing of 5 mm. The arc covers an angle of  $55.4^\circ$  and



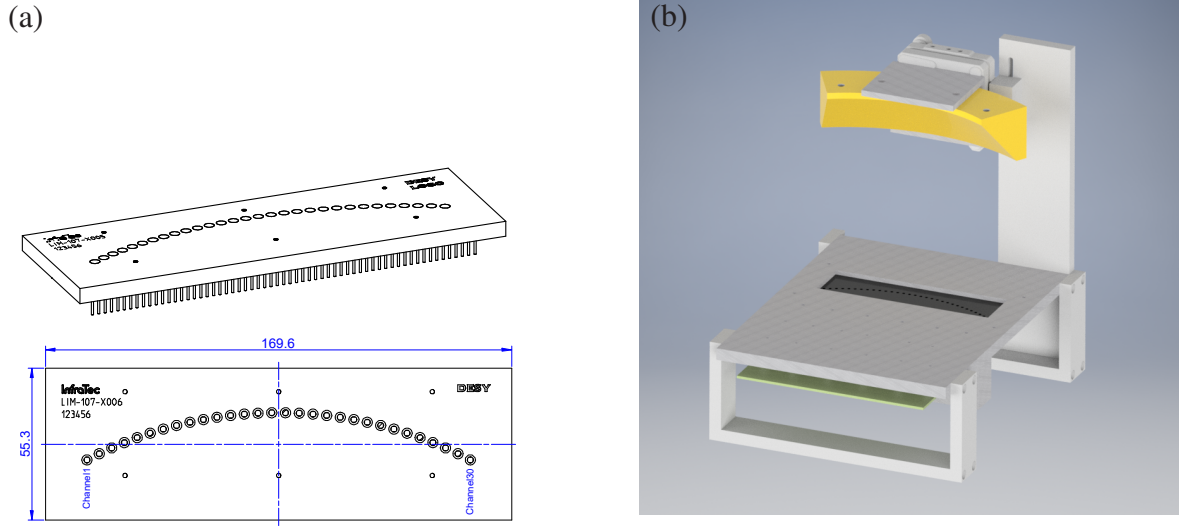


**Figure 4.15:** Schematic drawing of (a) the line array consisting of 30 individual pyroelectric crystals arranged in an arc, which is placed below the parabolic ring mirror as shown in (b).

is placed below the ring mirrors as illustrated in Fig. 4.15b.

The signal from the pyroelectric detectors is then amplified and shaped by custom circuit boards. A pre-amplifier board directly connected to the line array amplifies the signal using commercial Cremat CR100 charge sensitive amplifiers within the vacuum chamber. The differential signal is conducted by twisted pair cables to shaper amplifiers (Cremat CR200) placed outside the chamber and digitized by peak-sensing ADCs (Caen V78) with 12 bit resolution.

## 4.7 Laser beam alignment

The laser propagation axis in the experimental chamber was referenced by two marks. An aperture introduced into the laser beam allowed to align the position of the beam center to crosshairs marked on the backside of the focusing paraboloid. The second reference point was the beam's focal position, which was imaged by a CCD camera equipped with a 20x microscope objective. This procedure determined the beam direction.

The CTR diagnostics and involved optics were first aligned on air using a He-Ne laser referenced to the laser beam path. The incidence angle on the gratings of the mid-infrared spectrometer was determined by observing multiple higher order diffraction angles with respect to the pyroelectric elements. Since the angle between individual elements of  $1.6^\circ$  is known, fitting the grating equation (eq. (4.1)) to the diffraction orders allowed to determine the incidence angle as well as the angle of the individual pyro-detectors with respect to the grating normal to within  $0.5^\circ$ . This translates to an absolute error in wavelength calibration of less than 2.5%. Further, three reference points (crosshairs imaged by a CCD camera) for the mid-infrared spectrometer were set: one at the entrance of its vacuum chamber and one before each of the two grating stages. The first crosshairs possessed a hole with a diameter of  $\sim 0.5$  mm, which allowed to observe the beam pointing on the subsequent reference marks.

## 4. Experimental Setup

---

Under vacuum, the alignment of the CTR beam path was simplified by the fact that the electron beam co-propagates with the laser beam. The CTR beam thus overlaps with the laser axis and, by removing the tapes, its beam path under vacuum could be easily readjusted by aligning the center of the attenuated laser beam on the reference marks with the help of CCD cameras. The same procedure was also used to align the CTR beam to the entrance slits of the visible and near-infrared spectrometers.

### 4.8 Spectral response

The spectral response of the two commercial spectrometers in the visible and near-infrared range was established by the use of a blackbody radiator (Lot-Oriel LSB150) and a tungsten halogen lamp (Ocean Optics HL-2000-CAL). Since both sources were placed at the position of the CTR radiator, this calibration takes into account the frequency response of the imaging optics, the detectors, the gratings' diffraction efficiencies as well as the silicon wafers' transmission and reflection coefficients. The wavelength calibration was performed using the first three diffraction orders of a He-Ne laser. An absolute sensitivity calibration of the visible spectrometer was established using the He-Ne laser in conjunction with a chopper wheel. From the spectral overlap with the near-infrared spectrometer, an absolute calibration of the latter could be established as well.

The spectral response of the mid-infrared spectrometer was determined based on the calculated grating efficiencies, the mirror reflectivities, the transmission of the silicon wafer, the spectral bandwidth covered by each pyro-element and the spectral response of the pyro-elements (as determined by Behrens [149]). A detailed description of this procedure is given in Appendix A.



---

## Chapter 5

# Transmission of CTR through the detection optics

Besides the calibration of the spectral response of the individual elements involved in the diagnostic setup, the amount of detected CTR is further dependent on the CTR emission characteristics and its propagation along the imaging optics involved in the detection system, as the apertures of its components, diffraction of the beam and the size of the focal spot finally determine the amount of radiation that is incident on each detector pixel. Moreover, CTR is not only produced at the tape but also at the reflective pellicle, which was used to separate the CTR from the electron beam. This could possibly lead to interference effects between both sources and impact the measured spectrum. Therefore, the spectral transmission function of the detection system and the contribution of both CTR sources was modelled by a Fourier optics transport calculation, which is described in the following.

### 5.1 Fourier optics beam propagation

Recalling eq. (3.15), the complex CTR field amplitude in an observation plane with coordinate  $\mathbf{r}_1 = (x_1, y_1)$  that is placed at a distance  $z$  from the source plane (with coordinate  $\mathbf{r}_0 = (x_0, y_0)$ ) can be calculated by the Huygens-Fresnel principle

$$E_{\parallel/\perp}(\mathbf{r}_1, \omega) = -\frac{ik}{2\pi} \int_S \int E_{\parallel/\perp}(\mathbf{r}_0, \omega) \frac{\exp(ik|\mathbf{r}_1 - \mathbf{r}_0|)}{|\mathbf{r}_1 - \mathbf{r}_0|} d\mathbf{r}_0, \quad (5.1)$$

where  $\parallel$  and  $\perp$  denote the orthogonal linear polarisation components.

For a Cartesian coordinate system on both planes, the distance  $|\mathbf{r}_1 - \mathbf{r}_0|$  is given by

$$|\mathbf{r}_1 - \mathbf{r}_0| = \sqrt{z^2 + (x_1 - x_0)^2 + (y_1 - y_0)^2}. \quad (5.2)$$

Together with the source field given in eq. (3.12), the field distribution at any distance of the observation screen with  $z \gg \lambda$  can be evaluated.

When optical elements that modify the wavefront (apertures, lenses, etc.) are introduced in the beam path, the propagation has to be performed in a stepwise manner. First, the complex field amplitude is evaluated at the entrance plane of the optical element. After accounting for

## 5. Transmission of CTR through the detection optics

---

the wavefront modification imposed by this element, the field is then propagated to the entrance plane of the next element. Apart from simple model cases, this calculation has to be performed numerically. This is also the case in the present application, since the CTR near field expression of eq. (3.28) does not possess an analytical solution.

The exact calculation of the Huygens-Fresnel integral of eq. (5.1) is computationally expensive. A more usable expression can be obtained by applying the so-called *Fresnel approximation*, which is based on the expansion of the square root of eq. (5.2) up to 2<sup>nd</sup> order [110]

$$\begin{aligned} r_{01} &= \sqrt{z^2 + (x_1 - x_0)^2 + (y_1 - y_0)^2} \\ &\approx z + \frac{x_1^2 + y_1^2}{2z} - \frac{x_1 x_0 + y_1 y_0}{z} + \frac{x_0^2 + y_0^2}{2z}. \end{aligned} \quad (5.3)$$

The Fresnel approximation is valid when the distance between the source and the observation screen is large compared to the transverse extent of the field distribution. Plugging above expression into eq. (5.1) we finally obtain the Fresnel diffraction integral

$$E(x_1, y_1, z) = -\frac{ik}{2\pi z} \iint E(x_0, y_0, 0) \exp \left[ \frac{ik}{2z} \left( (x_1 - x_0)^2 + (y_1 - y_0)^2 \right) \right] dx_0 dy_0, \quad (5.4)$$

where an absolute phase factor  $\exp(ikz)$  has been neglected.

### Propagation by Fourier transformation

Equation (5.4) can be rewritten in the form

$$\begin{aligned} E(x_1, y_1, z) &= -\frac{ik}{2\pi z} P_z(x_1, y_1) \\ &\times \iint E(x_0, y_0, 0) P_0(x_0, y_0) \exp \left[ -ik \left( \frac{x_1 x_0 + y_1 y_0}{z} \right) \right] dx_0 dy_0 \end{aligned} \quad (5.5)$$

with

$$P_z(x, y) = \exp \left[ \frac{ik}{2z} (x^2 + y^2) \right]. \quad (5.6)$$

The field propagation along a distance  $z$  can thus be calculated by a two-dimensional Fourier transform for which efficient algorithms exist. The propagated field is found by multiplying the source field by a phase term  $P_0(x_0, y_0)$ , subsequent Fourier transformation with the transverse wave numbers  $k_x = kx_1/z$  and  $k_y = ky_1/z$ , followed by multiplication with a further phase factor  $P_z(x_1, y_1)$ . These phase terms account for the near-field diffraction. Note that in the case  $z \gg k(x^2 + y^2)$  the phase factor  $P_z \approx 1$  and the far-field Fraunhofer diffraction equation is recovered.

### Phase shift by optical elements

Due to their surface curvature, focusing optics introduce a relative path length difference on the beam as a function of its distance from the optical axis of the element. This imposes a varying

phase shift in the transverse plane. At the exit plane of the optical element, this phase shift is added to the incident beam, i.e

$$E(x,y)_{exit} = E(x,y)_{entrance} \exp(i\varphi(x,y)). \quad (5.7)$$

The phase term introduced by a parabolic mirror can be derived from the geometrical path difference between rays traveling at a distance  $r = \sqrt{x^2 + y^2}$  to the optical axis. For a paraboloid of focal length  $f$  it is given by [104]

$$\varphi(r) = -k \frac{r^2}{2f}. \quad (5.8)$$

## 5.2 Model representation

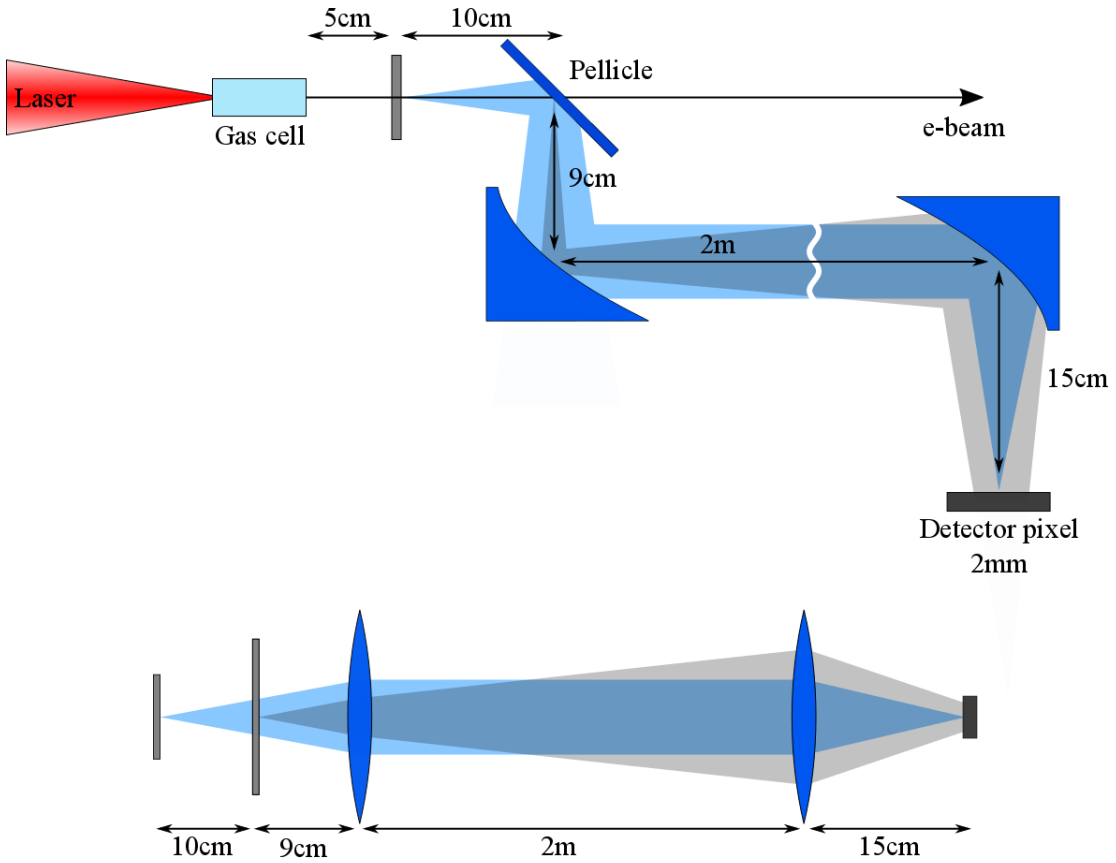


**Figure 5.1:** Schematic setup of the experiment (top) and modelling representation (bottom). In the case of the mid-infrared spectrometer, a grating (not drawn) in the 2m propagation leg provides spectral separation to different detector pixels. The aluminium coated pellicle is roughly at half the focal distance from the first collimating optic, which leads to a large difference in wavefront curvature between the CTR beams from the tape and the pellicle. In the sketch, the divergences are strongly exaggerated.

The imaging system used in the experimental setup collects CTR produced at the radiator foil with a collection half-angle of 133 mrad defined by the f-number of the first collimating paraboloid.

## 5. Transmission of CTR through the detection optics

Subsequently the CTR beam is split and transported to the three spectrometers, where the spectrally dispersed radiation is focused onto the respective detector pixels. The beam path is made up of the following distinct optical elements: plane mirrors, paraboloids, gratings and the parabolic ring mirrors. Since the calculation is performed for distinct CTR frequencies, the gratings that spectrally disperse the incident CTR are treated as normal plane mirrors, since no spatially dependent phase term is introduced in the diffracted monochromatic beam. The same is true for plane mirrors. Thus, only the parabolic mirrors introduce transversely varying phase factors that account for collimation and focusing of the CTR beam.

Figure 5.1 shows a schematic of the optical path and the representation of the setup used in the numerical calculation. The main purpose of the beam propagation is to quantify the frequency dependent CTR energy that is transported through the detection optics and focused on the detectors. Furthermore, as sketched in Fig. 5.1, CTR is not only produced at the tape but also at the reflective pellicle, which was needed to separate the CTR radiation from the electron beam. Although collection of CTR behind the electron spectrometer (where the electron bunch would have been deflected by the magnet from the CTR beam path) would have allowed to avoid the pellicle, the latter was needed in order to obtain a large collection angle, which ensured sufficient count rates on the pyroelectric detectors while avoiding excessively big optics. Moreover, separation of CTR from the electron beam before the electron spectrometer magnet prevented parasitic synchrotron radiation produced by the deflected electron beam from reaching the spectrometers.

### Transmission function

Recalling eq. (3.49), the form factor is related to the emitted spectral energy by

$$\frac{dW}{d\omega} \propto N^2 |F_{\parallel}(\omega)|^2 \int_{\Omega_{max}} \left| \int \mathbf{E}(\omega, \mathbf{p}) g(\mathbf{p}) d\mathbf{p} \right|^2 \cdot |F_{\perp}|^2 d\Omega, \quad (5.9)$$

where  $\Omega_{max}$  denotes the solid angle of collection. We now have to quantify the spectral energy emitted by the electron bunch that is actually transferred to the detection plane. Therefore, we introduce the spectral transmission function  $T(\omega, \mathbf{p})$  of the detection optics that describes the propagation of the collected CTR to the detection plane. Integrating over the area of one detector pixel, the detected spectral energy is related to the form factor by

$$\frac{dW}{d\omega} = N^2 |F_{\parallel}(\omega)|^2 2\epsilon_0 c \left| \int g(\mathbf{p}) T(\omega, \mathbf{p}) \mathbf{E}(\omega, \mathbf{p}) F_{\perp}(\omega) d\mathbf{p} \right|^2. \quad (5.10)$$

Simple rearrangement yields the magnitude of the longitudinal form factor:

$$|F_{\parallel}(\omega)|^2 = \frac{dW/d\omega}{2\epsilon_0 c N^2 \left| \int g(\mathbf{p}) T(\omega, \mathbf{p}) \mathbf{E}(\omega, \mathbf{p}) F_{\perp}(\omega) d\mathbf{p} \right|^2}. \quad (5.11)$$

By measurement of the electron energy spectrum and the transverse density distribution of the electron beam, the momentum distribution  $g(\mathbf{p})$  and the transverse form factor  $F_{\perp}(\omega)$  can be determined experimentally. Thus, with the knowledge of the transmission function  $T(\omega, \mathbf{p})$ , the absolute value of the longitudinal form factor can be obtained from the measured CTR spectrum.

### 5.3 Numerical calculation

In the following, the calculation of the denominator of eq. (5.11) is described in detail. Since the electron energy spectrum varies dependent on the experimental conditions, the calculation has to be performed for each single shot. As a complete numerical calculation of the CTR propagation for each shot is not feasible, the relevant experimental parameter space was divided into discrete steps. The parameter space includes the CTR frequency, electron energy, and transverse beam size. The latter varied in a controlled manner due to the different length settings of the gas cell, which resulted in a variation of the distance between the gas cell exit and the fixed radiator foil and consequently in a different transverse beam size at the CTR radiator.

The calculation was performed for 64 evenly spaced frequency intervals covering the measured spectral range from  $0.4 - 16 \mu\text{m}$ , 15 electron energies in the detection range from  $125 - 825 \text{ MeV}$  and 12 different transverse sizes of the electron beam, corresponding to the discrete distances between the exit of the gas cell and the radiator foil. For each unique set of parameters, the TR field pattern was propagated from the source to the detection plane.

As illustrated in Fig. 5.1, the calculation was done in a stepwise procedure. In the first step, the CTR spectral amplitude and phase in the near-field originating from the two sources (tape and pellicle) are computed at the entrance plane of the first lens according to eq. (3.29). In the calculation of the denominator of eq. (5.11) the longitudinal form factor is not considered ( $F_{\parallel}(\omega) = 1$ ), and thus the electron beam is modelled as a mono-energetic sheet of unit charge. Its transverse size at both radiators is given by the distance between the entrance plane, the position of the radiators and the divergence of the beam. The mutual phase delay  $\phi$  between both beams is taken into account, given by the velocity difference between electrons and TR times the distance  $d$  between tape and pellicle:  $\phi = 2\pi d/2\gamma^2\lambda$ . This step yields the radially symmetric complex amplitude of both beams at the entrance plane of the first paraboloid. Their spectral fluence is plotted in Fig. 5.2a. Due to the radial symmetry and the radial polarisation, the emission on axis cancels, which leads to a doughnut shaped beam. In a second step, the wavefront modification introduced by the collimating paraboloid is applied to the fields and both beams are propagated over 2 m to the entrance plane of the focusing optics. The spectral fluence at this position is displayed in Fig. 5.2b. In the third step, after applying the phase modification introduced by the second paraboloid, a further beam propagation of the complex amplitudes yields the field distribution of both beams in the detection plane. The radial lineouts of the focus distributions are plotted in Fig. 5.2c.

In the last step, as the field distribution for each point of the parameter space has been calculated, the denominator of eq. (5.11) is evaluated for each shot. The integral of eq. (5.11) with respect to  $p$  is performed by binning the measured electron energy spectrum  $g(p)$  into 50 MeV steps. Finally, the detected spectral energy is obtained by integrating the fluence over the area of each detector pixel.

## 5. Transmission of CTR through the detection optics

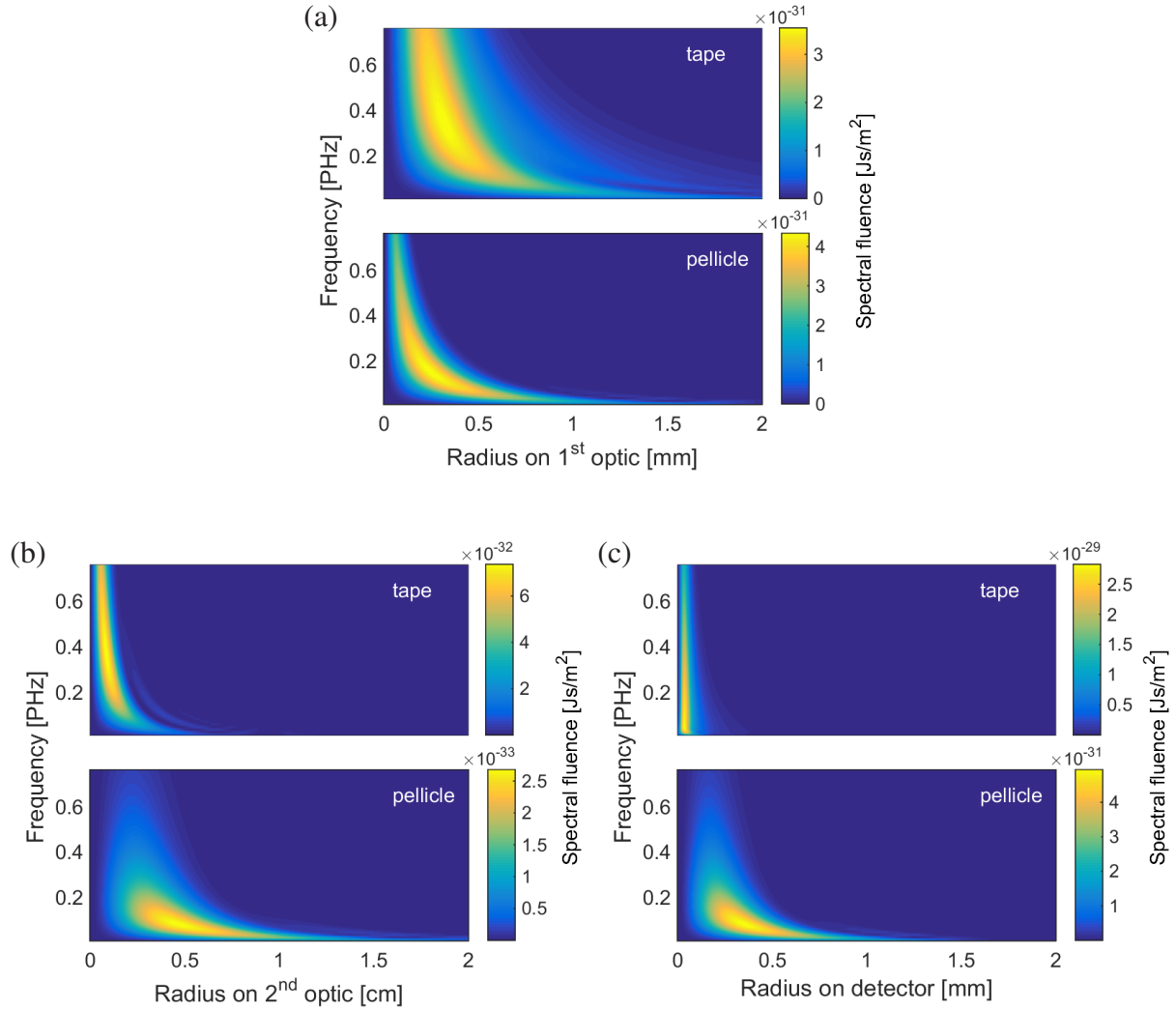


**Figure 5.2:** Spectral fluence of CTR on the detection optics. (a) shows the spectral fluence on the entrance plane of the first paraboloid, (b) on the entrance plane of the second paraboloid and (c) in the detection plane. The beam pattern is radially symmetric and radially polarised. An electron energy of 525 MeV and a divergence of 1.4 mrad FWHM is assumed.

## 5.4 Discussion

As seen in Fig. 5.2c, CTR from the tape is well focused in the detection plane compared to the beam from the pellicle, which forms a much larger spot due to its origin far from the geometrical object plane of the detection optics. The region of radii where interference can occur is limited to the very outer parts of the beam from the tape and inner parts of the beam from the pellicle. For both beams the finite transverse size of the electron bunch at the two radiators leads to a suppression of high frequency radiation into large angles due to reduced transverse coherence as  $F_{\perp}(\omega, \theta) < 1$ . This effect is more pronounced for CTR emerging from the pellicle since the electron bunch's transverse size has approximately tripled compared to its size at the tape.

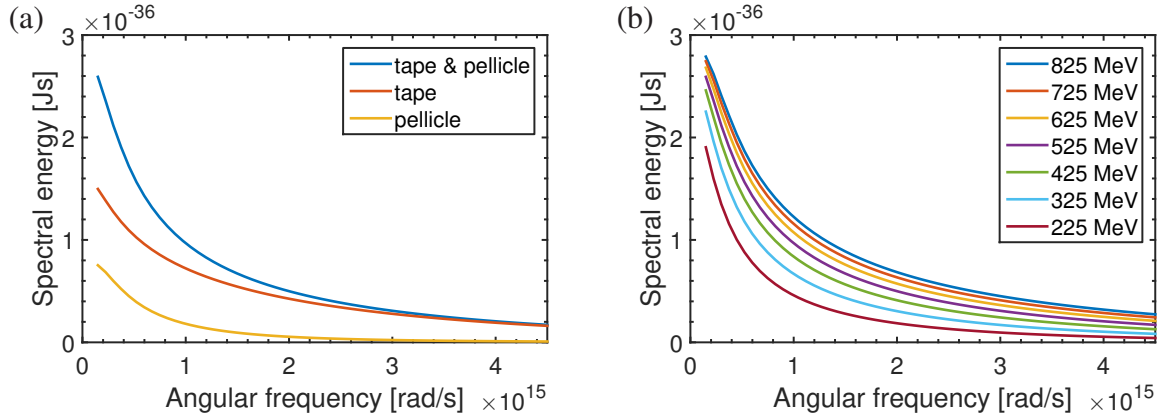


**Figure 5.3:** Transmitted spectral energy incident on the detector. (a) shows the computed spectral fluence integrated over one pixel of the detector. Plotted is the respective CTR energy from the tape and pellicle itself and their coherent sum for an electron energy of 525 MeV. (b) shows the combined signal from both radiators for mono-energetic electron sheets of different energy. A distance between the exit of the gas cell and the tape of 50 mm and a divergence of  $\sigma_{FWHM} = 1.4$  mrad is assumed. The beam charge  $Q$  is normalized to  $Q = -e$ .

Figure 5.3a shows the transmitted spectral energy produced individually at the tape and the pellicle as well as their coherent sum for an electron energy of 525 MeV in dependence of the CTR frequency. The CTR signal from the pellicle is weaker compared to that from the tape, because of the increased transverse electron beam size at the position of the pellicle and due to its lack of collimation after the first lens, such that only a part of the radiation is collected by the free aperture of the 2<sup>nd</sup> lens and focused onto the detector.

The combined signal of both radiators is shown in Fig. 5.3b for different electron energies. For fixed  $\omega$ , the curves roughly resemble the  $\ln \gamma$  dependence of the radiated energy expected from eq. (3.25). The knowledge of the transmission curves together with the measured electron energy spectrum finally allows to obtain  $|F_{||}(\omega)|$  from the measured CTR spectrum by eq. (5.11).

### Interference effect

The distribution of CTR emitted from the two radiators leads to interference in the detection plane due to the geometrical path difference to both sources. An additional energy-dependent relative phase is acquired by the difference between the particles' velocity and the radiation velocity  $c$  while propagating the distance  $d$  between both radiators, with the effective path difference given by  $d/(2\gamma)^2$ . The coherent enhancement due to interference between both radiation fields can be quantified by an

$$\text{Enhancement factor} = \frac{\int |E_t + E_p|^2 dA}{\int |E_t|^2 + |E_p|^2 dA}, \quad (5.12)$$

where  $E_t$  and  $E_p$  denote the electric field of the beams from the tape and the pellicle, respectively. The result is plotted in Fig. 5.4.



## 5. Transmission of CTR through the detection optics

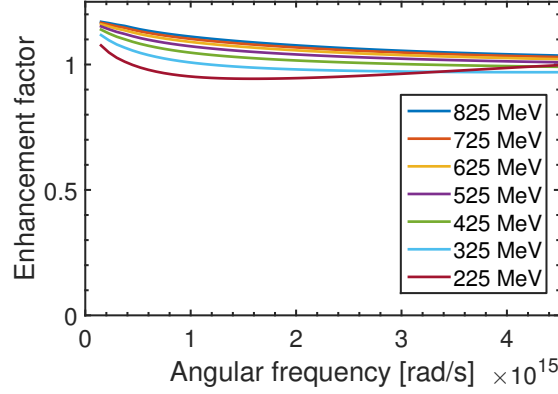


**Figure 5.4:** *Interference effect between both CTR radiators in the detection plane. The enhancement factor as defined in the text is plotted for different electron energies.*

For electron energies in the range of 225 – 725 MeV, a maximum deviation of  $\pm 13\%$  relative to the incoherent sum of both beams in the relevant frequency range is preserved. The effect is generally weak due to their different size in the detection plane, but more pronounced at higher electron energies due to a better spatial overlap caused by the lower divergence ( $1/\gamma$ ) of both beams. The effective path length difference is small and for  $\gamma = 1000$  and  $d = 10$  cm amounts to 50 nm. Due to the small absolute phase delay and little spatial overlap of the two beams, no oscillatory behaviour with wavelength occurs.

The analysis shows that despite the contribution of two CTR sources, the spectral energy in the detection plane is a smooth function of frequency. This is an important property as otherwise possible oscillations would have to be resolved by all spectrometers and the exact distance between both radiators could strongly influence the measured spectrum. Furthermore, quantifying the transmission of the detection optics is essential for an accurate determination of the absolute value of  $F_{\parallel}(\omega)$  from the measured CTR spectrum. The measured form factor can then be fed to the Bubblewrap algorithm to retrieve the longitudinal bunch profile  $\rho_{\parallel}(z)$  for each shot.



---

## Chapter 6

# Momentum and transverse spatial distribution of LWFA electron bunches from a length-variable gas target

As outlined in chapter 2, the dynamics of LWFA are governed by complex physical phenomena including laser pulse compression, self-focusing, depletion, diffraction and electron dephasing, many of which are inherently nonlinear and interdependent. As shown previously by Antonia Popp [136], measurement of the electron energy spectra in dependence of the plasma length allows to experimentally identify the process limiting acceleration at a specific density, be it pump depletion or electron dephasing. In the present work, the experimental setup employed by A. Popp was extended by the CTR diagnostics in order to simultaneously explore the dynamics of bunch evolution after different target lengths.

In this chapter, we first analyse the electron beam divergence and spatial profile recorded by the electron beam diagnostics to verify that the assumptions made in our model of the CTR emission are justified. We will then discuss the evolution of the electron energy spectra of two scans of the gas cell length conducted at different plasma densities. Experimental data of the longitudinal bunch profiles obtained during these scans will be presented in chapter 7.

### 6.1 Beam divergence

As described in chapter 4, at the scintillator screen S2 positioned behind the dipole magnet the bunch is energetically dispersed in the vertical direction. On the horizontal axis, a lineout of the spatial profile and thus the energy dependent divergence can be evaluated after 2.2 m of propagation.

Figure 6.1a shows this quantity obtained during a scan of the gas cell length in the range of 4 – 14 mm. At each discrete cell length (distinguished by different colours) the mean energy-resolved divergence is evaluated from 30 consecutive shots. The error bars show the shot-to-shot standard deviation of each 30-shot dataset. As seen from the plot, the divergence is not influenced significantly by the length of the gas cell as all data points agree with each other within the error margin of  $\pm 1$  standard deviation. In this experimental run, CTR was recorded simultaneously with the scintillator screen images. Therefore, the double tape drive was inserted into the electron

## 6. Momentum and transverse spatial distribution of LWFA electron bunches from a length-variable gas target

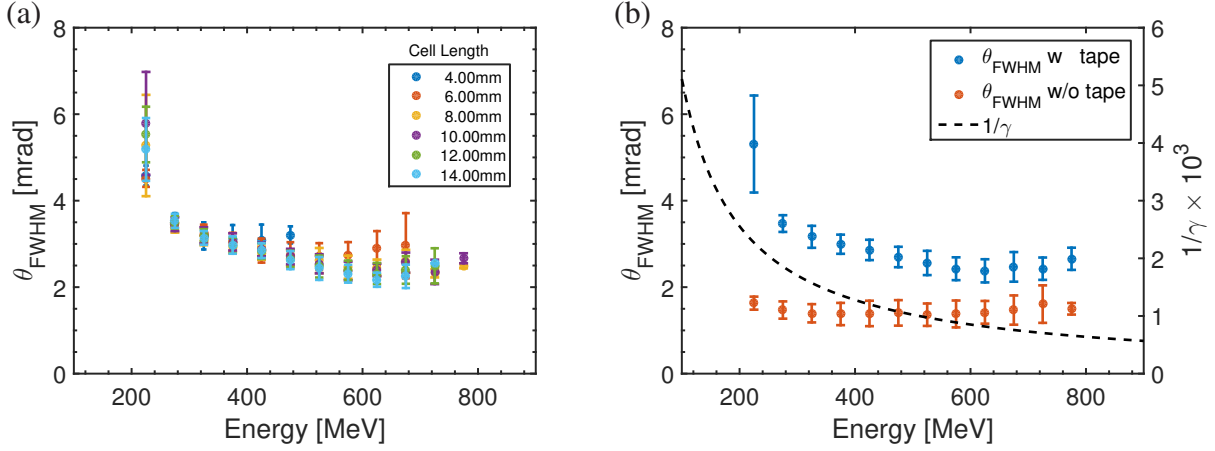


**Figure 6.1:** Energy resolved divergence  $\theta_{FWHM}$  of the electron bunch in the horizontal plane (perpendicular to the polarisation of the driver laser) determined from images of the scintillation screen S2 behind the spectrometer magnet. (a) shows the beam divergence with the **CTR** radiator inserted into the beam path for a backing pressure of 70mbar, corresponding to  $n_0 = 3.4 \times 10^{18} \text{ cm}^{-3}$ . For each discrete length setting of the gas cell a set of 30 consecutive shots was evaluated. Each such set is plotted in a different colour. Markers show its mean value, error bars indicate the shot-to-shot standard deviation. Due to crossing the steel tapes, the intrinsic divergence of the electron bunch is enlarged by multiple small-angle Coulomb scattering inside the metallic foils. In (b), red markers show the bunch divergence determined from a separate run under similar experimental conditions in which the tapes were removed from the beam path. The data points thus reflect the actual beam divergence before crossing the tapes. For comparison, blue markers show the divergence averaged over all gas cell lengths shown in (a). The dashed black line illustrates  $1/\gamma$ . This scaling would apply to the bunch divergence (due to adiabatic damping) if the normalized emittance would be conserved during acceleration.

beam path, which led to an increased angular distribution due to multiple small-angle Coulomb scattering within the steel tapes. The divergence determined in this scan thus only demonstrates its independence of gas cell length but is inappropriate to determine the bunch size at the tapes.

The intrinsic energy resolved divergence was therefore determined from a separate run in which the steel tapes were removed from the electron beam path. A comparison of these two measurements is shown in Fig. 6.1b. The values are significantly lower than those obtained with the **CTR** radiator in place and approximately constant with  $\theta_{FWHM} \sim 1.4 \text{ mrad}$ . Although adiabatic damping<sup>1</sup> would imply that the divergence scales with electron energy by  $1/\gamma$  (as indicated by the dashed black line), this is not the case. The near constant divergence is therefore contradictory to a purely longitudinal acceleration. The observed behaviour may be caused by a non-ideal shape of the plasma cavity or direct interaction of the electron bunch with the rear of the laser field.

1. Adiabatic damping refers to the fact that during longitudinal acceleration the divergence decreases with increasing energy because the ratio of transverse over longitudinal beam momentum is reduced.

### Spatial beam profile

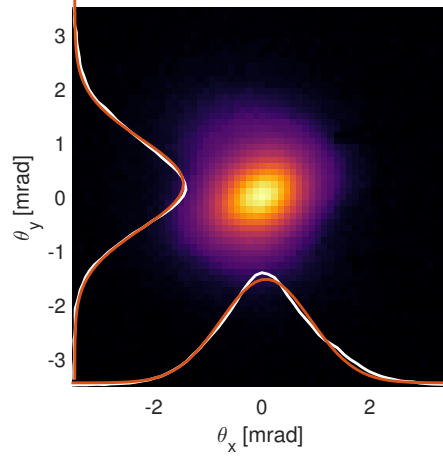


**Figure 6.2:** Projected transverse beam profile. Shown is a typical transverse beam profile observed at the scintillator screen S1 (before the electron spectrometer magnet). White lines display its projection on the  $x$ - and  $y$ -axis. The transverse profile is well approximated by a radially symmetric Gaussian distribution as revealed by the Gaussian fit to the respective projections, shown by the red lines.

As described in section 4.4, a second scintillator screen (S1) could optionally be inserted in front of the dipole magnet and allowed to monitor the transverse electron beam profile after 1.46 m of propagation. As exemplarily shown in Fig. 6.2, the transverse profile was found to be approximately Gaussian and radially symmetric.

## 6.2 Phase space separability

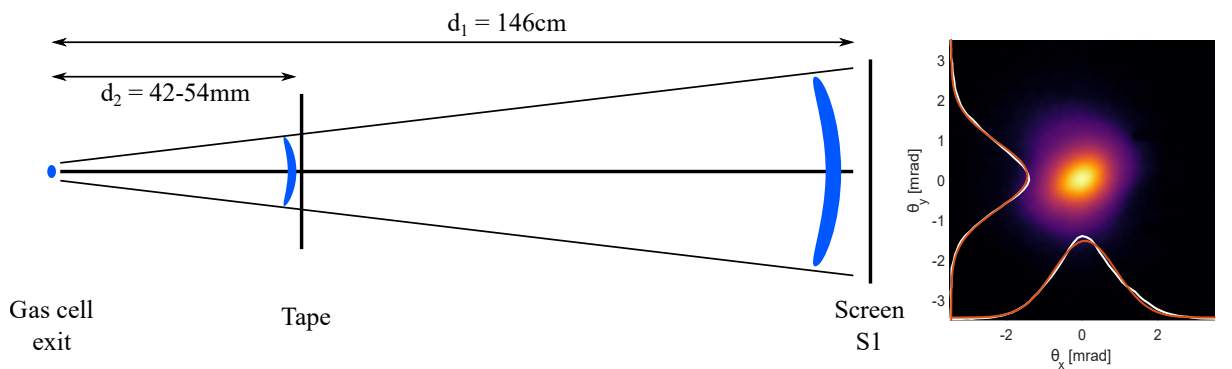


**Figure 6.3:** Sketch of the geometry used to determine the transverse charge profile before entering the electron spectrometer magnet. Also shown is the position of the **CTR** radiator that (if inserted) was positioned 42 – 54 mm behind the exit of the gas cell (dependent on the length setting of the cell). Due to the small source size, the beam diameter after the distance  $d_1$  and  $d_2$  is practically determined by the beam divergence.

In chapter 3, we made the following assumptions about the separability of the electron bunch's

## 6. Momentum and transverse spatial distribution of LWFA electron bunches from a length-variable gas target

phase space distribution  $h(\mathbf{r}, \mathbf{p})$ :

$$h(\mathbf{r}, \mathbf{p}) = \rho(\mathbf{r}) g(\mathbf{p}), \quad (6.1)$$

$$\rho(\mathbf{r}) = \rho_{\parallel}(z) \rho_{\perp}(r_{\perp}), \quad (6.2)$$

$$g(\mathbf{p}) = g_p(p) g_{\theta}(\theta) g_{\phi}(\phi), \quad (6.3)$$

where the momentum and spatial distributions were defined by  $g(\mathbf{p}) = \int h d\mathbf{r}$  and  $\rho(\mathbf{r}) = \int h d\mathbf{p}$ . Thus, we had assumed that the phase space distribution  $h$  is fully separable by

$$h(\mathbf{r}, \mathbf{p}) = h(z, r_{\perp}, p, \theta, \phi) \quad (6.4)$$

$$= \rho_{\parallel}(z) \rho_{\perp}(r_{\perp}) g_p(p) g_{\theta}(\theta) g_{\phi}(\phi). \quad (6.5)$$

We now investigate the validity of these assumptions by analysing the possible correlations of  $h = h(z, r_{\perp}, p, \theta, \phi)$ , where the respective projections of  $h$  on the coordinate axes  $z, r_{\perp}, p, \theta, \phi$  are denoted by  $\rho_{\parallel}, \rho_{\perp}, g_p, g_{\theta}, g_{\phi}$ . The correlation coefficient  $\text{cor}(X, Y)$  is defined by

$$\text{cor}(X, Y) = \frac{\langle \delta X \delta Y \rangle}{\sqrt{\langle \delta X^2 \rangle \langle \delta Y^2 \rangle}}, \quad (6.6)$$

where  $\langle \rangle$  denotes the integral over the distribution function  $h$ . In the following, we use of the conservation of the correlation coefficient under linear transformations

$$\text{cor}(a + bX, Y) = \text{cor}(X, Y) \quad a, b \in \mathbb{R}, b > 0 \quad (6.7)$$

and make the assumption that the beam divergence is *independent* of *energy* and *gas cell length*, as suggested by Fig. 6.1.

The source size of LWFA electron beams has been determined by various authors to be on the order of a few  $\mu\text{m}$  [20, 150, 151]. This is much smaller than the size of the projected transverse beam profile on the screen S1, which is given by  $\sin(\theta_{FWHM})d_1 \approx 2\text{ mm}$ , as sketched in Fig. 6.3. As a result, the electron charge distribution on S1 can be regarded as originating from a point source and its transverse size is only dependent on the angular distribution of  $g(\mathbf{p})$ .

The circular symmetry and beam size observed on the scintillator screen S1, which is consistent with the energy resolved divergence of  $\theta_{FWHM} \sim 1.4\text{ mrad}$ , suggest that the momentum distribution  $g(\mathbf{p})$  is circularly symmetric. The correlation coefficient  $\text{cor}(g_p, g_{\theta})$  vanishes because  $g_{\theta}$  is approximated as being energy independent. Thus, the momentum distribution is separable by  $g(\mathbf{p}) = g_p(p) g_{\theta}(\theta) g_{\phi}(\phi)$ .

We now proceed to analyse possible correlations of  $h = h(z, r_{\perp}, p, \theta)$ , starting with correlations of  $\rho_{\perp}$  with  $g(\mathbf{p})$ :

(i) It is crucial to realize that the actual CTR measurement takes place at the position of the tape, where  $h$  has evolved from its shape inside the wakefield by free space propagation. As above, the transverse spatial profile of the electron beam at the position of the radiator is only determined by the beam divergence, because its transverse beam size of  $\sin(\theta_{FWHM})d_2 \gtrsim 60\mu\text{m}$  is much larger than its source size inside the wakefield. Thus,  $\rho_{\perp}(\mathbf{r}_{\perp}) = \rho_{\perp}(r_{\perp}) \approx d_2 g_{\theta}$  and

$$\text{cor}(\rho_{\perp}, g_{\theta}) \approx \text{cor}(g_{\theta}, g_{\theta}) = 1. \quad (6.8)$$

However, as shown in subsection 3.2.4, the resulting transverse position-angle correlation has no significant effect on the measured CTR spectrum.

(ii) Since  $\rho_{\perp} \approx d_2 g_{\theta}$  and using our assumption that the beam divergence does not depend on electron energy, i.e.  $\text{cor}(g_p, g_{\theta}) = 0$ , we conclude

$$\text{cor}(\rho_{\perp}, g_p) \approx \text{cor}(g_{\theta}, g_p) = 0. \quad (6.9)$$

After having treated the correlations of  $\rho_{\perp}$  with  $g(\mathbf{p})$ , we are now left to investigate potential correlations of  $\rho_{\parallel}$ :

(iii) As observed in PIC simulations (to be presented in section 7.4), the electron bunch exhibits some degree of longitudinal position-momentum correlation, which can be approximated by a linear chirp. Hence, the longitudinal charge distribution of the bunch will be mapped to the energy axis, i.e.  $\rho_{\parallel} \approx a g_p$ , where  $a$  denotes a proportionality constant. We therefore conclude that inside the plasma

$$\text{cor}(\rho_{\parallel}, g_{\theta}) \approx \text{cor}(g_p, g_{\theta}) = 0. \quad (6.10)$$

(iv) A similar argument leads us to conclude that  $\rho_{\parallel}$  is not correlated with  $\rho_{\perp}$ :

$$\text{cor}(\rho_{\parallel}, \rho_{\perp}) \approx \text{cor}(a g_p, d_2 g_{\theta}) = \text{cor}(g_p, g_{\theta}) = 0. \quad (6.11)$$

Nevertheless, the free space drift from the plasma to the radiator will introduce a correlation between longitudinal and transverse position, manifested by a curved beam shape due to a geometric path difference to the radiator foil (cf. Fig. 6.3). However, as discussed in subsection 3.2.4, the effect is negligible.

(v) The only correlation left is

$$\text{cor}(\rho_{\parallel}, g_p), \quad (6.12)$$

i.e. an energy chirp in longitudinal phase space. Its effect on the radiated CTR spectrum along with the bunch lengthening of a chirped beam due to free-space propagation to the radiator foil has been discussed in subsection 3.2.4. A possible energy chirp accounts for an error in the retrieved bunch duration of  $< 15\%$ .

Within this error margin, our analysis shows that the assumption of phase space separability is indeed justified.

## 6.3 Energy evolution

The evolution of the longitudinal bunch profile in dependence of the gas cell length  $L$  was studied in two detailed scans conducted at different plasma density. The densities were changed by altering the nominal backing pressures of hydrogen at the gas cell reservoir (70 and 160 mbar), corresponding to plasma electron densities of  $n_1 = 3.4 \times 10^{18} \text{cm}^{-3}$  and  $n_2 = 7.7 \times 10^{18} \text{cm}^{-3}$ , respectively.  $L$  was varied in discrete steps and 30 consecutive shots were recorded at each length setting. In order to obtain an understanding of the dynamics involved in the acceleration process, we now examine the evolution of the electron bunch energy spectra analogous to the analysis presented by Popp [136].

## 6. Momentum and transverse spatial distribution of LWFA electron bunches from a length-variable gas target

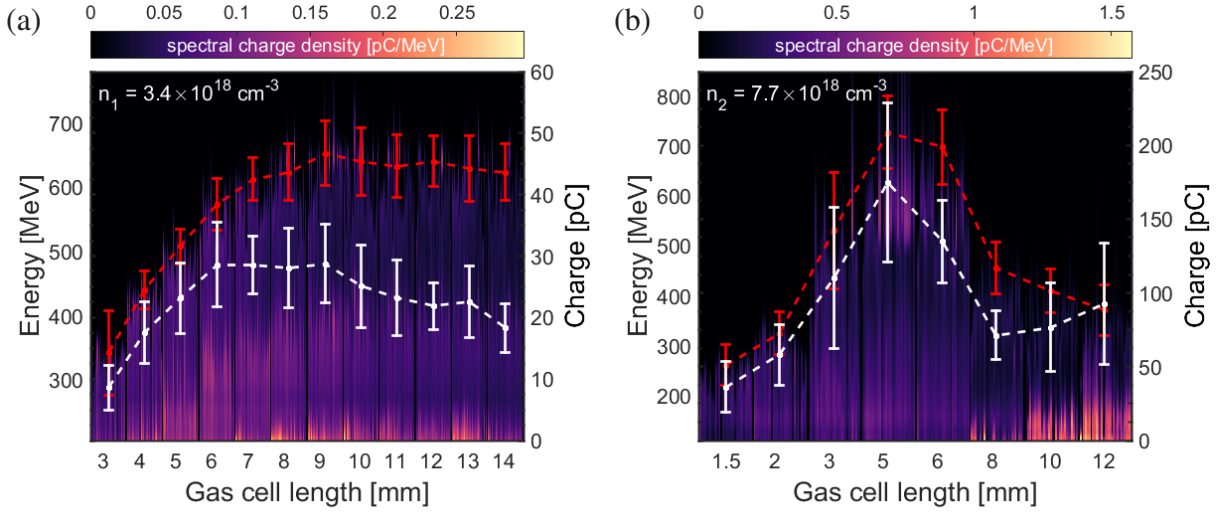


**Figure 6.4:** Evolution of the electron energy spectra in dependence of the gas cell length for two scans conducted at (a)  $n_1 = 3.4 \times 10^{18} \text{ cm}^{-3}$  and (b)  $n_2 = 7.7 \times 10^{18} \text{ cm}^{-3}$ . For each discrete length setting, 30 consecutive electron spectra are plotted as thin vertical lines. Red dots show the average cut-off energy<sup>1</sup> at each length, white dots show the average charge. Error bars show the respective shot-to-shot standard deviation. In (a), the gas cell was scanned between 3 mm and 14 mm in 1 mm steps. In (b), the scan range was 1.5 – 12 mm with uneven step sizes.

The electron energy evolution in dependence of the gas cell length is plotted in Fig. 6.4 for both densities. At each discrete cell length, the individual electron spectra of 30 consecutive shots are plotted as thin vertical lines. The average cut-off energy<sup>1</sup> at each length setting is shown in red, white dots show the average charge and error bars depict the shot-to-shot standard deviation. A clear difference in the evolution of the cut-off energies is found between the two scans. For the scan conducted at  $n_1$ , a stagnation of the cut-off energies is found for  $L \gtrsim 9$  mm. In contrast, the scan conducted at the higher plasma electron density  $n_2$  shows a different behaviour. After reaching the maximum cut-off energies at  $L = 5$  mm, further extension of the gas cell first leads to a strong decline in electron energies, followed by a region of less pronounced deceleration for  $L \gtrsim 8$  mm.

### Dephasing length

The scans permit to infer the respective electron dephasing length  $L_d$  from the measured energy spectra. Since in the nonlinear regime the longitudinal accelerating field  $E_z$  in the co-moving frame is well approximated by a linear slope (cf. subsection 2.3.3), the corresponding potential is of harmonic form. Once an electron gets injected at the rear side of the plasma cavity and is accelerated to relativistic velocities, it progresses towards the laser driver with a relative velocity of  $v \approx \beta c - v_{gr}$ . When reaching the middle of the plasma bucket where the electric field changes sign, it has travelled the dephasing length  $L_d$ , obtained the maximum kinetic energy and is subse-

1. The cut-off energy is defined as the highest energy for which the spectral charge density drops below 5 % of its maximum value.

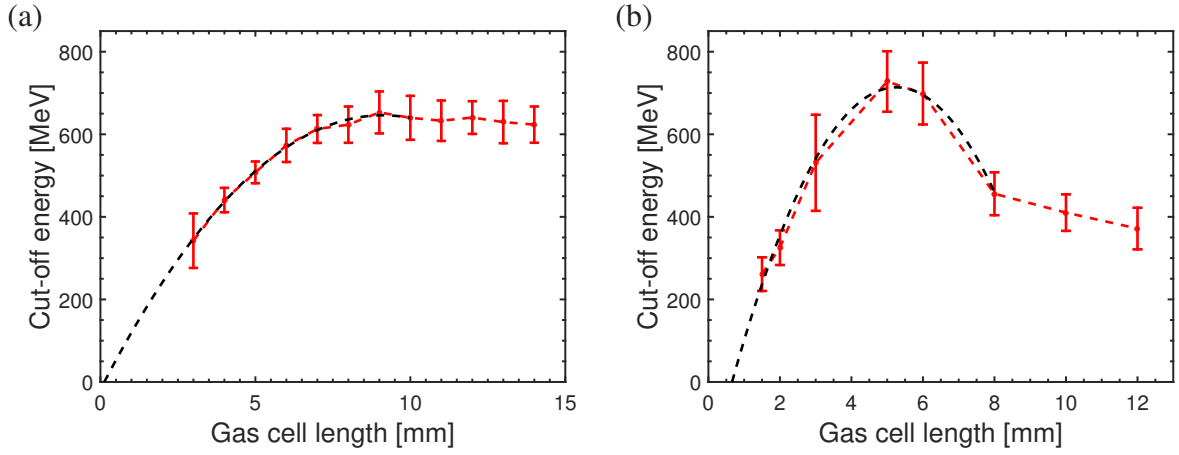


**Figure 6.5:** Evaluation of the dephasing length  $L_d$  from the evolution of the electron cut-off energies. Up to a certain gas cell length of (a) 10 mm and (b) 8 mm, the cut-off energies shown in Fig. 6.4 are well reproduced by a weighted nonlinear least-squares fit to a parabolic function, where the fit weights were given by the inverse shot-to-shot standard deviations. The relevant acceleration parameters are summarized in table 6.1.

quently decelerated again. Within the approximation of a static, linear electric field before laser depletion, its kinetic energy  $E$  in dependence of the acceleration length  $L_{acc}$  is given by

$$E = -1/2 e dE_z/dz (L_{acc} - L_d)^2 + E_{max} \quad (6.13)$$

where  $L_{acc} = L - L_{evo}$ . The latter denotes the length needed for evolution of the laser and wake-field properties before electron injection takes place. Figure 6.5 shows a fit of this model to the measured cut-off energies. For both scans the data points are well approximated by the fit and allow to deduce  $L_d$ . The fit parameters are summarized in table 6.1.

$n_0 [\text{cm}^{-3}]$	$L_d [\text{mm}]$	$E_{z,max} [\text{GV/m}]$	$E_{max} [\text{MeV}]$	$L_{evo} [\text{mm}]$
$3.4 \times 10^{18}$	$9.0 \pm 0.3$	$144 \pm 23$	$646 \pm 6$	$0.13 \pm 0.5$
$7.7 \times 10^{18}$	$4.6 \pm 0.2$	$310 \pm 83$	$714 \pm 34$	$0.66 \pm 0.6$

**Table 6.1:** Acceleration parameters obtained from a parabolic fit of the cut-off energies as shown in Fig. 6.5.  $L_{evo}$  denotes the gas cell length at which the fit curve crosses the  $E = 0$  axis, which corresponds to the position of electron injection and thus to the origin of the acceleration length  $L_{acc}$ . The peak accelerating field at this position is given by  $E_{z,max}$ . Error margins specify the  $1\sigma$  confidence interval.

$L_{evo}$  is determined by the crossing of the fit curve with the  $E = 0$  axis. For the  $n_2$  scan, its relatively large value, as compared to the lower density scan, indicates that a longer distance for laser evolution is required before electron injection occurs. Although such effects are not included in this simple model, it nevertheless shows a remarkable agreement with the energy evolution up to a certain value of  $L$ , once electrons have been injected into the wakefield.



## 6. Momentum and transverse spatial distribution of LWFA electron bunches from a length-variable gas target

---

### Laser pump depletion length

In both scans, after a certain gas cell length, the electron energies deviate from a parabolic curve and enter a regime characterized by a less significant energy variation. We therefore conclude that the electron bunch is no more subjected to a strong longitudinal electric field at this stage of the acceleration process. Thus, the laser intensity must have become too weak to drive a substantial plasma wave. Otherwise, a further energy gain or loss, the latter due to dephasing, would be expected.

While in the scan at  $n_1$  laser depletion approximately coincides with dephasing, this type of energy loss is observed at  $n_2$ . The adherence of the cut-off energies to a parabolic curve together with the high deceleration gradient indicate that in the  $n_2$  scan a laser-driven wakefield is still present after the dephasing length. Only for  $L \geq 8\text{mm}$  the curve flattens as the laser depletes. From Fig. 6.5, the laser pump depletion lengths  $L_{pd}$  are approximately given by  $L_{pd}(n_1) \sim 10\text{mm}$  and  $L_{pd}(n_2) \sim 8\text{mm}$ . Consequently, for longer gas cell lengths, the electron bunch is expected to co-propagate with the remnants of the diffracting laser pulse.

## 6.4 Comparison to theory

In the following sections we will now compare the experimentally observed behaviour with the theoretical description presented in chapter 2.

### Self-focused acceleration length

In vacuum, the waist of a Gaussian laser beam evolves by  $w = w_0 \sqrt{1 + (z/z_R)^2}$ , where  $w_0$  is the beam waist and  $z_R$  is the Rayleigh length given by  $z_R = \pi \omega_0^2 / \lambda$  [152]. For the  $f/22$  focusing geometry used in the experiment,  $z_R$  amounts to 1.37 mm. The measured energy evolution obviously shows that the effective acceleration distance greatly exceeds  $z_R$  and hence self-guiding plays an important role. This is to be expected, as the provided laser power of  $\sim 50\text{ TW}$  exceeds the critical power for self-focusing at the employed plasma electron densities, given by  $P_c(n_1) = 8.9\text{ TW}$  and  $P_c(n_2) = 3.6\text{ TW}$ , respectively (cf. eq. (2.109)).

To effectively accelerate electrons up to maximum electron energies, self-focusing has to be maintained over an acceleration length  $L_{acc}$  such that  $L_{acc} \sim L_d$ . By eq. (2.113), this is assured for an initial power of  $P_{L_d} = 1/8(\omega_L/\omega_p)^{6/5} P_c$ . For the two scans, the necessary power is given by  $P_{L_d}(n_1) = 47\text{ TW}$  and  $P_{L_d}(n_2) = 13\text{ TW}$ .

These values agree well with the experiment. For  $n_1$ , for which the laser power approximately equals  $P_{L_d}$ , the acceleration process terminates at  $L_{acc} \approx L_d$  since the remaining power is insufficient to maintain self-focusing over a longer distance, which would lead to electron dephasing. On the other hand, exactly this behaviour is observed at the higher plasma density  $n_2$ , as in this case the necessary power for self-focusing over  $L_d$  is greatly exceeded.

### Dephasing and depletion lengths

As outlined in chapter 2, expressions for  $L_{pd}$  and  $L_d$  can be derived from one-dimensional analytic theory and are functions of  $n_0$ ,  $\omega_L$  and  $a_0$ . Since the laser power provided in the experiment

$n_0[\text{cm}^{-3}]$	$P_{L_d}[\text{TW}]$	$a_{0,sf}$	$L_{pd,exp.}[\text{mm}]$	$L_{pd}[\text{mm}]$	$L_{d,exp.}[\text{mm}]$	$\frac{L_{d,nonlin.}}{L_{d,lin.}} [\text{mm}]$
$3.4 \times 10^{18}$	47	3.6	$\sim 10 \pm 1.5$	12.8	$9.0 \pm 0.3$	$\frac{12.9}{9.3}$
$7.7 \times 10^{18}$	13	4.7	$\sim 8 \pm 1.5$	3.7	$4.6 \pm 0.2$	$\frac{4.5}{2.4}$

**Table 6.2:** Comparison between the experimentally obtained values for the dephasing and depletion lengths and the theoretical predictions of 1D linear and nonlinear theory according to eq. (2.117) and eq. (2.119). The experimental value of  $L_{pd}$  is determined from the deviation of the cut-off energy evolution from a parabolic curve and is estimated to be accurate to within  $\pm 1.5$  mm.  $P_{L_d}$  denotes the initial laser power needed to maintain self-focusing over  $L_d$  and  $a_{0,sf}$  is the calculated peak laser vector potential after self-focusing to a matched spot size is reached.

exceeds  $P_c$ , an increase of  $a_0$  due to self-focusing as well as temporal pulse compression is to be expected and must be considered when determining the actual laser parameters present during wakefield excitation. However, these effects are not included in the analytic theory in which a non-evolving bullet-type driver is assumed.

Excluding temporal effects, the self-focused  $a_0$  can be roughly estimated by the following considerations. On the one hand, the evolution of the laser waist due to self-focusing is given by eq. (2.114):

$$\frac{w(z)^2}{w_0^2} = 1 + \left(1 - \frac{P}{P_c}\right) \frac{z^2}{z_R^2}.$$

On the other hand, a constant spot size is maintained if the matched condition of eq. (2.110),

$$k_p w = 2\sqrt{a_0(w)},$$

is satisfied. Neglecting energy loss due to pump depletion, the matched spot size and the resulting laser vector potential  $a_0$  can be obtained by numerically solving both equations.

The result is displayed in Fig. 6.6a for laser parameters of  $E = 1.5$  J,  $t_{FWHM} = 28$  fs and  $w_0 = 18.7 \mu\text{m}$  (as present in the experiment), corresponding to an initial  $a_0$  of 2.1. It is found that self-focusing leads to a significant enhancement of  $a_{0,sf}(n_1) = 3.6$  and  $a_{0,sf}(n_2) = 4.7$ . In both cases, the self-focused spot sized is reached within  $520 \mu\text{m}$  of propagation, such that the negligence of pump depletion is approximately accurate. Although this estimate can only serve as a lower bound for the actual  $a_0$  as it does not take into account temporal effects, it reflects the importance of laser self-modulation effects on the LWFA dynamics.

Once  $a_0$  is known, the pump depletion and dephasing lengths given by nonlinear 1D theory can be evaluated. A comparison of these with the experimentally determined values is given in table 6.2 and plotted in Fig. 6.6b, where the black line shows  $L_{pd}$  for a laser pulse with a Gaussian temporal profile in the limit of  $a_0 \gg 1$  (eq. (2.117)). The continuous and dashed blue lines depict the expressions for  $L_d$  in the nonlinear and linear regime, respectively. Note that in 1D theory  $L_d$  assumes a driver pulse with a square temporal profile<sup>1</sup>.

1. In nonlinear regime, the pump depletion length  $L_{pd}$  of a square driver also exactly coincides with  $L_d$  i.e.  $L_{pd,square} = L_{d,square}$  for  $a_0 \gg 1$  (cf. eq. (2.116) and eq. (2.119)).

## 6. Momentum and transverse spatial distribution of LWFA electron bunches from a length-variable gas target

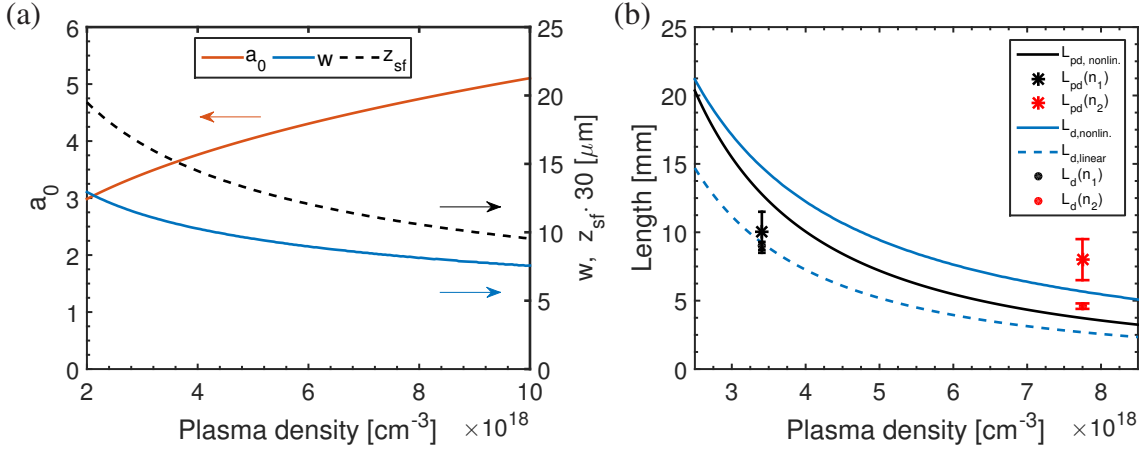


**Figure 6.6:** Depletion and dephasing lengths after laser self-focusing to a matched spot size. A laser pulse with  $E = 1.5 \text{ J}$ ,  $w_0 = 18.7 \mu\text{m}$  and  $t_{FWHM} = 28 \text{ fs}$  ( $a_0 = 2.1$ ) is assumed. (a) shows the resulting values of  $a_0$  and  $w$  after self-focusing to the matched spot size in dependence of the plasma density. The propagation distance needed to reach the matched spots size is given by  $z_{sf}$ . (b) shows  $L_{pd}$  and  $L_d$  as predicted by 1D theory together with the experimentally determined values.

### Discussion

For  $n_1 = 3.4 \times 10^{18} \text{ cm}^{-3}$ , the experimentally determined dephasing length  $L_d$  is in accordance with the prediction of linear theory and overestimated by nonlinear theory. In the latter, the experimental value of  $L_{d,exp.} = 9.0 \text{ mm}$  would require a reduced  $a_0 = 2.1$ . The root of this discrepancy may have different reasons: One possibility is a decreased laser energy in the main plasma channel, e.g. due to a non-Gaussian intensity distribution in the focal spot. Another possibility would be the injection of the electron bunch at an early stage of the self-focusing process, which could be triggered by oscillations of the beam waist due to a non-matched laser pulse which affects the nonlinear plasma wavelength and therefore the wake phase velocity and the trapping threshold according to eq. (2.100) and eq. (2.96). At this point,  $a_0$  and therefore  $\lambda_{p,nonlin.}$  may not have reached their peak values yet. For the higher plasma density  $n_2$ ,  $L_d$  approximately matches the nonlinear description.

Regarding laser depletion,  $L_{pd}$  is overestimated for  $n_1$  (by about  $\sim 30 \%$ ) and severely underestimated for  $n_2$ . However, it is important to note that eq. (2.117) is valid only in the limit of  $a_0 \gg 1$  and for pulse durations close to the linear resonant value of  $k_p t_{rms} = \sqrt{2}$ . The resonant pulse durations at the employed densities would be  $t_{FWHM}(n_1) \approx 32 \text{ fs}$  and  $t_{FWHM}(n_2) \approx 20 \text{ fs}$ . In the  $n_2$  scan, the relatively longer actual pulse duration of  $t_{FWHM} = 28 \text{ fs}$  may require an increased distance for laser etching to occur and therefore leads to a longer depletion length.

Although analytic theory provides a basic understanding of the acceleration dynamics, its application to predict experimental outcomes is not only hindered by the fundamental constraints of the one-dimensional treatment and the assumption of a static wake driver, but also by its strict validity for either the linear or the highly relativistic limit, while the experiment was performed with mildly relativistic laser pulses. Furthermore, the incomplete knowledge of the experimental

parameters due to the nonlinear processes occurring during pulse propagation adds to the uncertainty. In this regard, the values obtained for  $a_{0,sf}$  by the simple treatment presented above can only serve as a rough estimate. On the one hand,  $a_0$  may be well underestimated by the negligence of temporal effects, including self-compression (cf. section 2.6). On the other hand, intensity modulations of the beam profile in the focal region may lead to an energy loss in the main guiding channel. It also must be kept in mind that continuous laser depletion will further influence the acceleration dynamics.

## 6.5 Summary

- Low density case:  $n_1 = 3.4 \times 10^{18} \text{ cm}^{-3}$

In the low-density case, the power needed to maintain self-focusing and thus efficient wake generation up to  $L_d$  approximately equals the available laser power of  $\sim 50 \text{ TW}$ . Acceleration is therefore expected to stop at  $L \sim L_d$ , which agrees well with the experimental data. At  $L_{pd} \sim L_d$ , which matches 1D theory to within 30 %, the laser energy is depleted and no significant wakefields persist that could accelerate or decelerate the bunch. Thus, the electron bunch propagates undisturbed from a laser-induced wakefield. Only its own particle bunch-driven wakefield persists.

- High-density case:  $n_2 = 7.7 \times 10^{18} \text{ cm}^{-3}$

In the high-density case, the provided laser power exceeds the threshold needed to sustain self-focusing up to  $L_d$  by a factor of  $\sim 4$ . The scan of the electron energies presented in Fig. 6.4b clearly shows that an energetic laser pulse is still present beyond the dephasing length, as electrons are strongly decelerated for  $L > L_d$ . This implies  $L_{pd} > L_d$ , although this observation contradicts 1D theory. Apart from the shortcomings of 1D theory, this might be attributed to the non-resonant laser pulse length of  $t_{FWHM} = 28 \text{ fs}$ , while the optimal pulse duration would be  $t_{FWHM}(n_2) \sim 20 \text{ fs}$ , and lead to a significantly longer pump depletion length. Moreover, the pulse evolution driven by nonlinear effects can alter the pulse shape, and hence  $a_0$  during propagation in plasma of up to 8 mm.



---

## Chapter 7

# Characterisation of the longitudinal bunch profile by CTR

### 7.1 Single-shot bunch profile reconstruction

The setup and methods presented so far allow for the single-shot characterisation of the longitudinal bunch profile. In this section, the required steps are exemplary elaborated and discussed in detail.

Experimental data of the electron bunch diagnostics for two representative shots is presented in Fig. 7.1. The electron energy information, i.e the raw images of the scintillating screen together with the evaluated energy spectra, is shown in Fig. 7.1a and b. The measured CTR spectra, containing the data acquired by all three spectrometers, are displayed in Fig. 7.1c and d. Depending on the experimental conditions, the CTR spectra were found to be either mostly smooth (Fig. 7.1c) or contain a dominant single frequency modulation (Fig. 7.1d). The latter can be attributed to a double bunch structure being generated. The information contained in this feature will be discussed in the next section.

Plotted on a logarithmic y-axis, the insets of Fig. 7.1c, d further show that the spectral energy of CTR throughout the measured spectral range is more than 7 orders of magnitude above the level of incoherent TR (shown in grey) expected from the measured electron energy spectrum, which confirms the coherent nature of the radiation. Additional tests were performed to ensure that the measured signal is indeed CTR. First, when lowering the gas pressure in the cell such that the plasma density was too low for wave breaking to occur, no electron beam was generated and accordingly no CTR signal recorded. Second, under normal operating conditions, when placing a band-pass filter (Si-WBP, 8.0 – 14.0  $\mu\text{m}$ , by InfraTec [148]) in the CTR beam path, the signal was limited to the accordant wavelength range. Both tests allow to exclude the possibility of measurement artefacts due to parasitic electromagnetic pulses induced by the high peak current of the accelerated electron beam and confirm that the steel tapes together with the surrounding stray light shielding were opaque for the main laser pulse or any type of plasma glow.

The data shown in Fig. 7.1 contains all the necessary information to retrieve the longitudinal bunch profile. Recalling eq. (5.11), the modulus of the longitudinal form factor is related to the

## 7. Characterisation of the longitudinal bunch profile by CTR

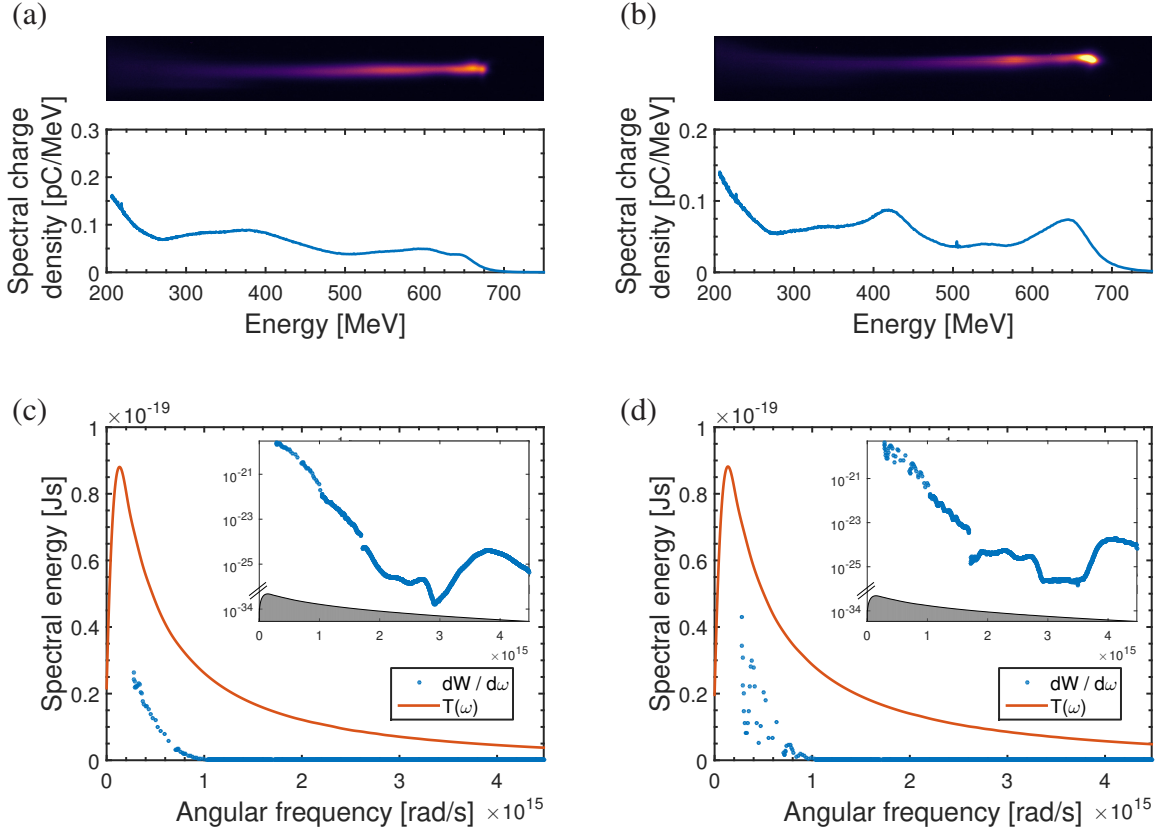


**Figure 7.1:** Single-shot data of the electron bunch diagnostics for two representative shots for gas cell lengths of 9 mm (left column) and 13 mm (right column). (a) and (b) show the respective raw image of the scintillator screen S2 behind the dipole magnet along with the evaluated electron energy spectrum. (c) and (d) show the respective **CTR** spectral energy measured by the three spectrometers (blue) and the transmission  $T'(\omega)$  of an infinitely short bunch with  $F_{\parallel}(\omega) = 1$ . The inset shows the measured spectral **CTR** energy and the expected amount of incoherent **TR** (grey), plotted on a logarithmic scale.

measured quantities by

$$|F_{\parallel}(\omega)| = \sqrt{\frac{dW/d\omega}{2\epsilon_0 c N^2 \left| \int g(\mathbf{p}) T(\omega, \mathbf{p}) \mathbf{E}(\omega, \mathbf{p}) F_{\perp}(\omega) d\mathbf{p} \right|^2}}. \quad (7.1)$$

The electron energy information, shown in Fig. 7.1a, b, is used as an input to calculate the denominator of eq. (7.1) as described in chapter 5,

$$T'(\omega) = 2\epsilon_0 c N^2 \left| \int g(\mathbf{p}) T(\omega, \mathbf{p}) \mathbf{E}(\omega, \mathbf{p}) F_{\perp}(\omega) d\mathbf{p} \right|^2. \quad (7.2)$$

$T'(\omega)$  describes the spectral energy of **CTR** that would be incident in the detection plane in the case of full coherence (i.e.  $F_{\parallel}(\omega) = 1$ ). For comparison, the transmission  $T'(\omega)$  is depicted in red alongside the measured **CTR** spectra (shown with blue markers) in Fig. 7.1c and d.



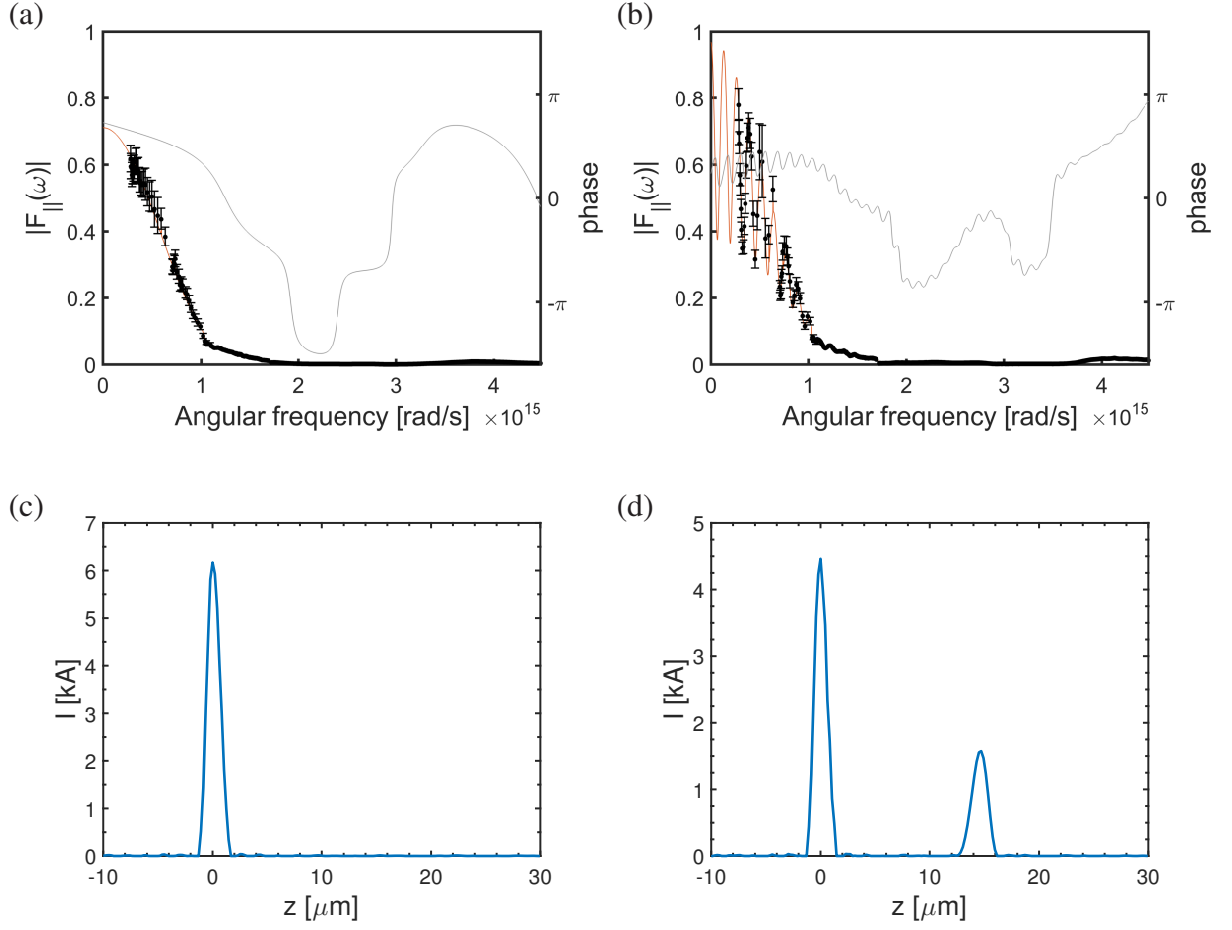


**Figure 7.2:** Measured and reconstructed longitudinal form factor  $|F_{\parallel}(\omega)|$  and reconstructed bunch profiles  $I(z)$  for the two shots presented in Fig. 7.1. (a) and (b) show the measured (black dots) and reconstructed (red) form factor and the reconstructed spectral phase (grey). Error bars depict the measurement uncertainty of the mid-infrared spectrometer (as described in Appendix A.1). The respective reconstructed longitudinal bunch profiles are shown in (c) and (d).

### Bunch profile retrieval

According to eq. (7.1), the form factor  $|F_{\parallel}(\omega)|$  is now obtained by taking the root of the measured CTR spectrum divided by  $T'(\omega)$ , shown by black data points in Fig. 7.2a and b, respectively. The Bubblewrap retrieval algorithm is then run on the measured values of the form factor to retrieve the longitudinal bunch profile for each shot. The resulting reconstructed form factors and bunch profiles are shown in Fig. 7.2a, b (red lines) and Fig. 7.2c, d, respectively.

### Spectral modulations

Depending on the experimental conditions, the recorded CTR spectra were found to exhibit strong spectral modulations (cf. Fig. 7.1d and Fig. 7.2b). These modulations are spectral interference fringes that are characteristic of multi-bunch structures and contain information about

## 7. Characterisation of the longitudinal bunch profile by CTR

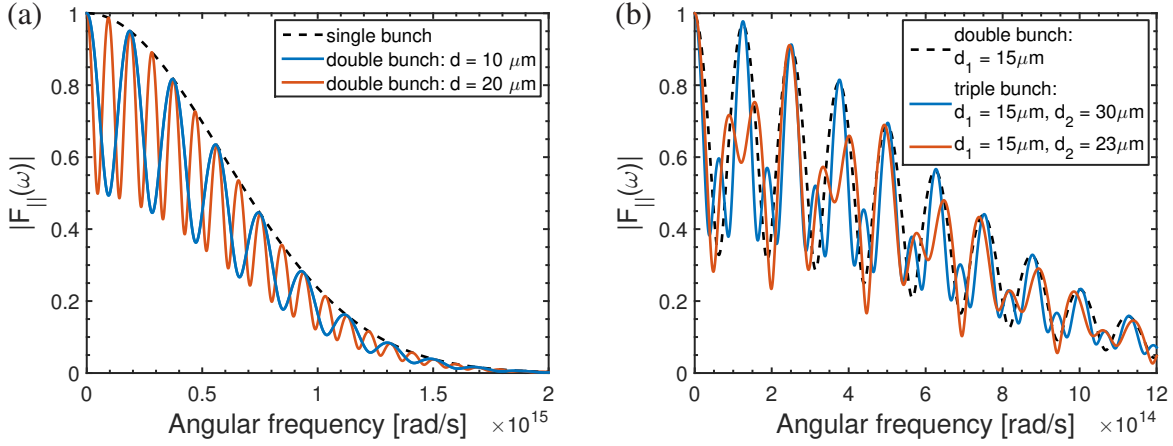


**Figure 7.3:** Longitudinal form factors of multi-bunch structures with Gaussian shape and equal bunch durations. (a) shows a comparison between the form factor of a single bunch and double bunches with different inter-bunch distances. For double bunches, the charge ratio between both bunches is fixed at  $q_1 = 3q_2$  and the form factor does not reach zero even for fully destructive interference. (b) shows the form factors of double and triple bunches with varying separations. Due to the spectral beating of more than one oscillation frequency, form factors containing more than two bunches generally exhibit a more complex shape. The charge ratio is  $q_1 = 3q_2 = 3q_3$ .

the individual bunch shapes and spacings. In the following, the effect of multiple bunches, their bunch separation, charge ratio and duration on the form factor will be elaborated.

In the simple case where the longitudinal bunch profile consists of two individual bunches separated by a distance  $d$ , the form factor can be expressed by

$$|F(\omega)| = \left| q_1 f_1(\omega) + q_2 f_2(\omega) e^{-\frac{id\omega}{c}} \right|. \quad (7.3)$$

Here  $q_{(1,2)}$  denotes the fraction of the charge contained in each bunch,  $d$  is the inter-bunch distance and  $f_{(1,2)}(\omega)$  is the respective Fourier transform of  $\rho_{(1,2)}(z)$ . For simplicity, we first assume two bunches of Gaussian shape with the same profile  $\sigma_1 = \sigma_2$  but different charge. Each bunch produces a smooth spectrum, but due to the time of flight difference the emitted CTR spectrum is modulated by interference. From eq. (7.3) it is readily seen that the oscillation frequency is directly related to the bunch separation by  $\Delta\omega = 2\pi c/d$ . This case of a single frequency modulation is depicted in Fig. 7.3a. In contrast, bunch trains consisting of more than two bunches lead to more complex form factors that contain more than one oscillation frequency due to the spectral beating between CTR emitted by the individual bunches, as shown in Fig. 7.3b.

### Fringe visibility

While the bunch separation determines the oscillation frequency, the charge ratio and the individual bunch durations are encoded in the fringe visibility  $V(\omega)$ . The latter can be defined by the minimum and maximum value of the form factor and, for the case of two Gaussian bunches, is

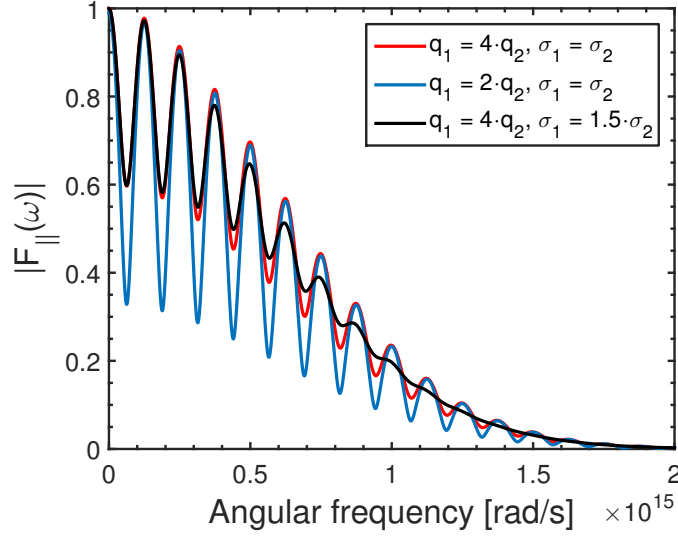


**Figure 7.4:** Effects of charge ratio and bunch duration on the form factor of a double bunch structure. For equal bunch shapes, the fringe visibility is only dependent on the charge ratio. For different bunch durations (or different transverse form factors), the lower spectral energy radiated by the longer bunch reduces the fringe visibility at higher frequencies. Nevertheless, the charge ratio can still be determined from  $V(\omega \rightarrow 0)$ .

given by [27]

$$V(\omega) = \frac{F_{\max} - F_{\min}}{F_{\max} + F_{\min}} = \frac{2\xi(\omega)}{1 + \xi(\omega)^2}, \quad (7.4)$$

where  $\xi$  denotes the ratio of the individual form factors

$$\xi = \frac{q_2 f_2(\omega)}{q_1 f_1(\omega)} = \frac{q_2}{q_1} e^{0.5(\sigma_{\parallel,1}^2 - \sigma_{\parallel,2}^2)\omega^2} e^{0.5(\sigma_{\perp,1}^2 - \sigma_{\perp,2}^2)\sin^2\theta\omega^2/c^2}. \quad (7.5)$$

The dependence of  $V(\omega)$  on  $q_{(1,2)}$  as well as  $\sigma_{(1,2)}$  is sketched in Fig. 7.4. For equal bunch duration and transverse size ( $\sigma_1 - \sigma_2 = 0$ ), both bunches radiate a **CTR** spectrum of equal shape and the fringe visibility is only dependent on their charge ratio. For such bunches, the charge ratio can be directly deduced from the fringe visibility. In general, this finding is not limited to the assumption of a specific (i.e. Gaussian) shape.

As seen from eq. (7.5), the fringe visibility for double bunches of different duration or transverse size ( $\sigma_1 - \sigma_2 \neq 0$ ) acquires an additional  $\omega$  dependence, caused by the interference of **CTR** spectra of different shape. With increasing frequency  $\omega$ , the longer (or transversely broader) bunch emits a relatively lower amount of **CTR**, which leads to a reduction of  $V(\omega)$ , manifested by a wash-out of the interference fringes as depicted in Fig. 7.4. Nevertheless, for such bunches, the charge ratio can be approximately determined from the fringe visibility at  $\lim_{\omega \rightarrow 0} V(\omega)$ .

### 7.2 Temporal evolution of the longitudinal bunch profile

With the presented reconstruction technique, the temporal bunch profile can be determined in dependence of the acceleration parameters. Here, the single-shot measurement allows to quantify shot-to-shot fluctuations and is beneficial to avoid disturbances in the measured CTR spectrum that are inherent to scanning techniques. We now focus on the CTR measurements that were recorded simultaneously with the electron energy spectra presented in section 6.3. Based on the length tunability of the gas cells, these measurements allow for the first time to observe the evolution of the temporal bunch profile after different stages of the acceleration process. In the following, both length scans taken at different plasma electron densities will be discussed successively.

#### 7.2.1 Bunch evolution at $n_1 = 3.4 \times 10^{18} \text{ cm}^{-3}$

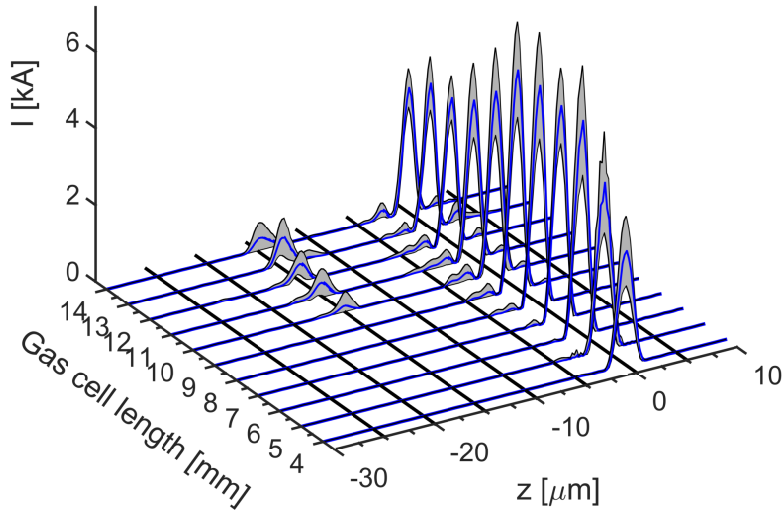


**Figure 7.5:** Bunch profile evolution at a plasma electron density of  $n_1 = 3.4 \times 10^{18} \text{ cm}^{-3}$ . The plot shows the mean retrieved bunch profiles at the different length settings of the gas cell averaged over 30 consecutive shots. The grey band shows  $\pm 1\sigma$ , where  $\sigma$  is the shot-to-shot standard deviation of each 30-shot dataset.

The average of the retrieved longitudinal bunch profiles at each discrete settings of the gas cell length scan conducted at  $n_1 = 3.4 \times 10^{18} \text{ cm}^{-3}$  is shown in Fig. 7.5. The grey band shows the shot-to-shot standard deviation of each 30-shot dataset. The scan reveals two qualitatively different regimes. For short gas cell lengths in the range of  $L \leq 9 \text{ mm}$ , a dominant single electron bunch is observed. In this regime, the CTR spectra generally exhibit a smooth shape, similar to that presented in Fig. 7.2a. The electron beam cut-off energy is maximized at a cell length of  $L = 9 \text{ mm}$ , at which  $E_{\text{cutoff}} = 653 \pm 51 \text{ MeV}$  and a charge of  $Q = 29 \pm 6 \text{ pC}$  is obtained. At this length, we find an average bunch duration of  $t_{\text{FWHM}} = 4.8 \pm 0.2 \text{ fs}$  and a peak current of

Authors	$n_0[\text{cm}^{-3}]$	$t_{FWHM}[\text{fs}]$	$I_{peak}[\text{kA}]$	$Q[\text{pC}]$	$E_{max}[\text{MeV}]$	$\Delta E[\text{MeV}]$
Buck et al. [22]	$3.2 \times 10^{19}$	$5.8^{+1.9}_{-2.1}$	N/A	$2.3 \pm 1.8$	$19.2 \pm 6.7$	$2.3 \pm 1.9$
Lundh et al. [21]	$1 \times 10^{19}$	$3.3 - 4.2$	$3 - 4$	$15 \pm 7$	$84 \pm 21$	$21 \pm 17$
current study	$3.4 \times 10^{18}$	$4.8 \pm 0.2$	$5.7 \pm 1.2$	$29 \pm 6$	$653 \pm 51$	(100%)

**Table 7.1:** Comparison with selected publications in which the bunch duration of LWFA electron beams was determined experimentally, either by a spectral measurement of CTR (Lundh et al. [21]) or by detecting the rotated polarisation of a probe beam due to the Faraday effect induced by the magnetic field of the relativistic electron bunch (Buck et al. [22]).

$5.7 \pm 1.2 \text{ kA}$ . The values are in agreement with those reported by other authors. A summary of comparable data taken from selected publications is given in table 7.1.

A different regime is found for  $L > 9 \text{ mm}$ , for which the retrieved bunch profiles reveal the emergence of a distinct 2<sup>nd</sup> electron bunch. The latter is separated by  $d = 14.9 \pm 0.5 \mu\text{m}$  from the dominant bunch. This is close to, albeit smaller than one plasma wavelength, which for a linearly driven wake is  $\lambda_p(n_1) = 18.1 \mu\text{m}$ . If driven nonlinearly by a pulse with  $a_0 > 1$ ,  $\lambda_{p,nonlin.}$  would only exceed this value due to the plasma electrons' relativistic mass increase and concomitant period lengthening of the wakefield. In either case, the retrieved bunch separation is thus smaller than one wakefield period.

Note that since the spectral phase of the CTR has not been measured directly, the time direction of the retrieved bunch profiles is ambiguous. Given that the bunch profile is a real-valued function, a time reversal of the bunch profile ( $\rho_{||}(t) \rightarrow \rho_{||}(-t)$ ) would produce the same CTR spectral amplitudes since  $|\mathcal{F}[\rho_{||}(-t)]| = |\overline{F_{||}(\omega)}| = |F_{||}(\omega)|$ . Therefore, the Bubblewrap algorithm reconstructs the same bunch profile for both cases. However, the dominant bunch is expected to be preceding, as the normal bunch formation processes by nonlinear wave breaking usually leads to injection at the rear side of a plasma cavity. It therefore appears highly unlikely that a 2<sup>nd</sup> bunch could be formed in front of the accelerated bunch. To our knowledge, such a scenario has also never been observed in PIC simulations.

### Evolution of the bunch parameters

We will now have a closer look at the bunch properties. Apparently, the emergence of the 2<sup>nd</sup> bunch is either linked to the point of laser pump depletion ( $L_{pd} \sim 10 \text{ mm}$ ) or electron dephasing ( $L_d \approx 9 \text{ mm}$ ). This can be deduced from Fig. 7.6a, which shows the evolution of the cut-off energies alongside the probability  $P_{2nd}$  that a 2<sup>nd</sup> bunch is found<sup>1</sup>. The probability of observing a double bunch structure is only  $P_{2nd} > 0$  for cell lengths  $L \geq 10 \text{ mm}$  and reaches a maximum of  $P_{2nd} = 93 \%$  at  $L = 13 \text{ mm}$ . Correspondingly, the shape of the CTR spectrum changes when the gas cell length is increased beyond  $L \geq 10 \text{ mm}$ . In this regime, the CTR spectra exhibit an intensity oscillation, dominated by a single frequency modulation similar to the example presented

1. The bunch profile is defined to contain two bunches if the peak current of the 2<sup>nd</sup> bunch exceeds 5 % of that of the dominant bunch.

## 7. Characterisation of the longitudinal bunch profile by CTR

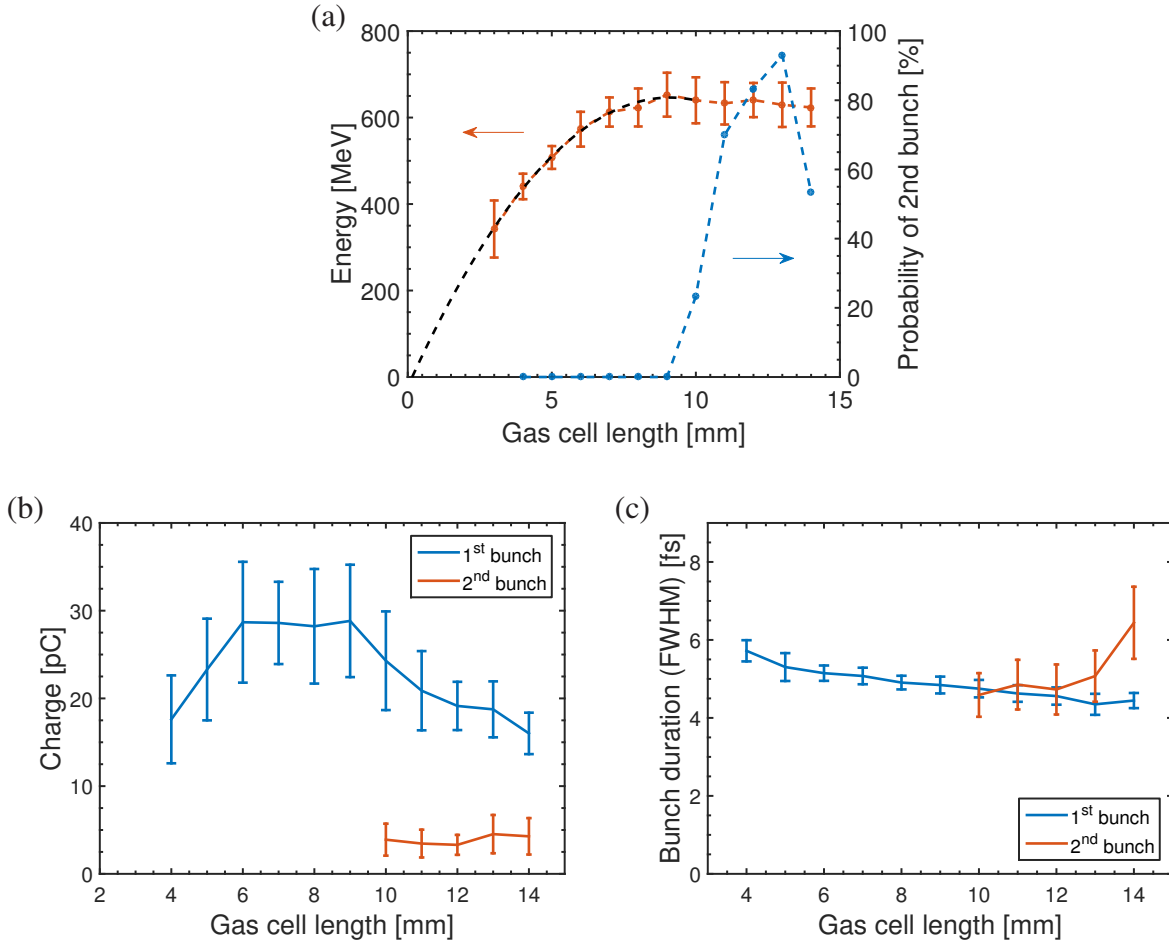


**Figure 7.6:** Evolution of the electron beam parameters in dependence of the gas cell length at a plasma density of  $n_1 = 3.4 \times 10^{18} \text{ cm}^{-3}$ . (a) shows the evolution of the electron cut-off energies along with the probability that a 2<sup>nd</sup> bunch is observed in the retrieved profile. (b) shows the charge contained in the 1<sup>st</sup> and 2<sup>nd</sup> bunch if the latter is present. The respective FWHM durations of both bunches are shown in (c). Error bars display the shot-to-shot rms fluctuation in each quantity at a specific gas cell length.

in Fig. 7.2b. The modulation frequency is consistent with the bunch separation retrieved by the Bubblewrap algorithm.

### Charge

The evolution of the charge contained in both bunches is plotted in Fig. 7.6b. The charge fraction of each bunch was obtained by integrating the normalized longitudinal charge distribution  $\rho_{\parallel}(z)$  over their respective extent, whereas the total charge  $Q$  was determined from the electron spectrometer. Note that due to the low energy cut-off of the electron spectrometer only electrons with energies  $E > 200 \text{ MeV}$  can be observed. Thus, the detected charge increases along with the cut-off energy and the data points for cell length  $L \lesssim 7 \text{ mm}$  are influenced by this effect. Nevertheless, for cell length  $L \gtrsim 8 \text{ mm}$ , the detected charge should be a constant fraction of the total bunch charge, as the spectrum is broadband and the cut-off energies are approximately constant.

However, for  $L \geq 9$  mm, the dominant bunch continuously loses charge and the emerging 2<sup>nd</sup> bunch contains a charge of  $5.5 \pm 2.7$  pC that is approximately constant within the error bars.

### Bunch durations

The individual **FWHM** bunch durations are depicted in Fig. 7.6c. The duration of the main bunch is found to slightly decrease from  $5.7 \pm 0.3$  fs at  $L = 4$  mm to a minimum value of  $4.3 \pm 0.3$  fs at  $L = 13$  mm. However, as before, data for cell lengths of  $L \lesssim 7$  mm must be regarded as less significant, as a larger fraction of charge resides outside the detection window of the electron spectrometer. The unknown part of the electron spectrum leads to a less accurate determination of the transmission function  $T'(\omega)$  and respectively the form factor. In the range of cell lengths with  $L \geq 7$  mm, the **FWHM** bunch duration can be regarded as roughly constant within the error bars with a mean value of  $4.7 \pm 0.3$  fs.

Within the range of its occurrence, the 2<sup>nd</sup> bunch shows a trend towards longer bunch durations with increasing  $L$ . Especially for  $L = 14$  mm its duration is significantly increased. Within the error bars and between  $L = 10 - 13$  mm, its duration is roughly constant with a mean value of  $t_{FWHM} = 4.8 \pm 0.7$  fs that is comparable to that of the 1<sup>st</sup> bunch.

### Measurement reliability

The error margins given so far specify the shot-to-shot **rms** error. The following section will comment on the measurement reliability and the error of a single-shot measurement.

In general, the spectral resolution in the visible and near-infrared region allows to resolve the spectral oscillation and fringe visibility with high accuracy. In contrast, the sparse number of sampling points and uneven frequency spacing in the mid-infrared region is not always sufficient to fully resolve these modulations.

- As the modulation frequency is typically constant throughout the measured spectral range, the bunch separation can also be determined from the spectral region sampled with high resolution by the visible and the near-infrared spectrometer. It is found that the bunch separation retrieved by the **Bubblewrap** algorithm agrees with these values to within  $\lesssim 0.1 \mu\text{m}$ .
- The total charge contained in the electron beam is determined from the fluorescence signal of the electron spectrometer's calibrated scintillator screen, but can also be roughly evaluated from the detected **CTR** intensity. The electron spectrometer reliably detects the number of electrons with energies above the detection limit. On the other hand, the **CTR** intensity may be lower due to pointing fluctuations of the beam stemming from fluctuations of the electron beam pointing ( $\sim 1.5$  mrad **rms**). Furthermore, the charge determined from the **CTR** intensity is calculated from  $\int \rho_{\parallel}(z) dz = F_{\parallel}(0)$  and thus relies on the reconstruction of the form factor at  $\omega = 0$ . In addition, electrons with energies below the detection limit contribute to the **CTR** intensity but are not detected by the electron spectrometer such that the determination of the transmission function  $T'(\omega)$  becomes less accurate. Nevertheless, the total charge detected by both methods agrees with each other within  $85 \pm 25$  %, where the **CTR** signal is usually slightly less than expected.
- In the case of a double bunch, the charge ratio between both bunches is given by the fringe visibility at  $\omega \rightarrow 0$ . As in this region the **CTR** spectral amplitudes have not been measured,



## 7. Characterisation of the longitudinal bunch profile by CTR

---

this ratio depends on the reliability of the reconstruction algorithm. In addition, the low sampling rate in the mid-infrared region can lead to an undersampling of the oscillation such that the reconstruction algorithm may underestimate the actual charge ratio.

- In the case of a single bunch, the accuracy of the retrieved bunch duration is limited by the measurement uncertainty in the spectral domain. The different sources contributing to this uncertainty are described in Appendix A.1. Since the measured spectrum and the bunch profile are related by a Fourier transform, a direct (analytic) calculation of the uncertainty in the retrieved bunch profile is not possible. Instead, the error in the time domain is assessed by retrieving the bunch profiles from CTR spectra corresponding to the upper and lower error margins for exemplary shots, as described in Appendix A.2. It was found that the uncertainty in the spectral domain translates to an uncertainty in bunch duration of  $\sim 0.3$  fs for spectra that correspond to bunch durations on the order of 4.5 fs. The relative error is therefore  $\lesssim 7\%$ . As previously shown in subsection 3.2.4, an additional relative error of  $< 15\%$  is due to a possible energy chirp in longitudinal phase space and the effect of free space propagation from the exit of the gas cell to the CTR radiator. The error in determination of the bunch duration is thus  $\lesssim 22\%$ .
- The bunch duration of the 2<sup>nd</sup> bunch is determined by the fringe visibility  $V(\omega)$  as described in section 7.1. Hence, as the form factor decreases with increasing  $\omega$ , the measurement uncertainty of the quotient  $q_2 f_2 / q_1 f_1$  increases and introduces a larger error in the duration of the 2<sup>nd</sup> bunch. Additionally, the sparse sampling points at low frequency may introduce an error by underestimating  $V(\omega)$  and therefore the charge ratio  $q_2 / q_1$ .

These statements show that the properties of the 2<sup>nd</sup> bunch are afflicted by a relatively larger error margin. Since there is no analytical treatment to transfer the error margins into the time domain, these could only be assessed by retrieving the bunch profile for all possible CTR spectra that are located within the measurement uncertainty. This is impossible due to the large computational effort that would be required for each single-shot measurement. However, for a large series of shots, the existing shot-to-shot fluctuations intrinsically sample the measurement uncertainty. For this reason, the relative shot-to-shot error in the bunch duration and charge of the 2<sup>nd</sup> bunch is larger compared to that of the dominant bunch (cf. Fig. 7.6).

### 7.2.2 Bunch evolution at $n_2 = 7.7 \times 10^{18} \text{ cm}^{-3}$

Before discussing the acceleration dynamics, it is helpful to compare the bunch evolution presented above to that obtained from the length scan conducted at the plasma density of  $n_2 = 7.7 \times 10^{18} \text{ cm}^{-3}$ . In contrast to the scan conducted at  $n_1$ , in this scan the injection probability was  $< 100\%$ . Thus, in contrast to the data set presented above, at each length setting a subset of the best 80 % of 30 consecutive shots (in terms of charge, corresponding to 24 shots at each length) was taken into account. Additionally, due to the on average much higher injected charge, the mid-infrared spectrometer saturated for some shots, which were excluded as well.

The average longitudinal bunch profile obtained from this data set is shown in Fig. 7.7. Similar to the behaviour found at  $n_1$ , a 2<sup>nd</sup> electron bunch emerges after a certain gas cell length. Analogous to the low-density case, additional insight is obtained by relating the bunch profile evolution with the respective energy evolution, as shown in Fig. 7.8a. In contrast to the scan at lower plasma

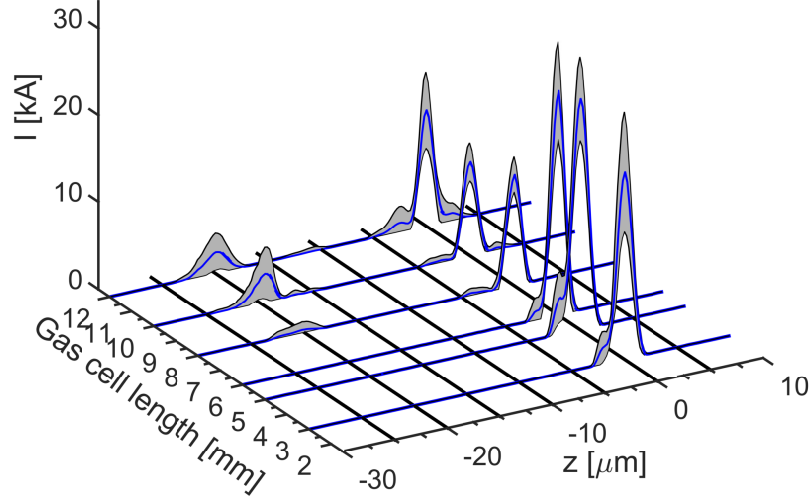


**Figure 7.7:** Bunch profile evolution at a plasma electron density of  $n_2 = 7.7 \times 10^{18} \text{ cm}^{-3}$ . Blue lines show the average retrieved bunch profile at the different length settings of the gas cell for a subset of the best 80 % out of 30 consecutive shots. Additionally, shots with saturated *CTR* spectra were excluded from the data set. The grey band shows the *rms* shot-to-shot fluctuations of the bunch profile at each length setting of the gas cell.

density, this scan exhibits a distinct maximum in the electron energy evolution for  $L = 5 \text{ mm}$ , at which an average bunch duration of  $t_{FWHM} = 5.8 \pm 0.2 \text{ fs}$ , a peak current of  $27 \pm 5 \text{ kA}$ , a cut-off energy of  $E_{cutoff} = 730 \pm 58 \text{ MeV}$  and a charge of  $Q = 174 \pm 33 \text{ pC}$  is obtained.

As seen from Fig. 7.8a, the 2<sup>nd</sup> bunch is not yet observed during the following onset of the decline of the electron energies, but only once the gas cell is extended to  $L \geq 8 \text{ mm}$  for which the energy evolution is characterized by a less significant energy loss. As discussed in section 6.3, this regime is attributed to cell lengths that exceed the pump depletion length ( $L \gtrsim L_{pd}$ ), where the bunch is no longer exposed to a laser-driven wakefield.

These findings bear similarities, but also complement those observed at  $n_1$ . Because in the latter it was found that  $L_d \sim L_{pd}$ , it was not possible to link the emergence of a 2<sup>nd</sup> bunch to either electron dephasing or laser pump depletion, whereas the present scan reveals that the emergence of the 2<sup>nd</sup> bunch occurs between  $L_d$  and  $L_{pd}$ .

The evolution of the individual charge and the bunch durations is plotted in Fig. 7.8b and c. Due to the strong variations in cut-off energy between the individual length settings, the charge determined from the electron spectrometer is affected by the undetected part of the spectrum with energies below the detection limit. Consequently, the amount of detected charge correlates strongly with the electron cut-off energies and is of less significance.

Nevertheless, the *FWHM* bunch durations show the same qualitative behaviour as in the low-density case, with an approximately constant bunch duration of the main bunch and a slightly increased duration of the emerging bunch. Quantitatively, their average durations are found to

## 7. Characterisation of the longitudinal bunch profile by CTR

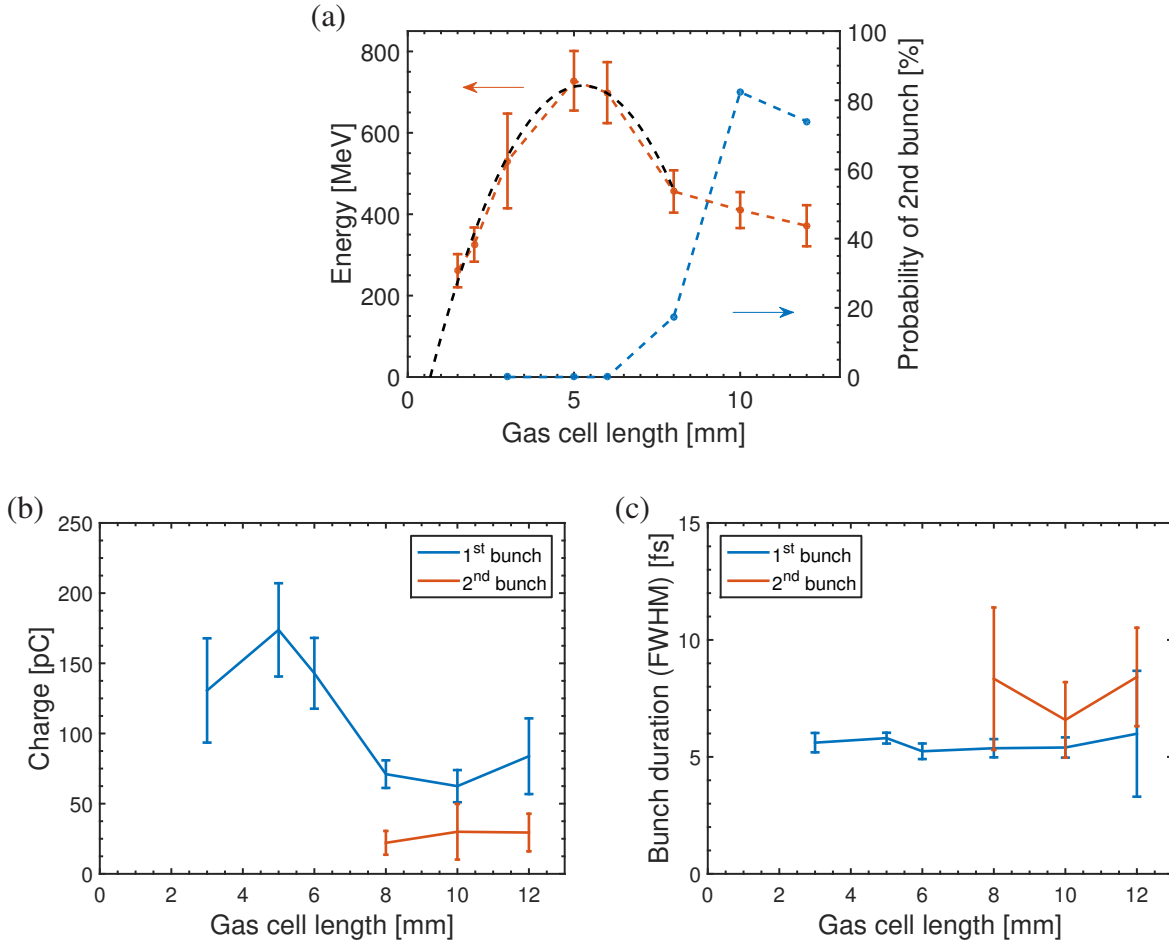


**Figure 7.8:** Evolution of the electron beam parameters in dependence of the gas cell length at a plasma density of  $n_1 = 7.7 \times 10^{18} \text{ cm}^{-3}$ . (a) shows the evolution of the electron cut-off energies along with the probability that a 2<sup>nd</sup> bunch is observed in the retrieved profile. (b) shows the charge contained in the 1<sup>st</sup> and 2<sup>nd</sup> bunch if the latter is present. The respective *FWHM* durations of both bunches are shown in (c). Error bars display the shot-to-shot *rms* fluctuation in each quantity at a specific gas cell length.

be larger than those found at  $n_1$ , with *FWHM* values of  $5.6 \pm 1.4 \text{ fs}$  and  $7.8 \pm 2.2 \text{ fs}$ , respectively. In the  $n_2$  scan, the mean charge contained in the 2<sup>nd</sup> bunch is significantly higher with  $Q_{2nd} = 27 \pm 16 \text{ pC}$ .

Besides the maximum in the energy evolution, one striking difference to the low-density case is the bunch separation  $d$ . The linear plasma wavelength corresponding to the electron density determined from the nominal applied backing pressure is given by  $\lambda_p(n_2) = 11.5 \mu\text{m}$ , while a bunch separation of  $d = 20.0 \pm 0.5 \mu\text{m}$  is found. Hence, at  $n_2$ , the bunch separation exceeds the length scale set by  $\lambda_p$ , while in the low-density case  $d < \lambda_p$ . For comparison, the measured quantities of both scans are summarized in table 7.2.

$n_0$ [cm <sup>-3</sup> ]	$3.4 \times 10^{18}$	$7.7 \times 10^{18}$
$\lambda_p$ [μm]	18.1	12.0
$d$ [μm]	$14.9 \pm 0.5$	$20.0 \pm 0.5$
$L_{pd,exp.}$ [mm]	$\sim 10$	$\sim 8$
$L(P_{2nd} > 0)$ [mm]	$\geq 10$	$\geq 8$
$t_{FWHM, 1st}$ [fs]	$4.7 \pm 0.3$	$5.6 \pm 1.4$
$t_{FWHM, 2nd}$ [fs]	$4.8 \pm 0.7$	$7.8 \pm 2.2$
$Q_{1st}$ [pC]	$29 \pm 6$	$174 \pm 33$
$Q_{2nd}$ [pC]	$4 \pm 2$	$27 \pm 16$
$n_b/n_0$	$\sim 6.1$	$\sim 5.5$

**Table 7.2:** Overview of the key parameters of both length scans. Specified error margins denote the shot-to-shot standard deviations.  $\lambda_p$  is the linear plasma wavelength expected at the applied backing pressure.  $L(P_{2nd} > 0)$  denotes the range of gas cell lengths for which secondary bunches are observed.  $n_b/n_0$  gives the ratio of the peak charge density of the first bunch over the plasma density at the point of laser pump depletion.

### 7.2.3 Discussion

Both scans show a similar behaviour in the bunch profile evolution, where a 2<sup>nd</sup> bunch is formed for acceleration lengths that exceed the dephasing length  $L_d$ . While in the low-density scan  $L_d \sim L_{pd}$ , the  $n_2$  scan allows to separate both length scales and shows that injection occurs between  $L_d \lesssim L \lesssim L_{pd}$ . Thus, injection of a 2<sup>nd</sup> bunch becomes possible after electron dephasing and is likely supported by laser energy depletion.

For  $L \gtrsim L_{pd}$ , the cut-off energies deviate from a parabolic evolution and are characterized by a stagnation ( $n_1$ ) or slight energy decrease ( $n_2$ ). In this regime, the nearly constant electron energies are evidence that the bunch is not exposed to a longitudinal electric field any more and the remaining laser intensity is insufficient to excite a significant wakefield. However, even a fraction of the initial laser energy is sufficient to provide a fully ionized plasma (cf. section 2.2). It is therefore safe to assume that the electron bunch propagates through fully ionized plasma.

As outlined in section 2.3, an electron bunch of sufficient charge density can drive its own wakefield and even excite a nonlinear plasma wave in the blowout regime. A simple assessment of the charge density shows that these densities are indeed reached in the experiment. Assuming a Gaussian transverse profile, the peak beam density  $n_b$  is given by

$$n_b = \frac{N \rho_{\parallel,peak}}{2\pi \sigma_{\perp,rms}^2}, \quad (7.6)$$

where  $N$  denotes the number of electrons and  $\rho_{\parallel,peak}$  is the peak value of the normalized longitudinal charge distribution  $\rho_{\parallel}$ . The transverse source size inside the plasma was determined previously by Weingartner et al. [20] to  $\sigma_{\perp,rms} = 0.95 \mu\text{m}$ . The experimental setup employed similar backing pressures, the same gas target and laser system as the present experiment. Using the retrieved longitudinal profiles  $\rho_{\parallel}(z)$  at  $L_{pd}$  and eq. (7.6), the charge density of the main bunch amounts to  $n_b(n_1) \sim 2.1 \times 10^{19} \text{cm}^{-3}$  and  $n_b(n_2) \sim 4.6 \times 10^{19} \text{cm}^{-3}$ . In both cases, this is higher than the background plasma electron density with  $n_b/n_1 \sim 6.1$  and  $n_b/n_2 \sim 5.5$ , respectively. Due to the LWFA mechanism, the transverse and longitudinal bunch dimensions are naturally confined

## 7. Characterisation of the longitudinal bunch profile by CTR

---

to the size of the plasma bucket. In the present experiment,  $k_p \sigma_{\perp} \approx 0.33$ ,  $k_p \sigma_{\parallel} \approx 0.21$  at  $n_1$  and  $k_p \sigma_{\perp} \approx 0.50$ ,  $k_p \sigma_{\parallel} \approx 0.36$  at  $n_2$ . Thus, all prerequisites are fulfilled that are needed for the main bunch to drive a nonlinear wakefield in the blowout regime of PWFA.

This implies that during the final stage of laser depletion, the electron bunch itself is able to sustain a plasma wave. Finally, a mode transition from laser-driven to a particle bunch-driven wakefield occurs at  $L \gtrsim L_{pd}$ . With the emergence of a second bunch closely linked to this transition, the question arises which mechanism leads to plasma dynamics that can result in a 2<sup>nd</sup> injection process. In the following, the possibilities of nonlinear wave breaking in either a purely laser- or beam-driven mode, or a laser- to beam-driven mode transition are discussed.

### Self-injection in purely laser- or beam-driven mode

A laser induced self-injection process due to nonlinear wave breaking is unlikely to occur at this late stage of the acceleration process. After travelling the depletion length, the remaining laser power is insufficient to drive a strong wakefield. The electron energy evolution for  $L \geq L_{pd}$  confirms the absence of a significant wakefield strength that could possibly reach the wave breaking limit.

Additionally, accompanying depletion, the decreasing nonlinearity of the laser-driven plasma wave and the resulting contraction of  $\lambda_{p,nonlin.}$  towards  $\lambda_p$  leads to an effectively increased wake phase velocity. As outlined in section 2.4, an increase of  $\gamma_{ph}$  will only raise the injection and wave breaking threshold (cf. eq. (2.90) and eq. (2.97)).

For a purely electron beam-driven wakefield, the phase velocity of the wake of  $v_{ph} \approx c$  is too large to trap background electron initially at rest and the wave breaking threshold of  $E_{WB} = E_0 \sqrt{2(\gamma_{ph} - 1)}$  (eq. (2.90)) is dramatically increased. Thus, for the present case of a homogeneous plasma density, self-injection of the purely bunch-driven wake can be ruled out as well.

### Injection due to a laser- to beam-driven mode transition

The preceding arguments suggests that renewed injection by either a purely laser- or beam-driven wake is implausible. Yet, as a third possibility, the transition from a laser- to a bunch-driven wakefield may trigger a renewed injection process.

First, after an acceleration length exceeding  $L_d$ , the remaining laser-driven wakefield and the bunch-driven wakefield become more and more in phase and the overall wakefield amplitude increases (cf. section 2.5). Second, the injection can further be assisted by a temporal slowdown of the wake's phase velocity during the mode transition:

After an acceleration length of  $L_{pd}$ , the electron bunch is located close to ( $n_1$ ) or after the point of dephasing ( $n_2$ ), where its distance to the laser driver is in the range of  $0 - \lambda_p/2$ . After the laser ceases to drive an effective wake and diffracts, the front of the plasma wave slips back until the electron bunch itself acts as the main wake driver. The displacement of the front of the plasma wave relative to the electron bunch therefore leads to a temporary slow-down of the wake's phase velocity, which can assist a renewed trapping process. Assuming a transition region of  $\Delta z = 0.5$  mm in which the wake's front slips back by  $\lambda_p/2$ , the instantaneous phase velocity, given by

$$v_{ph} = v_{gr}(1 - \lambda_p/(2\Delta z)) \quad (7.7)$$

is roughly reduced to  $\sim 0.98c$  or  $\gamma_{ph} \sim 5 - 6$ . This would constitute a significant slow-down from its initial velocity determined by the group velocity of the laser pulse, which corresponds to  $\gamma_{gr} = 14 - 21$  (at  $n_2$  and  $n_1$ , respectively). This mode transition would act analogous to density down-ramp injection, for which the reduced plasma wave phase velocity has been shown both theoretically and experimentally to enable an efficient trapping of plasma electrons [71, 154].

### Electron deceleration and dephasing

Another possible formation mechanism is based upon deceleration of bunch electrons. In PWFA mode, the wakefield generated by the bunch itself leads to a decelerating field that is strongest at its rear side (cf. Fig. 2.7). Once these electrons are decelerated to sub-relativistic velocities, they slip back with respect to the driving bunch. These electrons can then be trapped in the accelerating field at the rear side of the cavity and form a second bunch. Such behaviour has been observed in PIC simulations that have been carried out in the framework of a PhD thesis by Chou [155]. This phenomenon is not limited to the PWFA mode but can also result from electron dephasing in LWFA mode, once electrons are decelerated to  $\gamma < \gamma_{ph}$  [119]. This process should lead to the formation of a second bunch in the same wave bucket. However, in our case, a continuous transition, i.e a fill-up of the electron density between both bunches, is not observed.

## 7.3 Dependence of the bunch separation on plasma density

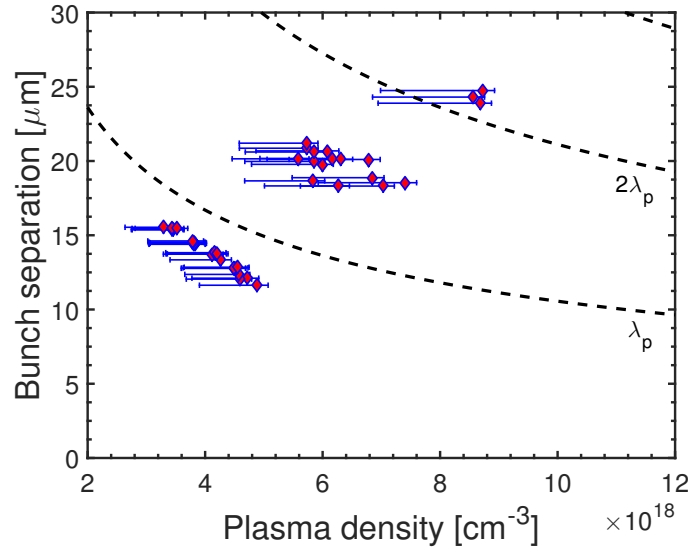


**Figure 7.9:** Retrieved bunch separation as a function of the background plasma electron density  $n_0$  at a fixed gas cell length of  $L = 12$  mm. Error bars on the x-axis represent the uncertainty of the hydrogen pressure inside the cell of  $^{+4}_{-20}\%$ . The dashed black line indicates multiples of the plasma wavelength  $\lambda_p$ .

So far possible mechanisms leading to the formation of a double bunch structure have been discussed. However, the distance  $d$  between both bunches has not yet been taken into account. As mentioned before, it is found that at  $n_1 = 3.4 \times 10^{18} \text{ cm}^{-3}$  the bunch distance  $d$  is smaller than



## 7. Characterisation of the longitudinal bunch profile by CTR

the plasma wavelength  $\lambda_p$ , while at  $n_2 = 7.7 \times 10^{18} \text{ cm}^{-3}$   $d$  is larger than  $\lambda_p$ . To obtain a more detailed insight into the scaling of  $d$  with  $n_0$ , the gas cell length was fixed at  $L = 12 \text{ mm}$ , while the backing pressure of hydrogen and therefore the plasma density inside the cell was varied in the range of  $n_0 = (3 - 9) \times 10^{18} \text{ cm}^{-3}$ .

Figure 7.9 shows the retrieved bunch separation in dependence of the plasma electron density. Error bars on the x-axis indicate the uncertainty regarding the actual plasma density inside the cell. The asymmetric shape corresponds to an uncertainty of  $^{+4\text{mbar}}_{-20\%}$ , where the upper limit is given by the maximum deviation of the closed-loop regulator from the target value and the lower limit takes into account a possibly lower gas pressure inside the cell due to gas flow through the gas cell's laser entrance and exit holes. Here, a conservative margin of 20 % is assumed.

The plot reveals density regimes that are separated by discrete steps of the bunch separation. Multiples of the (linear) plasma wavelength are depicted by dashed lines. In the range of  $n_0 = (3 - 5) \times 10^{18} \text{ cm}^{-3}$ , which includes  $n_1$ ,  $d < \lambda_p$  and approximately follows the density dependence of the plasma wavelength given by  $\lambda_p \propto 1/\sqrt{n_0}$ .

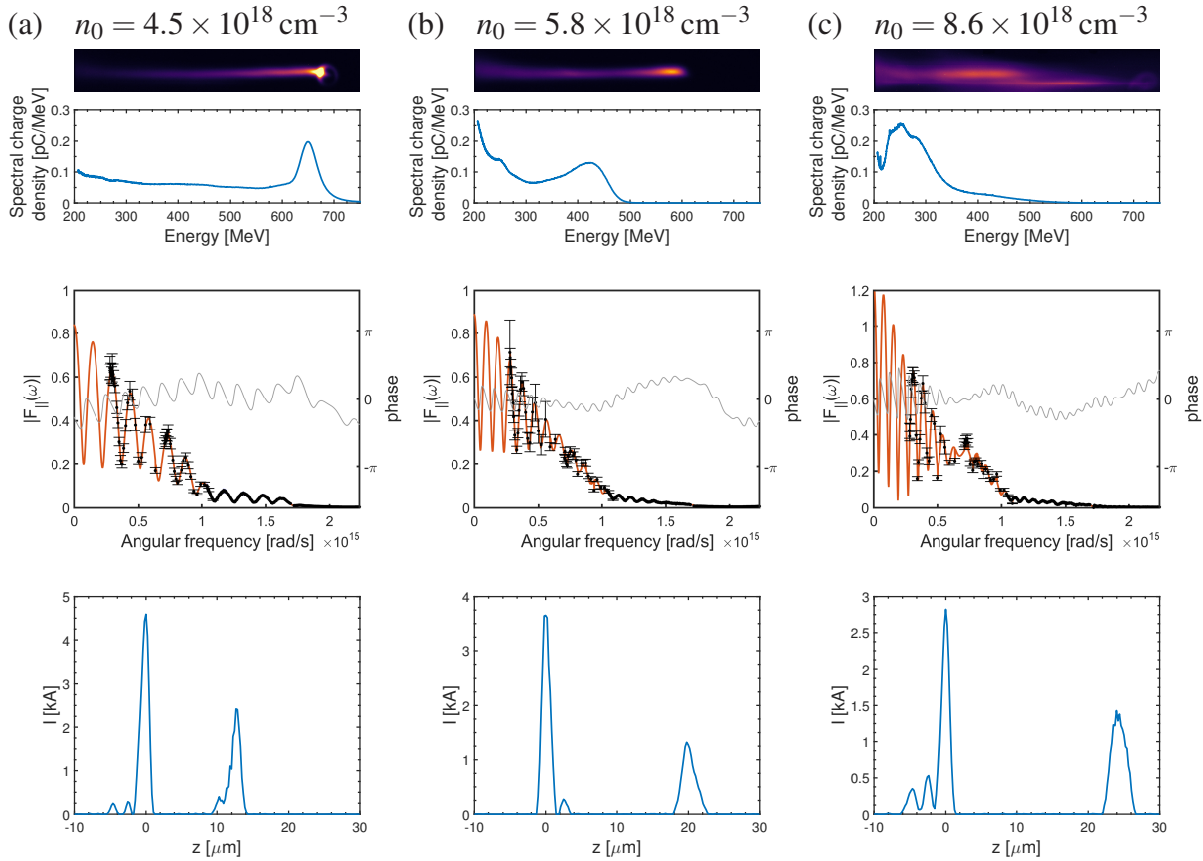


**Figure 7.10:** Single-shot data obtained at different plasma densities. Each column shows the respective electron energy spectrum, the measured and retrieved form factor and the retrieved bunch profile of a single shot. (a) corresponds to  $n_0 = 4.5 \times 10^{18} \text{ cm}^{-3}$ , (b) to  $n_0 = 5.8 \times 10^{18} \text{ cm}^{-3}$  and (c) to  $n_0 = 8.6 \times 10^{18} \text{ cm}^{-3}$ . The CTR modulation frequency increases with increasing plasma density. Accordingly, the retrieved bunch separation becomes larger.



At slightly higher plasma densities of  $n_0 = (5 - 8) \times 10^{18} \text{ cm}^{-3}$ , a sudden jump to  $d \sim 20 \mu\text{m}$  is observed, consistent with the bunch separation obtained in the length scan conducted at  $n_2$ . For even higher densities, a further increase to  $d \sim 25 \mu\text{m}$  is found. Data of three exemplary single shots corresponding to these density ranges is presented in Fig. 7.10. The plots show that the increase in bunch separation with increasing plasma density is clearly reflected by a higher modulation frequency in the CTR spectrum.

### Energy spectra

To correlate these finding with the electron energy spectra, images of the electron spectrometer's scintillator screen S2 together with the retrieved bunch separations are plotted in Fig. 7.11 for a selection of single shots. The shots are ordered such that the plasma density (specified by green diamonds) increases with shot number (denoted by the x-axis). Note that the scintillator screen images have been corrected for the magnet's dispersion curve, such that the vertical dimension corresponds to a linear increase in electron energy as given by the left (black) y-axis. The retrieved bunch separation is given by red squares.

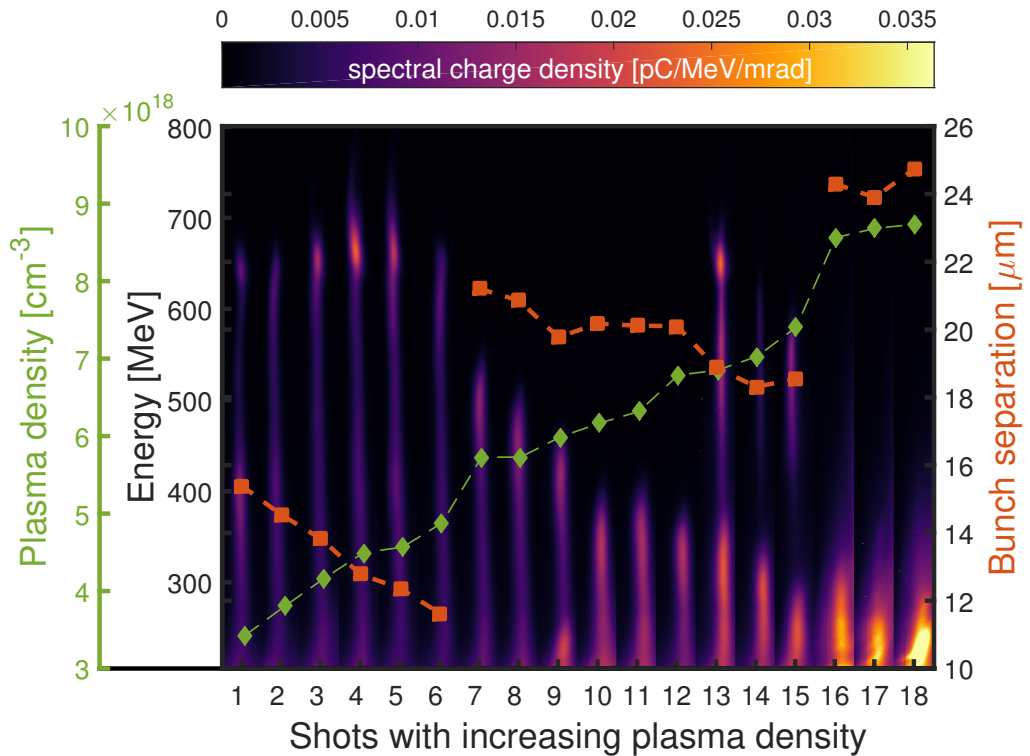


**Figure 7.11:** Evolution of the electron energy spectrum in dependence of the plasma density at a fixed gas cell length of 12 mm. The plot shows selected single-shot images of the electron spectrometer's scintillator screen S2. The images have been corrected for the magnet's dispersion such that the energy axis is linear. The shots (numbered by the x-axis) are arranged by increasing plasma density, as specified by green diamonds. Red squares show the retrieved bunch separation.

## 7. Characterisation of the longitudinal bunch profile by CTR

---

- For  $n_0 < 5 \times 10^{18} \text{ cm}^{-3}$ , the cut-off energies are roughly constant. Analogous to the length scan at  $n_1$ , in this regime  $L_d \sim L_{pd}$ . The electron energies increase only slightly with increasing density, as the higher acceleration gradient is counterbalanced by a shorter pump depletion length.
- In the range of  $n_0 = (5 - 8) \times 10^{18} \text{ cm}^{-3}$ , at first the cut-off energies decrease with increasing density (shots #7 – 12). Similar to the length scan performed at  $n_2$ , this behaviour can be attributed to an energy loss by dephasing, as for increased  $n_0$  the dephasing length is reduced. For shots #13 – 15, which still lie within the range of densities for which  $d \sim 20 \mu\text{m}$ , the electron spectra show an distinct regain in cut-off energy. Furthermore, a local minimum of the spectral charge density around 400 MeV lends itself to the interpretation that the two parts of the energy spectrum might be attributable to the electron populations of the two individual bunches. For increasing shot number from #7 – 15, this interpretation would be consistent with deceleration of the first bunch from 500 – 300 MeV, while a second bunch with initially lower energy is accelerated from  $\lesssim 200 \text{ MeV}$  (e.g. the low energy tail of shot #9) to similar energies as the first bunch (shots #10 – 12) and finally up to energies between 500 – 700 MeV for shots #13 – 15. This would constitute a substantial energy transfer from the first to the second bunch of  $\sim 15 \%$  (assuming equal maximum energies of both bunches, the energy transfer is given by their charge ratio). However, significantly higher energies than that attained at lower plasma densities of  $\sim 700 \text{ MeV}$  are not observed.
- The last three electron spectra obtained at  $n_0 > 8 \times 10^{18} \text{ cm}^{-3}$  are likewise limited by dephasing and characterized by a pronounced charge density at low energies. These spectra are accompanied by a long tail towards higher energies (also seen in Fig. 7.10c).

The data presented so far shows that the measured bunch separations can be divided into three classes. These classes also find a representation in the electron energy spectra observed on the scintillator screen S2 and can be characterized as being limited by pump depletion or electron dephasing. For plasma densities of  $n_0 > 8 \times 10^{18} \text{ cm}^{-3}$  (with  $d \sim 25 \mu\text{m}$ ), high-charge electron bunches with mostly low electron energies and an increased beam divergence are generated.

It is worth mentioning that throughout the measured density range only two dominant bunches are observed simultaneously. If additional bunches containing a significant fraction of the total charge would be existent, the CTR spectra would exhibit a more complex shape, as outlined in section 7.1. Nevertheless, a three bunch scenario can not be ultimately ruled out for the regime of  $n_0 > 8 \times 10^{18} \text{ cm}^{-3}$ , due to the few number of shots and the high modulation frequency that is not thoroughly resolved by the mid-infrared spectrometer.

## 7.4 Comparison with PIC simulations

To obtain a better understanding of the physics and to confirm the suggested LWFA to PWFA transition, PIC simulations were conducted to explore the plasma dynamics that lead to the formation of a secondary bunch at a late stage of the acceleration process. Since the inner workings of PIC codes shall not be discussed here, the reader is referred to more specialized publications such as ref.[29].

A major drawback of PIC simulations are the extensive computational resources needed to model a three-dimensional plasma with sufficient resolution over interaction lengths of several mm. In particular, this applies to simulations including laser drivers, which not only need to resolve the plasma wavelength but also the typically much shorter length scale set by  $\lambda_L$ . Although two-dimensional simulations need much less computational effort, these usually assume a translational invariance in transverse direction and therefore fail to capture the exact plasma dynamics present in the experiment and can only serve to qualitatively understand the involved physics.

### 7.4.1 LWFA to PWFA transition

The following simulation was performed with the PIC code OSIRIS [156, 157], assuming a fully pre-ionized plasma. The purpose of this simulation was to obtain a single self-injected electron bunch and subsequently observe the plasma dynamics occurring during the point of electron dephasing and laser depletion. The 3D simulation was set up with a matched laser pulse such that the required distance for laser self-focusing is minimized. The pulse energy was chosen such that the electron bunch has progressed to the dephasing point before the laser-driven wake structure collapses due to laser depletion.

A plasma density of  $n_0 = 3.4 \times 10^{18} \text{ cm}^{-3}$ , consistent with the low-density length scan at  $n_1$ , was chosen. The laser pulse with a Gaussian waist of  $w_{0,FWHM} = 13.5 \mu\text{m}$  and a pulse duration of  $t_{FWHM} = 29 \text{ fs}$  is initialized in vacuum and focused at the beginning of a plasma density plateau following an up-ramp of  $250 \mu\text{m}$ . A vector potential of  $a_0 = 2.9$ , corresponding to a laser pulse energy of 1.1 J, proved to be sufficient to achieve self-injection and laser depletion within a simulation length of 8 mm. The size of the simulation box is  $86 \times 121 \times 121 \mu\text{m}^3$  with  $3840 \times 240 \times 240$  grid points and 2 macro-particles per cell, where each macro-particle represents approximately  $10^4$  electrons.

The parameters which differ from the experimental conditions are the transverse beam size (PIC:  $13.5 \mu\text{m}$ , experiment:  $22 \mu\text{m}$ ) and the laser pulse energy (PIC: 1.1 J, experiment: 1.5 J). The smaller but matched beam size was chosen in order to limit the computation time as it avoids an additional simulation length that would be needed for self-focusing to occur. The slightly lower energy of 1.1 J was chosen in order to obtain laser depletion approximately at the point of electron dephasing. The slightly larger nominal experimental value can be attributed to a deviation of the laser focus from an ideal Gaussian intensity distribution (cf. Fig. 4.3), which may lead to a loss of laser energy in the main guiding channel.

Characteristic snap-shots of this PIC simulation are shown in Fig. 7.12. The upper row depicts the electron density (blue colormap) together with a lineout of the longitudinal electric field along the laser propagation axis (black line). The lower row shows the longitudinal phase space. On the basis of these time steps, the acceleration process can be described as follows.

## 7. Characterisation of the longitudinal bunch profile by CTR

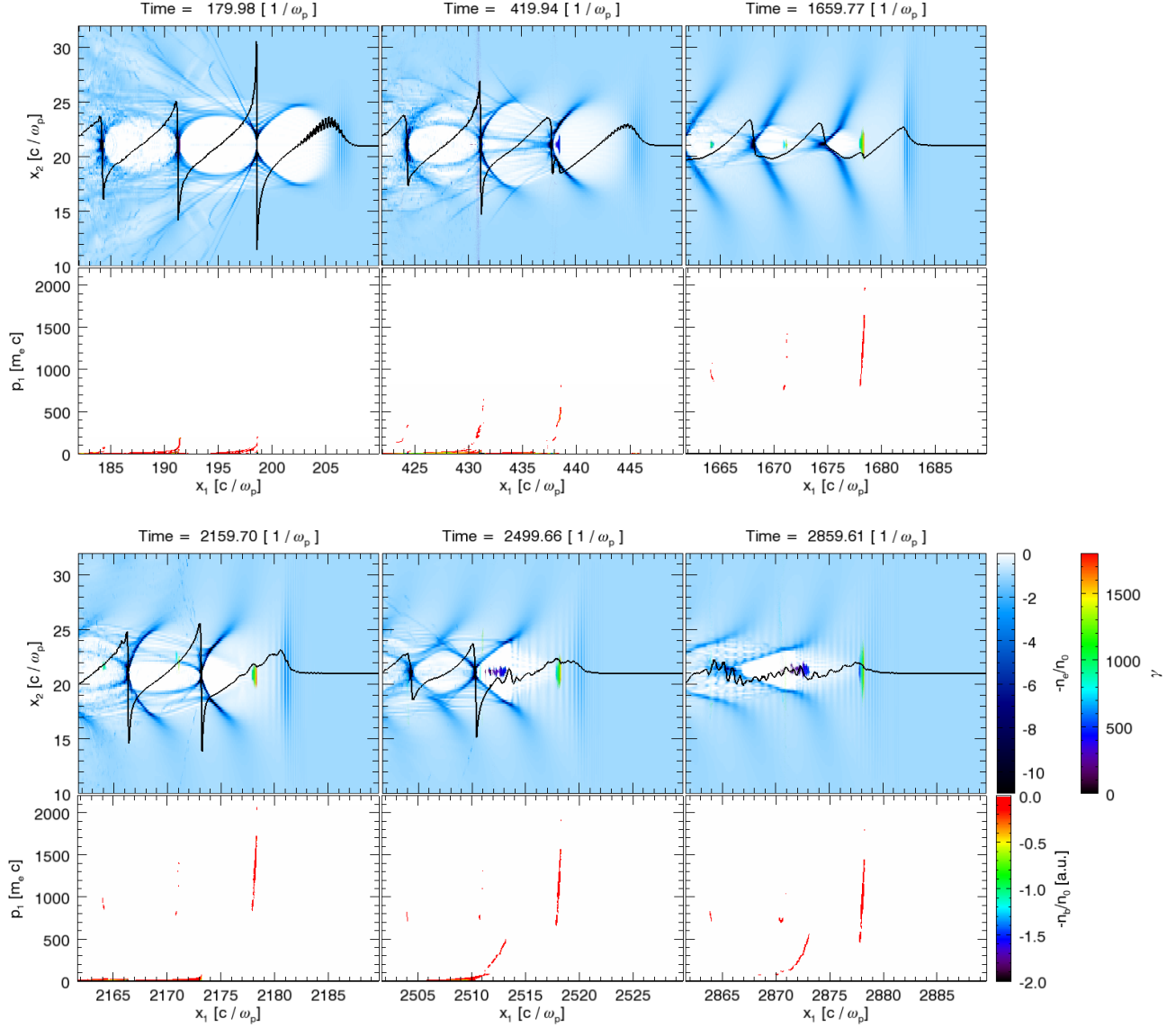


**Figure 7.12:** 3D PIC simulation (using the code *OSIRIS*) reproducing an LWFA to PWFA transition accompanied with injection of a 2<sup>nd</sup> bunch. The respective upper row shows characteristic snap-shots of the electron density perturbation (blue colormap), where the electron bunch energies are given by the rainbow colormap. Plotted are the central slices of the simulation box. Black lineouts represent the longitudinal electric field along the laser propagation axis ([a.u.]). The lower row shows a plot of the respective longitudinal phase space. For a description of the time steps and the simulation parameters see main text.

After entering the plasma, the laser drives a nonlinear wakefield characterized by a large electric field spike at the crest of the 1<sup>st</sup> wave bucket. After an electron bunch is injected at the rear side of the cavity, the superposition of the wakefields driven by the laser and the electron bunch leads to a reduction of the total field amplitude by beam loading (cf. section 2.5). This prevents further injection and limits the injection process to a short time interval. Low-charge bunches are also observed to be injected in the 2<sup>nd</sup> and 3<sup>rd</sup> wake period. During subsequent LWFA, the relativistic electron bunches gradually advance towards the laser pulse. Note that the 1<sup>st</sup> bunch's charge density is sufficient to significantly modify the longitudinal electric field at the position of the bunch. Its deviation from a linear slope shows that beam loading is strong enough to modify the acceleration gradient within the bunch.

When reaching the middle of the plasma period, the bunch has reached the dephasing point and obtained its maximum energy. As the distance between the laser and 1<sup>st</sup> electron bunch continues to decrease, both wakefields become more and more in phase and the electric field amplitude at the rear side of the cavity increases again. With further propagation, the field-strength at the crest of the 1<sup>st</sup> wave bucket exceeds the wave-breaking threshold, which leads to self-injection of a 2<sup>nd</sup> bunch at the rear side of the 1<sup>st</sup> wave bucket. During further propagation, the 1<sup>st</sup> bunch is then decelerated by its own wakefield and that driven by the remnants of the laser driver, while the newly injected 2<sup>nd</sup> bunch experiences an energy gain.

At this stage of the acceleration process, the chirp of the 1<sup>st</sup> bunch does not change sign as would be the case in a dephasing process, where electrons in the head of the bunch experience a stronger deceleration than those at its tail. The deceleration of the 1<sup>st</sup> bunch with nearly unaltered chirp is a consequence of its own bunch driven wakefield being dominant after laser energy depletion.

### Energy evolution

The acceleration process can be intuitively visualized by plotting the on-axis electron density as well as the evolution of the electron energy spectrum as shown in Fig. 7.13. Each vertical line in Fig. 7.13a shows the charge density on the central laser propagation axis in the simulation box (co-moving with  $c$ ) for subsequent time steps, i.e. after different propagations lengths  $L$ . The laser pulse, initially located at  $x_1 = 79 \mu\text{m}$ , close to the beginning of the simulation box, slips backwards as  $v_{gr} < c$ . The same is true for the crests of the first three wave periods, which appear as oblique lines of increased electron density. The slope of these lines intuitively visualizes the corresponding wake phase velocity  $v_{ph}$ . Electrons injected from the wake crests and accelerated in the respective wake periods are recognized as vertical lines due to their relativistic velocity of  $v \approx c$ . Figure 7.13b shows the corresponding energy evolution, where each vertical line represents the energy spectrum of all macro-particles with  $\gamma \geq 100$  in dependence of  $L$ .

In conjunction with the longitudinal phase space plotted in Fig. 7.12, the injection at  $L \lesssim 1 \text{ mm}$  and subsequent acceleration can be ascribed to macro-particles forming the bunch inside the 1<sup>st</sup> wave bucket. At  $L \approx 1.5 \text{ mm}$ , low-charge bunches are also injected and accelerated in the 2<sup>nd</sup> and 3<sup>rd</sup> wave bucket.

After reaching the dephasing point at  $L \approx 6 \text{ mm}$ , the electron energies temporarily decline due to the onset of dephasing. With further propagation ( $L \gtrsim 6 \text{ mm}$ ), the 2<sup>nd</sup> bunch is injected into the 1<sup>st</sup> wave bucket and a subset of its electrons is accelerated up to  $E_{max} \sim 300 \text{ MeV}$  at  $L \approx 12 \text{ mm}$ . The injection is due to a temporarily reduced wake phase velocity caused by two effects: (i) the



## 7. Characterisation of the longitudinal bunch profile by CTR

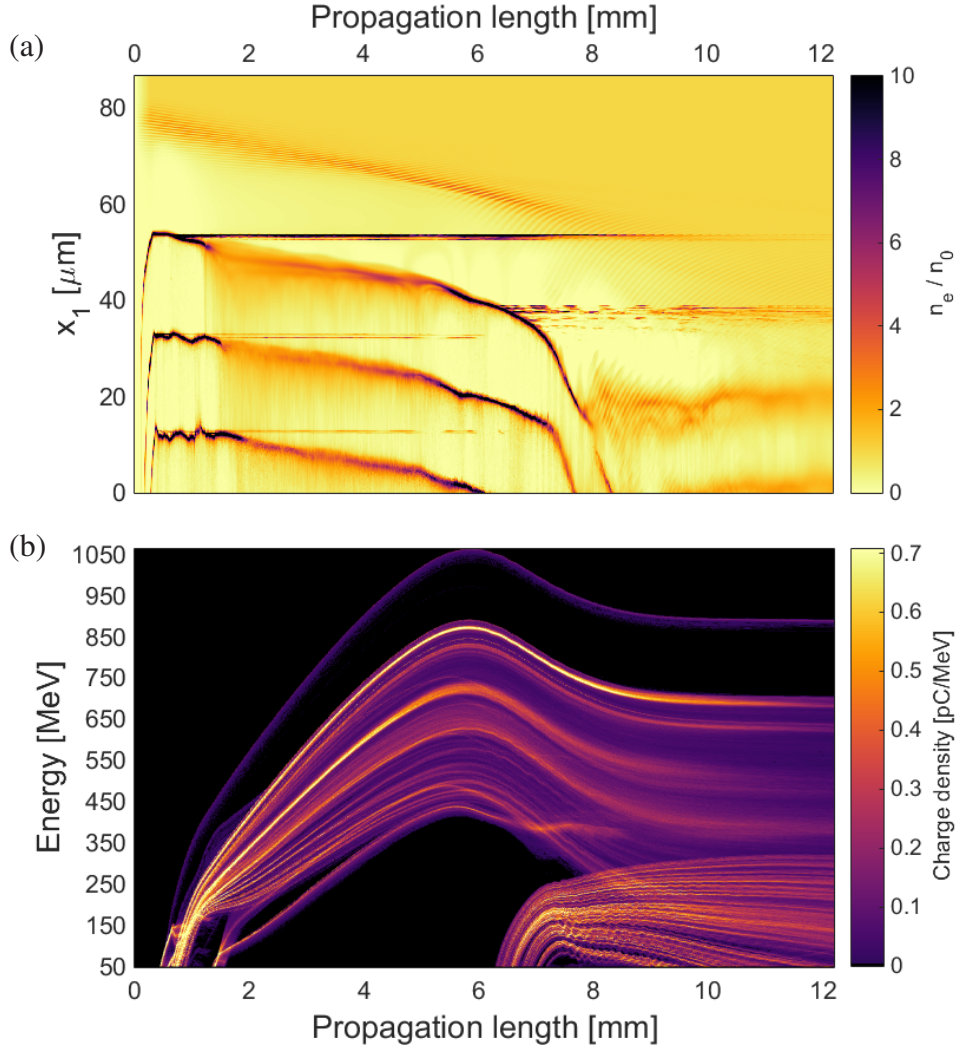


**Figure 7.13:** Evolution of the on-axis electron density (a) and the electron energy spectrum (b) in dependence of the simulated propagation length. The vertical dimension of (a) shows a lineout of the electron density through the center of the simulations box after different time steps. The spectrally resolved charge density extracted from the *PIC* simulation is shown in (b). Only the contribution of electrons with  $\gamma \geq 100$  is shown.

density spike at the crest of the 1<sup>st</sup> wake bucket slipping back because of the more nonlinear nature of the wakefield and (ii) the relocation of the front of the wake towards the *PWFA* driver because of the onset of laser energy depletion, manifested in Fig. 7.13a around  $L \sim 6$  mm by a steeper slope of the crest of the 1<sup>st</sup> plasma period due to the reduced phase velocity.

At  $L \gtrsim 8$  mm the deceleration rate of the 1<sup>st</sup> bunch decreases as the laser is depleted. The now lower deceleration gradient is caused by its own bunch-driven wakefield.

It is further seen that the low-charge bunches injected in the 2<sup>nd</sup> and 3<sup>rd</sup> wave bucket disappear at  $L \approx 7$  mm. These are first decelerated by dephasing and later exposed to the defocusing region near the crest of the preceding plasma period. Low-charge bunches from trailing plasma

cavities are also not observed experimentally during the initial LWFA stage. Similarly, this can be ascribed to the density down ramp present at the exit of the gas cell, in which the plasma wavelength is continuously elongated such that these bunches become likewise exposed to the defocusing fields of the preceding wave crests.

### Bunch profile evolution

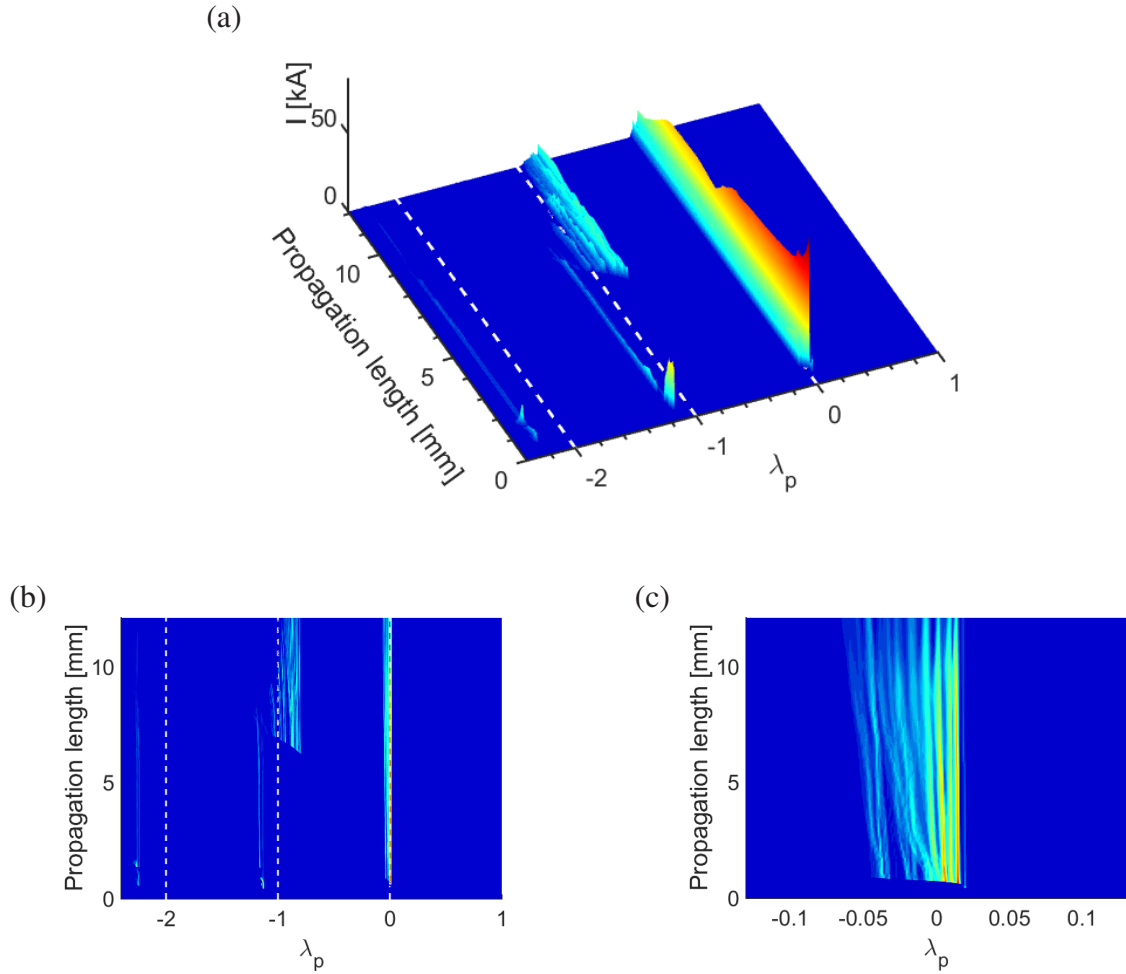


**Figure 7.14:** Bunch profile evolution extracted from the *PIC* simulation. (a) shows a 3D plot of all simulated macro-particles with  $\gamma \geq 100$  projected onto the  $z$ -axis and binned by  $\lambda_p/450$ . Dashed white lines illustrate multiples of  $\lambda_p$ . (b) shows a top view of (a), illustrating the bunch separation  $d$ . (c) shows a close-up view of the 1<sup>st</sup> bunch's profile evolution with high resolution (bin size  $\lambda_p/1000$ ).

The evolution of the longitudinal bunch profile extracted from the simulation is plotted in Fig. 7.14a. The striking similarity to the experimentally measured evolution suggests that the simulated plasma dynamics resemble those of the experimental scan conducted at the plasma density  $n_1$ . As in the experiment, a second injection process occurs late in the acceleration process at  $L \gtrsim L_d$ . The bunch separation of  $d < \lambda_p$  also matches the experimental observation. From



## 7. Characterisation of the longitudinal bunch profile by CTR

---

the simulation we find  $d \approx 0.85 \lambda_p$  (cf. Fig. 7.14b), while  $d(n_1) = 0.82^{+0.05}_{-0.17} \lambda_p$ , where the error margins stem from the uncertainty in backing pressure of  $70^{+4}_{-20\%}$  mbar. Both values therefore agree well within the error margin.

As seen from the energy evolution presented in Fig. 7.13b, despite its short length in the fs range, the accelerated bunch develops a broadband energy spectrum. This is caused by beam loading, which results in a local dependence of the accelerating field along the bunch's longitudinal extent (cf. Fig. 7.12). Nevertheless, the induced velocity spread does not lead to a significant elongation of the bunch duration, due to rapid acceleration to relativistic energies. A close-up view of the 1<sup>st</sup> bunch's profile evolution is shown in Fig. 7.14c. Its duration after injection amounts to  $t_{FWHM} = 2.1$  fs and is only slightly elongated by the velocity spread to  $t_{FWHM} = 2.5$  fs at  $L = 12$  mm.

Apart from the shorter duration of the 1<sup>st</sup> bunch and an increased charge of 70 pC, the experimental results presented in subsection 7.2.1 are thus largely reproduced by the PIC simulation, which corroborates the inferred LWFA to PWFA transition.

### 7.4.2 Bunch separations exceeding $\lambda_p$

The simulation presented above resembles the plasma dynamics found in the length scan conducted at  $n_1$ . In contrast, a bunch separation of  $d > \lambda_p$  as observed in the gas cell length scan at  $n_2 = 7.7 \times 10^{18} \text{ cm}^{-3}$  could not be reproduced in 3D simulations. This may well be attributed to the fact that the computational resources were not sufficient to explore a much wider range of input parameters within a reasonable time frame. Nevertheless, 2D PIC simulations can be utilized to simulate individual events of the plasma dynamics during acceleration and are helpful to explore the physics of wakefield evolution.

#### Rapid reduction of $\lambda_{p,nonlin.}$

A potential mechanism leading to separations of  $d > \lambda_p$  could be identified in 2D simulations, which are depicted in Fig. 7.15. Both columns show a series of snap-shots of two simulations with mostly identical input parameters. In these simulations, an electron bunch with  $n_b/n_0 = 6.1$  was initialized as a non-evolving bullet-type charge distribution with an electron energy of 400 MeV and a bi-Gaussian spatial charge profile, representing the first injected bunch close to dephasing. The simulations differ in that the simulation shown in the right column assumes a weaker laser, a shorter distance between the electron bunch and the laser pulse as well as a shorter bunch driver, which, despite exhibiting the same peak current, contains less charge.

In both simulations, the nonlinear wakefield excited by the laser and the electron bunch is driven strong enough for wave breaking to occur, such that a 2<sup>nd</sup> electron bunch is injected and accelerated in the 1<sup>st</sup> wake period. At the point of laser depletion, the wakefield strength decreases and the plasma period rapidly shortens. Depending on the strength of the PWFA driver and its distance to the laser, the 2<sup>nd</sup> electron bunch can get trapped in the first plasma cavity (left column) or be exposed to and overtaken by the defocusing region at the rear side of the cavity (right column). In the latter case a portion of the 2<sup>nd</sup> bunch's electrons can then get trapped in the 2<sup>nd</sup> plasma cavity. After a sufficient propagation length, the 2<sup>nd</sup> electron bunch resides in the middle of the 2<sup>nd</sup> wave bucket at  $d \sim 1.5 \lambda_p$ .

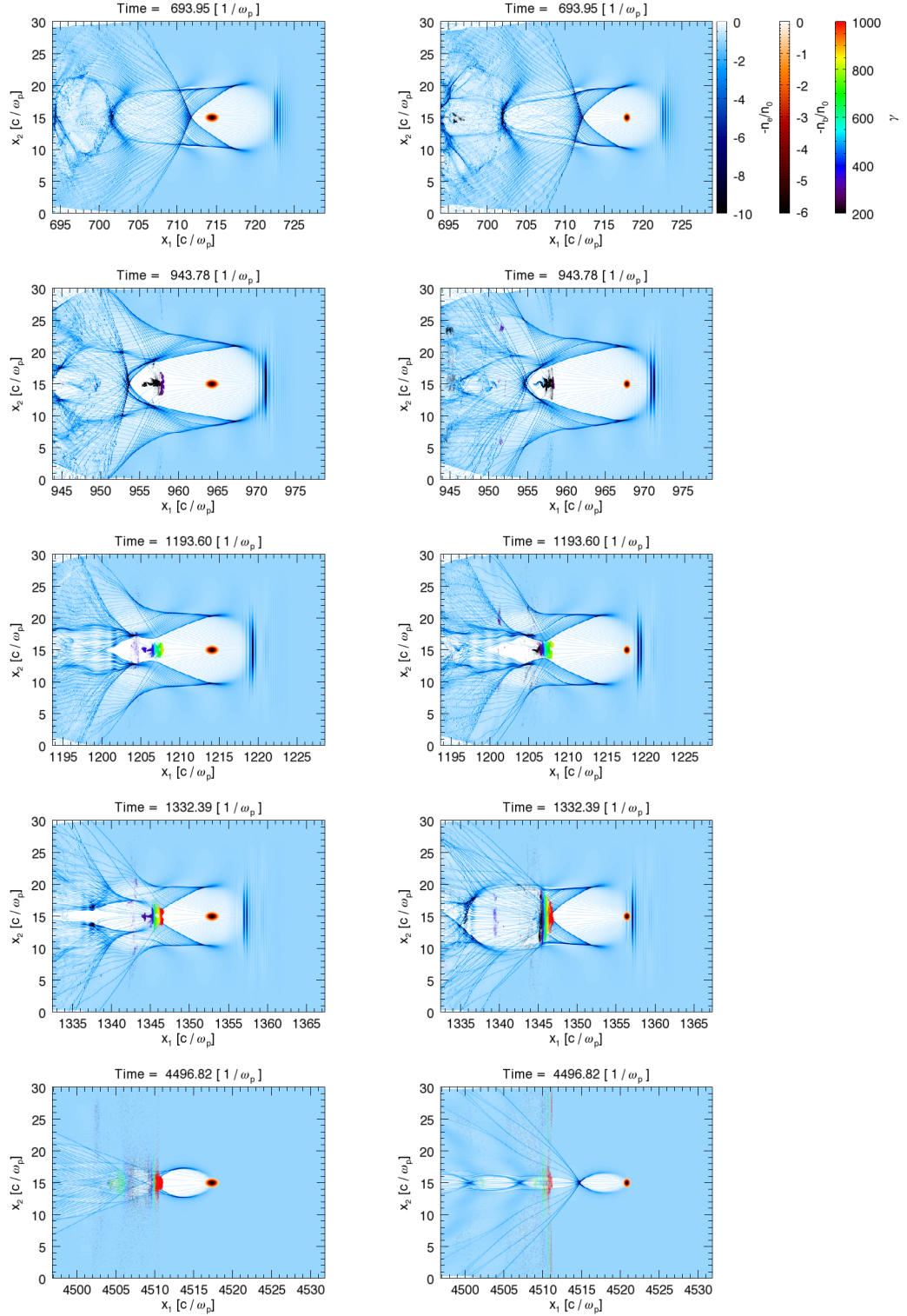


**Figure 7.15:** 2D PIC simulations showing trapping of a 2<sup>nd</sup> bunch in either the 1<sup>st</sup> or the 2<sup>nd</sup> wake period. The simulation shown in the left column assumes a stronger laser and beam driver and an increased distance between the laser and the electron bunch. The simulation parameters are  $n_0 = 7.7 \times 10^{18} \text{ cm}^{-3}$ ,  $w_0 = 12 \mu\text{m}$ ,  $t_{FWHM} = 28 \text{ fs}$  and:

left column:  $a_0 = 3.3$  and  $n_b/n_0 = 6.1$ , with  $k_p \sigma_{\parallel} = 0.4$  and  $k_p \sigma_{\perp} = 0.3$ ,  
 right column:  $a_0 = 3.1$  and  $n_b/n_0 = 6.1$ , with  $k_p \sigma_{\parallel} = 0.2$  and  $k_p \sigma_{\perp} = 0.3$ .

## 7. Characterisation of the longitudinal bunch profile by CTR

---

Although this mechanism would need to be verified by 3D simulations, it reproduces the separation of  $d \sim 1.5\lambda_p$  observed experimentally.

### Lower trapping threshold with increasing distance to the driver

Analogous to the 3D PIC simulation presented before, an alternative scenario leading to bunch separations of  $d > \lambda_p$  may equally rely on a transiently reduced wake phase velocity caused by the superposition of the laser- and bunch-driven wakefields during electron dephasing. Since, by eq. (2.100), the accompanying nonlinear elongation of  $\lambda_p$  reduces the local phase velocity of the wake with increasing distance to the driver, the injection threshold may only be exceeded for distances  $\xi$  corresponding to the 2<sup>nd</sup> or subsequent wake periods. This explanation would also enable bunch separations  $d > 2\lambda_p$  as observed experimentally for plasma densities of  $n_0 > 8 \times 10^{18} \text{ cm}^{-3}$ .

This process would require the superposition of the wakefields to be too weak to reach the wave breaking threshold within the 1<sup>st</sup> wave period. However, in contrast to the low density scan performed at  $n_1$ , the higher plasma density in the  $n_2$  scan should theoretically reduce the wave breaking threshold, due to a lower laser group velocity (cf. eq. (2.47) and eq. (2.96)). It therefore remains unclear if this process can indeed happen and additional large-scale 3D PIC simulations would be required.

### 7.4.3 Conclusion

At the stage of the acceleration process at which the laser pulse depletes, the dense electron bunch will take over as the wakefield driver. As argued in subsection 7.2.3, and confirmed by PIC simulations, the plasma dynamics triggered by the re-phasing of the wakefield during the LWFA to PWFA transition can lead to injection of a 2<sup>nd</sup> bunch at the crest of the 1<sup>st</sup> wave bucket. This scenario is observed experimentally at a plasma density of  $n_1 = 3.4 \times 10^{18} \text{ cm}^{-3}$ , for which the laser pump depletion length roughly equals the electron dephasing length. The experimentally retrieved bunch separation of  $d = 14.9 \mu\text{m}$  at  $n_1$  agrees within the error bars with the value determined from the PIC simulation (PIC:  $d/\lambda_p \approx 0.85$ , experimental:  $d/\lambda_p = 0.82^{+0.05}_{-0.17}$ ).

In the experiment, a clear signature of a 2<sup>nd</sup> bunch is not observed by the electron energy diagnostics. It must thus be concluded that its energy spectrum is either broadband or has energies  $< 200 \text{ MeV}$  that are below the detection window. Also this finding is supported by the simulation, which shows that, in spite of their short durations, both bunches carry a broadband energy spectrum caused by beam loading, which hinders their identification by a measurement of the energy spectrum alone.

For the range of higher plasma densities of  $n_0 = (5 - 8) \times 10^{18} \text{ cm}^{-3}$ , including the length scan at  $n_2$ , the experimentally observed bunch separations are approximately given by  $d \sim 1.5\lambda_p$ . Both bunches could only reside in the same plasma cavity if  $\lambda_p$  would be elongated significantly. The plasma wavelength in the purely beam driven case was therefore quantified by additional 3D PIC simulations. These simulations show that the nonlinear plasma wavelength driven by an electron bunch with the experimentally determined parameters is only elongated by  $\sim 15\%$  over its linear value. A distance of  $d \sim 1.5\lambda_p$  is therefore not consistent with both bunches residing in the same plasma cavity. The observed bunch separation would be consistent with a rapid contraction of the plasma wavelength after laser depletion, as suggested by the presented 2D PIC simulations.

For even higher densities  $n_0 > 8 \times 10^{18} \text{ cm}^{-3}$ , the few number of recorded shots at a fixed gas cell length of  $L = 12 \text{ mm}$  impedes a thorough analysis. Based on analogous arguments as given above, the measured bunch separation of  $d \gtrsim 2\lambda_p$  is interpreted as the 2<sup>nd</sup> electron bunch residing in the 3<sup>rd</sup> plasma cavity trailing the laser pulse. The beam quality in this regime is reduced by a larger beam divergence and an almost thermal-like electron energy spectrum caused by advanced electron dephasing as well as strong beam loading effects due to a large beam charge. However, the low-charge tail towards energies around 600 MeV observed in the respective electron energy spectra suggests that acceleration by a beam-driven wake could still be possible for some of the 2<sup>nd</sup> bunch's electrons.

To assess the exact plasma dynamics for densities of  $n_0 \geq 5 \times 10^{18} \text{ cm}^{-3}$ , further investigation will be required, in part by conduction 3D PIC simulations, and by extending the experimental setup to gather additional information. For example, a transverse probe beam, as established in ref. [22, 158], could be utilized to take shadowgraphic snap-shots of the electron density distribution, which would allow to observe the period lengthening of the plasma wave during the transition from a laser- to a beam-driven wakefield.

As argued in this chapter, the renewed injection of a 2<sup>nd</sup> bunch is always related to this transition, irrespective of the plasma density. For  $n_0 \geq 5 \times 10^{18} \text{ cm}^{-3}$ , the uneven spacing in terms of  $\lambda_p$  between both bunches supports this interpretation, since, for purely LWFA driven wakefields, injection of trailing bunches into subsequent wave buckets should lead to multi bunch structures separated by an integer amount of plasma wavelengths  $\lambda_p$  (as observed using colliding pulse injection in ref. [27]). Furthermore, these bunches are expected to be injected at an early stage of the acceleration process in which the laser driver is strong enough for wave breaking to occur. In contrast, in the present case the emergence of the double bunch structure occurs at a late stage of the acceleration process, where nonlinear wave breaking is unlikely to occur due to advanced laser pump depletion.

### 7.5 Coherent enhancement at visible frequencies

A feature, which is observed in the measured CTR spectra but has so far been unregarded, is a local enhancement of the CTR spectrum at visible frequencies. The high of this feature is typically on the order of  $|F_{||}(\omega_{peak})| \leq 5\%$ , located at  $\omega_{peak} \sim 4 \times 10^{15}$  rad/s, which corresponds to a CTR wavelength of  $\lambda \sim 470$  nm. In both length scans, this local maximum is present in almost all recorded CTR spectra (97 % of all shots at  $n_1$  and 87 % of the shots at  $n_2$  with  $L \leq 6$  mm), independent of the number of retrieved bunches. Figure 7.16 shows a magnification of the relevant spectral range for two representative shots. As seen in Fig. 7.16b, this part of the spectrum is also modulated whenever the low-frequency part of the spectrum is and exhibits the same modulation frequency. This confirms that the signal is indeed CTR rather than the second harmonic of laser light penetrating the stray light shielding.

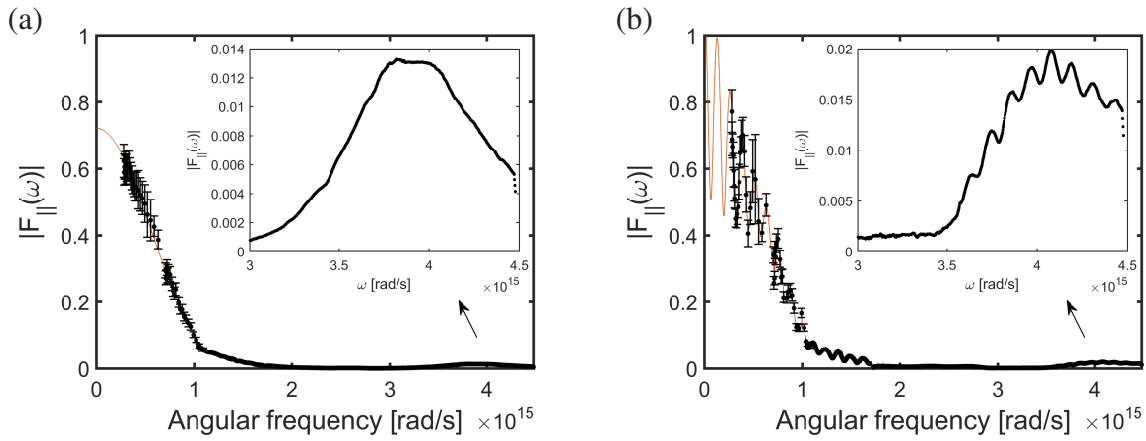


**Figure 7.16:** Local enhancement of the form factor at visible frequencies. (a) shows the measured form factor of a single bunch and (b) of a double bunch structure. The insets show a magnification of the feature in the visible part of the spectrum. If a double bunch is present, the modulation frequency is the same as that of the low-frequency part of the spectrum.

We first discuss an unmodulated CTR spectrum from a single bunch as shown in Fig. 7.16a. Since the bunch profile and the form factor are related by a Fourier transform, the central frequency of the feature indicates a modulation of the bunch profile on the scale of  $2\pi c/\omega_{peak} \sim 470$  nm. An alternative point of view is to consider the local enhancement as arising from a low frequency modulation in  $|F_{||}(\omega)|$  with  $\Delta\omega = \omega_{peak}$  and hence a multi-bunch structure with a bunch separation of  $d = 2\pi c/\Delta\omega = \lambda_{peak}$ . Similar to the case of two bunches, which was described in section 7.1, the fringe visibility  $V(\omega)$  eventually depends on the shape of each individual bunch, their charge ratio and, in the case of a periodic bunch train, on the number of bunches and their individual separations. However, as the fringe visibility for more than two bunches depends on a large number of parameters, all of these cannot be inferred from a single measurement. Yet, by introducing the following two assumptions, the shape of the local enhancement allows to draw conclusions about the bunch profile:

- (i) We first assume that the bunch profile  $\rho_{||}(t)$  exhibits a modulation with a *constant* frequency  $\omega_0 = 2\pi/T$ . Its shape can then be regarded as a macro-bunch consisting of indi-



vidual micro-bunches with constant spacing  $T$  and an outline determined by an envelope function  $E(t)$ .

(ii) We further assume an *equal shape* of each micro-bunch.

We now model a pulse train of micro-bunches by a convolution of their individual shapes  $S_m(t)$  with a Dirac comb  $\text{comb}_T$ . The outline of the macro-bunch is obtained by multiplying the micro-bunch train with the envelope function  $E(t)$ , resulting in a macro-bunch profile as depicted in Fig. 7.17a. Its profile can thus be expressed by

$$\rho_{\parallel}(t) = (\text{comb}_T * S_m(t)) \cdot E(t). \quad (7.8)$$

Recalling eq. (3.48), the longitudinal form factor is determined from  $\rho_{\parallel}(t)$  by  $F_{\parallel}(\omega) = \mathcal{F}[\rho_{\parallel}]$ . Denoting the form factor of a single micro-bunch by  $F_{\parallel, \text{micro}} = \mathcal{F}[S_m]$  and that of the macro-bunch's envelope by  $F_{\parallel, \text{macro}} = \mathcal{F}[E]$ , the resulting form factor reads

$$\begin{aligned} F_{\parallel}(\omega) &= \mathcal{F}[(\text{comb}_T * S_m(t)) \cdot E(t)], \\ &= (\text{comb}_{\omega_0} \cdot \mathcal{F}[S_m(\omega)]) * \mathcal{F}[E(\omega)], \\ &= (\text{comb}_{\omega_0} \cdot F_{\parallel, \text{micro}}(\omega)) * F_{\parallel, \text{macro}}(\omega), \\ &= \left( \sum_{n=0, n \in \mathbb{N}}^{\infty} \delta(\omega - n\omega_0) F_{\parallel, \text{micro}}(\omega) \right) * F_{\parallel, \text{macro}}(\omega), \\ &= \sum_{n=0, n \in \mathbb{N}}^{\infty} F_{\parallel, \text{micro}}(n\omega_0) \cdot F_{\parallel, \text{macro}}(\omega - n\omega_0), \end{aligned} \quad (7.9)$$

We will now have a closer look at the corresponding CTR spectrum. The magnitude of the resulting form factor is plotted in Fig. 7.17 for the case of a Gaussian envelope as well as micro-bunches of Gaussian shape for different micro- and macro-pulse durations and  $\omega_0 = \omega_{\text{peak}}$ . In Fig. 7.17b the macro-bunch duration is kept constant and the micro-bunch duration is varied, while in Fig. 7.17c the situation is vice versa. As seen from these plots, the modulated bunch profiles reproduce the local enhancement in the measured form factor at  $\omega_{\text{peak}}$ .

Equation (7.9) allows a simple assessment of its properties. The magnitude of the enhancement is given by the micro-bunch's form factor  $F_{\parallel, \text{micro}}(\omega_{\text{peak}})$  (for  $n = 1$ ), as illustrated by dashed lines in Fig. 7.17b and c. The shape of the feature is given by the convolution of  $F_{\parallel, \text{macro}}$  with  $\delta(\omega - \omega_{\text{peak}})$ , which, according to the Fourier shifting theorem, corresponds to a simple frequency shift by  $\omega_{\text{peak}}$  (cf. Fig. 7.17d). Hence, the shape of the local maximum directly resembles electron bunch's envelope function  $E(t)$ .

It has to be emphasized that the analysis presented above relies on the assumption of a constant modulation frequency  $\omega_0$ . In this case,  $F_{\parallel, \text{macro}}(\omega)$  is convoluted with a complex constant, whose phase is irrelevant to the modulus of the form factor  $|F_{\parallel}(\omega)|$ . In contrast, a varying modulation frequency would correspond to the convolution of two complex functions. Then, the shape of  $|F_{\parallel}(\omega)|$  would no longer be uniquely defined by  $F_{\parallel, \text{macro}}(\omega) = \mathcal{F}[E(t)]$  alone.

## 7. Characterisation of the longitudinal bunch profile by CTR

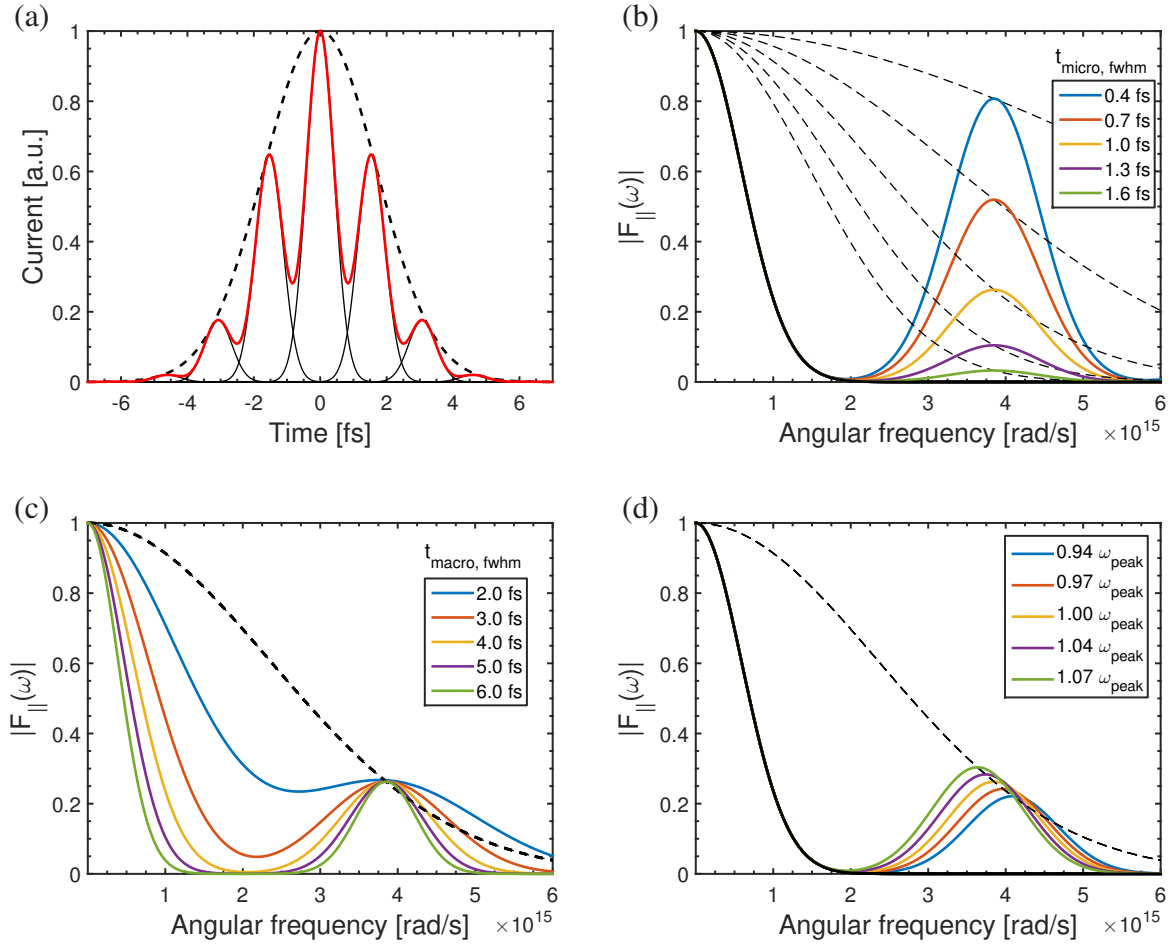


**Figure 7.17:** CTR spectra emitted by a modulated bunch profile. (a) shows the longitudinal profile of the modelled bunch. The macro-bunch profile (red line) consists of micro-bunches of equal shape (shown with black lines) following the outline of a Gaussian envelope function (dashed black line). (b) shows the computed form factor of a series of macro-bunches with a FWHM duration of 4 fs, a modulation frequency of  $\omega_{\text{peak}} = 4 \times 10^{15} \text{ rad/s}$  and different FWHM micro-bunch durations. Dashed lines show the form factors of the respective micro-bunches and the solid black line shows the form factor of the envelope function. In (c), the macro-bunch duration is varied and  $t_{\text{micro,FWHM}}$  is kept constant at 1 fs. In (d), the macro- and micro-bunch duration is kept constant at 4 fs and 1 fs, respectively, and the modulation frequency  $\omega_{\text{peak}}$  is varied.

We now analyse the feature in the recorded CTR spectra. It may not only be used to cross check the retrieved bunch durations, but also delivers more insight into the acceleration process. For both scans of the gas cell lengths, the width of the form factor and the width of the local maximum were determined for each shot by fitting a Gaussian to the respective spectral ranges as illustrated in Fig. 7.18a. The bunch durations of the corresponding Gaussian temporal bunch profiles are plotted in Fig. 7.18b and c, where markers correspond to the mean value of all shots obtained at each discrete gas cell length and error bars show the shot-to-shot standard deviation.

It is found that the bunch durations obtained from a simple Gaussian fit to the form factor (in



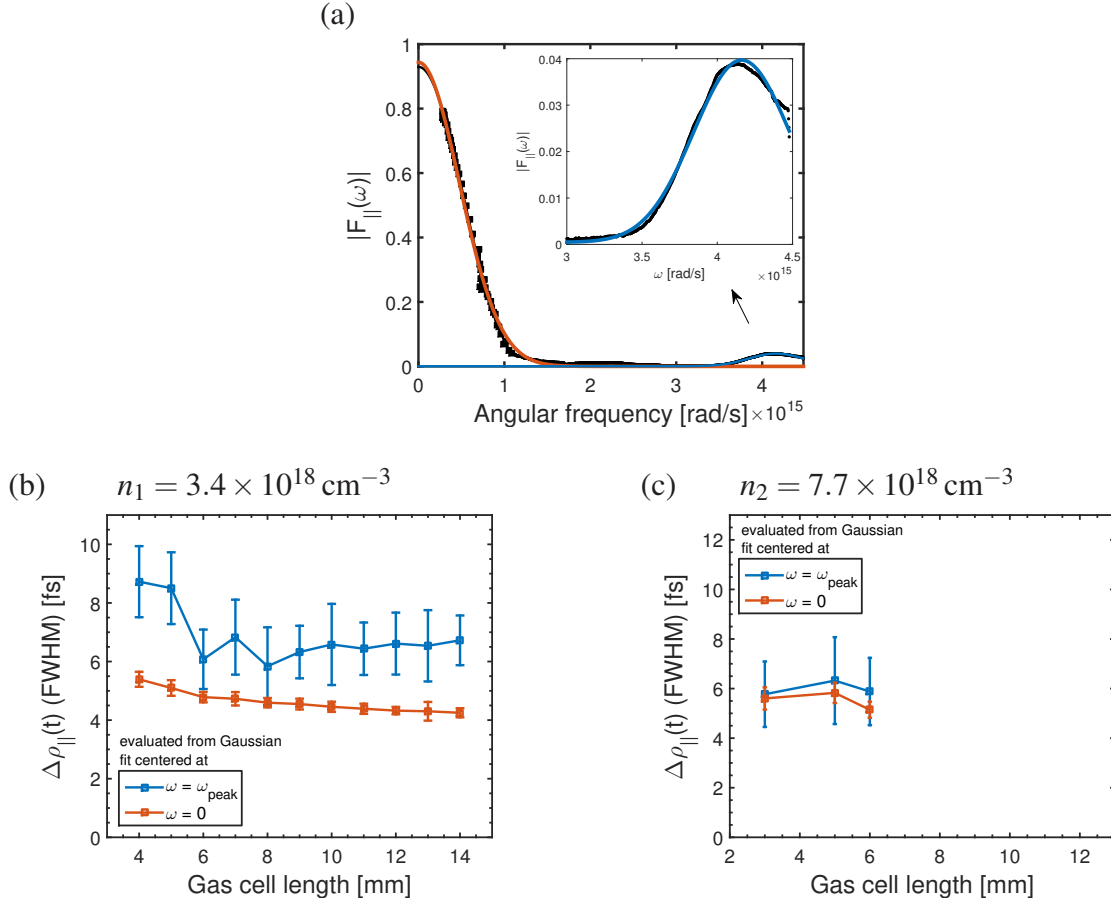


**Figure 7.18:** Width of the enhancement. (a) illustrates the fitting process. A Gaussian was either fitted to the complete form factor (red line) or only to the spectral range around  $4 \times 10^{15}$  [rad/s] (blue line). The widths of the corresponding Gaussian temporal bunch profiles are shown in (b) and (c) for the scan conducted at  $n_1$  and  $n_2$ , respectively. Data points show the mean values obtained at each length setting of the gas cell and error bars display the shot-to-shot *rms* variations.

the complete frequency range, shown in red) agree well with those obtained by the [Bubblewrap](#) algorithm (cf. Fig. 7.6c and Fig. 7.8c in section 7.2).

Blue data points show the macro-bunch durations determined from the fit to the local maximum. In the low-density scan at  $n_1$  (Fig. 7.18b), the width of this feature is smaller and would correspond to a longer duration of approximately 150 %, albeit afflicted with large shot-to-shot fluctuations. As noted before, this discrepancy may reveal that some of the applied assumptions are violated, e.g. the presence of a non-constant micro-bunch spacing.

In the  $n_2$  scan shown in Fig. 7.18c, both widths approximately coincide up to a gas cell length of  $L \leq 6$  mm. For longer acceleration lengths a distinct maximum at  $\omega_{\text{peak}}$  can no longer be identified, as exemplary shown by the [CTR](#) spectra plotted in Fig. 7.19, presumably due to changes of the longitudinal beam structure induced by dephasing or increased interaction of the electron bunch with the rear of the laser pulse.

## 7. Characterisation of the longitudinal bunch profile by CTR

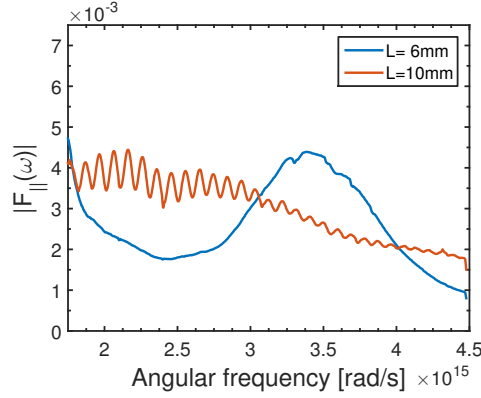


**Figure 7.19:** Example of the CTR emission in the optical range before and after dephasing of the 1<sup>st</sup> bunch in the high-density ( $n_2$ ) case. For  $L < 8$  mm a distinct peak is observable for almost all recorded shots, while for  $L \geq 8$  mm this is not the case. The comparable amount of CTR indicates that small scale features, although more randomly distributed, are still present in the longitudinal bunch profile.

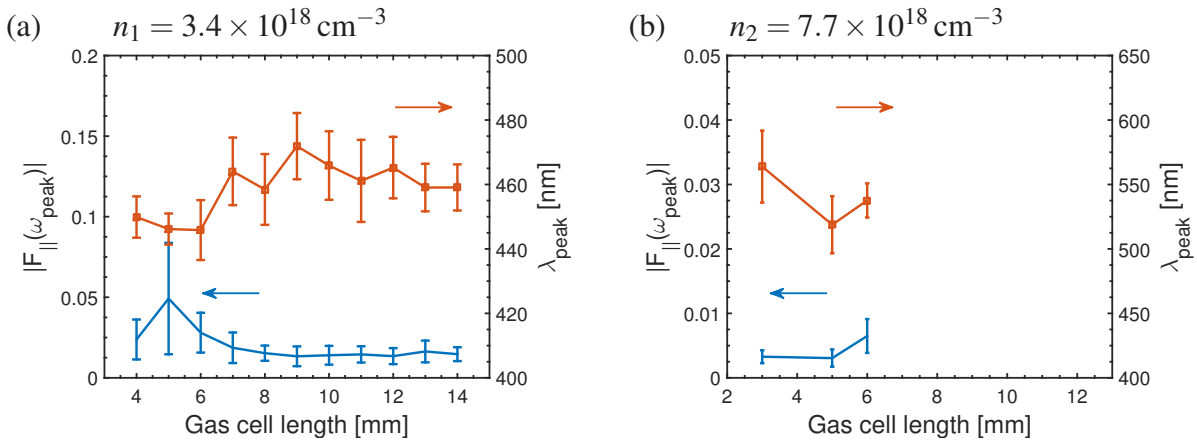


**Figure 7.20:** Center wavelength and amplitude of the enhancement. (a) and (b) show the center wavelength  $\lambda_{peak}$  and amplitude  $|F_{\parallel}(\omega_{peak})|$  of the feature for the length scan conducted at  $n_1$  and  $n_2$ , respectively. Data points show the mean values obtained at each length setting of the gas cell and error bars display the shot-to-shot rms variations.

The height and position  $\lambda_{peak}$  of the feature are plotted in Fig. 7.20a and b. It is observed that its height is roughly constant within the error bars and therefore approximately independent of  $L$ . Thus, the modulation of the bunch profile with  $\lambda_{peak}$  is present even for short acceleration distances.

### Possible origin of the bunch profile modulation

The fact that the modulation period is remarkably close to half the laser wavelength  $\lambda_L$  suggests that the short scale modulations of the bunch profile are related to the frequency of the laser field.

Micro-bunching of the electron beam has been observed previously in PIC simulations. These publications ascribe the micro-structure to partially coherent betatron oscillations, for which the

modulation period resembles the wavelength of the local laser field, leading to a micro-bunching at twice the laser frequency due to the  $\mathbf{v} \times \mathbf{B}$  force [159–161]. Since the interaction is caused by the overlap of the electron bunch with the rear of the laser pulse, the modulation depth is expected to grow with propagation length, due to a longer interaction time and an increasing vector potential as the distance between the electron bunch and the laser pulse decreases by electron dephasing. However, in the present case, the amplitude of the enhancement is independent of acceleration length. Hence, it must be concluded that the micro-structure is either imprinted during a very early stage of acceleration or by the injection process itself.

With respect to latter, the injection probability could potentially be modified by an electron's initial longitudinal momentum. As outlined in section 2.1, the trajectory of a single electron exposed to the laser field consists out of a transverse motion with  $\omega_L$  and a forward motion caused by the  $\mathbf{v} \times \mathbf{B}$  force. Omitting the cycle average in the derivation of the ponderomotive force, an electron's final momentum after interaction with the laser pulse is ultimately determined by the initial laser phase and its transverse position with respect to the focus. Since in plasma  $v_{ph}$  and  $v_{gr}$  differ, the phase of the carrier wave with respect to the pulse envelope changes with propagation. This so-called *carrier-envelope phase* (CEP) increases by  $2\pi$  after a time  $t_{CEP} = \lambda_L / (v_{ph} - v_{gr})$ . During this time, a trapped relativistic electron bunch progresses a distance  $d = (c - v_{gr}) t_{CEP}$  towards the driver pulse. Using eqs. (2.43, 2.44), this yields

$$d = \frac{c - v_{gr}}{v_{ph} - v_{gr}} \lambda_L = \frac{1}{\eta(1 + \eta)} \lambda_L \approx \frac{1}{2} \lambda_L. \quad (7.10)$$

Assuming an asymmetric laser focus, electrons pushed out by the intensity gradient therefore carry a difference in their obtained energy and longitudinal momentum dependent on the CEP of the laser pulse, which translates into a periodicity of  $\lambda_L/2$  in a trapped electron bunch's co-moving frame. Close to the trapping threshold, this difference may determine if an electron has a sufficient longitudinal momentum to get injected in the wakefield, which would relate the observed enhancement to the initial electron-laser interaction.

In conclusion, the local enhancement of the form factor at  $\omega_{peak}$  provides strong evidence for a slight micro-bunching of the longitudinal bunch profile caused by an interaction with the laser pulse. This finding certainly warrants further investigation by carrying out additional studies of its dependence on the experimental parameters as well as performing PIC simulations to identify the definitive mechanism. For example, decreasing the laser pulse duration and increasing the laser vector potential  $a_0$  while lowering the plasma density to tune the wakefield strength close to the injection threshold may enhance the effect, leading to a higher modulation depth and a more well-defined micro-bunch spacing.

As shown in this section, imprinting a constant modulation onto the bunch profile is a convenient way to produce a replica of the bunch's form factor in the visible range of the spectrum, which is experimentally accessible by much simpler means. Regarding practical applications, the signal may then be analysed by standard ultra-short pulse measurement techniques such as FROG, which are able to simultaneously retrieve the spectral phase information. Such measurements would allow to determine the longitudinal bunch profile by a simple Fourier transform, significantly simplifying both the measurement and the retrieval process in future experiments.



---

# Chapter 8

## Outlook

The presented work shows that a bunch profile diagnostic based on the detection of [CTR](#) provides an important tool that can not only be used to characterize ultra-short bunch lengths, but which also proved to be crucial for a deeper understanding of the physical mechanisms involved in [LWFA](#).

In the presented experiments, single electron bunches with a determined duration of  $4.8 \pm 0.2$  fs [FWHM](#) and a peak current of  $5.7 \pm 1.2$  kA were accelerated up to  $653 \pm 51$  MeV within an acceleration length of 9 mm. At a higher plasma density, peak currents of  $27 \pm 5$  kA could be obtained with a slightly increased pulse duration of  $5.8 \pm 0.2$  fs [FWHM](#) and a maximum energy of  $730 \pm 58$  MeV within 5 mm of acceleration. The evaluated peak charge densities are sufficient to drive a significant beam-driven wakefield. In combination with a gas target of variable length, the presented single-shot measurement technique further allowed new insights into the evolution of the temporal bunch profile in dependence of the target length. Supported by [PIC](#) simulations, the results revealed that the beam-driven wakefield can lead to the injection of a second bunch if the acceleration length exceeds the electron dephasing length. Besides determining important beam parameters, this work contributes to a better understanding of the physics of bunch evolution and the dynamics of electron injection in wakefield accelerators. The results and methods presented in this thesis are of interest for future developments, especially in the view of the growing aspirations of [PWFA](#) as well as for studies of plasma accelerators driving compact X-ray light sources.

In recent years, [PWFA](#) has attracted increasing attention as a potential technology for next generation high energy colliders, due to the significantly higher acceleration gradients compared to conventional accelerators, potentially reducing the required acceleration length from several tens of kilometres to the scale of meters. For this purpose, existing conventional accelerator infrastructure could be used to provide a high-charge bunch to drive a wakefield, while a lower-charge witness bunch residing in the wakefield's accelerating phase is efficiently accelerated to high energy [23]. Several conventional accelerator facilities have started research aimed at establishing the foundations of this concept [162]. For these state-of-the-art accelerators, generating high-current, ultra-short bunches is still a demanding task, requiring substantial effort for compressing, timing and focusing of two ultra-short electron beams with respect to the microscopic dimensions of the plasma wave.

By choosing an appropriate target length to facilitate injection of a 2<sup>nd</sup> bunch, the plasma dy-

## 8. Outlook

namics observed in this work open up the possibility to conveniently generate such double bunch structures. This approach allows to study the physics of **PWFA** at low energy in a second plasma stage without the need for a large-scale accelerator, significantly simplifying the experimental setup and extending the scope also to university laboratories.

On the other hand, the intrinsically short bunch durations provided by **LWFAs** are well suited to drive a variety of compact and cost-effective, though ultra-short and highly brilliant X-ray sources, based for example on Thomson-scattering or betatron radiation [150, 163–165]. By delivering peak currents in the kA range, **LWFAs** even possess the potential for realizing table-top **FELs** [166, 167]. These next-generation light sources promise few-femtosecond X-ray pulses intrinsically synchronized to a laser pulse, thus enabling pump-probe experiments with femtosecond resolution.

Up to date, **FEL** operation and **PWFA** experiments routinely rely on conventional **RF** accelerators. Due to their purpose of providing high peak currents, these represent the most advanced short-pulse linear accelerators currently available worldwide. Table 8.1 gives an overview of some of their main beam parameters and those of **LWFA** electron beams as determined in this thesis.

	LCLS [168, 169]	FACET [170]	FLASH [171, 172]	LWFA
Electron energy [GeV]	2 – 16	23	1.25	0.7
Energy spread	$\lesssim 1\%$	3 %	N/A	100%
Bunch charge [pC]	20 – 250	3000	70	30 – 175
Peak current [kA]	$\sim 3$	$\sim 20$	$\sim 2.5$	6 – 27
Bunch length (rms) [fs]	3 – 30	80	80	2 – 2.5
Emittance [ $\mu\text{m rad}$ ]	0.4 – 1	$50(\epsilon_x)/5(\epsilon_y)$	2	0.7
Repetition rate [Hz]	120	10	10	5

**Table 8.1:** Comparison of the electron beam parameters of current ultra-short-pulse linear accelerators and the beam properties obtained by **LWFA** as determined in this thesis. The value for the emittance of **LWFA** was taken from ref. [20]. Apart from the final beam energy and the energy spread, the properties of **LWFA** beams are comparable to those of state-of-the-art accelerators. Note that in order to achieve the shortest possible bunch length and smallest emittance, the **LCLS** beam charge corresponds to the lower margin.

**LCLS** and **FACET** refer to two linear accelerators located at **SLAC** National Accelerator Laboratory, Stanford, USA, that are used to seed the **LCLS**’s **FEL** and enable **PWFA** experiments, respectively. **FLASH** refers to the electron accelerator located at **DESY**, Hamburg, that drives the **FLASH**’s **FEL**. Unlike **LWFAs**, in which the injected electron bunch is intrinsically short, these accelerators need to imprint a positive energy chirp on the beam, such that it can finally be compressed in a magnetic chicane. After compression, the time slice that leads to free-electron lasing contains less than the nominal charge as it typically has to possess an energy spread on the sub-percent level.

As seen from table 8.1, except for the final beam energy and the energy spread, the properties of **LWFA** electron beams are comparable to these sources, at a fraction of their size and cost. Further improvement of the **LWFA** beam parameters could enable the envisioned table-top **FELs** in the near future. While electron beams with 4.2 GeV (6 % **rms** energy spread) have been reported

---

[17], methods for controlling the injection process hold promise for a further decrease of the energy spread. For example, by using a sharp plasma density transition, Buck et al. [19] obtained a constant absolute energy spread of  $\sim 5$  MeV FWHM for electron bunches in a tunable energy range between 10 – 130 MeV. If this spread can be maintained while increasing the final beam energy, relative energy spreads below 1 % become feasible.

Nevertheless, FELs currently in operation usually require an even lower slice energy spread to achieve free-electron lasing. For example, the slice energy spread at LCLS is  $\sigma_E/E \approx 0.01$  % [5]. Although the energy chirp of LWFA beams has not yet been determined experimentally, the PIC simulations presented in section 7.4 indicate that the electron bunch carries a negative energy chirp which is not compressible by magnetic chicanes. However, due to the correlation, its time slices possess a much smaller slice energy spread that may prove satisfactory. It will therefore be important to not only characterize the bunch length but the complete longitudinal phase space in future experiments. With this knowledge, the impact of the energy spread may further be mitigated by using a tapered undulator design and a chromatically elongated electron beam focus, such that the respective energy slices experience optimal resonance along the tapered undulator, a concept called chromatic focus matching [173, 174].

To design such an optimized undulator setup, a detailed knowledge of the beam's longitudinal phase space distribution will be necessary. For this purpose, the bunch profile diagnostic developed in this thesis can be utilized in conjunction with a magnetic chicane to record the bunch profile in dependence of an additionally induced chirp, which would enable a limited angle phase space tomography. Theoretical work towards this goal of a full longitudinal phase space reconstruction is currently carried out in the framework of a PhD thesis by Sebastian Raith [175]. Once the longitudinal phase space distribution is determined, a tapered undulator and associated focusing optics can be designed that take advantage of the intrinsic energy chirp and the ultra-high peak currents of LWFA electrons. This may pave the way for table-top FELs in the near future, which would dramatically reduce the cost of beamtime, bringing the prospect of access to ultra-short, highly brilliant X-ray sources even to university-scale laboratories as well as industry and medicine.





---

## Appendix A

# Spectral response of the mid-infrared spectrometer

Recalling eq. (5.11), the absolute value of the longitudinal form factor is given by

$$|F_{\parallel}(\omega)| = \sqrt{\frac{dW/d\omega}{2\epsilon_0 c N^2 \left| \int g(\mathbf{p}) T(\omega, \mathbf{p}) \mathbf{E}(\omega, \mathbf{p}) F_{\perp}(\omega) d\mathbf{p} \right|^2}}. \quad (\text{A.1})$$

The experimentally accessible quantities are the electron energy spectrum  $g(\mathbf{p})$  and the CTR spectral energy  $dW/d\omega$ .

The spectral energy measured by the mid-infrared spectrometer is determined from the raw signal counts  $S_n$  of the readout channel  $n$  by

$$\frac{dW}{d\omega_n} = \frac{S_n R(\omega_n) A}{\Delta\omega_n}, \quad (\text{A.2})$$

where  $\omega_n$  denotes the central frequency covered by the  $n^{\text{th}}$  pyroelectric detector,  $\Delta\omega_n$  denotes the covered frequency interval,  $R(\omega_n)$  is the relative spectral response of the detector and the proportionality constant  $A$  corresponds to an absolute calibration factor given in [nJ/count].

The integral in the denominator of eq. (A.1) is determined from the electron energy spectrum as described in chapter 5 and yields the transmission function  $T'(\omega)$ , given by

$$T'(\omega) = 2\epsilon_0 c N^2 \left| \int g(\mathbf{p}) T(\omega, \mathbf{p}) \mathbf{E}(\omega, \mathbf{p}) F_{\perp}(\omega) d\mathbf{p} \right|^2. \quad (\text{A.3})$$

Thus, eq. (A.1) can be expressed by

$$|F_{\parallel}(\omega_n)| = \sqrt{\frac{S_n R(\omega_n) A}{\Delta\omega_n T'(\omega_n)}}. \quad (\text{A.4})$$

Based on the last equation, we will proceed to discuss the contribution of the different terms to the measurement uncertainty of  $|F_{\parallel}(\omega_n)|$ .

In contrast to the visible and near-infrared CTR spectrometers, which were calibrated by commonly available light sources, an experimental calibration of the mid-infrared detector was not

## A. Spectral response of the mid-infrared spectrometer

---

performed, although an attempt for a calibration during a dedicated beamtime at FELBE (an FEL located at the Forschungszentrum Dresden-Rossendorf, Germany) was undertaken. This was due to the challenging properties required: On the one hand, the radiation has to be pulsed with durations  $< 8 \mu\text{s}$ , a limitation set by the shaping amplifiers in the readout electronics. On the other hand, pulse energies on the order of several nJ per detector element are necessary to obtain a sufficient signal-to-noise ratio (these requirements already exclude the use of simple constant light sources such as blackbody radiators, but coherent light sources are required). However, the FEL's macro-pulse duration  $> 200 \mu\text{s}$  was too long to provide a step-like input signal to the spectrometer's shaping amplifiers. Furthermore, the spectral bandwidth was too large to focus the FEL beam to a single pyroelectric detector pixel with the gratings in place. In the end, the accumulated uncertainty in the actual pulse energy incident on each detector pixel did not allow to obtain a reliable calibration.

Therefore, it was opted to base the relative calibration of the mid-infrared spectrometer on the available spectral response curves of its components. The calibration was later compared to the expected response, which allowed a fine-tuning of  $R(\omega_n)$ . This procedure will be described below.

### Relative calibration $R(\omega_n)$

The relative calibration  $R(\omega_n)$  includes the contribution of the following terms: the transmittivity of the silicon wafer, the gratings' diffraction efficiencies, the spectral response of a generic pyroelectric crystal and variations in sensitivity between the individual readout channels. These sources will now be discussed. An overview over these quantities is plotted in Fig. A.1.

- As shown in Fig. A.1a, the transmission through the silicon low-pass filter is  $52.5 \pm 2.5 \%$  throughout the relevant spectral range from  $1.7 - 7.1 \mu\text{m}$ .
- The gratings' diffraction efficiencies, exemplarily shown in Fig. A.1b, rely on numerical calculation. A deviation from the expected efficiencies due to imperfections in the manufacturing process can not be assessed by the software.
- Figure A.1c shows the spectral response of a particular pyroelectric crystal connected to the read-out electronics, which has been determined at the FEL light source Felix in the diploma thesis of Christopher Behrens [149]. This data only covers 17 of the long-wavelength channels of our setup, as the response for  $\lambda < 5.1 \mu\text{m}$  had not been measured. For the unmeasured wavelengths, initially a flat response equal to the shortest measured wavelength was assumed.
- The absolute efficiency of the 60 pyroelectric detector elements at a wavelength of  $1064 \text{ nm}$  was determined using a Q-switched Nd:YAG laser. The raw signal counts of each channel, when illuminated with a pulse energy of  $25 \text{ nJ}$ , are shown in Fig. A.1d, where 230 measurements were taken for each channel. The statistical error amounts to  $1 - 8$  raw signal counts depending on the channel number. Apart from 5 faulty channels, variations in detection efficiency between individual channels are clearly observed, corresponding to a standard deviation between the channels of  $11 \%$ .

The relative calibration was thus hampered by two issues. First, spectral response data of a single pyro-element was unavailable in the range of  $\lambda = 1.7 - 5.1 \mu\text{m}$  and, even if it were present, the rather strong differences in detection efficiency at  $\lambda = 1064 \mu\text{m}$  between individual readout channels suggest that such variations may also be present in the individual spectral response curves.

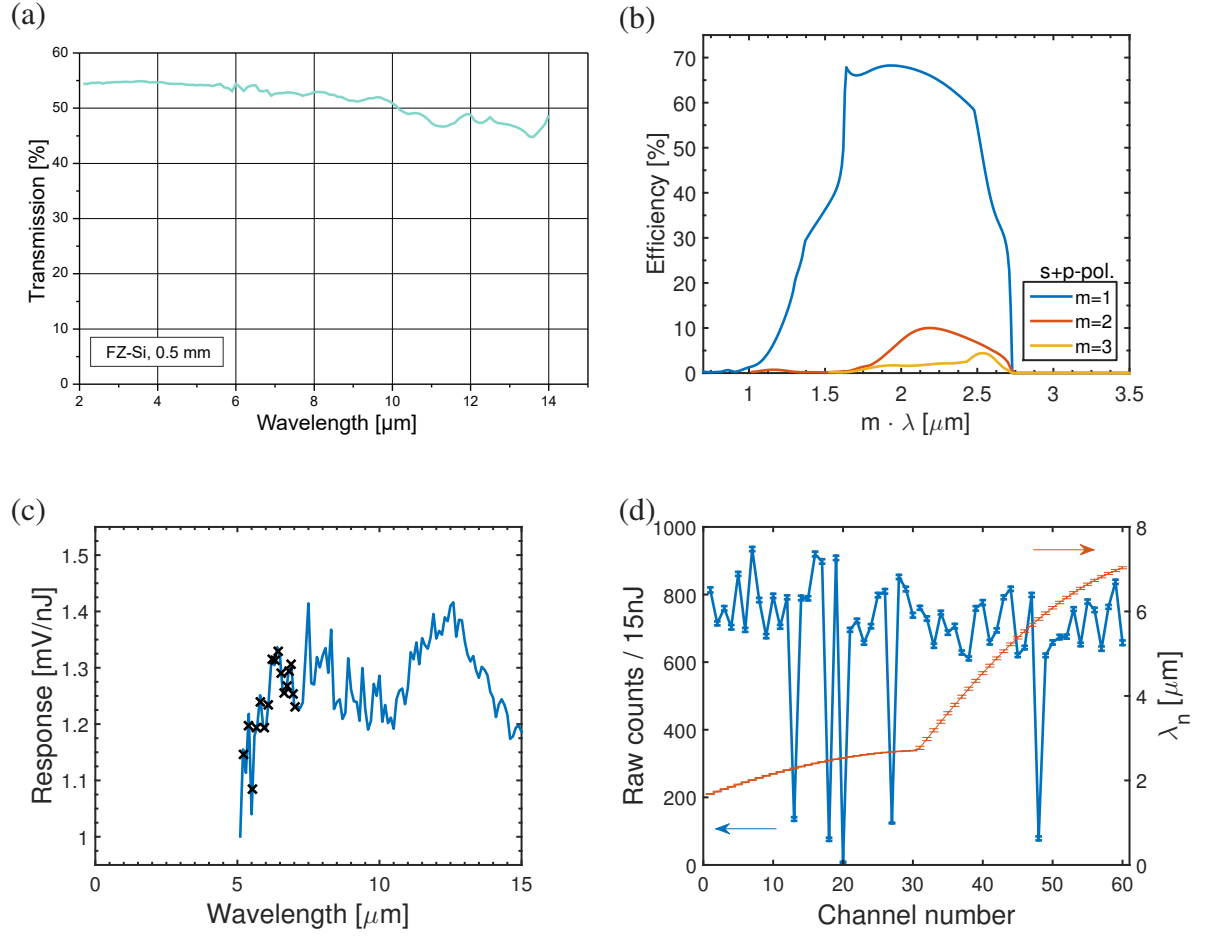


**Figure A.1:** Overview of the different sources that contribute to the relative spectral response function  $R(\omega)$ . (a) Transmission of CTR through the silicon wafer. (b) Grating efficiency of 1<sup>st</sup> order diffraction. (c) Spectral response of a single pyroelectric detector of type InfraTec X003 for wavelengths  $\lambda \geq 5.1 \mu\text{m}$ . Data courtesy of Behrens [149]. Data points mark the 17 channels of the mid-infrared spectrometer that reside within the measured spectral range. (d) Raw response of each detector channel (blue) when illuminated with 25 nJ pulses from a Q-switched Nd:YAG laser at a wavelength of  $\lambda = 1064 \text{ nm}$ . Error bars indicate the statistical error of 230 shots. Besides a couple of dead channels, the deviation between individual channels corresponds to 11% *rms*. Shown in red is the central wavelength  $\lambda_n$  covered by each pyrodetector in the experiment, where error bars indicate the  $1\sigma$  confidence interval ( $< 1.5\%$ ) due to the uncertainty in the gratings' incidence and diffraction angles. Note that due to the known dispersive power of the gratings, the wavelength interval  $\Delta\omega_n$  covered by each pyrodetector is accurate to within  $< 0.5\%$ .

In the course of the data analysis it was found that systematic variations in efficiency were indeed present, as some channels showed a consistent difference in signal strength compared to their neighbours. This finding was independent of the experimental conditions such as the length of gas cell or the plasma density. These systematic variations in efficiency add apparent artificial noise in the measured single-shot signal and typically caused the longitudinal bunch profile returned by the [Bubblewrap](#) algorithm to contain small subsidiary bunches. The systematic variations were therefore corrected in the following way:

## A. Spectral response of the mid-infrared spectrometer

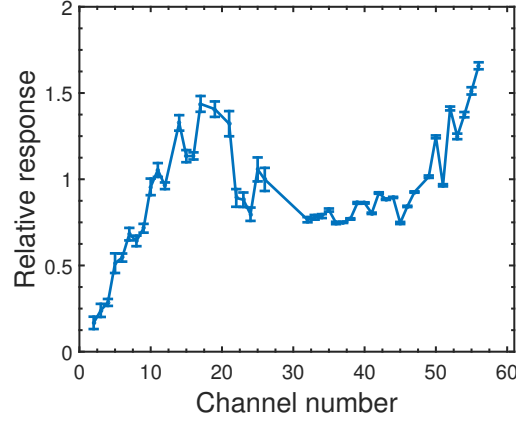


**Figure A.2:** Relative spectral response  $R(\omega_n)$ . Shown is the linear correction factor applied to each pyroelectric detector channel. Error bars indicate the 68 % confidence interval of the least-squares linear fit.

For a specific run ( $L = 5$  mm,  $n_0 = 3.4 \times 10^{18} \text{ cm}^{-3}$ , 30 consecutive shots), in which only a single bunch was generated, as confirmed by the smooth shape in the visible and near-infrared spectrometers, the subsidiary electron bunches in the retrieved spectra were filtered out, which allowed to calculate the CTR spectra generated by a single bunch. These spectra were then compared to the measured data and a linear fit between expected and measured signal counts yielded a linear correction factor for each pyroelectric detector channel. The resulting relative calibration curve  $R(\omega_n)$  is shown in Fig. A.2 and was subsequently applied in the analysis of all other data.  $R(\omega_n)$  includes any deviation of the transmittivity of the silicon wafer from the curve provided by the manufacturer, deviations of the gratings' diffraction efficiencies from the calculated values as well as differences in the detection efficiency and spectral response of the individual pyrodetectors.

### Absolute calibration

The absolute correspondence between the raw signal counts and the incident radiation energy was determined with a Nd:YAG laser. It was assumed that the absorption at  $\lambda = 1064 \text{ nm}$  equals that of the first detector channel located at  $\lambda_1 = 1.67 \mu\text{m}$ . Further, the reflectivity of the gold mirrors used in the detection system was taken into account, assuming a flat reflectivity of 97 % for each reflection. Depending on frequency, CTR was either detected by the first or the second grating stage, which included 5 or 6 reflections, respectively.

## A.1 Measurement uncertainty in the frequency domain

According to eq. (A.4), the relative error of  $|F_{||}|$  is given by

$$\sigma_{F_{||}} = \frac{1}{2} \sqrt{\sigma_{T'}^2 + \sigma_R^2 + \sigma_{S_n}^2 + \sigma_{\Delta\omega}^2}, \quad (\text{A.5})$$

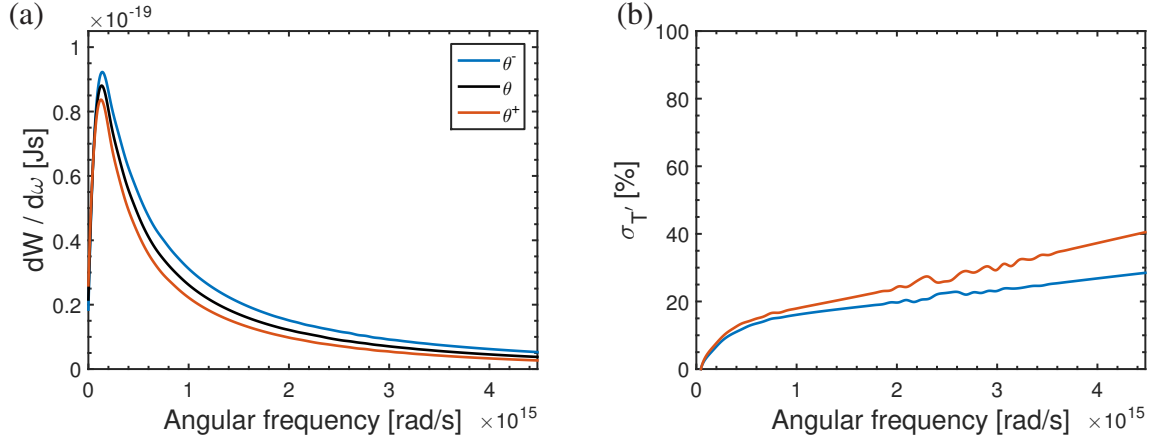


**Figure A.3:** Influence of the beam divergence on the CTR transmission function  $T'(\omega)$  for a typical shot. (a) shows the frequency dependent CTR transmission for the mean divergence  $\theta$  (black line) determined from a 30 shot dataset.  $\theta^+$  and  $\theta^-$  correspond to a divergence of  $\pm$  one standard deviation from the mean. (b) shows the corresponding relative error margins using the same colour code as (a), i.e.  $|T_{\theta^\pm} - T_\theta|/T_{\theta^\pm}$ .

where  $\sigma$  denotes the relative error in each quantity. Their contributions to  $\sigma_{F_\parallel}$  will now be discussed individually:

$\sigma'_T$ :

The most significant measurement error originates from the uncertainty in bunch divergence, which translates into an uncertainty in the transverse electron beam size at both CTR radiators. By eq. (A.3), the resulting error in  $F_\perp$  leads to an error in  $T'(\omega)$ , due to a reduced CTR emission with increased opening angle if the bunch divergence is increased (cf. section 3.2).

To quantify the relative error  $\sigma'_T$ , the CTR transport calculation was performed for bunch divergences of  $\theta^\pm = \theta \pm \sigma_\theta$ , where  $\sigma_\theta$  denotes the shot-to-shot standard deviation of the 30 shot dataset evaluated in section 6.1 and  $\theta$  is its mean value. The resulting transmission curves are plotted in Fig. A.3a, showing the decrease of CTR radiation with increased divergence and source size at the radiators. Figure A.3b shows the resulting relative error  $\sigma'_T$ .

$\sigma_R$ :

The second source of error stems from the relative spectral response  $R(\omega_n)$  described in the last section, which includes the sources of error shown in Fig. A.1. Here, the confidence interval of the linear correction factor for each channel (shown as error bars in Fig. A.2) divided by its mean is taken as the relative error  $\sigma_R$ .

$\sigma_{S_n}$ :

A third uncertainty is introduced by the readout noise of  $S_n$  (the count rate determined by the pyroelectric detector electronics), which amounts to 4 – 6 raw counts. The relative error is therefore dependent on the signal level  $S_n$  of each channel and has to be evaluated for each shot.

$\sigma_{\Delta\omega_n}$ :

Since the gratings' incidence and emergence angles could be determined to within  $\pm 0.5^\circ$ , the relative error regarding the frequency range  $\Delta\omega_n$  covered by each pyroelectric crystal amounts to  $\sigma_{\Delta\omega_n} < 0.5\%$  and is therefore negligible.

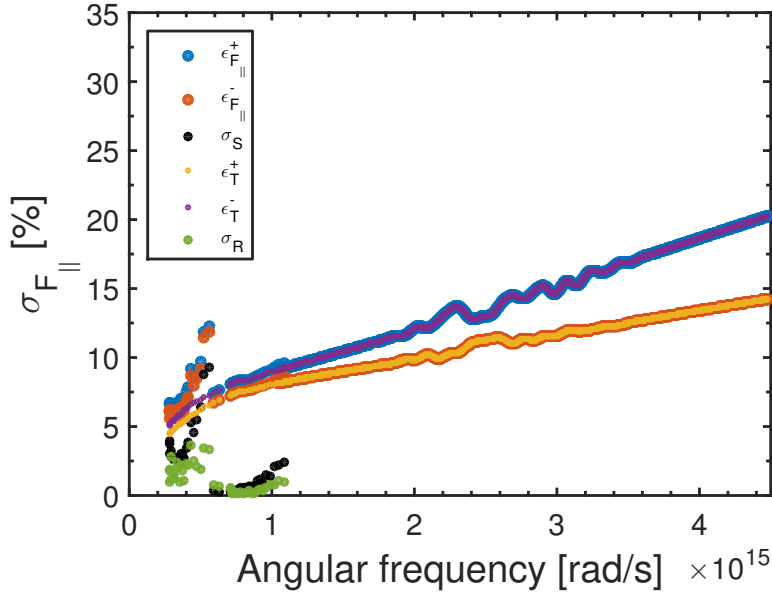


**Figure A.4:** Relative error  $\sigma_{F_{\parallel}}$  in the measurement of the longitudinal form factor. Error margins are given for the 68 % confidence interval. Lower and upper error margins are denoted by  $\epsilon^{(+,-)}$ , symmetrically distributed errors are denoted by  $\sigma$ .

The relative error  $\sigma_{F_{\parallel}}$ , resulting from the combination of these error sources is plotted in Fig. A.4 for a CTR measurement with a typical count rate of the pyroelectric detectors. The dominant error stems from the uncertainty in bunch divergence and hence  $\sigma_{T'}$ . In the spectral region up to  $2 \times 10^{15}$  rad/s, which contains the main part of the CTR energy, the relative error amounts to  $\lesssim 15\%$ .

The absolute measurement error of the mid-infrared spectrometer is caused the difference in detector efficiency at the calibration wavelength of  $\lambda = 1064$  nm and the first detector frequency bin at  $\lambda = 1.67 \mu\text{m}$ , as well as the actual mirror reflectivities that were assumed to be 97 %. However, in the context of the determination of the bunch profile, the absolute error is of minor interest as the shape of the bunch profile is encoded in the shape of the CTR spectrum.

## A.2 Measurement uncertainty in the time domain

Since the measured longitudinal form factor and the bunch profile are related by a Fourier transform, the measurement uncertainty in the frequency domain cannot be analytically transferred in the temporal domain. Nevertheless, the induced uncertainty in the time domain can be roughly assessed by retrieving the bunch profile from different form factors, which correspond to the upper and lower error margins of the measurement. This procedure is shown in Fig. A.5 for two exemplary shots.

In Fig. A.5a and b, the measured data points are shown along with the reconstructed form factors, for which the initial spectrum fed to the retrieval algorithm was set to the measured data points (red) as well as the upper (blue) and lower (yellow) error limits. The respective retrieved



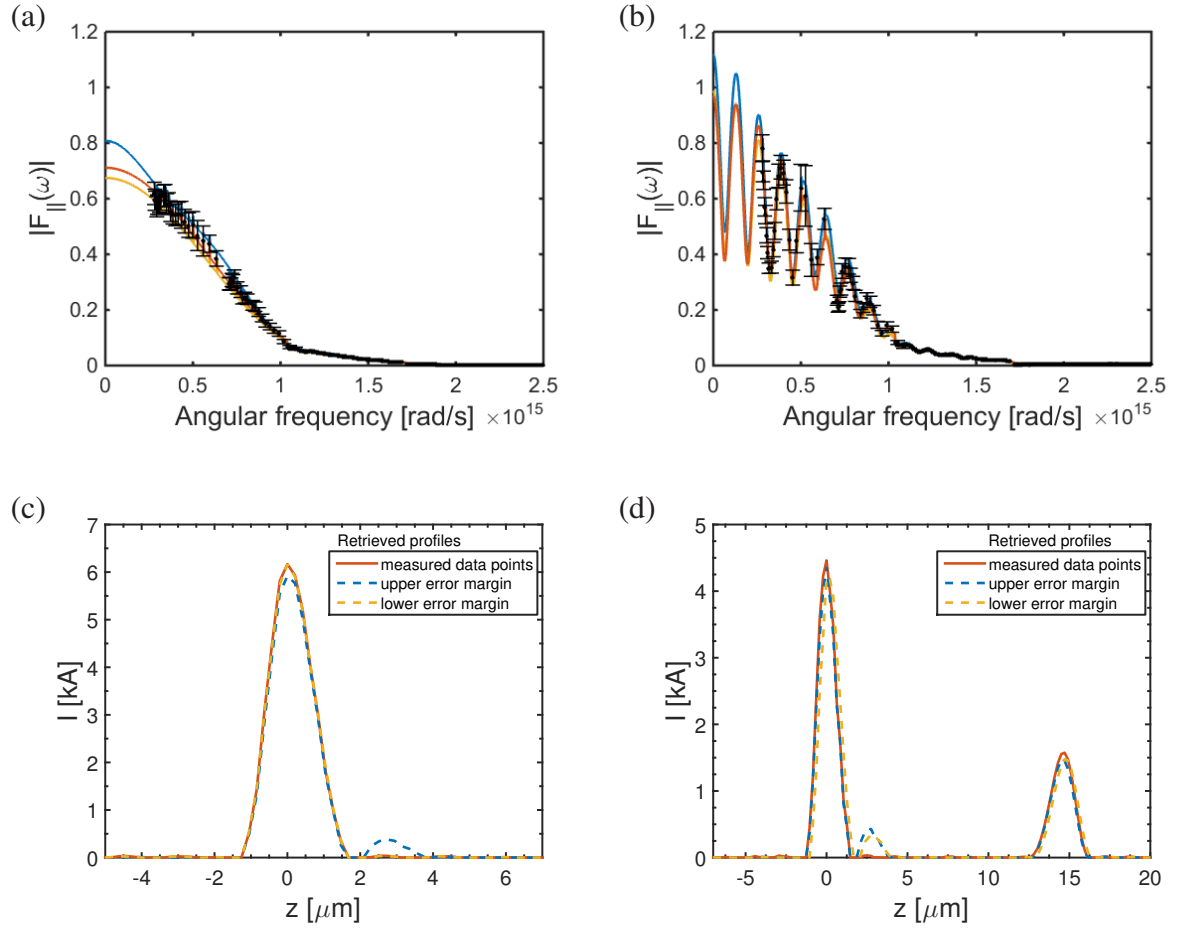


**Figure A.5:** Assessment of the measurement uncertainty in the time domain. (a) and (b) show the measured data points (black) from two single-shots. The *Bubblewrap* retrieval algorithm was started from the measured data points and afterwards from an input spectrum corresponding to the upper and lower error margins. The retrieved spectra are shown in red, blue and yellow, respectively. The retrieved bunch profiles are shown in (c) and (d) with the same colour code.

bunch profiles are shown in Fig. A.5c and d. For the single shot shown in Fig. A.5a and c, the retrieved *FWHM* bunch durations are 4.83 fs, 4.85 fs and 4.85 fs for the measured data points and the upper and lower error margin, respectively. For the shot shown in Fig. A.5b and d, the retrieved durations are 4.41 fs, 4.44 fs and 4.67 fs, respectively. As demonstrated for these two exemplary shots, the uncertainty in the spectral domain leads to an uncertainty in the time domain of  $\lesssim 0.3$  fs for *CTR* spectra corresponding to bunch durations of  $\sim 4.5$  fs *FWHM*. This translates into a relative measurement error in the time domain of  $\lesssim 7\%$ .



# Bibliography

- [1] The CMS Collaboration. *Evidence for the direct decay of the 125 GeV Higgs boson to fermions*. [Nature Physics](#), 10(8):557, 2014.
- [2] Barbalat, O. *Applications of particle accelerators*. Technical report, CERN, 1994.
- [3] Anderson, M.H., Ensher, J.R., Matthews, M.R., Wieman, C.E., and Cornell, E.A. *Observation of Bose-Einstein Condensation in a Dilute Atomic Vapor*. [Science](#), 269(5221):198, 1995.
- [4] Ayvazyan, V., Baboi, N., Bohnet, I., Brinkmann, R., Castellano, M., Castro, P., Catani, L., Choroba, S., Cianchi, A., Dohlus, M., Edwards, H.T., Faatz, B., Fateev, A.A., Feldhaus, J., Flöttmann, K., Gamp, A., Garvey, T., Genz, H., Gerth, C., Gretchko, V., et al. *Generation of GW Radiation Pulses from a VUV Free-Electron Laser Operating in the Femtosecond Regime*. [Physical Review Letters](#), 88(10):104802, 2002.
- [5] Emma, P., Akre, R., Arthur, J., Bionta, R., Bostedt, C., Bozek, J., Brachmann, A., Bucksbaum, P., Coffee, R., Decker, F.J., Ding, Y., Dowell, D., Edstrom, S., Fisher, A., Frisch, J., Gilevich, S., Hastings, J., Hays, G., Hering, P., Huang, Z., et al. *First lasing and operation of an ångstrom-wavelength free-electron laser*. [Nature Photonics](#), 4(9):641, 2010.
- [6] Aquila, A., Barty, A., Bostedt, C., Boutet, S., Carini, G., dePonte, D., Drell, P., Doniach, S., Downing, K.H., Earnest, T., Elmlund, H., Elser, V., Gühr, M., Hajdu, J., Hastings, J., Hau-Riege, S.P., Huang, Z., Lattman, E.E., Maia, F.R.N.C., Marchesini, S., et al. *The linac coherent light source single particle imaging road map*. [Structural Dynamics](#), 2(4):041701, 2015.
- [7] Chapman, H.N., Barty, A., Bogan, M.J., Boutet, S., Frank, M., Hau-Riege, S.P., Marchesini, S., Woods, B.W., Bajt, S., Benner, W.H., London, R.A., Plönjes, E., Kuhlmann, M., Treusch, R., Düsterer, S., Tschentscher, T., Schneider, J.R., Spiller, E., Möller, T., Bostedt, C., et al. *Femtosecond diffractive imaging with a soft-X-ray free-electron laser*. [Nature Physics](#), 2(12):839, 2006.
- [8] Adolphsen, C., Barone, M., Barish, B., Buesser, K., Burrows, P., Carwardine, J., Clark, J., Durand, H.M., Dugan, G., Elsen, E., Enomoto, A., Foster, B., Fukuda, S., Gai, W., Gastal, M., Geng, R., Ginsburg, C., Guiducci, S., Harrison, M., Hayano, H., et al. *The International Linear Collider Technical Design Report - Volume 3.I: Accelerator R&D in the Technical Design Phase*. [Technical Report arXiv:1306.6353](#), Geneva, 2013.

## Bibliography

---

- [9] Inagaki, T., Kondo, C., Maesaka, H., Ohshima, T., Otake, Y., Sakurai, T., Shirasawa, K., and Shintake, T. *High-gradient C-band linac for a compact x-ray free-electron laser facility*. [Physical Review Special Topics - Accelerators and Beams](#), 17(8):080702, 2014.
- [10] Tajima, T. and Dawson, J.M. *Laser Electron Accelerator*. [Physical Review Letters](#), 43(4):267, 1979.
- [11] Chen, P., Dawson, J.M., Huff, R.W., and Katsouleas, T. *Acceleration of Electrons by the Interaction of a Bunched Electron Beam with a Plasma*. [Physical Review Letters](#), 54(7):693, 1985.
- [12] Esarey, E., Schroeder, C.B., and Leemans, W.P. *Physics of laser-driven plasma-based electron accelerators*. [Reviews of Modern Physics](#), 81(3):1229, 2009.
- [13] Blumenfeld, I., Clayton, C.E., Decker, F.J., Hogan, M.J., Huang, C., Ischebeck, R., Iversen, R., Joshi, C., Katsouleas, T., Kirby, N., Lu, W., Marsh, K.A., Mori, W.B., Muggli, P., Oz, E., Siemann, R.H., Walz, D., and Zhou, M. *Energy doubling of 42 GeV electrons in a metre-scale plasma wakefield accelerator*. [Nature](#), 445(7129):741, 2007.
- [14] Mangles, S.P.D., Murphy, C.D., Najmudin, Z., Thomas, A.G.R., Collier, J.L., Dangor, A.E., Divall, E.J., Foster, P.S., Gallacher, J.G., Hooker, C.J., Jaroszynski, D.A., Langley, A.J., Mori, W.B., Norreys, P.A., Tsung, F.S., Viskup, R., Walton, B.R., and Krushelnick, K. *Monoenergetic beams of relativistic electrons from intense laser-plasma interactions*. [Nature](#), 431(7008):535, 2004.
- [15] Geddes, C.G.R., Toth, C., van Tilborg, J., Esarey, E., Schroeder, C.B., Bruhwiler, D., Nieter, C., Cary, J., and Leemans, W.P. *High-quality electron beams from a laser wakefield accelerator using plasma-channel guiding*. [Nature](#), 431(7008):538, 2004.
- [16] Faure, J., Glinec, Y., Pukhov, A., Kiselev, S., Gordienko, S., Lefebvre, E., Rousseau, J.P., Burgy, F., and Malka, V. *A laser-plasma accelerator producing monoenergetic electron beams*. [Nature](#), 431(7008):541, 2004.
- [17] Leemans, W.P., Gonsalves, A.J., Mao, H.S., Nakamura, K., Benedetti, C., Schroeder, C.B., Tóth, C., Daniels, J., Mittelberger, D.E., Bulanov, S.S., Vay, J.L., Geddes, C.G.R., and Esarey, E. *Multi-GeV Electron Beams from Capillary-Discharge-Guided Subpetawatt Laser Pulses in the Self-Trapping Regime*. [Physical Review Letters](#), 113(24):245002, 2014.
- [18] Osterhoff, J., Popp, A., Major, Z., Marx, B., Rowlands-Rees, T.P., Fuchs, M., Geissler, M., Hörlein, R., Hidding, B., Becker, S., Peralta, E.A., Schramm, U., Grüner, F., Habs, D., Krausz, F., Hooker, S.M., and Karsch, S. *Generation of Stable, Low-Divergence Electron Beams by Laser-Wakefield Acceleration in a Steady-State-Flow Gas Cell*. [Physical Review Letters](#), 101(8):085002, 2008.
- [19] Buck, A., Wenz, J., Xu, J., Khrennikov, K., Schmid, K., Heigoldt, M., Mikhailova, J.M., Geissler, M., Shen, B., Krausz, F., Karsch, S., and Veisz, L. *Shock-Front Injector for High-Quality Laser-Plasma Acceleration*. [Physical Review Letters](#), 110(18):185006, 2013.

- 
- [20] Weingartner, R., Raith, S., Popp, A., Chou, S., Wenz, J., Khrennikov, K., Heigoldt, M., Maier, A.R., Kajumba, N., Fuchs, M., Zeitler, B., Krausz, F., Karsch, S., and Grüner, F. *Ultralow emittance electron beams from a laser-wakefield accelerator*. [Physical Review Special Topics - Accelerators and Beams](#), **15**(11):111302, 2012.
- [21] Lundh, O., Lim, J., Rechatin, C., Ammoura, L., Ben-Ismaïl, A., Davoine, X., Gallot, G., Goddet, J.P., Lefebvre, E., Malka, V., and Faure, J. *Few femtosecond, few kiloampere electron bunch produced by a laser-plasma accelerator*. [Nature Physics](#), **7**(3):219, 2011.
- [22] Buck, A., Nicolai, M., Schmid, K., Sears, C.M.S., Savert, A., Mikhailova, J.M., Krausz, F., Kaluza, M.C., and Veisz, L. *Real-time observation of laser-driven electron acceleration*. [Nature Physics](#), **7**(7):543, 2011.
- [23] Litos, M., Adli, E., An, W., Clarke, C.I., Clayton, C.E., Corde, S., Delahaye, J.P., England, R.J., Fisher, A.S., Frederico, J., Gessner, S., Green, S.Z., Hogan, M.J., Joshi, C., Lu, W., Marsh, K.A., Mori, W.B., Muggli, P., Vafaei-Najafabadi, N., Walz, D., et al. *High-efficiency acceleration of an electron beam in a plasma wakefield accelerator*. [Nature](#), **515**(7525):92, 2014.
- [24] Seggebrock, T., Maier, A.R., Dornmair, I., and Grüner, F. *Bunch decompression for laser-plasma driven free-electron laser demonstration schemes*. [Physical Review Special Topics - Accelerators and Beams](#), **16**(7):070703, 2013.
- [25] Hidding, B., Königstein, T., Osterholz, J., Karsch, S., Willi, O., and Pretzler, G. *Monoeenergetic Energy Doubling in a Hybrid Laser-Plasma Wakefield Accelerator*. [Physical Review Letters](#), **104**(19):195002, 2010.
- [26] Debus, A.D., Bussmann, M., Schramm, U., Sauerbrey, R., Murphy, C.D., Major, Z., Hörlein, R., Veisz, L., Schmid, K., Schreiber, J., Witte, K., Jamison, S.P., Gallacher, J.G., Jaroszynski, D.A., Kaluza, M.C., Hidding, B., Kiselev, S., Heathcote, R., Foster, P.S., Neely, D., et al. *Electron Bunch Length Measurements from Laser-Accelerated Electrons Using Single-Shot THz Time-Domain Interferometry*. [Physical Review Letters](#), **104**(8):084802, 2010.
- [27] Lundh, O., Rechatin, C., Lim, J., Malka, V., and Faure, J. *Experimental Measurements of Electron-Bunch Trains in a Laser-Plasma Accelerator*. [Physical Review Letters](#), **110**(6):065005, 2013.
- [28] Bajlekov, S.I., Heigoldt, M., Popp, A., Wenz, J., Khrennikov, K., Karsch, S., and Hooker, S.M. *Longitudinal electron bunch profile reconstruction by performing phase retrieval on coherent transition radiation spectra*. [Physical Review Special Topics - Accelerators and Beams](#), **16**(4):040701, 2013.
- [29] Mehrling, T. *Theoretical and Numerical Studies on the Transport of Transverse Beam Quality in Plasma-Based Accelerators*. PhD thesis, [Hamburg University](#), 2014.
- [30] Jackson, J.D. *Classical electrodynamics*. [Wiley](#), New York, NY, 3rd edition, 1999.
- [31] Batani, D. *Atoms, Solids, and Plasmas in Super-Intense Laser Fields*. [Springer US](#), 2001.

## Bibliography

---

- [32] Noether, E. *Invariante Variationsprobleme*. *Nachrichten von der Gesellschaft der Wissenschaften zu Göttingen, Mathematisch-Physikalische Klasse*, 1918:235, 1918.
- [33] Weyl, H. *Elektron und Gravitation. I*. *Zeitschrift für Physik*, 56:330, 1929.
- [34] Bauer, D., Mulser, P., and Steeb, W.H. *Relativistic Ponderomotive Force, Uphill Acceleration, and Transition to Chaos*. *Physical Review Letters*, 75(25):4622, 1995.
- [35] Chen, F. *Introduction to Plasma Physics and Controlled Fusion: Volume 1: Plasma Physics*. Springer US, 2010.
- [36] Boyd, T.J.M. and Sanderson, J.J. *The Physics of Plasmas*. Cambridge University Press, 2003.
- [37] Keldysh, L.V. *Ionization in the field of a strong electromagnetic wave*. *Soviet Physics JETP*, 20:1307, 1965.
- [38] Gibbon, P. *Short Pulse Laser Interactions with Matter: An Introduction*. Imperial College Press, 2005.
- [39] Mulser, P. and Bauer, D. *High Power Laser-Matter Interaction*. Springer Tracts in Modern Physics. Springer Berlin Heidelberg, 2010.
- [40] Bohm, D. and Gross, E.P. *Theory of Plasma Oscillations. A. Origin of Medium-Like Behavior*. *Physical Review*, 75(12):1851, 1949.
- [41] Chen, X.L. and Sudan, R.N. *Two-dimensional self-focusing of short intense laser pulse in underdense plasma*. *Physics of Fluids B: Plasma Physics*, 5(4):1336, 1993.
- [42] Katsouleas, T., Wilks, S., Chen, P., Dawson, J.M., and Su, J.J. *Beam loading in plasma accelerators*. *Particle Accelerators*, 22(1):81, 1987.
- [43] Esarey, E., Sprangle, P., Krall, J., and Ting, A. *Self-focusing and guiding of short laser pulses in ionizing gases and plasmas*. *IEEE Journal of Quantum Electronics*, 33(11):1879, 1997.
- [44] Sprangle, P., Esarey, E., and Ting, A. *Nonlinear theory of intense laser-plasma interactions*. *Physical Review Letters*, 64(17):2011, 1990.
- [45] Fubiani, G., Esarey, E., Schroeder, C.B., and Leemans, W.P. *Beat wave injection of electrons into plasma waves using two interfering laser pulses*. *Physical Review E*, 70(1):016402, 2004.
- [46] Lu, W., Huang, C., Zhou, M.M., Mori, W.B., and Katsouleas, T. *Limits of linear plasma wakefield theory for electron or positron beams*. *Physics of Plasmas*, 12(6):063101, 2005.
- [47] Amiranoff, F., Baton, S., Bernard, D., Cros, B., Descamps, D., Dorchies, F., Jacquet, F., Malka, V., Marquès, J.R., Matthieussent, G., Miné, P., Modena, A., Mora, P., Morillo, J., and Najmudin, Z. *Observation of Laser Wakefield Acceleration of Electrons*. *Physical Review Letters*, 81(5):995, 1998.

- 
- [48] Gorbunov, L.M. and Kirsanov, V.I. *Excitation of plasma waves by an electromagnetic wave packet*. *Soviet Physics JETP*, 66:290, 1987.
- [49] Panofsky, W.K.H. and Wenzel, W.A. *Some Considerations Concerning the Transverse Deflection of Charged Particles in Radio-Frequency Fields*. *Review of Scientific Instruments*, 27(11):967, 1956.
- [50] Muggli, P. *Beam-driven, Plasma-based Particle Accelerators*. *CERN Yellow Reports*, 1(0):119, 2016.
- [51] Berezhiani, V.I. and Murusidze, I.G. *Relativistic wake-field generation by an intense laser pulse in a plasma*. *Physics Letters A*, 148(6):338, 1990.
- [52] Dawson, J.M. *Nonlinear Electron Oscillations in a Cold Plasma*. *Physical Review*, 113(2):383, 1959.
- [53] Akhiezer, A.I. and Polovin, R.V. *Theory of Wave Motion of an Electron Plasma*. *Soviet Physics JETP*, Vol: 3, 1956.
- [54] Sheng, Z.M. and Meyer-ter Vehn, J. *Relativistic wave breaking in warm plasmas*. *Physics of Plasmas*, 4(2):493, 1997.
- [55] Coffey, T.P. *Breaking of Large Amplitude Plasma Oscillations*. *Physics of Fluids*, 14(7):1402, 1971.
- [56] Katsouleas, T. and Mori, W.B. *Wave-Breaking Amplitude of Relativistic Oscillations in a Thermal Plasma*. *Physical Review Letters*, 61(1):90, 1988.
- [57] Lu, W. *Nonlinear plasma wakefield theory and optimum scaling for laser wakefield acceleration in the blowout regime*. PhD thesis, University of California, Los Angeles, 2006.
- [58] Rosenzweig, J.B., Breizman, B., Katsouleas, T., and Su, J.J. *Acceleration and focusing of electrons in two-dimensional nonlinear plasma wake fields*. *Physical Review A*, 44(10):R6189, 1991.
- [59] Pukhov, A. and Meyer-ter Vehn, J. *Laser wake field acceleration: the highly non-linear broken-wave regime*. *Applied Physics B*, 74(4-5):355, 2002.
- [60] Lu, W., Huang, C., Zhou, M., Mori, W.B., and Katsouleas, T. *Nonlinear Theory for Relativistic Plasma Wakefields in the Blowout Regime*. *Physical Review Letters*, 96(16):165002, 2006.
- [61] Lu, W., Tzoufras, M., Joshi, C., Tsung, F.S., Mori, W.B., Vieira, J., Fonseca, R.A., and Silva, L.O. *Generating multi-GeV electron bunches using single stage laser wakefield acceleration in a 3d nonlinear regime*. *Physical Review Special Topics - Accelerators and Beams*, 10(6):061301, 2007.
- [62] Kostyukov, I., Pukhov, A., and Kiselev, S. *Phenomenological theory of laser-plasma interaction in “bubble” regime*. *Physics of Plasmas*, 11(11):5256, 2004.



## Bibliography

---

- [63] Esirkepov, T., Bulanov, S.V., Yamagiwa, M., and Tajima, T. *Electron, Positron, and Photon Wakefield Acceleration: Trapping, Wake Overtaking, and Ponderomotive Acceleration*. [Physical Review Letters](#), 96(1):014803, 2006.
- [64] Schroeder, C.B., Esarey, E., Shadwick, B.A., and Leemans, W.P. *Trapping, dark current, and wave breaking in nonlinear plasma waves*. [Physics of Plasmas](#), 13(3):033103, 2006.
- [65] Esarey, E. and Pilloff, M. *Trapping and acceleration in nonlinear plasma waves*. [Physics of Plasmas](#), 2(5):1432, 1995.
- [66] Thomas, A.G.R. *Scalings for radiation from plasma bubbles*. [Physics of Plasmas](#), 17(5):056708, 2010.
- [67] Mangles, S.P.D., Genoud, G., Bloom, M.S., Burza, M., Najmudin, Z., Persson, A., Svensson, K., Thomas, A.G.R., and Wahlström, C.G. *Self-injection threshold in self-guided laser wakefield accelerators*. [Physical Review Special Topics - Accelerators and Beams](#), 15(1):011302, 2012.
- [68] Umstadter, D., Kim, J.K., and Dodd, E. *Laser Injection of Ultrashort Electron Pulses into Wakefield Plasma Waves*. [Physical Review Letters](#), 76(12):2073, 1996.
- [69] Faure, J., Rechatin, C., Norlin, A., Lifschitz, A., Glinec, Y., and Malka, V. *Controlled injection and acceleration of electrons in plasma wakefields by colliding laser pulses*. [Nature](#), 444(7120):737, 2006.
- [70] Pak, A., Marsh, K.A., Martins, S.F., Lu, W., Mori, W.B., and Joshi, C. *Injection and Trapping of Tunnel-Ionized Electrons into Laser-Produced Wakes*. [Physical Review Letters](#), 104(2):025003, 2010.
- [71] Fubiani, G., Esarey, E., Schroeder, C.B., and Leemans, W.P. *Improvement of electron beam quality in optical injection schemes using negative plasma density gradients*. [Physical Review E](#), 73(2):026402, 2006.
- [72] Bulanov, S., Naumova, N., Pegoraro, F., and Sakai, J. *Particle injection into the wave acceleration phase due to nonlinear wake wave breaking*. [Physical Review E](#), 58(5):R5257, 1998.
- [73] Schmid, K., Buck, A., Sears, C.M.S., Mikhailova, J.M., Tautz, R., Herrmann, D., Geissler, M., Krausz, F., and Veisz, L. *Density-transition based electron injector for laser driven wakefield accelerators*. [Physical Review Special Topics - Accelerators and Beams](#), 13(9):091301, 2010.
- [74] Hansson, M., Aurand, B., Davoine, X., Ekerfelt, H., Svensson, K., Persson, A., Wahlström, C.G., and Lundh, O. *Down-ramp injection and independently controlled acceleration of electrons in a tailored laser wakefield accelerator*. [Physical Review Special Topics - Accelerators and Beams](#), 18(7):071303, 2015.

- 
- [75] Grebenyuk, J., Martinez de la Ossa, A., Mehrling, T., and Osterhoff, J. *Beam-driven plasma-based acceleration of electrons with density down-ramp injection at FLASHForward*. *Nuclear Instruments and Methods in Physics Research Section A: Accelerators, Spectrometers, Detectors and Associated Equipment*, 740:246, 2014.
- [76] Tzoufras, M., Lu, W., Tsung, F.S., Huang, C., Mori, W.B., Katsouleas, T., Vieira, J., Fonseca, R.A., and Silva, L.O. *Beam Loading in the Nonlinear Regime of Plasma-Based Acceleration*. *Physical Review Letters*, 101(14):145002, 2008.
- [77] Mori, W.B. *The physics of the nonlinear optics of plasmas at relativistic intensities for short-pulse lasers*. *IEEE Journal of Quantum Electronics*, 33(11):1942, 1997.
- [78] Decker, C.D., Mori, W.B., Tzeng, K.C., and Katsouleas, T. *The evolution of ultra-intense, short-pulse lasers in underdense plasmas*. *Physics of Plasmas*, 3(5):2047, 1996.
- [79] Sprangle, P., Tang, C.M., and Esarey, E. *Relativistic Self-Focusing of Short-Pulse Radiation Beams in Plasmas*. *IEEE Transactions on Plasma Science*, 15(2):145, 1987.
- [80] Feit, M.D., Komashko, A.M., Musher, S.L., Rubenchik, A.M., and Turitsyn, S.K. *Electron cavitation and relativistic self-focusing in underdense plasma*. *Physical Review E*, 57(6):7122, 1998.
- [81] Feit, M.D., Komashko, A.M., and Rubenchik, A.M. *Relativistic self-focusing in underdense plasma*. *Physica D: Nonlinear Phenomena*, 152–153:705, 2001.
- [82] Ibbotson, T.P.A., Bourgeois, N., Rowlands-Rees, T.P., Caballero, L.S., Bajlekov, S.I., Walker, P.A., Kneip, S., Mangles, S.P.D., Nagel, S.R., Palmer, C.A.J., Delerue, N., Doucas, G., Urner, D., Chekhlov, O., Clarke, R.J., Divall, E., Ertel, K., P Foster, Hawkes, S.J., Hooker, C.J., et al. *Investigation of the role of plasma channels as waveguides for laser-wakefield accelerators*. *New Journal of Physics*, 12(4):045008, 2010.
- [83] Gordon, D.F., Hafizi, B., Hubbard, R.F., Peñano, J.R., Sprangle, P., and Ting, A. *Asymmetric Self-Phase Modulation and Compression of Short Laser Pulses in Plasma Channels*. *Physical Review Letters*, 90(21):215001, 2003.
- [84] Sprangle, P., Hafizi, B., Peñano, J.R., Hubbard, R.F., Ting, A., Moore, C.I., Gordon, D.F., Zigler, A., Kaganovich, D., and Antonsen, T.M. *Wakefield generation and GeV acceleration in tapered plasma channels*. *Physical Review E*, 63(5):056405, 2001.
- [85] Schreiber, J., Bellei, C., Mangles, S.P.D., Kamperidis, C., Kneip, S., Nagel, S.R., Palmer, C.A.J., Rajeev, P.P., Streeter, M.J.V., and Najmudin, Z. *Complete Temporal Characterization of Asymmetric Pulse Compression in a Laser Wakefield*. *Physical Review Letters*, 105(23):235003, 2010.
- [86] Faure, J., Glinec, Y., Santos, J.J., Ewald, F., Rousseau, J.P., Kiselev, S., Pukhov, A., Hosokai, T., and Malka, V. *Observation of Laser-Pulse Shortening in Nonlinear Plasma Waves*. *Physical Review Letters*, 95(20):205003, 2005.

## Bibliography

---

- [87] Esarey, E., Shadwick, B.A., Schroeder, C.B., and Leemans, W.P. *Nonlinear Pump Depletion and Electron Dephasing in Laser Wakefield Accelerators*. [AIP Conference Proceedings](#), **737**(1):578, 2004.
- [88] Shadwick, B.A., Schroeder, C.B., and Esarey, E. *Nonlinear laser energy depletion in laser-plasma accelerators*. [Physics of Plasmas](#), **16**(5):056704, 2009.
- [89] Rosenzweig, J.B. *Trapping, thermal effects, and wave breaking in the nonlinear plasma wake-field accelerator*. [Physical Review A](#), **38**(7):3634, 1988.
- [90] Katsouleas, T. and Dawson, J.M. *Unlimited Electron Acceleration in Laser-Driven Plasma Waves*. [Physical Review Letters](#), **51**(5):392, 1983.
- [91] Guillaume, E., Döpp, A., Thaury, C., Ta Phuoc, K., Lifschitz, A., Grittani, G., Goddet, J.P., Tafzi, A., Chou, S.W., Veisz, L., and Malka, V. *Electron Rephasing in a Laser-Wakefield Accelerator*. [Physical Review Letters](#), **115**(15):155002, 2015.
- [92] Blumenfeld, I., Clayton, C.E., Decker, F.J., Hogan, M.J., Huang, C., Ischebeck, R., Iverson, R.H., Joshi, C., Katsouleas, T., Kirby, N., Lu, W., Marsh, K.A., Mori, W.B., Muggli, P., Oz, E., Siemann, R.H., Walz, D.R., and Zhou, M. *Scaling of the longitudinal electric field and transformer ratio in a nonlinear plasma wakefield accelerator*. [Physical Review Special Topics - Accelerators and Beams](#), **13**(11):111301, 2010.
- [93] Ruth, R.D., Morton, P.L., Wilson, P.B., and Chao, A.W. *A plasma wake field accelerator*. [Particle Accelerators](#), **17**(SLAC-PUB-3374):171, 1984.
- [94] England, R.J., Ng, C.K., Frederico, J., Hogan, M.J., Litos, M., Muggli, P., Joshi, C., An, W., Andonian, G., Mori, W., and Lu, W. *High transformer ratio drive beams for wakefield accelerator studies*. In *AIP Conference Proceedings*, volume **1507**, pages 553–558. [AIP Publishing](#), 2012.
- [95] Joshi, C., Blue, B., Clayton, C.E., Dodd, E., Huang, C., Marsh, K.A., Mori, W.B., Wang, S., Hogan, M.J., O’Connell, C., Siemann, R., Watz, D., Muggli, P., Katsouleas, T., and Lee, S. *High energy density plasma science with an ultrarelativistic electron beam*. [Physics of Plasmas](#), **9**(5):1845, 2002.
- [96] Frank, I.M. and Ginzburg, V.L. *Radiation of a uniform moving electron due to its transition from one medium into another*. *Journal of Physics (USSR)*, **9**:353, 1945.
- [97] Dnestrovskii, Y.N. and Kostomarov, D.P. *Radiation of a Modulated Beam of Charged Particles in Passing Through a Round Opening in a Flat Screen*. [Soviet Physics Doklady](#), **4**:132, 1959.
- [98] Cianchi, A., Castellano, M., Catani, L., Chiadroni, E., Honkavaara, K., and Kube, G. *Nonintercepting electron beam size monitor using optical diffraction radiation interference*. [Physical Review Special Topics - Accelerators and Beams](#), **14**(10):102803, 2011.

- 
- [99] Sütterlin, D., Erni, D., Dehler, M., Jäckel, H., Sigg, H., and Schlott, V. *An analytic formalism for the emission of coherent transition radiation from an oblique finite thin metallic target screen*. [Nuclear Instruments and Methods in Physics Research Section B: Beam Interactions with Materials and Atoms](#), 264(2):361, 2007.
- [100] Ter-Mikaelian, M.L. *High energy electromagnetic processes in condensed media*. Interscience tracts on physics and astronomy. Wiley, New York, 1972.
- [101] Ginzburg, V.L. and Tsytovich, V.N. *Transition radiation and transition scattering*. [A. Hilger, New York](#), 1990.
- [102] Williams, E.J. *Correlation of certain collision problems with radiation theory*. [Levin & Munksgaard](#), 1935.
- [103] Dobrovolsky, S.N. and Shul'ga, N.F. *Transversal spatial distribution of transition radiation by relativistic electron in the formation zone by the dotted detector*. [Nuclear Instruments and Methods in Physics Research Section B: Beam Interactions with Materials and Atoms](#), 201(1):123, 2003.
- [104] Casalbuoni, S., Schmidt, B., and Schmäser, P. *Far-Infrared Transition and Diffraction Radiation Part I: Production, Diffraction Effects and Optical Propagation*. [TESLA-FEL Report](#), 2005.
- [105] Kube, G. *Imaging with Optical Transition Radiation Transverse Beam Diagnostics for the XFEL*. [TESLA-FEL Report](#), 2008.
- [106] Castellano, M., Ciani, A., Orlandi, G., and Verzilov, V.A. *Effects of diffraction and target finite size on coherent transition radiation spectra in bunch length measurements*. [Nuclear Instruments and Methods in Physics Research Section A: Accelerators, Spectrometers, Detectors and Associated Equipment](#), 435(3):297, 1999.
- [107] Shkvarunets, A.G. and Fiorito, R.B. *Vector electromagnetic theory of transition and diffraction radiation with application to the measurement of longitudinal bunch size*. [Physical Review Special Topics - Accelerators and Beams](#), 11(1):012801, 2008.
- [108] Xiang, D. and Huang, W.H. *Properties of diffraction radiation in practical conditions: Finite size target effect, surface roughness and pre-wave zone*. [Nuclear Instruments and Methods in Physics Research Section B: Beam Interactions with Materials and Atoms](#), 248(1):163, 2006.
- [109] Brau, C. *Modern Problems in Classical Electromagnetics*. [Oxford Univ. Press, Oxford](#), 2004.
- [110] Goodman, J. *Introduction to Fourier Optics*. McGraw-Hill, 2nd edition, 1996.
- [111] Schroeder, C.B., Esarey, E., van Tilborg, J., and Leemans, W.P. *Theory of coherent transition radiation generated at a plasma-vacuum interface*. [Physical Review E](#), 69(1):016501, 2004.

## Bibliography

---

- [112] Verzilov, V.A. *Transition radiation in the pre-wave zone*. [Physics Letters A](#), 273(1–2):135, 2000.
- [113] Wesch, S. *Echtzeitbestimmung longitudinaler Elektronenstrahlparameter mittels absoluter Intensitäts- und Spektralmessung einzelner kohärenter THz Strahlungspulse*. PhD thesis, [Universität Hamburg](#), 2012.
- [114] Floettmann, K. *Some basic features of the beam emittance*. [Physical Review Special Topics - Accelerators and Beams](#), 6(3):034202, 2003.
- [115] Reiser, M. *Beam Physics Research from 1993 to 2007*. In *Theory and Design of Charged Particle Beams*, pages 507–598. [Wiley-VCH Verlag GmbH & Co. KGaA](#), 2008.
- [116] McDonald, K. and Russell, D. *Methods of emittance measurement*. In *Frontiers of Particle Beams; Observation, Diagnosis and Correction*, pages 122–132. 1989.
- [117] Cowan, T.E., Fuchs, J., Ruhl, H., Kemp, A., Audebert, P., Roth, M., Stephens, R., Barton, I., Blazevic, A., Brambrink, E., Cobble, J., Fernández, J., Gauthier, J.C., Geissel, M., Hegelich, M., Kaae, J., Karsch, S., Le Sage, G.P., Letzring, S., Manclossi, M., et al. *Ultralow Emittance, Multi-MeV Proton Beams from a Laser Virtual-Cathode Plasma Accelerator*. [Physical Review Letters](#), 92(20):204801, 2004.
- [118] Zhang, C.J., Hua, J.F., Wan, Y., Guo, B., Pai, C.H., Wu, Y.P., Li, F., Chu, H.H., Gu, Y.Q., Mori, W.B., Joshi, C., Wang, J., and Lu, W. *Temporal characterization of ultrashort linearly chirped electron bunches generated from a laser wakefield accelerator*. [Physical Review Accelerators and Beams](#), 19(6):062802, 2016.
- [119] Khachatryan, A.G., Irman, A., van Goor, F.A., and Boller, K.J. *Femtosecond electron-bunch dynamics in laser wakefields and vacuum*. [Physical Review Special Topics - Accelerators and Beams](#), 10(12):121301, 2007.
- [120] Lai, R. and Sievers, A.J. *On using the coherent far IR radiation produced by a charged-particle bunch to determine its shape: I Analysis*. [Nuclear Instruments and Methods in Physics Research Section A: Accelerators, Spectrometers, Detectors and Associated Equipment](#), 397(2–3):221, 1997.
- [121] Mihalcea, D., Bohn, C.L., Happek, U., and Piot, P. *Longitudinal electron bunch diagnostics using coherent transition radiation*. [Physical Review Special Topics - Accelerators and Beams](#), 9(8):082801, 2006.
- [122] Pelliccia, D. and Sen, T. *A two-step method for retrieving the longitudinal profile of an electron bunch from its coherent radiation*. [Nuclear Instruments and Methods in Physics Research Section A: Accelerators, Spectrometers, Detectors and Associated Equipment](#), 764:206, 2014.
- [123] Bechhoefer, J. *Kramers–Kronig, Bode, and the meaning of zero*. [American Journal of Physics](#), 79(10):1053, 2011.



- 
- [124] Lai, R. and Sievers, A.J. *Phase problem associated with the determination of the longitudinal shape of a charged particle bunch from its coherent far-ir spectrum.* [Physical Review E](#), 52(4):4576, 1995.
- [125] Marchesini, S., He, H., Chapman, H.N., Hau-Riege, S.P., Noy, A., Howells, M.R., Weierstall, U., and Spence, J.C.H. *X-ray image reconstruction from a diffraction pattern alone.* [Physical Review B](#), 68(14):140101, 2003.
- [126] Nugent, K.A. *Coherent methods in the X-ray sciences.* [Advances in Physics](#), 59(1):1, 2010.
- [127] Fienup, J.R. *Reconstruction And Synthesis Applications Of An Iterative Algorithm.* [Proceedings of SPIE](#), 0373:147, 1984.
- [128] Bourgeois, N., Heigoldt, M., Rittershofer, W., Popp, A., Khrennikov, K., Bajlekov, S.I., Karsh, S., and Hooker, S.M. *Transverse beam profile measurements of laser accelerated electrons using coherent optical radiation.* [AIP Conference Proceedings](#), 1507(1):258, 2012.
- [129] Marinelli, A., Dunning, M., Weathersby, S., Hemsing, E., Xiang, D., Andonian, G., O'Shea, F., Miao, J., Hast, C., and Rosenzweig, J.B. *Single-Shot Coherent Diffraction Imaging of Microbunched Relativistic Electron Beams for Free-Electron Laser Applications.* [Physical Review Letters](#), 110:094802, 2013.
- [130] Bajlekov, S. *Towards a free-electron laser driven by electrons from a laser-wakefield accelerator: simulations and bunch diagnostics.* PhD thesis, [Oxford University](#), 2011.
- [131] Fienup, J.R. *Phase retrieval algorithms: a comparison.* [Applied Optics](#), 21(15):2758, 1982.
- [132] Guizar-Sicairos, M. and Fienup, J.R. *Understanding the twin-image problem in phase retrieval.* [Journal of the Optical Society of America A](#), 29(11):2367, 2012.
- [133] Bakkali Taheri, F., Konoplev, I.V., Doucas, G., Baddoo, P., Bartolini, R., Cowley, J., and Hooker, S.M. *Electron bunch profile reconstruction based on phase-constrained iterative algorithm.* [Physical Review Accelerators and Beams](#), 19(3):032801, 2016.
- [134] Strickland, D. and Mourou, G. *Compression of amplified chirped optical pulses.* [Optics Communications](#), 55(6):447, 1985.
- [135] Cheriaux, G., Walker, B., Dimauro, L.F., Rousseau, P., Salin, F., and Chambaret, J.P. *Aberration-free stretcher design for ultrashort-pulse amplification.* [Optics Letters](#), 21(6):414, 1996.
- [136] Popp, A. *Dynamics of electron-acceleration in laser-driven wakefields: Acceleration limits and asymmetric plasma waves.* PhD thesis, [Ludwig-Maximilians-Universität München](#), 2011.

## Bibliography

---

- [137] Weller, H.G., Tabor, G., Jasak, H., and Fureby, C. *A tensorial approach to computational continuum mechanics using object-oriented techniques*. *Computers in Physics*, 12(6):620, 1998.
- [138] Göppner, B. *Density gradients in discharge capillary waveguides*. MSc thesis, Ludwig-Maximilians-Universität München, 2011.
- [139] *General Particle Tracer*. URL <http://www.pulsar.nl/gpt/>.
- [140] CAWO Solutions. URL <http://www.cawo.com/products/intensifying-screens/green-emitting/>.
- [141] Buck, A., Zeil, K., Popp, A., Schmid, K., Jochmann, A., Kraft, S.D., Hidding, B., Kudryakov, T., Sears, C.M.S., Veisz, L., Karsch, S., Pawelke, J., Sauerbrey, R., Cowan, T., Krausz, F., and Schramm, U. *Absolute charge calibration of scintillating screens for relativistic electron detection*. *Review of Scientific Instruments*, 81(3):033301, 2010.
- [142] Wesch, S., Schmidt, B., Behrens, C., Delsim-Hashemi, H., and Schmäser, P. *A multi-channel THz and infrared spectrometer for femtosecond electron bunch diagnostics by single-shot spectroscopy of coherent radiation*. *Nuclear Instruments and Methods in Physics Research Section A: Accelerators, Spectrometers, Detectors and Associated Equipment*, 665(0):40, 2011.
- [143] Green, M.A. *Self-consistent optical parameters of intrinsic silicon at 300 K including temperature coefficients*. *Solar Energy Materials and Solar Cells*, 92(11):1305, 2008.
- [144] Li, H.H. *Refractive index of silicon and germanium and its wavelength and temperature derivatives*. *Journal of Physical and Chemical Reference Data*, 9(3):561, 1980.
- [145] Tydex. URL <http://www.tydexoptics.com/>.
- [146] Delsim-Hashemi, H. *Infrared single shot diagnostics for the longitudinal profile of the electron bunches at FLASH*. PhD thesis, *Universität Hamburg*, 2008.
- [147] Moharam, M.G., Pommet, D.A., Grann, E.B., and Gaylord, T.K. *Stable implementation of the rigorous coupled-wave analysis for surface-relief gratings: enhanced transmittance matrix approach*. *Journal of the Optical Society of America A*, 12(5):1077, 1995.
- [148] *InfraTec GmbH*. URL <http://www.infratec.eu/>.
- [149] Behrens, C. *Detection and spectral measurements of coherent synchrotron radiation at FLASH*. Diploma thesis, *Universität Hamburg*, 2008.
- [150] Wenz, J., Schleede, S., Khrennikov, K., Bech, M., Thibault, P., Heigoldt, M., Pfeiffer, F., and Karsch, S. *Quantitative X-ray phase-contrast microtomography from a compact laser-driven betatron source*. *Nature Communications*, 6, 2015.
- [151] Golovin, G., Banerjee, S., Liu, C., Chen, S., Zhang, J., Zhao, B., Zhang, P., Veale, M., Wilson, M., Seller, P., and Umstadter, D. *Intrinsic beam emittance of laser-accelerated electrons measured by x-ray spectroscopic imaging*. *Scientific Reports*, 6:24622, 2016.



- 
- [152] Siegman, A. *Lasers*. University Science Books, 1986.
- [153] Barov, N., Rosenzweig, J.B., Conde, M.E., Gai, W., and Power, J.G. *Observation of plasma wakefield acceleration in the underdense regime*. *Physical Review Special Topics - Accelerators and Beams*, 3(1):011301, 2000.
- [154] Gonsalves, A.J., Nakamura, K., Lin, C., Panasenkov, D., Shiraishi, S., Sokollik, T., Benedetti, C., Schroeder, C.B., Geddes, C.G.R., van Tilborg, J., Osterhoff, J., Esarey, E., Toth, C., and Leemans, W.P. *Tunable laser plasma accelerator based on longitudinal density tailoring*. *Nature Physics*, 7(11):862, 2011.
- [155] Chou, S.W. *Investigation of electron acceleration and deceleration in plasmas*. PhD thesis, Ludwig-Maximilians-Universität München, 2016.
- [156] Fonseca, R., Silva, L., Tsung, F., Decyk, V., Lu, W., Ren, C., Mori, W., Deng, S., Lee, S., Katsouleas, T., and Adam, J. *OSIRIS: A Three-Dimensional, Fully Relativistic Particle in Cell Code for Modeling Plasma Based Accelerators*. In *Computational Science - ICCS 2002*, volume 2331 of *Lecture Notes in Computer Science*. Springer Berlin Heidelberg, 2002.
- [157] Fonseca, R.A., Vieira, J., Fiuza, F., Davidson, A., Tsung, F.S., Mori, W.B., and Silva, L.O. *Exploiting multi-scale parallelism for large scale numerical modelling of laser wakefield accelerators*. *Plasma Physics and Controlled Fusion*, 55(12):124011, 2013.
- [158] Sävert, A., Mangles, S.P.D., Schnell, M., Siminos, E., Cole, J.M., Leier, M., Reuter, M., Schwab, M.B., Möller, M., Poder, K., Jäckel, O., Paulus, G.G., Spielmann, C., Skupin, S., Najmudin, Z., and Kaluza, M.C. *Direct Observation of the Injection Dynamics of a Laser Wakefield Accelerator Using Few-Femtosecond Shadowgraphy*. *Physical Review Letters*, 115(5):055002, 2015.
- [159] Németh, K., Shen, B., Li, Y., Shang, H., Crowell, R., Harkay, K.C., and Cary, J.R. *Laser-Driven Coherent Betatron Oscillation in a Laser-Wakefield Cavity*. *Physical Review Letters*, 100(9):095002, 2008.
- [160] Pukhov, A., Sheng, Z.M., and Meyer-ter Vehn, J. *Particle acceleration in relativistic laser channels*. *Physics of Plasmas*, 6(7):2847, 1999.
- [161] Mangles, S.P.D., Walton, B.R., Tzoufras, M., Najmudin, Z., Clarke, R.J., Dangor, A.E., Evans, R.G., Fritsler, S., Gopal, A., Hernandez-Gomez, C., Mori, W.B., Rozmus, W., Tatarakis, M., Thomas, A.G.R., Tsung, F.S., Wei, M.S., and Krushelnick, K. *Electron Acceleration in Cavitated Channels Formed by a Petawatt Laser in Low-Density Plasma*. *Physical Review Letters*, 94(24):245001, 2005.
- [162] Gschwendtner, E. *AWAKE, A Particle-driven Plasma Wakefield Acceleration Experiment*. *CERN Yellow Reports*, 1(0):271, 2016.
- [163] Khrennikov, K., Wenz, J., Buck, A., Xu, J., Heigoldt, M., Veisz, L., and Karsch, S. *Tunable All-Optical Quasimonochromatic Thomson X-Ray Source in the Nonlinear Regime*. *Physical Review Letters*, 114(19):195003, 2015.

## Bibliography

---

- [164] Powers, N.D., Ghebregziabher, I., Golovin, G., Liu, C., Chen, S., Banerjee, S., Zhang, J., and Umstadter, D.P. *Quasi-monoenergetic and tunable X-rays from a laser-driven Compton light source*. *Nature Photonics*, 8(1):28, 2014.
- [165] Rousse, A., Phuoc, K.T., Shah, R., Pukhov, A., Lefebvre, E., Malka, V., Kiselev, S., Burgy, F., Rousseau, J.P., Umstadter, D., and Hulin, D. *Production of a keV X-Ray Beam from Synchrotron Radiation in Relativistic Laser-Plasma Interaction*. *Physical Review Letters*, 93(13):135005, 2004.
- [166] Maier, A.R., Meseck, A., Reiche, S., Schroeder, C.B., Seggebrock, T., and Grüner, F. *Demonstration Scheme for a Laser-Plasma-Driven Free-Electron Laser*. *Physical Review X*, 2(3):031019, 2012.
- [167] Couprie, M.E., Labat, M., Evain, C., Marteau, F., Briquez, F., Khojoyan, M., Benabderahmane, C., Chapuis, L., Hubert, N., C Bourassin-Bouchet, Ajjouri, M.E., Bouvet, F., Dietrich, Y., Valléau, M., Sharma, G., Yang, W., Marcouillé, O., J Vétérin, Berteaud, P., Ajjouri, T.E., et al. *An application of laser-plasma acceleration: towards a free-electron laser amplification*. *Plasma Physics and Controlled Fusion*, 58(3):034020, 2016.
- [168] Ding, Y., Bane, K.L.F., Colocho, W., Decker, F.J., Emma, P., Frisch, J., Guetg, M.W., Huang, Z., Iverson, R., Krzywinski, J., Loos, H., Lutman, A., Maxwell, T.J., Nuhn, H.D., Ratner, D., Turner, J., Welch, J., and Zhou, F. *Beam shaping to improve the free-electron laser performance at the Linac Coherent Light Source*. *Physical Review Accelerators and Beams*, 19(10):100703, 2016.
- [169] Ding, Y., Brachmann, A., Decker, F.J., Dowell, D., Emma, P., Frisch, J., Gilevich, S., Hays, G., Hering, P., Huang, Z., Iverson, R., Loos, H., Miahnahri, A., Nuhn, H.D., Ratner, D., Turner, J., Welch, J., White, W., and Wu, J. *Measurements and Simulations of Ultralow Emittance and Ultrashort Electron Beams in the Linac Coherent Light Source*. *Physical Review Letters*, 102(25):254801, 2009.
- [170] Hogan, M.J., Raubenheimer, T.O., Seryi, A., Muggli, P., Katsouleas, T., Huang, C., Lu, W., An, W., Marsh, K.A., Mori, W.B., Clayton, C.E., and Joshi, C. *Plasma wakefield acceleration experiments at FACET*. *New Journal of Physics*, 12(5):055030, 2010.
- [171] Balandin, V., Brenner, G., Gerth, C., Golubeva, N., Mavric, U., Schlarb, H., Schneidmiller, E.A., Schreiber, S., Steffen, B., Yan, M., and Yurkov, M.V. *Operation of Free Electron Laser FLASH Driven by Short Electron Pulses*. *The 7th International Particle Accelerator Conference, Busan, Korea*, 2016.
- [172] *FLASH accelerator website*. URL <https://flash.desy.de/accelerator/>.
- [173] Seggebrock, T. *Conceptual design of a laser-plasma accelerator driven free-electron laser demonstration experiment*. PhD thesis, *Ludwig-Maximilians-Universität München*, 2015.
- [174] Loulergue, A., Labat, M., Evain, C., Benabderrahmane, C., Malka, V., and Couprie, M.E. *Beam manipulation for compact laser wakefield accelerator based free-electron lasers*. *New Journal of Physics*, 17(2):023028, 2015.

- [175] Raith, S. *Longitudinal phase space dynamics in laser-wakefield acceleration*. PhD thesis, Ludwig-Maximilians-Universität München. To be published.



# List of abbreviations

<b>TR</b>	transition radiation
<b>CTR</b>	coherent transition radiation
<b>COTR</b>	coherent optical transition radiation
<b>LWFA</b>	laser wakefield acceleration
<b>PWFA</b>	plasma wakefield acceleration
<b>PIC</b>	particle-in-cell
<b>FWHM</b>	full width at half maximum
<b>rms</b>	root mean square
<b>CEP</b>	carrier-envelope phase
<b>Ti:Sa</b>	titanium-sapphire
<b>ATLAS</b>	Advanced Titanium-Sapphire Laser System
<b>CPA</b>	chirped pulse amplification
<b>MPQ</b>	Max Planck Institut für Quantenoptik
<b>LEX</b>	Laboratory for Extreme Photonics
<b>LMU</b>	Ludwig-Maximilians-Universität München
<b>DESY</b>	Deutsches Elektronen-Synchrotron
<b>SLAC</b>	SLAC National Accelerator Laboratory
<b>CCD</b>	charge-coupled device
<b>PID</b>	proportional-integral-derivative
<b>FROG</b>	frequency-resolved optical gating
<b>Bubblewrap</b>	a reconstruction algorithm to retrieve the longitudinal bunch profile from the CTR spectrum, developed by our collaborators from Oxford University <a href="#">[28]</a>

<b>OSIRIS</b>	3D particle-in-cell code developed by the OSIRIS consortium [ <a href="#">156</a> , <a href="#">157</a> ]
<b>FEL</b>	free-electron laser
<b>SASE</b>	self-amplified spontaneous emission
<b>FACET</b>	Facility for Advanced Accelerator Experimental Tests
<b>LCLS</b>	Linac Coherent Light Source
<b>LHC</b>	Large Hadron Collider
<b>ILC</b>	International Linear Collider
<b>FLASH</b>	Free-electron LASer in Hamburg
<b>RF</b>	radio frequency

# List of publications

During the work for this thesis the following articles have been published in peer-reviewed journals:

- Chou, S., Xu, J., Khrennikov, K., Cardenas, D.E., Wenz, J., **Heigoldt, M.**, Hofmann, L., Veisz, L., and Karsch, S. *Collective Deceleration of Laser-Driven Electron Bunches*. [Physical Review Letters](#), 117(14):144801, 2016.
- **Heigoldt, M.**, Popp, A., Khrennikov, K., Wenz, J., Chou, S.W., Karsch, S., Bajlekov, S.I., Hooker, S.M., and Schmidt, B. *Temporal evolution of longitudinal bunch profile in a laser wakefield accelerator*. [Physical Review Special Topics - Accelerators and Beams](#), 18(12):121302, 2015.
- Wenz, J., Schleede, S., Khrennikov, K., Bech, M., Thibault, P., **Heigoldt, M.**, Pfeiffer, F., and Karsch, S. *Quantitative X-ray phase-contrast microtomography from a compact laser-driven betatron source*. [Nature Communications](#), 6:7568, 2015.
- Khrennikov, K., Wenz, J., Buck, A., Xu, J., **Heigoldt, M.**, Veisz, L., and Karsch, S. *Tunable All-Optical Quasimonochromatic Thomson X-Ray Source in the Nonlinear Regime*. [Physical Review Letters](#), 114(19):195003, 2015.
- Heissler, P., Lugovoy, E., Hörlein, R., Waldecker, L., Wenz, J., **Heigoldt, M.**, Khrennikov, K., Karsch, S., Krausz, F., Abel, B., and Tsakiris, G.D. *Using the third state of matter: high harmonic generation from liquid targets*. [New Journal of Physics](#), 16(11):113045, 2014.
- Bajlekov, S.I., **Heigoldt, M.**, Popp, A., Wenz, J., Khrennikov, K., Karsch, S., and Hooker, S.M. *Longitudinal electron bunch profile reconstruction by performing phase retrieval on coherent transition radiation spectra*. [Physical Review Special Topics - Accelerators and Beams](#), 16(4):040701, 2013.
- Buck, A., Wenz, J., Xu, J., Khrennikov, K., Schmid, K., **Heigoldt, M.**, Mikhailova, J.M., Geissler, M., Shen, B., Krausz, F., Karsch, S., and Veisz, L. *Shock-Front Injector for High-Quality Laser-Plasma Acceleration*. [Physical Review Letters](#), 110(18):185006, 2013.
- Weingartner, R., Raith, S., Popp, A., Chou, S., Wenz, J., Khrennikov, K., **Heigoldt, M.**, Maier, A.R., Kajumba, N., Fuchs, M., Zeitler, B., Krausz, F., Karsch, S., and Grüner, F. *Ultralow emittance electron beams from a laser-wakefield accelerator*. [Physical Review Special Topics - Accelerators and Beams](#), 15(11):111302, 2012.



## List of publications

---

- Weingartner, R., Fuchs, M., Popp, A., Raith, S., Becker, S., Chou, S., **Heigoldt, M.**, Khrennikov, K., Wenz, J., Seggebrock, T., Zeitler, B., Major, Z., Osterhoff, J., Krausz, F., Karsch, S., and Grüner, F. *Imaging laser-wakefield-accelerated electrons using miniature magnetic quadrupole lenses*. [Physical Review Special Topics - Accelerators and Beams](#), **14(5):052801**, 2011.
- Waldecker, L., Heissler, P., Hörlein, R., Allinger, K., **Heigoldt, M.**, Khrennikov, K., Wenz, J., Karsch, S., Krausz, F., and Tsakiris, G.D. *Focusing of high order harmonics from solid density plasmas*. [Plasma Physics and Controlled Fusion](#), **53(12):124021**, 2011.

# List of figures & data archiving

The experimental raw data, the evaluation files and the figures can be found on the Data Archive Server of the Laboratory for Attosecond Physics at the Max Planck Institut für Quantenoptik. On the next pages, the path and name of the respective file(s) used for the data evaluation and the plot of each figure is given relative to the base directory. Typically, these Matlab files generate the .pdf images located in the directory "pics/". If no file is given the image is a drawing. The raw data is placed in a separate folder together with additional information on the data evaluation.

2.1	Electron motion in a plane wave laser field.	
	•plot file: matlab_scripts/LWFA_PlaneWaveMotion.m . . . . .	9
2.2	Ionization mechanisms.	
	•plot file: matlab_scripts/LWFA_Ionization.m . . . . .	12
2.3	Longitudinal and radial electric field of a linear laser-driven wakefield.	
	•plot file: matlab_scripts/LWFA_linWake.m . . . . .	18
2.4	One-dimensional nonlinear laser driven wakefield.	
	•plot file: matlab_scripts/LWFA_1DWakeAndSeparatrix.m . . . . .	21
2.5	PIC simulations showing the shape of the wakefield in the blow-out regime. . . .	23
2.6	Longitudinal phase space of an electron in a 1D nonlinear wakefield.	
	•plot file: matlab_scripts/LWFA_1DWakeAndSeparatrix.m . . . . .	25
2.7	Effects of beam loading.	
	•plot file: matlab_scripts/LWFA_Beamloading.m . . . . .	29
2.8	Optimal laser parameters in the bubble regime.	
	•plot file: matlab_scripts/LWFA_Limits.m . . . . .	36
3.1	Sketch of the coordinate system used to calculate the TR diffraction integral. . . .	41
3.2	Angular distribution of TR in the far-field.	
	•plot file: matlab_scripts/CTR_GF.m . . . . .	43
3.3	Angular distribution of TR in the far-field for a finite size radiator.	
	•plot file: matlab_scripts/CTR_FiniteSize.m . . . . .	44
3.4	Angular distribution of TR in the near-field.	
	•plot file: matlab_scripts/CTR_NearField.m . . . . .	45
3.5	Schematic drawing of the coordinate system used to describe the electron bunch density distribution. . . . .	47
3.6	Illustration of the incoherent and coherent superposition of TR from individual bunch electrons. . . . .	48

---

3.7	Transverse form factor.	
	•plot file: matlab_scripts/CTR_FormFactor.m . . . . .	50
3.8	Longitudinal form factor.	
	•plot file: matlab_scripts/CTR_FormFactor.m . . . . .	51
3.9	Impact of beam divergence on the CTR spectrum.	
	•plot file: matlab_scripts/CTR_Divergence.m . . . . .	52
3.10	Illustration of the transverse phase space.	54
3.11	Effect of a transverse phase space correlation.	
	•plot/evaluation file: evaluation/PhaseSpaceCorrelations/ PositionAngleCorrelation.m . . . . .	56
3.12	Effect of a longitudinal phase space correlation.	
	•plot/evaluation file: evaluation/PhaseSpaceCorrelations/ a) quadraticEnergyChirp.m b) broadbandSpec.m c) exponentialSpec.m . . . . .	58
3.13	Flowchart of the Gerchberg-Saxton algorithm.	60
3.14	Adaptive support selection.	62
4.1	Chirped pulse amplification.	66
4.2	Schematic layout of the ATLAS laser system.	66
4.3	Intensity distribution of the ATLAS laser in the focal plane.	
	•plot file: evaluation/Laser/analyzeFocus.m . . . . .	67
4.4	Overview of the experimental setup.	68
4.5	Sketch of the length-variable gas target.	69
4.6	Electron spectrometer.	
	•b) plot file: evaluation/Plot_scripts/EXP_Espec_deflection.m . . . . .	70
4.7	Rendering of the CTR diagnostic setup.	71
4.8	Optical properties of silicon in the visible to near-infrared frequency range.	
	•a) plot file: matlab_scripts/EXP_Silicon.m . . . . .	72
4.9	Layout of the mid-infrared spectrometer.	73
4.10	Sketch of the diffraction geometry of a blazed reflection grating.	74
4.11	Diffraction efficiency of a blazed reflection grating for s- and p-polarisation.	
	•plot file: evaluation/plotScripts/plotGratingEffs.m •evaluation instructions: evaluation/Grating_calculation/README.txt . . . . .	76
4.12	Sketch of the cascading principle of the mid-infrared spectrometer.	77
4.13	Total diffraction efficiency of the cascaded setup.	
	•plot file: evaluation/plotScripts/plotGratingEffs.m •evaluation instructions: evaluation/Grating_calculation/README.txt . . . . .	77
4.14	Sketch of the parabolic ring mirror used in the mid-infrared spectrometer.	78
4.15	Schematic drawing of the pyroelectric line array.	79
5.1	Modelling representation of the CTR beam path.	83
5.2	Spectral fluence of CTR on the detection optics.	
	•plot file: evaluation/CTR_propagation/plot_CTR_transmission.m •evaluation file: evaluation/CTR_propagation/propagate_Fields.m . . . . .	86

---

5.3	Transmitted spectral energy incident on the detector.	
	•plot file: evaluation/CTR_propagation/plot_CTR_transmission.m	
	•evaluation file: evaluation/CTR_propagation/propagate_Fields.m . . . . .	87
5.4	Interference effect between both CTR radiators in the detection plane.	
	•plot file: evaluation/CTR_propagation/plot_CTR_transmission.m	
	•evaluation file: evaluation/CTR_propagation/propagate_Fields.m . . . . .	88
6.1	Energy resolved divergence of the electron bunch in the horizontal plane.	
	•evaluation/plot file: evaluation/divergence/bunchDivergence.m . . . . .	90
6.2	Projected transverse beam profile.	
	•plot file: evaluation/divergence/transverseProfile.m . . . . .	91
6.3	Sketch of the geometry of the electron beam pointing screen. . . . .	91
6.4	Electron energy evolution in dependence of the acceleration length.	
	•a) evaluation/plot file: evaluation/Lengthscans/eEnergyEvolution_n1.m	
	•b) evaluation/plot file: evaluation/Lengthscans/eEnergyEvolution_n2.m . . . . .	94
6.5	Evaluation of $L_d$ based on the evolution of the electron energies.	
	•a) evaluation/plot file: evaluation/Lengthscans/eEnergyEvolution_n1.m	
	•b) evaluation/plot file: evaluation/Lengthscans/eEnergyEvolution_n2.m . . . . .	95
6.6	Depletion and dephasing lengths after laser self-focusing to a matched spot size.	
	•plot file: matlab_scripts/EA_dephasing_depletion_length.m . . . . .	98
7.1	Single-shot data of the electron bunch diagnostics.	
	•plot file: evaluation/LengthScans/plotSingleShot.m . . . . .	102
7.2	Measured and reconstructed longitudinal form factors and reconstructed bunch profiles for two representative shots.	
	•plot file: evaluation/LengthScans/plotSingleShot.m . . . . .	103
7.3	Longitudinal form factors of multi-bunch structures with Gaussian shape.	
	•plot file: evaluation/plotScripts/plotSpecsMultiBunches.m . . . . .	104
7.4	Effects of charge ratio and bunch duration on the form factor of a double bunch structure.	
	•plot file: evaluation/plotScripts/plotSpecsMultiBunches.m . . . . .	105
7.5	Bunch profile evolution at a plasma electron density of $n_1 = 3.4 \times 10^{18} \text{ cm}^{-3}$ .	
	•plot file: evaluation/LengthScans/analyzeLengthscanN1.m . . . . .	106
7.6	Evolution of the electron beam parameters in dependence of the gas cell length at a plasma density of $n_1 = 3.4 \times 10^{18} \text{ cm}^{-3}$ .	
	•a) plot file: evaluation/LengthScans/combinedPlots.m	
	•b,c) plot file: evaluation/LengthScans/analyzeLengthscanN1.m . . . . .	108
7.7	Bunch profile evolution at $n_2 = 7.7 \times 10^{18} \text{ cm}^{-3}$ .	
	•plot file: evaluation/LengthScans/analyzeLengthscanN2.m . . . . .	111
7.8	Evolution of the electron beam parameters in dependence of the gas cell length at a plasma density of $n_1 = 7.7 \times 10^{18} \text{ cm}^{-3}$ .	
	•a) plot file: evaluation/LengthScans/combinedPlots.m	
	•b,c) plot file: evaluation/LengthScans/analyzeLengthscanN2.m . . . . .	112
7.9	Bunch separation in dependence of the plasma electron density.	
	•plot file: evaluation/LengthScans/analyzePscan.m . . . . .	115

---

7.10	Single-shot CTR spectra obtained at different plasma densities.	
	•plot file: evaluation/LengthScans/plotSingleShot.m . . . . .	116
7.11	Evolution of the electron energy spectrum in dependence of the plasma density.	
	•plot file: evaluation/LengthScans/analyzePscan.m . . . . .	117
7.12	3D PIC simulation reproducing an LWFA to PWFA transition.	
	•OSIRIS input file: evaluation/PIC/inputFiles/3Dhr	
	•OSIRIS data: OSIRIS_data/ne34_3Dhr . . . . .	120
7.13	Evolution of the on-axis electron density and the electron energy spectrum in dependence of the simulated propagation length.	
	•OSIRIS input file: evaluation/PIC/inputFiles/3Dhr	
	•OSIRIS data: OSIRIS_data/ne34_3Dhr	
	•plot file: evaluation/PIC/plotPICsim.m . . . . .	122
7.14	Bunch profile evolution extracted from the PIC simulation.	
	•OSIRIS input file: evaluation/PIC/inputFiles/3Dhr	
	•OSIRIS data: OSIRIS_data/ne34_3Dhr	
	•plot file: evaluation/PIC/plotPICsim.m . . . . .	123
7.15	2D PIC simulations showing trapping of a 2 <sup>nd</sup> bunch in either the 1 <sup>st</sup> or the 2 <sup>nd</sup> wake period.	
	left column:	
	•OSIRIS input file: evaluation/PIC/inputFiles/2D1st	
	•OSIRIS data: OSIRIS_data/2D1st	
	right column:	
	•OSIRIS input file: evaluation/PIC/inputFiles/2D2nd	
	•OSIRIS data: OSIRIS_data/2D2nd . . . . .	125
7.16	Local enhancement of the form factor at visible frequencies.	
	•plot file: evaluation/LengthScans/plotSingleShot.m . . . . .	128
7.17	CTR spectra emitted by a modulated bunch profile.	
	•plot file: matlab_scripts/plotMacroBunchSpecs.m . . . . .	130
7.18	Width of the enhancement.	
	•plot file: evaluation/LengthScans/analyzeBump.m . . . . .	131
7.19	CTR emission in the optical range before and after injection of a 2 <sup>nd</sup> bunch in the $n_2$ case.	
	•plot file: evaluation/LengthScans/plotSingleShot.m . . . . .	132
7.20	Center wavelength and amplitude of the enhancement.	
	•plot file: evaluation/LengthScans/analyzeBump.m . . . . .	132
A.1	Overview of the different sources that contribute to the spectrometers' relative spectral response function.	
	•b) plot file: evaluation/plotScripts/plotGratingEffs.m	
	•c,d) plot file: evaluation/plotScripts/plotPyroResponse.m . . . . .	141
A.2	Relative spectral response.	
	•plot file: evaluation/Lengthscans/plotPyroResponse.m . . . . .	142
A.3	Influence of the beam divergence on the CTR transmission function.	
	•plot file: evaluation/LengthScans/plotSingleShot.m . . . . .	143

---

A.4	Relative error $\sigma_{F_{\parallel}}$ in the measurement of the longitudinal form factor.	
	•plot file: evaluation/LengthScans/plotSingleShot.m . . . . .	144
A.5	Measurement uncertainty in the time domain.	
	•evaluation file: evaluation/LengthScans/analyzeLengthscanN1.m	
	•plot file: evaluation/LengthScans/plotSingleShot.m . . . . .	145





# Acknowledgements

- Foremost, I would like to thank my doctoral advisor **Prof. Dr. Stefan Karsch** for accepting me as his PhD student, his guidance during this thesis, the knowledge transfer (including his exceptional lab skills) and the (almost) never-ending contract extensions.
- Equally, I thank **Prof. Dr. Ferenc Krausz** for the opportunity to pursue my PhD at his chair, which provides such an excellent research environment, as well as for securing the funding that enables all the outstanding experimental equipment.
- Furthermore, I want to thank **Prof. Dr. Malte Kaluza** for reviewing this thesis.
- I am also indebted to **Prof. Dr. Simon Hooker** and **Dr. Svetoslav Bajlekov**, not only for their assistance during the experimental campaign, but also for their efforts in terms of the bunch profile retrieval process that led to the development of the [Bubblewrap](#) algorithm as well as for reviewing and improving my manuscript.
- I would also like to thank **Dr. Bernhard Schmidt** and his group at [DESY](#) for supplying the custom pyroelectric detector arrays and readout electronics.
- Many thanks also to **Jorge Viera** and the **OSIRIS consortium** for providing access to their [PIC](#) code.
- I owe my deepest gratitude to my co-workers Shao-Wei Chou, Konstantin Khrennikov, Dr. Antonia Schmalz, Johannes Wenz and all my other colleagues at [LMU](#) and [MPQ](#). It was a great pleasure working with you.
- Finally, I want to thank my family for all the support during my journey through life so far.